Insertion cathode materials based on borate compounds

Florian Strauss

Université Pierre et Marie Curie

Ecole doctorale 397 Physique et Chimie des Matériaux

Collège de France, Laboratoire de Chimie du Solide et de l'Energie

University of Ljubljana

Faculty of chemistry and chemical technology

National Institute of Chemistry, Laboratory of materials chemistry

Insertion cathode materials based on borate compounds

by Florian Alexander STRAUSS

PhD thesis in Chemistry

Directed by Robert Dominko and Jean-Marie Tarascon

To be presented and defended in public on November 25th, 2016

In front of the jury:

Prof. Maximilian Fichtner	Professor, Helmholtz-Institute Ulm	Referee
Prof. Lorenzo Stievano	Professor, Université Montpellier II	Referee
Prof. Miran Gaberšček	Professor, University of Ljubljana	Examiner
Prof. Anton Meden	Professor, University of Ljubljana	Examiner
Dr. David Portehault	CNRS Researcher, UPMC	Examiner
Dr. Gwenaëlle Rousse	associate Professor, Collège de France	Examiner

Université Pierre et Marie Curie

Ecole doctorale 397 Physique et Chimie des Matériaux

Collège de France, Laboratoire de Chimie du Solide et de l'Energie

Université de Ljubljana

Faculty of chemistry and chemical technology

National Institute of Chemistry, Laboratory of materials chemistry

Matériaux d'insertion de cathode d'insertion à base des borate

Par Florian Alexander STRAUSS

Thèse de doctorate de Chimie des Matériaux

Dirigée par Robert Dominko and Jean-Marie Tarascon

Présentée et soutenue publiquement le 25 November 2016

Devant un jury composéee de:

Prof. Maximilian Fichtner	Professeur, Helmholtz-Institute Ulm	Referee
Prof. Lorenzo Stievano	Professeur, Université Montpellier II	Referee
Prof. Miran Gaberšček	Professeur, Université de Ljubljana	Examiner
Prof. Anton Meden	Professeur, Université de Ljubljana	Examiner
Dr. David Portehault	Directeur de recherche CNRS, UPMC	Examiner
Dr. Gwenaëlle Rousse	Maitre de conferences, Collège de France	Examiner

Acknowledgement

At the most prior, I want to sincerely acknowledge my thesis supervisors Dr. Robert Dominko and Prof. Jean-Marie Tarascon whose support and guidance made the completion of this work possible. It has been a great opportunity and experience to learn various aspects of solids state- and electrochemistry from them and improve my scientific skills. Furthermore I really appreciate the close collaboration on a daily basis providing a very inspiring atmosphere, leading to new ideas and encouraging me throughout my PhD period.

I would extend my sincere thanks to Dr. Gwenaëlle Rousse for her guidance and support mainly on crystallography and diffraction experiments. She introduced and provided me useful advices for structural work during my thesis, improving my skills in this field, and I wish to thank her for close collaboration throughout my thesis work.

In addition I would also thank all my colleges at the National Institute of Chemistry, Slovenia and Collège de France, Paris for a very pleasant social and working atmosphere. Many fruitful discussions brought me to new thinking and ideas related to my work, but also in general about science related to energy conversion and storage.

In addition ALISTORE-ERI is greatfully acknowledged for financial support of the PhD thesis. Use of the 11-BM mail service of the APS at Argonne National Laboratory for synchrotron X-ray diffraction measurements was supported by the U.S. Department of Energy under Contract No. DE-AC02-06CH11357 and is greatly acknowledged.

Especially I would like to thank Daniel Alves Dalla Corte (Collège de France) for help and assistance in conductivity measurements and SEM imaging, Matthieu Courty (Université Picardie Jules Verne, Amiens) for conducting thermal analysis, and moreover Mingxue Tang (Université d'Orléans) and Hérve Vezin (Université Lille) for recording EPR and NMR spectroscopy. I would like to thank Carlotta Ciacobe (ESRF – The European Synchrotron, Grenoble) for conducting the high temperature synchrotron XRD measurements. Moulay Tahar Sougrati (Université de Montpellier) is acknowledged for conducting Mössbauer measurements, Mohammed Ben Hassine (Ecole centrale Paris) and Dmitry Batuk (Univerity of Antwerp) for their work on SEM and TEM and Matthieu Saubanere (Université de Montpellier) for providing DFT calculations.

Abstract

The increased need of energy storage via the development of Li- and Na-ion batteries requires a continuous search for new positive electrode materials having higher energy density while being safe and sustainable. For this purpose we explored borate based compounds capable of reacting with Li/ Na-ions in a reversible way either through intercalation/deintercalation or conversion reactions. During this survey we focused on identifying candidates possessing a polyborate anion (B_xO_y with $x > 1$), that are expected to show elevated redox potentials compared to BO_3 based materials. Using $Li_6CuB_4O_{10}$ as a model compound we showed the possibility to achieve redox potentials of 4.2 and 3.9 V vs. Li^+/Li^0 for the α- and β-polymorphs, respectively. This redox activity was rationalized through complementary EPR spectroscopy and DFT calculations. We further reveal the structural and synthetic relation between the two polymorphs and show a surprisingly high ionic conductivity of 1.4 $mS \cdot cm^{-1}$ at 500°C for α-$Li_6CuB_4O_{10}$, related to a structural transition. Moreover we were able to prepare two new sodium transition metal pentaborates $Na_3MB_5O_{10}$ (M = Fe, Co) possessing an open structure feasible for Na^+ migration. For M = Fe we observed a reversible Na intercalation at an average potential of 2.5 V vs. Na^+/Na^0, opposed to $Na_3CoB_5O_{10}$ which turned out to be electrochemical inactive. Finally deviating from classical insertion/ deinsertion compounds, we studied the electrochemical driven reaction mechanism of a bismuth oxyborate $Bi_4B_2O_9$ versus Li through electrochemical measurements combined with XRD and TEM investigations. Remarkably, we found that it is possible to reversibly cycle this material between 1.7 and 3.5 V with an average redox potential of 2.3 V vs. Li^+/Li^0 with only 5wt% carbon additive and a small polarization ~300 mV. Owing to the complexity of 3d-metal borate chemistry encountered through this PhD, the chances of having a borate based positive electrode for next generation Li-ion batteries is rather slim.

Keywords: Li/Na-ion batteries, cathode materials, borates, ionic conductivity

Povzetek

Povečana potreba po shranjevanju energije in s tem razvoj Li- in Na-ionskih akumulatorjev zahteva kontinuirno iskanje novih katodnih elektrodnih materialov, ki imajo višjo energijsko gostoto in so obenem varne za uporabo ter iz široko dostopnih elementov. V ta namen smo preučevali spojine na osnovi boratov, ki lahko reverzibilno izmenjujejo Li ali Na ione s klasično vgradnjo/izgradnjo v/iz strukture ali pa z konverzijsko elektrokemijsko reakcijo. Raziskave smo usmerili v identifikacijo materialov z poliboratnim anionom (B_xO_y, kjer je x > 1), od katerih se pričakuje višji redoks potencial glede na spojine, ki imajo BO_3 skupino v strukturi. Z uporabo $Li_6CuB_4O_{10}$ kot modelne spojine smo pokazali, da je mogoče doseči redoks potencial 4.2 in 3.9 V glede na Li^+/Li^0 za α- in β-polimorf. Redoks aktivnost bakra smo dodatno dokazali z EPR spektroskopijo in DFT izračuni. Nadalje smo preučevali odvisnost sinteznih pogojev in strukture dveh polimorfov, kjer smo pokazali, da ima α-$Li_6CuB_4O_{10}$ pri 500°C prevodnost 1.4 $mS \cdot cm^{-1}$. Dodatno smo pripravili dve novi natrijivi spojini na osnovi prehodne kovine in pentaborata $Na_3MB_5O_{10}$ (M = Fe, Co). Za M=Fe smo izmerili reverzibilno insercijo natrija pri napetosti 2.5 V glede na Na^+/Na^0, medtem ko se je izkazalo, da je $Na_3CoB_5O_{10}$ elektrokemijsko neaktiven. Z iskanjem novih aktivnih poliboratnih spojin smo zapustili klasične materiale v katere se alkalne kovine vgrajujejo in smo se odločili za študij elektrokemijskega mehanizma konverzije $Bi_4B_2O_9$ glede na Li^+/Li^0 v povezavi z XRD in TEM meritvami. Spojino je mogoče reverzibilno galvanostatsko ciklati med 1.7 in 3.5V s povprečno napetostjo 2.3 V glede na Li^+/Li^0 pri čemer smo uporabili samo 5ut% ogljika, obenem pa smo dobili zelo majhno polarizacijo ~300 mV. Glede na kompleksnost boratne kemije z 3d prehodnimi kovinami s katerimi smo se ukvarjali tekom tega doktorata, so šanse, da bi imeli boratne spojine, kot katode za Li-ionske akumulatorje za naslednjo generacijo zelo majhne.

Ključne besede: Li / Na-ionske baterije, katodni materiali, boratov, ionsko prevodnost

Résumé

Le besoin accru de stockage d'énergie via le développement de Li- et batteries Na-ion nécessite une recherche continue de nouveaux matériaux d'électrodes positives ayant une densité d'énergie plus élevée tout en étant sûre et durable. A cet effet, nous avons exploré les composés de base de borate capables de réagir avec Li / Na-ions de manière réversible soit par intercalation / désintercalation ou de conversion des réactions. Au cours de cette enquête, nous avons mis l'accent sur l'identification des candidats possédant un anion polyborate (B_xO_y avec x> 1), qui devraient montrer des potentiels redox élevés par rapport aux matériaux à base BO_3. $Li_6CuB_4O_{10}$ utilisant comme composé modèle, nous avons montré la possibilité d'obtenir des potentiels d'oxydo-réduction de 4.2 et 3.9 V vs. Li^+/Li^0 les a et ß polymorphes, respectivement. Cette activité redox a été rationalisée par spectroscopie EPR complémentaire et calculs DFT. Nous révélons en outre la relation structurelle et synthétique entre les deux polymorphes et montrons une conductivité ionique étonnamment élevé de 1.4 $mS \cdot cm^{-1}$ à 500°C pour les α-$Li_6CuB_4O_{10}$, liée à une transition structurelle. De plus, nous avons pu préparer deux nouveaux pentaborates transition de sodium métalliques $Na_3MB_5O_{10}$ (M = Fe, Co) possédant une structure ouverte possible pour la migration Na^+. M = Fe, nous avons observé une intercalation Na réversible à un potentiel moyen de 2.5 V par rapport à Na^+/Na^0, opposé à $Na_3CoB_5O_{10}$ qui se révéla être inactif électrochimique. Enfin déviant de composés d'insertion / désinsertion de classiques, nous avons étudié le mécanisme d'un oxyborate de bismuth par rapport $Bi_4B_2O_9$ Li réaction électrochimique entraînée par des mesures électrochimiques combinées à XRD et TEM investigations. Fait étonnant, nous avons trouvé qu'il est possible de faire défiler ce matériau réversible entre 1.7 et 3.5 V avec un potentiel d'oxydo-réduction moyenne de 2.3 V vs. Li^+/Li^0 avec seulement 5 wt% d'additif de carbone et une faible polarisation ~300 mV. En raison de la complexité de la chimie de borate 3d-métal rencontré par le biais de cette thèse, les chances d'avoir une électrode positive à base de borate pour les batteries Li/Na-ion de nouvelle génération est plutôt mince.

Mots clés : batteries à ions Li/Na, matériaux de cathode, borates, conductivité ionique

Table of content

1 Introduction

The energy demand of our modern society is continuously growing, however the global consumed energy is nowadays mainly produced through the combustion of fossil resources, whereas only a small proportion of 8% of the total consumed energy is supplied through renewables (Figure 1a).

It is widely accepted that geopolitical issues and global greenhouse gas emissions (in particular CO_2) originating from the utilization of energy production by burning fossil fuels, have a huge impact on our modern society, with future consequences which cannot yet been entirely predicted. More than 50% of the global CO_2 emitted, is generated by the production of electricity and heat as well as powering our global transportation (Figure 1b).[1,2]

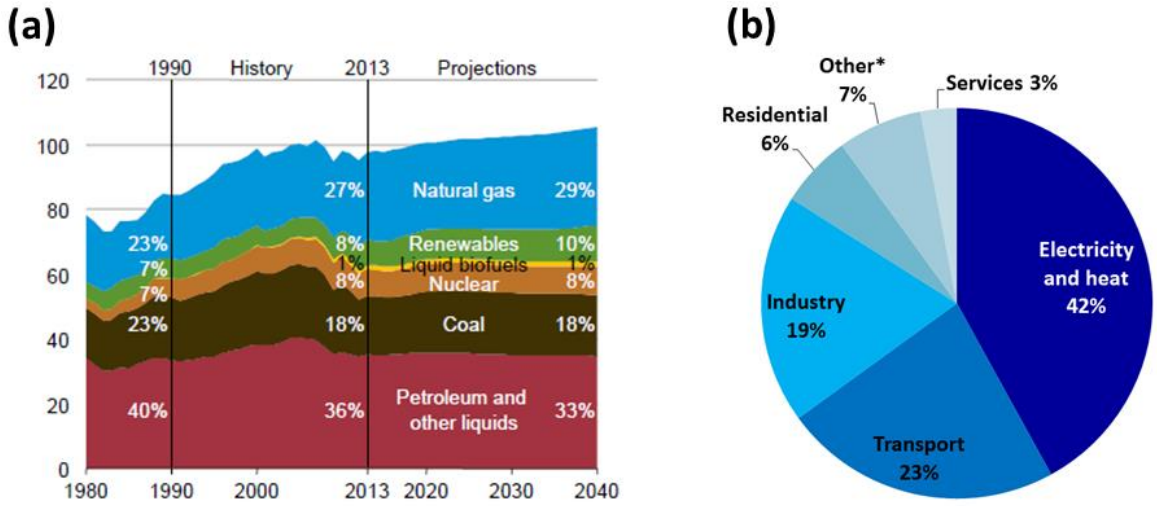

Figure 1: (a) *Total primary global energy consumption from 1980 to 2040 by fuel (Mtoe).*[1] ***(b)*** *World CO_2 emission by sector in 2013.*[2]

To circumvent the global dependence on fossil fuels and minimize the global warming, an increased interest has been aroused for the development of renewable energy supply for electricity generation and transportation. Over the last 20 years global renewable energy production has been strongly raised (Figure 2), not only driven by their sustainability and positive effect on the environment but also due to the continuous raise of the prices for fossil fuels (although temporary fluctuations can occur) since it is supposed that their maximum production is reached.

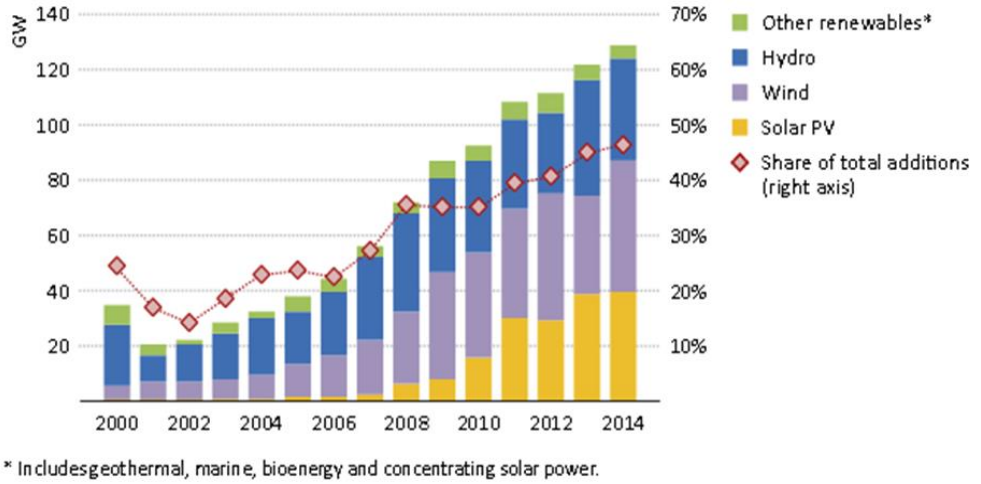

Figure 2: *Global renewables-based power capacity additions by type and share of total capacity additions.*[3]

To change the energy supply from fossil fuels to renewables, one major issue has to be solved in order to fully implement and benefit from them. This major issue of renewable energy production is their non-continuously power supply, since the amount of energy harvested is a function of time, place, and weather conditions. In order to balance the energy production from renewables with the consumption demands, smart solutions are needed. Obviously one can think about storing excess energy in hydroelectric power stations, unfortunately their availability is limited to the local landscape, requires large areas and comes along with low roundtrip efficiencies.[4]

Several energy storage technologies like the afore mentioned pumped hydro, compressed air, flywheels and electrochemical energy storage devices (batteries, capacitors) have been proposed in the past, however it is important to note that none of these technologies is able to manage all kinds of different demands, if comparing for instance transportation versus grid scale energy storage, but batteries may play an important role for electric powered transportation and grid support (Figure 3).[5]

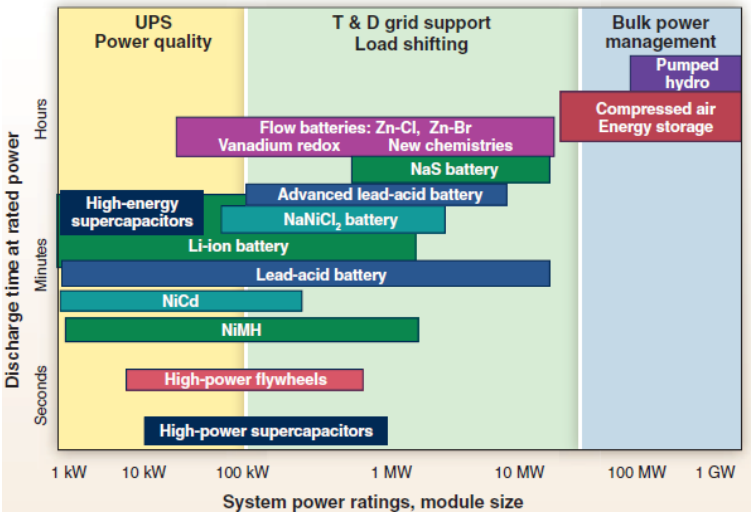

Figure 3: *Comparison of discharge time and power rating for various electrochemical energy storage technologies.*[5]

Regarding energy supply for transportation, today's available rechargeable batteries are still not competitive with gasoline in terms of range and costs, hence the percentage of electricity used for transportation is negligible and the prediction of the increase are poor as well (Figure 4).[6] Fuel cells are considered as a serious candidate to power electric vehicles, but only in 2015 one of the first commercial fuel cell cars was unveiled by *Toyota*, despite 200 years of research in this field.[7,8] By contrast, a broad commercialization of affordable Li-ion battery powered EVs, only about 20 years after the first commercialization of Li-ion battery itself is expected within the next 5 years.[9,10]

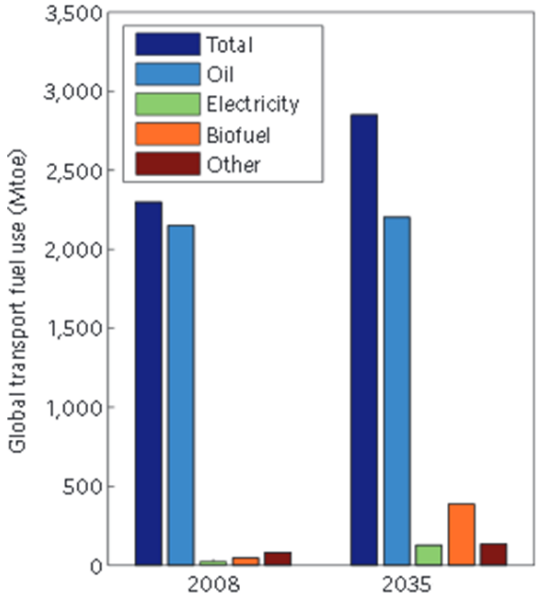

Figure 4: *Energy supply for transportation by fuels/ electricity in 2008 compared to the predictions for 2035.*[6]

In order to make the rechargeable battery technology serious contender for electrical energy storage (as power supply in EVs or grid support), new chemistries and battery concepts need to be explored. For example if made of earth abundant and cheap materials with high energy density, the same materials could be used for small as well as large scale applications lowering the overall production costs and coming along with a lower environmental impact.[11,12]

1.1 Batteries for electrochemical energy storage

Batteries as provider of electricity have been known since the invention of the first battery, the so called 'voltaic pile' by the Italian physicist Alessandro Volta in 1799. This device consisted of an alternating stack of copper and zinc plates separated by the electrolyte which can be either diluted sulfuric acid or just simple a saltwater solution. This device was the first being able to supply a continuous flow of electricity, opening a variety of pathways

for new discoveries in natural science (water electrolysis, discovery of new elements by molten salt electrolysis, etc.).[13]

Although this first battery had a rather short lifetime and could not be recharged, also named primary battery, it already was based on the same concept like all other batteries to date, whether primary or secondary.

In brief all batteries consist of two electrodes, a negative and a positive one (often called anode and cathode respectively, Figure 5) which are separated by an ion conductive but electrical insulating medium, the so called electrolyte. The two electrodes have a different chemical potential depending on their redox couple. When the electrodes are connected through an external circuit, the electrochemical reactions proceed at both sides, causing a flow of electrons (current) from the more negative to the more positive side. At the same time electro-neutrality is ensured by ions travelling the opposite direction through the electrolyte. If one of the redox reactions is finished, the current stops, and the battery is completely discharged. If this process can be reversed by applying an external voltage, the battery can be recharged and is called secondary battery.

$$V_{OC} = \frac{(\mu_A - \mu_C)}{e} \qquad \textbf{(1)}$$

From equation 1, the open circuit potential of an electrochemical cell *Voc* is defined by the difference between the electrochemical potentials μ_A and μ_C of the anode and cathode respectively, divided by the elementary charge *e*. The voltage is limited by the energy gap between the highest occupied molecular orbital HOMO and the lowest unoccupied molecular orbital LUMO of the electrolyte (voltage window). [14,15]

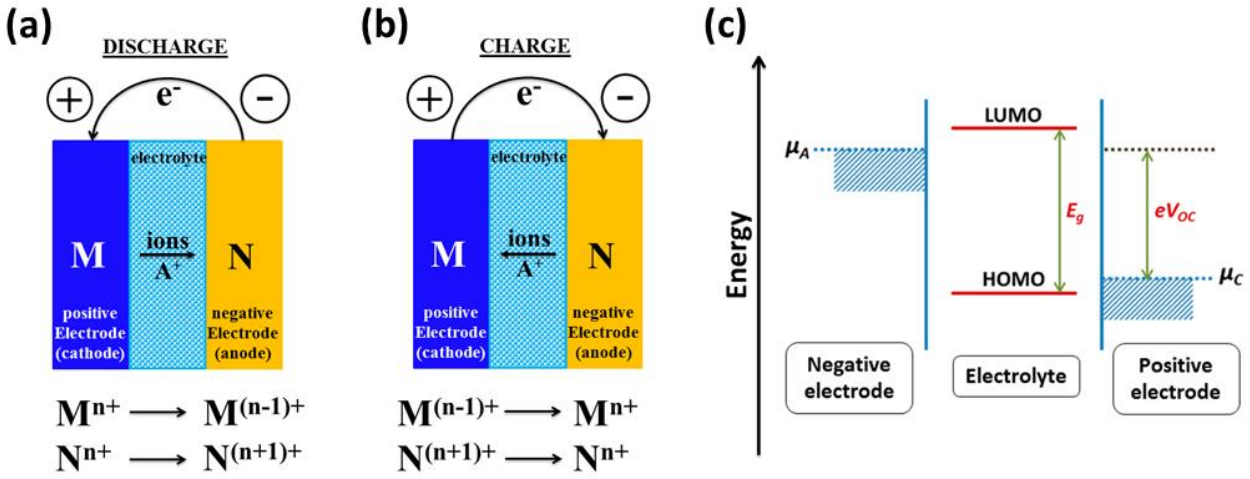

Figure 5: *Schematic illustration of an electrochemical cell during (a) discharge and (b). (c) Energy diagram of an electrochemical cell .*[14,15]

In general the two electrodes can be chosen from any kind of materials possessing a different chemical potential. However for practical considerations the chosen redox couple needs to fulfill several criteria like specific mass of the materials, their costs, safety and durability. The amount of electrical energy stored in batteries can be expressed in terms of unit per weight (Wh kg^{-1}) or unit per volume (Wh L^{-1}) which are linked to the battery's voltage (V) and gravimetric capacity (Ah kg^{-1}). The last two terms are directly correlated to the battery's chemistry and can therefore be tuned depending on requirements. Among various explored technologies, the most established and common rechargeable systems are lead-acid, nickel-cadmium, nickel-metal hydride batteries and lithium-ion batteries. A summary about their characteristics is given in Table 1.[15]

Table 1: *Characteristic of commonly used rechargeable batteries.*

Battery type	Lead-acid	Nickel-cadmium	Nickel-metal hydride	Li-ion
Voltage (V)	2.1	1.3	1.3	4.1
Practical energy density	70 Wh/L 35 Wh/kg	100 Wh/L 35 Wh/kg	240 Wh/L 75 Wh/kg	400 Wh/L 150 Wh/kg
Power density (W/kg)	180	150	250-1000	250-340
Cycles	500-800	2000	500-1000	400-1200

Among various existing technologies (Figure. 6) Li-ion batteries have encountered the global market as the most promising one, due to their favorable energy densities and flexibility in terms of design and chemistries.[14,16] A brief overview about their historical development with emphasis on different cathode materials is given in the next and following sections.

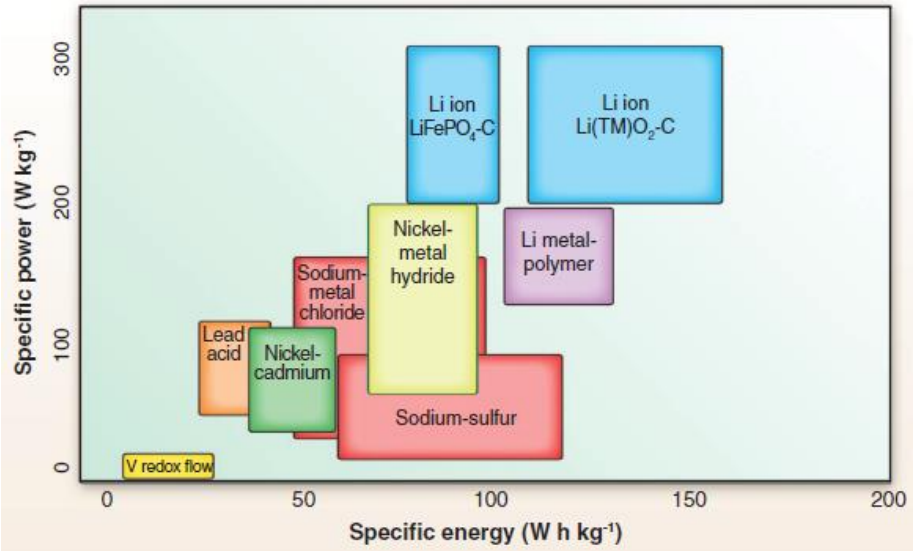

Figure 6: *Comparison of different battery technologies in terms of their gravimetric and volumetric energy density.*[5]

1.2 Lithium- and sodium ion batteries

1.2.1 Lithium ion batteries

One of the main motivations employing lithium in rechargeable batteries is the fact that lithium represents the lightest metal (molar weight 6.94 g mol^{-1}, gravimetric density ρ = 0.53 g cm^{-3}) and owns the highest reduction potential among all alkali metals (-3.04 vs. SHE), thus potentially leading to high energy densities. Due to the incompatibility of alkali metals with aqueous electrolytes and the elevated voltage which would lead to water electrolysis, organic electrolytes have to be employed in lithium secondary batteries. In the 1970s several inorganic compounds were shown to reversibly intercalate alkali metals, especially transition metal chalcogenides.[17,18,19] In 1972 *Exxon* demonstrated a first non-aqueous rechargeable lithium cell based on TiS_2 as a positive and lithium metal as the negative electrode.[20] Unfortunately this concept soon encountered two main issues, first the combination of lithium

metal with a liquid electrolyte and second the dendritic lithium growth which occurred as a consequence of lithium deposition during subsequent charge-discharge cycles, leading to explosion hazards. Following this first demonstration, researchers investigated several other chalocogenides as positive electrode materials and started soon considering transition metal oxide materials showing higher capacities and redox potentials. Based on this pathway, *Goodenough* and coworkers proposed the family of lithium transition metal oxides Li_xMO_2 (M = Co, Ni, Mn) materials which are still used in today's lithium- and sodium-ion batteries.[21,22]

To circumvent the safety issues coming along with the use of metallic lithium as an anode, first the use of a lithium-aluminium alloy instead of pure lithium was proposed and solved the dendrite issue, but the electrodes survived only a certain number of cycles due to the large volume change during charge/ discharge.[23] At the early 1990s a second approach was proposed, substituting the metallic lithium by another insertion material.[24,25] This concept has led to the development of the so called lithium-ion or rocking-chair technology. Because lithium does not occur in a metallic state anymore in this type of cells, the dendrite issue is solved and Li-ion cells are therefore in principle much safer than Li-metal cells. To compensate for the overall voltage loss because of the increased redox potential of the anode, high voltage cathode materials are needed. According to these new demands for the cathode, the focus of research shifted from layered- transition metal sulfides to layered-, or three-dimensional transition metal oxides.[22] However it took almost ten years to commercialize the Li-ion battery. The delay was attributed to find suitable electrolytes, as well as anode materials. Only the discovery on Li-intercalation in carbonaceous materials,[26] based on earlier research,[27] led to the design of the first $LiCoO_2$/graphite cell (Figure 7) commercialized in 1991 by *SONY*.[28] This type of cell had a potential exceeding 3.6 V and gravimetric energy densities around 120-150 Wh/kg, a schematic view is drawn in Figure 7, which concept is still found in most of the today's Li-ion cells.

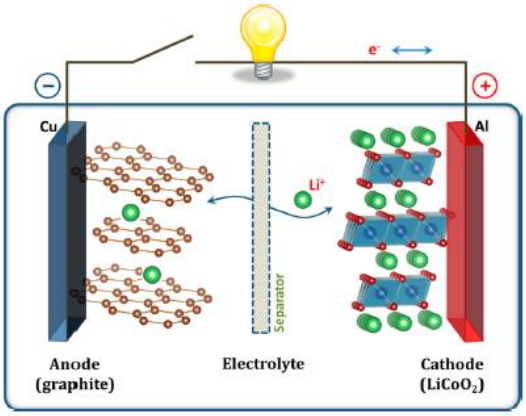

Figure 7: *Schematic view of a Li-ion cell based on a $LiCoO_2$ cathode and a graphite anode.*[14]

1.2.2 Sodium ion batteries

Thanks to the great success of Li-ion batteries, Na-ion batteries are seriously considered for the post-lithium batteries, although the Na-ion concept is not new and has been studied along with the Li-ion chemistry.[29] Similar chemical approaches, including synthetic strategies and characterization methods can be adopted from the field of Li-ion batteries. Despite a lower potential (~0.3 V) and energy density of Na-ion versus Li-ion batteries, the utilization of sodium may push the price per stored energy even further down, due to the natural earth abundance, which is more than 1000 times higher for sodium compared to lithium.[11] Components and electrochemical energy storage mechanism are basically the same like for Li-ion batteries, with the main difference is that hard carbon has to be used instead of graphite[1] as negative electrode material (Figure 9).[30–33]

[1] Hard carbon is a disordered carbon where the graphene sheets are not parallely aligned as in graphite.

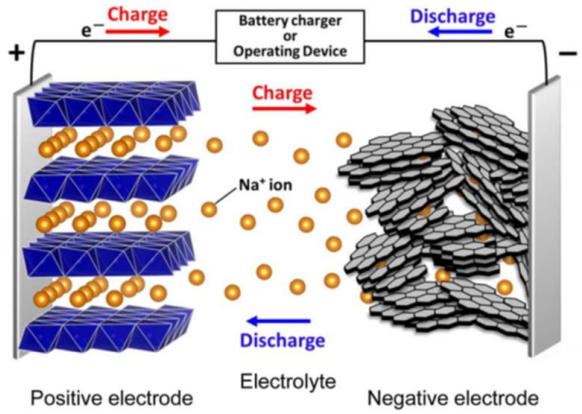

Figure 8: *Schematic illustration of a Na-ion battery.*[31]

1.3 Cathode materials for lithium- and sodium –ion batteries

In the following section an overview over the most studied class of cathode materials for lithium- and sodium ion-batteries is given. In particular different examples of positive electrode materials, namely transition metal oxides and important polyanionic materials are described in detail and finally conversion type materials are briefly reviewed.

Contrary to other battery technologies, lithium- and sodium-ion batteries can rely on a variety of different electrode materials, for both the positive and negative side. Obviously as shown in Figure 10, the main limiting factor for energy density is in both cases the lack of a high capacity positive electrode material. Therefore most of the work during the last decades has been focused on the search for new positive cathode materials displaying higher capacity and voltage, mainly for lithium batteries, however emerging more and more for sodium ion batteries.

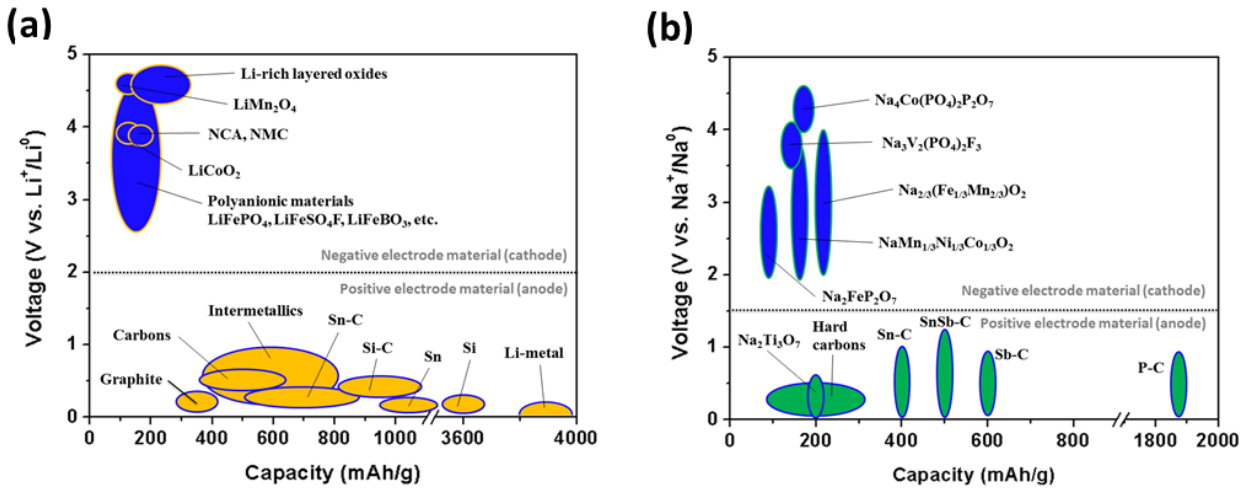

Figure 9: *Overview of different positive and negative electrode materials for* ***(a)*** *Li-ion and* ***(b)*** *Na-ion batteries, with respect to their redox potential and theoretical capacity.*[11,16,34]

In general an ideal positive electrode materials would possess a relative high redox potential (within the electrochemical stability of currently used electrolytes, a potential greater than 4.8 V vs. Li^+/Li^0 in combination with a high specific capacity. The specific capacity depends proportional on the number of exchanged Li-ions, and is lower, the higher the molar weight of the material. These two main requirements are by far not the only ones which need to be taken into account when searching for a new electrode material. It also should react with lithium/ sodium in a highly reversible way, preferable an insertion/ deinsertion mechanism so the crystal structure is maintained during charge discharge cycling leading to a longer lifetime of the material. Furthermore the electrode materials should be capable in conducting both, electrons and ions, since these two properties are the main limiting kinetic factors for the redox reaction and determining thus the rate capability of the material.

Besides the afore-mentioned properties, non-toxicity of the used elements, high thermal stability and lithium in the pristine material to avoid the use of lithium metal in the full cell or pre-lithiation step before the cell assembly are also important factors especially in terms of practical application.

1.3.1 Lithium- and sodium transition metal oxides

As mentioned before, following the studies of lithium intercalation in sulfides, researchers turned into the study of transition metal oxides soon, since they were expected to

present higher redox potentials versus lithium. Indeed replacing sulfur by the more electronegative oxygen enhances the ionic character of the M─X (M = transition metal, X = S, O, etc.) bond leading to an increase in the $M^{n+}/M^{(n+1)}$ redox potential.

1.3.1.1 Layered oxides

Goodenough and coworkers showed in 1980 that lithium could be reversibly removed electrochemically from $LiCoO_2$ around 3.9 V vs. Li^+/Li^0, thus making it suitable cathode material,[21] still used intensively in commercial Li-ion cells up to date. The crystal structure of layered oxides is built of a cubic close packing *ccp* of oxygen anions with Co^{3+} and Li^+ sitting in octahedral sites in alternating layers (Figure 11). This material delivers attractive volumetric energy densities, excellent cyclability and a high rate capability, equivalent with the removal of 0.5 Li^+ per Co, therefore leading to a limited capacity of ~150 mAh/g. If more than 0.5 Li^+ are electrochemically removed (going to higher voltages vs. Li), the 2D layered structure rearranges giving a *hcp* hexagonal close packing of the oxygen anions in CoO_2.[35] This is commonly observed for all lithium transition metal oxides Li_xMO_2 for x<0.5 releasing oxygen from the lattice and showing a limited thermal stability in the delithiated state. Although $LiCoO_2$ is limited in gravimetric capacity and shows some concerns for large scale applications (thermal safety, high cost and toxicity of cobalt), *SONY* combined this material with a carbon anode to release the first commercial Li-ion battery.[28] Recent development showed that by surface modifications or partial substitution of Co through Ni and Al ($LiNi_{0.80}Co_{0.15}Al_{0.05}O_2$,NCA)., the amount of reversibly

extracted lithium could be increased up to 0.7 Li^+ per formula unit, leading to reversible capacities around 185 mAh/g.[36,37]

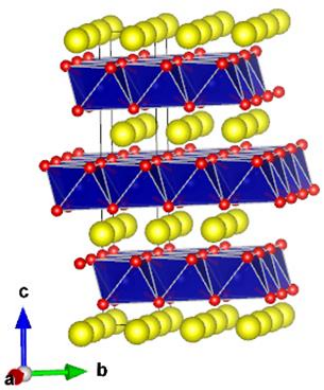

Figure 10: *Schematic view of the crystal structures of layered $LiCoO_2$ with Li-, Co- and O atoms drawn in yellow, blue and red respectively.*

Many sodium counterparts Na_xMO_2 have been investigated already since the 1970s in terms of their structure[38,39] but due to the different coordination environment of Li and Na, ion-exchange reaction between them comes along with a change in the MO_2 layer stacking.[40,41] All Na_xMO_2 phases reversible intercalate Na ions, but M = Mn and Co have been the most studied, showing in general a multistep voltage-composition curve with several solid-solution and biphasic domains for different x-values due to Na-vacancy ordering or gliding of the transition metal planes.[42,43] Although a variety of different compounds show a promising electrochemical behavior, the understanding and minimizing of irreversible structural changes affecting the cycling behavior represents still an issue which remains to be solved in the future along with the discovery of new compounds.[44] Along the Na-layered oxides P2-type $Na_x[Fe_{1/2}Mn_{1/2}]O_2$ is one of the most promising one due to the earth-abundant composition and a reversible capacity around 190 mAh/g (Figure 12).[45]

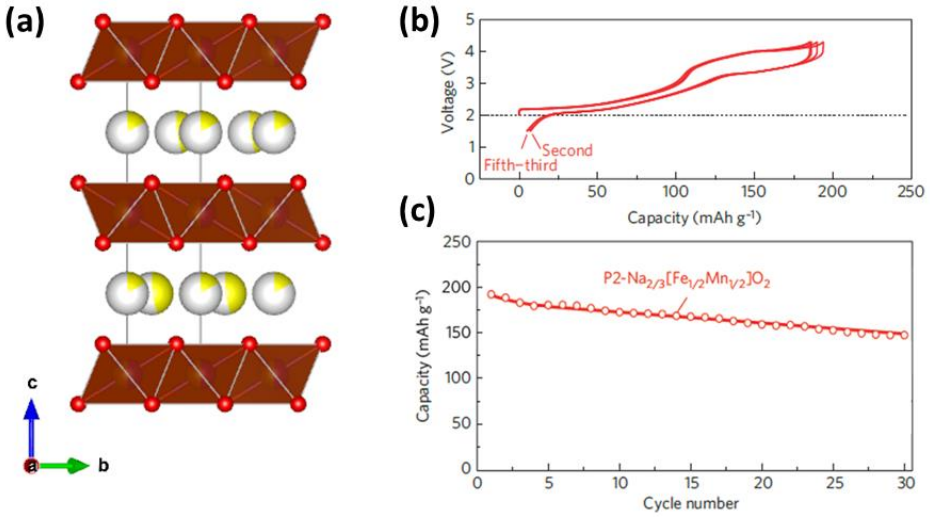

Figure 11: (a) *Structure of the P2-$Na_{2/3}[Fe_{1/2}Mn_{1/2}]O_2$ its* ***(b)*** *galvanostatic cycling and the corresponding capacity retention.*[45]

1.3.1.2 Spinel manganese oxide

Unlike cobalt and nickel, the straight forward synthesis of $LiMnO_2$ with the $LiCoO_2$ structure is not possible. It can only be obtained by ion exchange from α-$NaMnO_2$, but

converts easily from the layered to a spinel type structure upon lithium insertion/ deinsertion.[46,47] By contrast for a 1:2 Mn:O ratio stable phases are formed, e.g. $Li_{0.5}MnO_2$ or $LiMn_2O_4$ with spinel type structure. This material was originally proposed as a cathode material by *Thackeray et al.*,[22] and has been extensively studied in the *Bellcore* labs.[48,49] Spinel $LiMn_2O_4$ is built up of MnO_6 octahedra connected through edge-sharing to forming a 3D network of conduction path for lithium ions sitting in tetrahedral sites (Figure 13a). One half of the manganese occurs in a +III oxidation state while the other half is in +IV oxidation state, thus leading to an amphoteric electrode material. This means that the material can be either oxidized leading to the formation of γ-MnO_2 with a potential centered around 4.1V vs. Li^+/Li^0, or reduced to $Li_2Mn_2O_4$ at an average potential of 3.1V vs. Li^+/Li^0 (Figure 13b). However for Li-ion batteries only the high-voltage plateau can be used, since there is no other source of lithium inside a full cell except the cathode material, thus limiting the practical reversible capacity to 148 mAh/g.

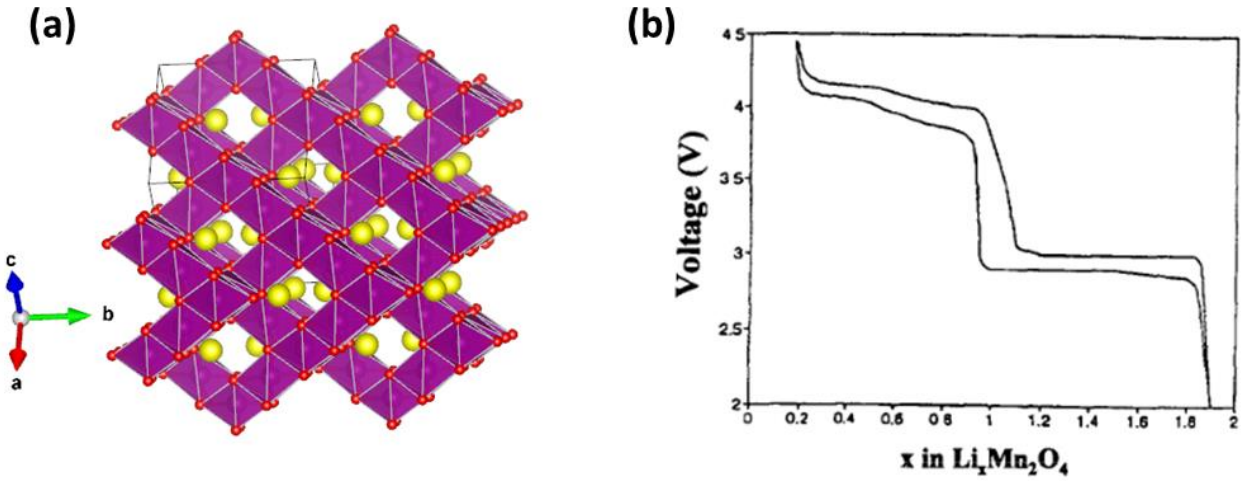

Figure 12: (a) *Structure of the spinel $LiMn_2O_4$ where MnO_6 octahedra, lithium- and oxygen atoms are shown in purple, yellow and red respectively.* ***(b)*** *Voltage-composition curve of $LixMn_2O_4$ for $0<x<2$.*[50]

Despite the slightly lower capacity compared to other lithium transition metal oxides, $LiMn_2O_4$ has several advantages for application in commercial cells like high voltage, non-toxicity and low-cost of manganese.[51] Therefore this material has been serious considered as a material for high-power applications, prevented by unsolved issues, regarding cycling at elevated temperature (~50°C) or manganese dissolution over time.[50] Several solutions regarding these issues have been proposed, including excess lithium,[52] metal substitutions[53] or mixing the spinel with a layered phase.[54]

1.3.1.3 Li- and Na-rich layered oxides

Continuing the research for new cheap, safe and non-toxic cathode materials, two significant advances in the synthesis and electrochemistry of manganese based layered materials were made. In particular Li_2MnO_3 turned into the most interesting candidate to further improve oxide based cathode materials. It has a rocksalt structure which can be represented in the conventional layered $LiMO_2$ notation as $Li[Li_{0.33}Mn_{0.67}]O_2$ as ¼ of the Li-atoms of Li_2MnO_3 are sitting in the transition metal sheets (Figure 14).[55,56] First the discovery that Li_2MnO_3, which should be electrochemically inactive for lithium insertion/ extraction from a structural point of view since manganese is already in its highest oxidation state +IV, could be activated either chemically by acid leaching of Li_2O leading to a new compound with the stoichiometry $Li_{2-x}MnO_{3-x/2}$, or electrochemical by charging a Li_2MnO_3/Li cell to a high voltage (> 4.5 V vs. Li^+/Li^0), renewed the interest in this class of materials.[57,58] Substituting Mn by other 3d transition metals like Ni and Co led to the discovery of a new class of materials $xLi_2MnO_3 \cdot (1-x)LiMO_2$. Several groups reported capacities exceeding 250 mAh/g for this class of materials, therefore being the number one candidate as cathode materials for next generation Li-ion batteries. The unusual high capacity achieved could not be explained satisfactory, by only taking into account the cationic redox process ($M^{n+} \leftrightarrow M^{(n+1)+}$), however our group showed recently the participation of a reversible anionic redox process ($O^{2-} \leftrightarrow O_2^{2-}$) for lithium- and sodium rich layered oxides, opening a new route in the search for high capacity cathode materials.[59–61]

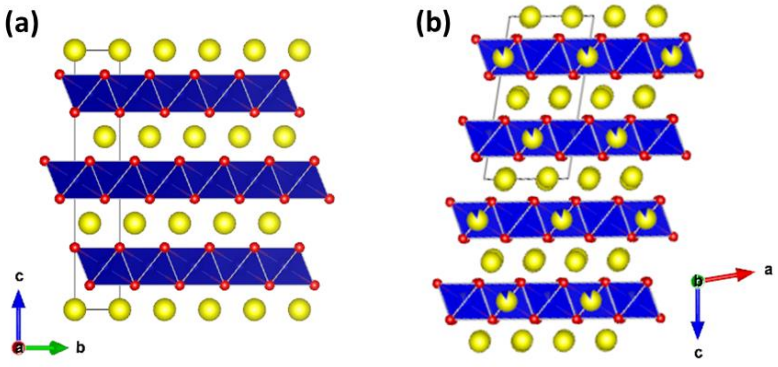

Figure 13: *Layered structures of* ***(a)*** *$LiMO_2$ (M = Co, Ni, Mn) and* ***(b)*** *Li_2MnO_3.*[62]

1.3.2 Polyanionic cathode materials and the inductive effect

Besides oxide based cathode materials, polyanionic materials consisting of a transition metal and a polyanionic group $(XO_n)^{m-}$ (X = C, B, P, S, Si, Mo, W, etc.) have gained strong interest since the discovery of electrochemically active lithium iron phosphate $LiFePO_4$ in 1997.[63] Although additional weight is introduced by the presence of the polyanionic group leading to a reduced gravimetric capacity, polyanionic electrode materials have several advantages as follows. First, they provide a stable anionic framework essential for long term stable cycling and safety issues (oxygen release in the case of oxides is circumvented). Second the redox potential of the $Mn^{n+}/M^{(n-1)+}$ redox couple can be modified through the inductive effect of the polyanionic group (described in detail in the next paragraph) and leads to higher values compared to oxide compounds, and finally these class of compounds offer a very rich chemistry due to a variety of different crystal structures and possible substitutions.[64,65]

In the following section an overview about different polyanionic materials is given, however since numerous compounds have been investigated, materials mainly based on the Fe^{3+}/Fe^{2+} redox couple are presented hereinafter.

1.3.2.1 NASICON-type compounds $A_xM_2(XO_4)_3$ (A = Li, Na)

In the 1980s it was demonstrated for the first time possible electrochemical reversible intercalation of Li or Na into *3D* framework *NASICON* (*NA*-Super*I*onic *CON*ductors) phases $Fe_2(MoO_4)_3$ (Figure 14) and (Li, Na)$Ti_2(PO_4)_3$.[66–68] In general they can be expressed by formula $A_xMM'(XO_4)_3$ and are built up on a framework of MO_6 and $M'O_6$ octahedra sharing all their corners with XO_4 tetrahedras, with alkali metal ions sitting interstitial spaces, enabling fast ion conduction.

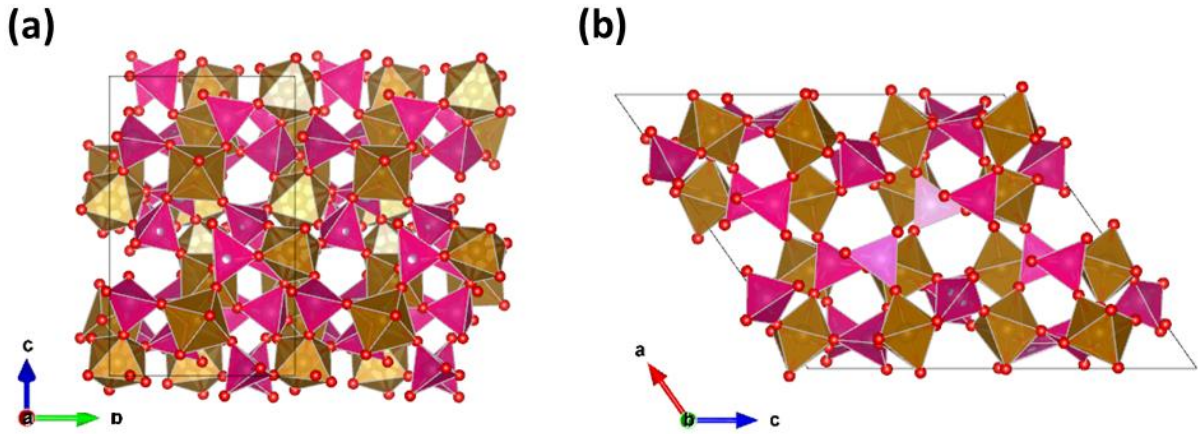

Figure 14: *Crystal structure of the NASICON type compound $Fe_2(MoO_4)_3$ along the* ***(a)*** *a- and* ***(b)*** *b-axis. FeO_6 octahedra and MoO_4 tetrahedra are shown in brown and purple respectively.*

Later *Goodenough* showed by substitution of the polyanionic group of $Li_3Fe_2(XO_4)_3$ (X = As, P, Mo, S), that the redox potential of the Fe^{3+}/Fe^{2+} couple could be shifted up 3.6 V vs. Li^+/Li^0 (Figure 16a).[69,70] Given that all three compounds possess more or less the same metal to oxygen distance, they concluded that this increase in redox potential was due to the large electronegativity of the SO_4^{2-} group, thus increasing the ionic character of the metal oxygen bond. The more electronegative X is, the stronger the covalent X─O bond, the weaker the M─O bond leading to a higher potential of the Fe^{3+}/Fe^{2+} redox couple (Figure 16b), giving birth to the concept of inductive effect for polyanionic type compounds.

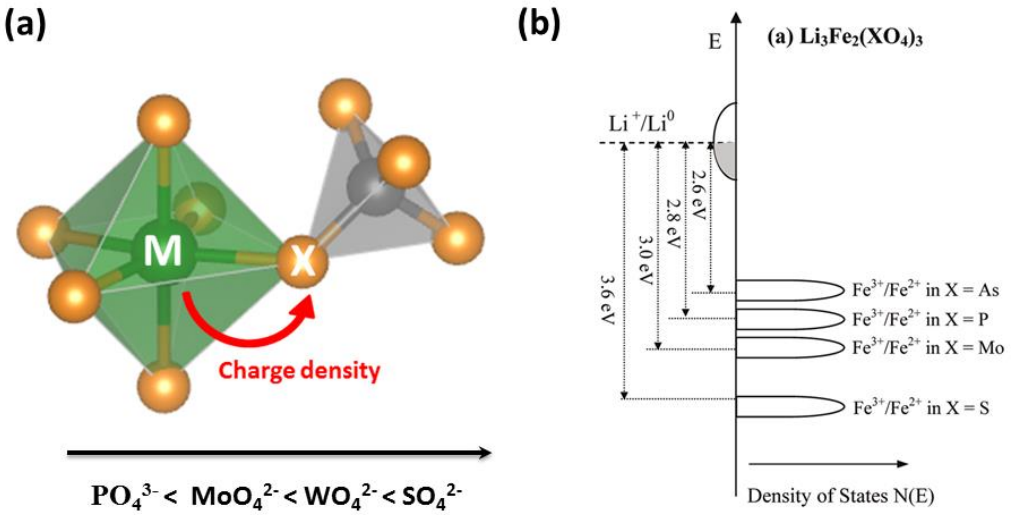

Figure 15: *Schematic representation of the inductive effect.* ***(a)*** *MO_6 octahedra connected over one bridging oxygen to the XO_4 tetrahedra.* ***(b)*** *Depending on the electronegativity of the polyanionic group, the redox potential of the Fe^{3+}/Fe^{2+} can be shifted up from 2.8 to 3.6 V vs. Li^+/Li^0.*[71]

Using this concept, the different redox potentials for different polyanionic environment could be sufficiently explained and new potential cathode materials with attractive voltage could be identified, however suffering from the high molecular weight thus theoretical capacities around 120 mAh/g. Subsequently the family was extended to phosphate based *NASICON*-type phases having the general formula $Li_xMM'(XO_4)_3$, summarized in Figure 17.

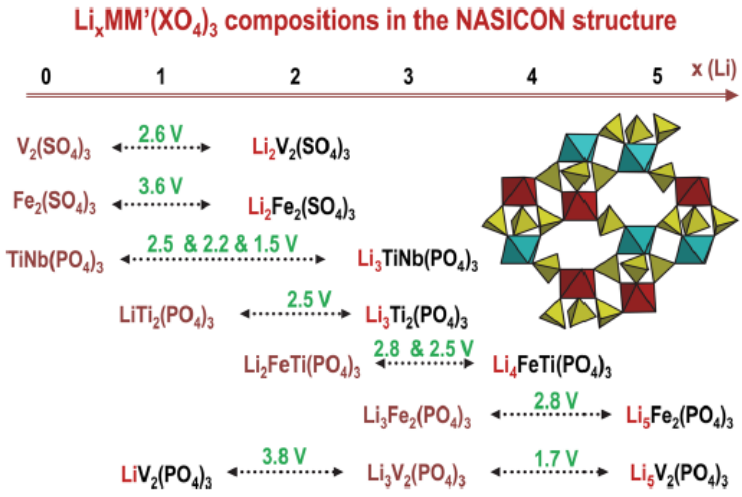

Figure 16: *Different NASICON-type compounds with a $Li_xMM'(XO_4)_3$ composition and different $M^{(n+1)+}/M^{n+}$ redox couples.*[72]

Consequently this new concept called for investigating all different kind of polyanionic structures in combination with different transition metals, the most popular being iron due to its cost and safety (non-toxic element) advantages. In the course of this study *Goodenough* and coworkers identified a new compound lithium iron phosphate $LiFePO_4$ as a potential cathode material.[63]

1.3.2.2 Phosphate based materials $AMPO_4$ and $A_2MP_2O_7$ (A = Li, Na; M = Mn, Fe, Co)

Lithium iron phosphate $LiFePO_4$ (LFP), the most famous compound among the family of phosphor-olivines, also known as the mineral *triphylite*, crystallizes in an orthorhombic space group and consists of edge sharing FeO_6 octahedra which are ordered in parallel layers. These layers are bridged by PO_4-groups forming tunnels along the [010] axis which is also the

preferred path for the *1D* Li-ion conduction (Figure 18). The theoretical capacitity of LFP is 170 mAh/g, comparable to that of layered oxides, but with lower redox potential of 3.45 V vs. Li^+/Li^0.

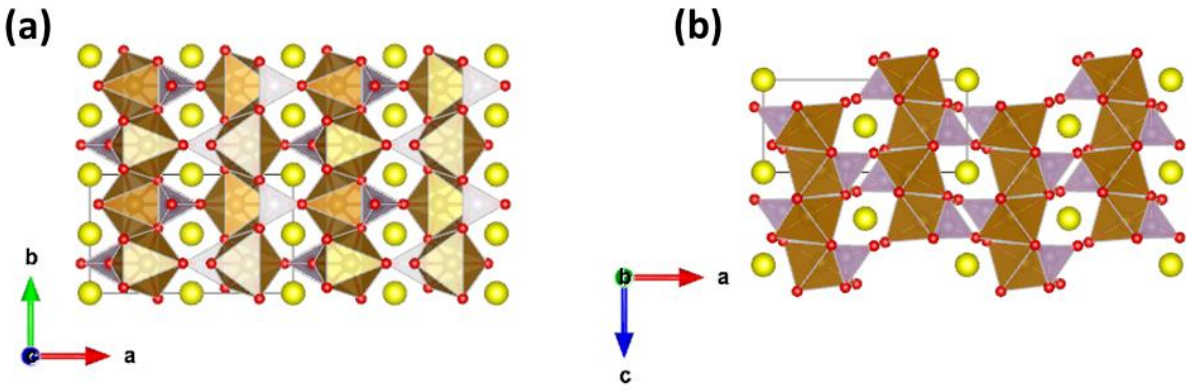

Figure 17: *Structure of $LiFePO_4$ viewed along the **(a)** c- and the **(b)** b-axis. FeO_6 octahedras, PO_4 groups, oxygen and lithium atoms are represented in brown, purple, red and yellow.*

Initially Goodenough et al. were only able to achieve ~80% of the theoretical capacity at slow charge/ discharge rates. Then it was shown that the full capacity could be achieved by the nanosizing approach and nanocoating with carbon, even at fast rates for several hundred of cycles (Figure 19), hence commercialized by A123 in 2005. [73–76]

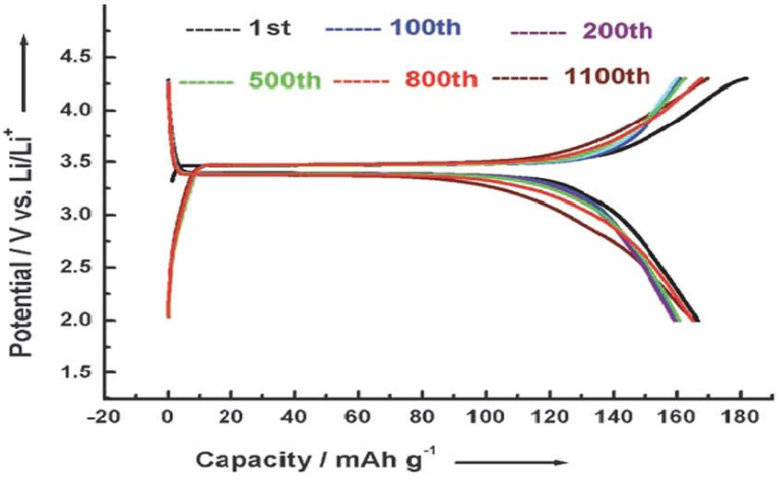

Figure 18: *Voltage-composition curve for galvanostatic cycling of carbon coated $LiFePO_4$.*[74]

Based on the promising results for LFP, other phosphor-olivines $LiMPO_4$ (M = Mn, Co, Ni) were also investigated as potential electrode materials, while the latter two exhibit a

redox potential outside of the stability window of the common used liquid organic electrolytes[2] (Table 2).[77]

Table 2: *Redox potentials versus lithium and theoretical capacities for different transition metal phopho-olivines.*

Phospho-olivine	Redox potential (V vs. Li^+/Li^0)	Theoretical capacity (mAh/g)
$LiFePO_4$	3.45	170
$LiMnPO_4$	4.1	171
$LiCoPO_4$	4.8	167
$LiNiPO_4$	5.1	167

Following that success for LFP in Li-ion batteries, the search for a Na equivalent was obvious, however the thermodynamically stable phase $NaFePO_4$ does not crystallize in the *triphylite*- but rather in the *maricite* structure (Figure 19). The fact that Na^+ ions are trapped in cavities inside the *maricite* structure renders this material not suitable as electrode material since it does not show any reversible redox behavior.[78] However the *triphylite* $NaFePO_4$ could only be prepared starting from LFP through chemical/ electrochemical ion exchange.[79–81]

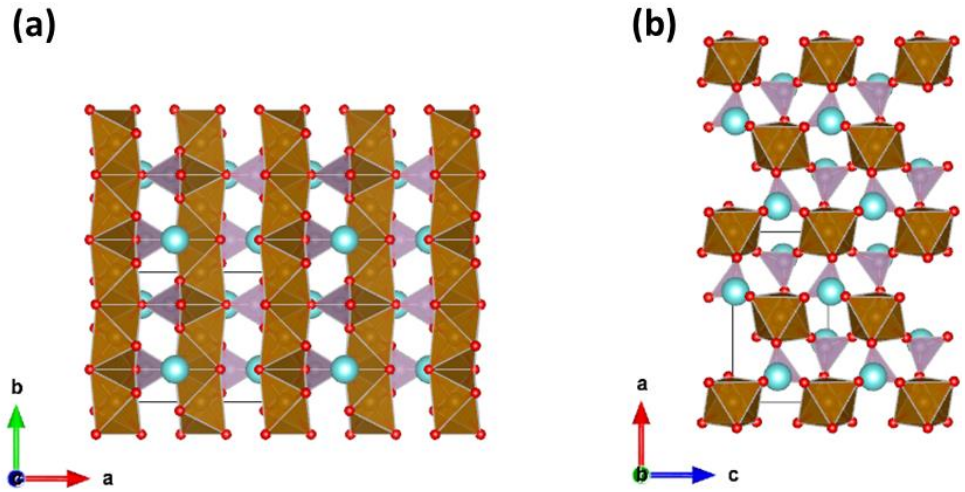

Figure 19: *Structure of maricite $NaFePO_4$ along the* ***(a)*** *c- and* ***(b)*** *b-axis. FeO_6 octahedra, PO_4 tetrahedra, oxygen- and sodium-atoms are represented in brown, purple, red and blue respectively.*

[2] Commonly used electrolytes for Li-ion batteries (a) 1M $LiPF_6$ in ethylene carbonate EC / dimetylcarbonate DMC 1/1 w/w or (b) 1M $LiPF_6$ in ethylene carbonate EC/ dimetylcarbonate DMC/ propylene carbonate PC 1/1/3 w/w/w.

Finally to explore other phosphate based cathode materials, which display a higher voltage in contrast to the PO_4^{3-} compounds, so called *pyrophosphate* or *diphosphate* group $[P_2O_7]^{4-}$ have drawn attention to battery researchers.

Preliminary studies have focused on the electrochemical activity of pyrophosphate based compounds $LiMP_2O_7$ where M represents a trivalent metal e.g. Fe^{3+} or V^{3+}.[65,82] Starting on Li insertion for $LiFeP_2O_7$, this compounds showed a redox process for around 3.0 V vs. Li^+/Li^0 and a limited capacity of around 80 mAh/g in the case of M = Fe.[83,84] Following these first investigations, the interest turned into lithium pyrophosphates containing a divalent metal and two lithium in the pristine material $A_2MnP_2O_7$ (A = Li, Na), where it should be theoretically possible to extract two Li^+ per transition metal.[85]

A variety of different compounds, their solid solutions and polymorphs with the general formula $A_2MP_2O_7$ (M = Mn, Fe, Co, Ni; A = Li, Na) have been reported in literature.[83,86–89] Figure 20a shows the structure of $Li_2FeP_2O_7$, crystallizing in a monoclinic space group $P2_1/a$. Fe occupies three different crystallographic sites, one of them FeO_6 octahedra, the other two distorted FeO_5 trigonal bipyramids. Li is coordinates by oxygen forming LiO_4 tetrahedra and LiO_5 trigonal bipyramids leading to a 2D network along the b-c-plane (Figure 20a). *Yamada's* group showed that it is possible to extract approximately $1Li^+$ reversibly, giving around 110 mAh/g at an average redox potential of 3.5V vs. Li^+/Li^0 playing with the Fe^{3+}/Fe^{2+} redox couple, the highest redox potential observed for Fe^{3+}/Fe^{2+} in phosphate based materials (500 mV higher than for LFP).[86]

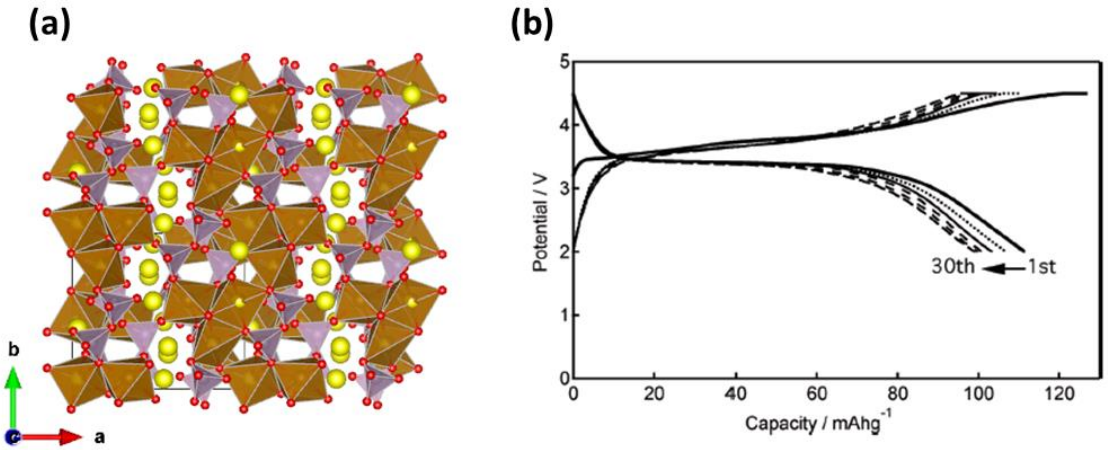

Figure 20: (a) *Crystal structure of $Li_2FeP_2O_7$ (Li in green, FeO5, FeO_6 in brown and P_2O_7 in purple) and* ***(b)*** *galvanostatic cycling vs. Li at a C/20 rate.*[86]

Following the work done on $Li_2FeP_2O_7$, the Na counterpart $Na_2FeP_2O_7$ was studied as a potential cathode material for Na-ion batteries. It adopts a triclinic space group P-1 and is built from corner sharing FeO_6–FeO_6 [Fe_2O_{11}] dimers, which are interconnected by [P_2O_7] units to create three-dimensional zigzag channels for Na^+-ion migration (Figure 21a). This enables to reach a reversible capacity around 80 mAh/g at an redox potential of 3.0V vs. Na^+/Na^0 (Figure 26b).[89–91]

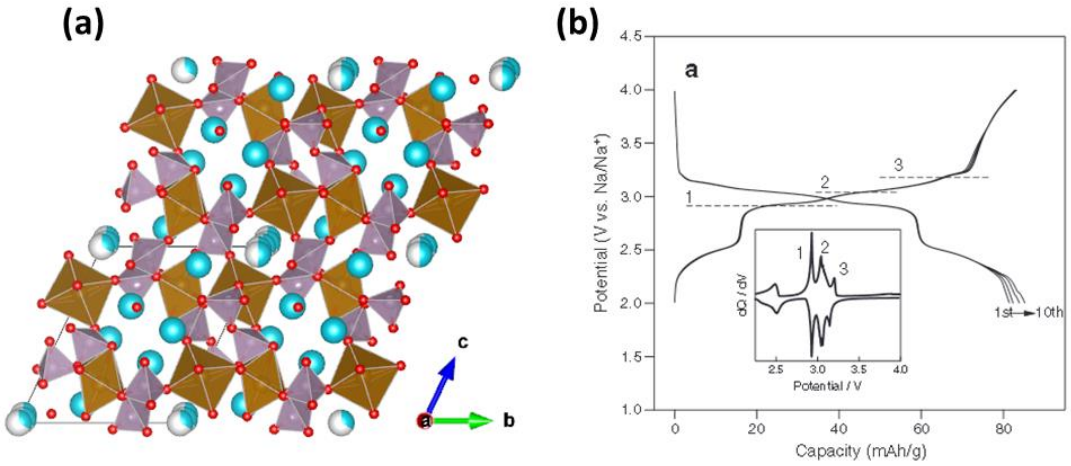

Figure 21: (a) *Crystal structure of $Na_2FeP_2O_7$ (Na in yellow, FeO_6 in green and P_2O_7 in purple.* ***(b)*** *The voltage capacity curve.*[92]

Despite the theoretical possibility of two-electron reaction per transition metal (theoretical capacity 220 mAh/g), more than a one-electron process per transition metal was never observed and other transition metals like Co or Mn show limited electrochemical activities versus Na or Li (<80 mAh/g).[87,88,93,94]

All the polyanionic based cathode materials presented before come along with moderate capacities and lower redox potentials if compared to state-of-the-art oxide based materials. To circumvent this disadvantage different solutions have been proposed through the past years. First, increase the specific capacity by lowering the molecular weight of the polyanionic group, or achieving more than 1 Li^+ transfer per transition metal. Second, increase the redox potential and hence the energy density of the material, applying strongly electronegative polyanionic groups. Both of the mentioned directions were further explored with borates and silicates for the former, and fluorosulfates and fluorophosphates for the latter one, discussed in the following sections.

1.3.2.3 Silicates Li_2MSiO_4

Following the path to achieve more than one Li^+ exchange per transition metal, the family of lithium transition metal silicates Li_2MSiO_4 (M = Fe, Mn, Co) was early identified as a candidate to master this challenge and intensive research efforts have been put into afterwards, revealing limited electrochemical performance.[95,96]

The crystal structures of Li_2MSiO_4 consist of a distorted *hcp* of the oxygen anions with ½ of the tetrahedral sited occupied by Li, Si an M, where a variety of different polymorphs is possible depending on the occupancy of the tetrahedral sites. All of them are related to the structure of Li_3PO_4, either the low temperature- or the high-temperature polymorph, denoted as β- and γ-Li_3PO_4 respectively. The only difference in between all these polymorphs is basically the ordering/ distribution of the cations within the tetrahedral sites, thus leading to a large variety (for sake of clarity only the two existing polymorphs of Li_2FeSiO_4 are shown in Figure 22).[97–99]

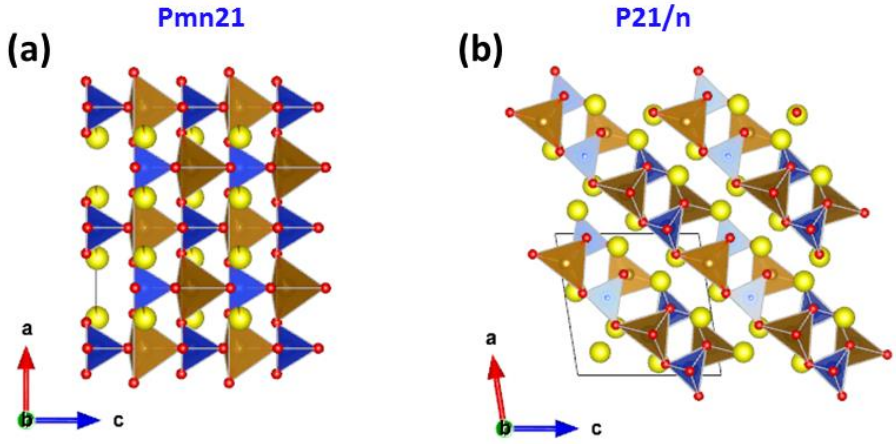

Figure 22: *Two known polymorphs of Li2FeSiO4 crystallizing in* ***(a)*** *P2mn21 and* ***(b)*** *P21/n space group. FeO_4 tetrahedra, SiO_4 tetradedra and Li are drawn in brown, blue and yellow respectively.*

Regarding the application of silicates as cathode material, one of the drawbacks of this family is the low intrinsic conductivity at room temperature ($5 \cdot 10^{-16}$ S/cm for Li_2MnSiO_4 and $6 \cdot 10^{-14}$ S/cm for Li_2FeSiO_4).[100] This limitation could be overcome through an optimized synthesis including nanoparticles and conductive carbon coating.[101–103] Although optimized, it is not possible to extract more than $1Li^+$ per formula unit affiliated to the Fe^{3+}/Fe^{2+} redox couple at 3.1 and 2.8 V vs. Li^+/Li^0 for the initial and subsequent charge/ discharge cycles (Figure 23) leading to a reversible capacity 120-140 mAh/g. The change in potential from the

first to the subsequent oxidations is due to a structural rearrangement after the first oxidation, minimizing the repulsion between Fe^{3+} and Si^{4+} in the charged state. Theoretical the second redox process involving the Fe^{4+}/Fe^{3+} couple should show up at 4.7 V vs. Li^{+}/Li^{0} (limit of the stability window of common electrolytes) but was never observed.[99]

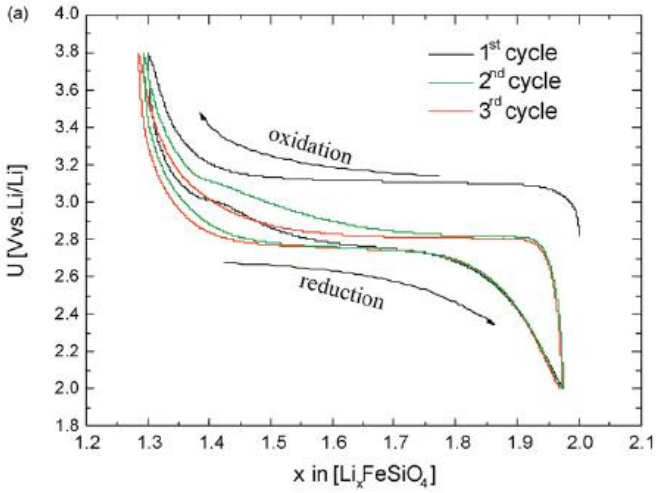

Figure 23: *Voltage-composition curve of Li_2FeSiO_4 versus lithium at a C/20 rate.*[100]

In contrast to Li_2FeSiO_4, the other members of the silicate family Li_2MnSiO_4 and Li_2CoSiO_4 have not shown promising electrochemical activity. Additionally to electronic and ionic limitations of Li_2MnSiO_4, Mn^{3+}(d4) cations are not stable in a tetrahedral environment, leading to a serious distortion of the crystallinity during the first oxidation and a poor reversibility on following cycles. Even for the solid-solution member $Li_2Mn_{0.2}Fe_{0.8}SiO_4$ it was show that only Fe is taking part in the reversible redox process, hence Mn being non active.[104]

1.3.2.4 Sulfate based materials

As already observed by *Padhi et al.* in the late 1990's, the redox potential of iron could be shifted up ~0.8 V by replacing the phosphate in *NASICON* type compounds by a sulfate group (Figure 16). Following this work a variety of new materials out of the sulfate family were proposed as cathode materials for Li- and Na-ion batteries. To achieve even higher voltage compared to bare sulfate polyanionic compounds, the introduction of fluorine into the structure should lead to elevated redox potentials as F^{-} is even more electron withdrawing.

The first fluorosulfate reported in literature was $LiMgSO_4F$ with *tavorite* structure, however ceramic methods to synthesize $LiFeSO_4F$ failed.[105] Only eight years later *tavorite* $LiFeSO_4F$ could be stabilized using an ionothermal route at low temperatures.[106] As it turned out this material decomposes around 375°C and is water soluble, explaining why it was not possible to synthesize $LiFeSO_4F$ by conventional ceramic synthesis or solution chemistry in aqueous media. In addition, the use of monohydrate iron(II) sulfate precursor $FeSO_4{\cdot}H_2O$ was essential to obtain $LiFeSO_4F$, since the structure of $FeSO_4{\cdot}H2O$ and *tavorite* $LiFeSO_4F$ a closely related. During the reaction of LiF with $FeSO_4{\cdot}H2O$ in ionic liquid media *1-Ethyl-3-methylimidazolium bis (trifluoromethylsulfonyl) imide* (EMI-TFSI) the water molecules linked to iron are replaced by fluorine and lithium is inserted into the structure for charge balance (Figure 24).[107]

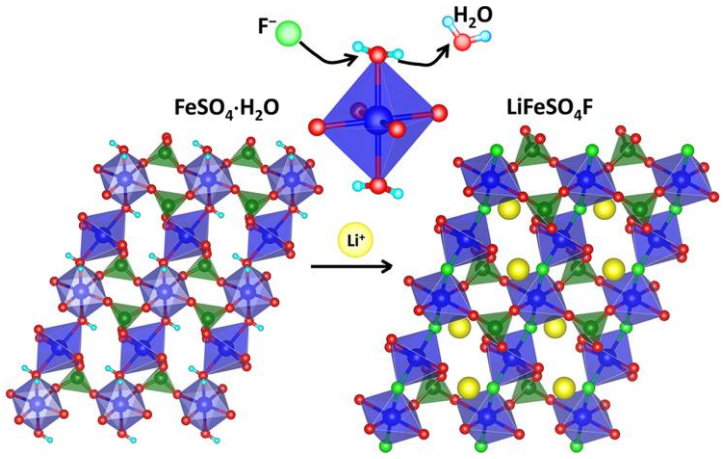

Figure 24: *Structural relationship between the precursor $FeSO_4{\cdot}H2O$ and the tavorite $LiFeSO_4F$.*[107]

Tavorite $LiFeSO_4F$ operates at a redox potential of 3.6 V vs. Li^+/Li^0 and delivers a reversible capacity of 135 mAh/g (exchange of 0.8 Li^+, Figure 25b). However, contrary to LFP no carbon coating is needed to achieve this electrochemical performance, making LiFeSO4F a serious contender if it would not undergo fast degradation in ambient atmosphere.[108]

Following the synthetic strategy developed for *tavorite* $LiFeSO_4F$, a great variety of other different compounds with the same stoichiometry $AMSO_4F$ (A = Li, Na, K; M = Fe, Co, Ni, Mn, Zn) crystallizing in different polymorphs could be prepared.[109,110] During this in-depth examination another polymorph for $LiFeSO_4F$ was revealed, crystallizing in a *triplite* structure (Figure 25c) and displaying with 3.9 V vs. Li^+/Li^0 (Figure 25d) the highest redox potential for Fe-based polyanionic compounds ever reported.[111,112]

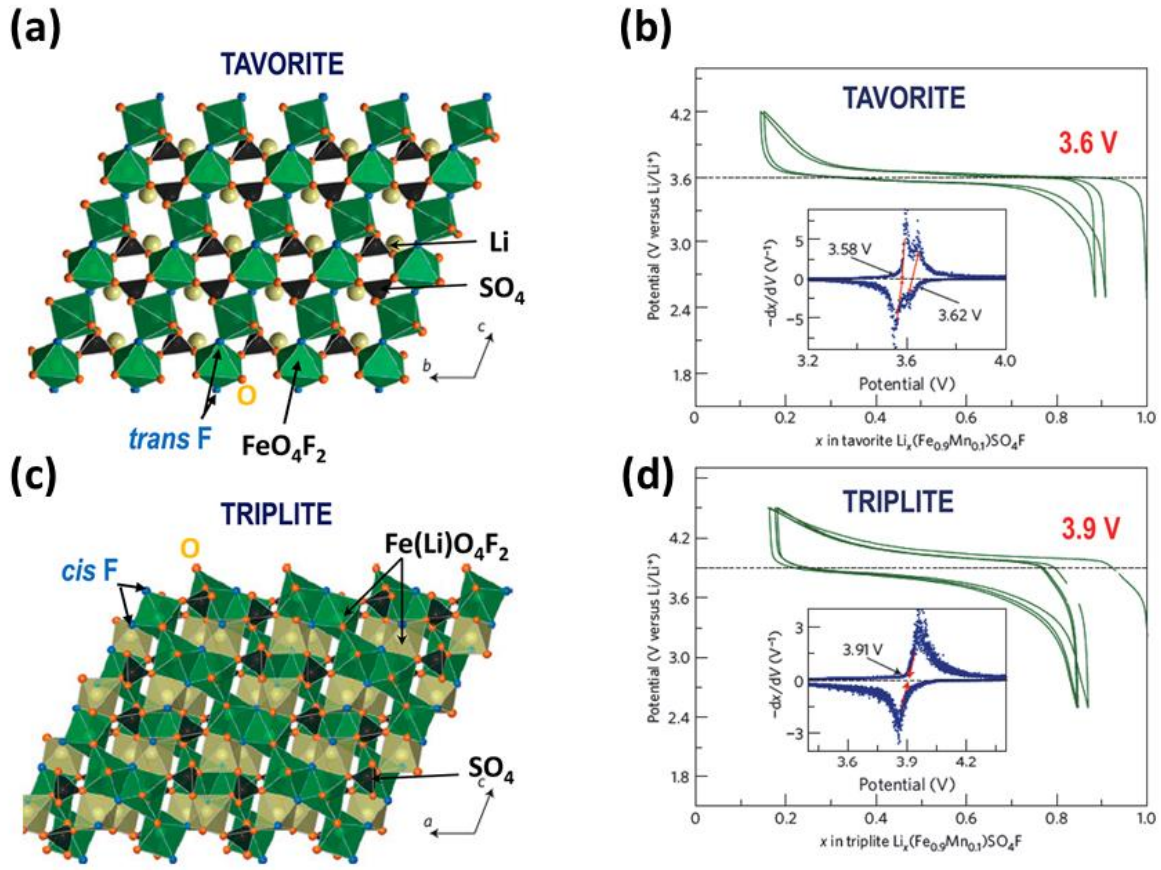

Figure 25 (a,c) *Structure and* ***(b,d)*** *galvanostatic charge-discharge curves for tavorite- and triplite* $LiFeSO_4F$.[111]

Since the presence of fluorine in a cathode material could be problematic from the toxicity point of view, the replacement of F^- with OH^- was investigated. Starting from an investigation of the mixed F/OH compound $FeSO_4F_{1-y}OH_y$,[113] led to the discovery of a layered materials $LiFeSO_4OH$ which showed good electrochemical performance versus lithium around 3.6 V with an average capacity of ~110 mAh/g.[114]

As described in previous sections, it is possible to achieve high redox potentials for insertion type positive electrode materials, close to the boarder of the stability window of standard electrolytes (max. 4.8 V vs. Li^+/Li^0), however the specific capacity and energy density still remains low compared to the negative side of a lithium ion battery.

1.3.3 Conversion type cathode materials

All the before discussed cathode materials store electrical energy through an insertion/ deinsertion (topotactic) reaction of Li/Na ions in a host structure (Figure 26). To further push the development of Li-ion batteries, reversible conversion reactions have been intensively investigated since the 2000's. The following section will give a short introduction and overview about conversion cathode materials for Li- and Na-ion batteries.

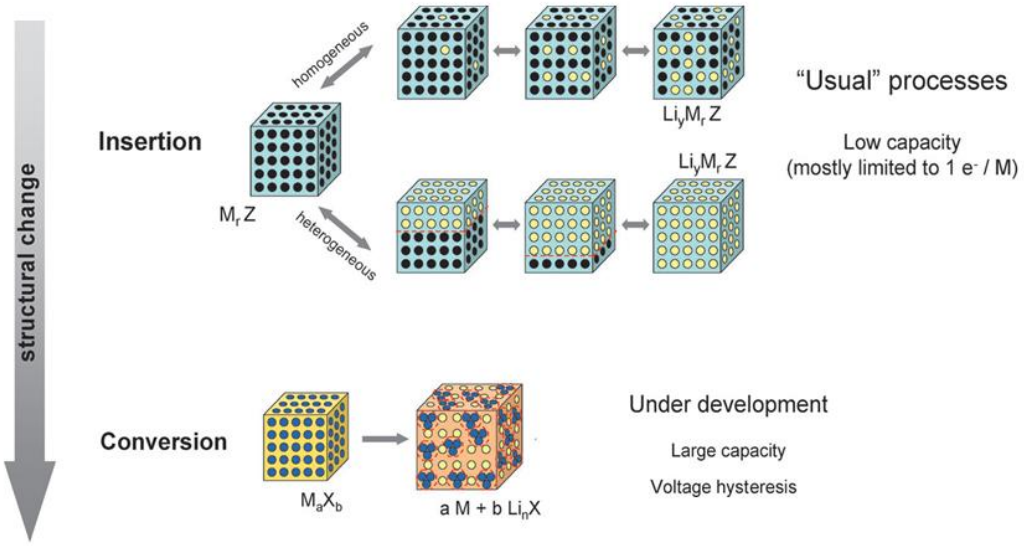

Figure 26: *Schematic illustration of insertion and conversion type reaction investigated as electrode materials for Li- and Na-ion batteries.*[15]

In order to use all the possible oxidation states of the TM, thus increasing the specific capacity drastically, conversion type reactions have been investigated since decades for primary batteries exclusively,[115] because it was believed that such reactions are irreversible. *Besenhard et al.* however showed in 1978 a reversible conversion reaction for a non-transition metal sulfide, namely Bi_2S_3. During discharge elemental bismuth Bi^0 and LiS were formed, nevertheless during the subsequent charge only about 75% could be converted back into Bi_2S_3. Furthermore the reversibility of the discharge-charge could be demonstrated only for one cycle.[116]

The first real reversible conversion reaction could be demonstrated for TM oxides in 2000, drawing renewed attention on the investigation of conversion type electrode materials for rechargeable batteries. The conversion process of these compounds can be described as

follows: the metal M is reduced to elemental M^0 and simultaneously the corresponding lithium compound LiX is formed (equation 1, X = O, S, P, etc.).

$$M_aX_b + n\,e^- + n\,Li^+ \underset{\text{charge}}{\overset{\text{discharge}}{\rightleftharpoons}} a\,M^0 + b\,Li_nX \qquad \textbf{(2)}$$

Although the conversion reaction of the TM-oxides delivers much higher gravimetric capacities compared to insertion type electrode materials (Figure 27), the redox potential versus lithium of 1 to 1.5 V vs. Li^+/Li^0, is too low for practical applications.[117]

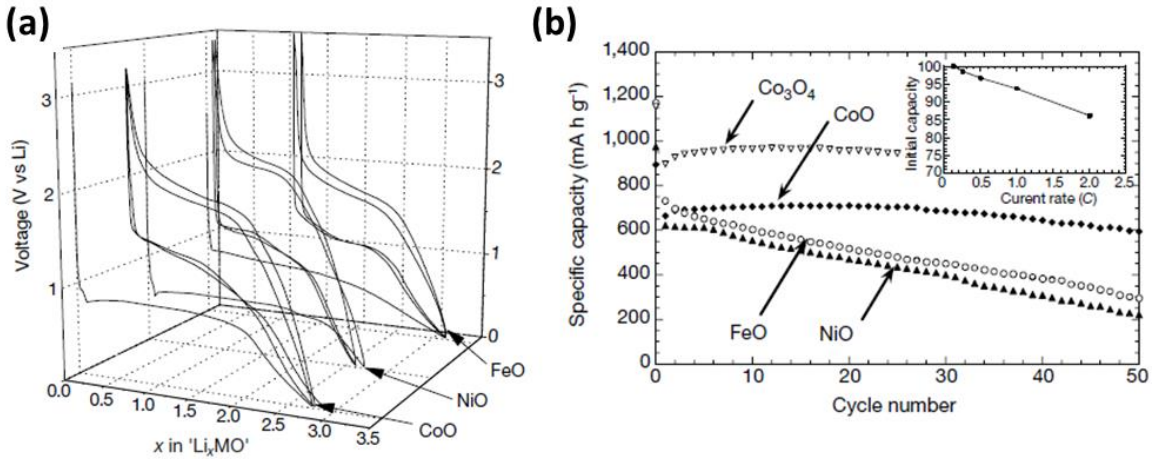

Figure 27: (a) *Voltage composition curves for different TM oxides and* ***(b)*** *the corresponding capacity retention. Co_3O_4 is shown to proof that not only divalent TM oxides can be applied. The inset show the rate capability of CoO.*[117]

In order to increase the redox potential, more ionic TM compounds like the corresponding sulfides,[118] -nitrides[119] and especially fluorides[120,121] were investigated for conversion reaction versus lithium. Among them iron fluoride FeF_3 is one of the most promising one, but due to its insulating nature it has to be "activated" to be used as electrode material. This activation is usually achieved by forming an iron fluoride carbon composite FeF_3/C (ca. 20 wt% carbon) during a prolonged high energy milling. Cycling this composite versus lithium between 1.5 and 4.5 V, around 600 mAh/g capacity can be achieved (Figure 28).

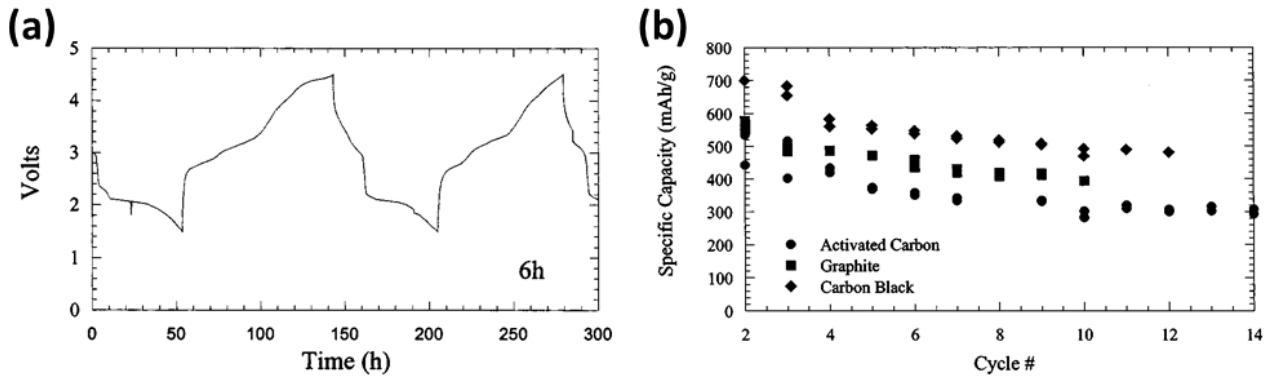

Figure 28: (a) *Voltage versus time curve of a FeF_3-activated carbon nanocomposite ball milled for 6h and* ***(b)*** *the corresponding capacity retention for different kind of carbon.*[120]

The energy density of this FeF_3/C composite is rather low due to the high carbon content in the composite without considering the low gravimetric density of FeF_3 itself compared to other positive electrode materials (Table 3).[120,122] However one main drawback of FeF_3 cathode composites is the large polarization, which has been explained by the different reaction pathways during discharge/ charge.[123]

Table 3: *Energy densities, specific capacities, redox potentials and voltage hysteresis of positive insertion- and conversion type electrode materials.*[124]

Compound	Redox potential vs. Li^+/Li^0 (V)	Gravimetric capacity (mAh/g) theo/exp $Mn^+ \rightarrow M^0$	Gravimetric energy density (Wh/kg) theo	Volumetric density (g/cm3)	Volumetric energy density (Wh/L)	Voltage hysteresis (V)	Carbon percentage (wt%)
$LiCoO_2$	3.9	274/148	1068	5.1	5447	0.01	5
$LiFePO_4$	3.4	170/165	589	3.6	2120	0.02	5
FeF_3	2.74	713/600	1954	3.87	7562	0.8-1.6	20
BiF_3	3.18	303/230	964	5.32	5128	0.5-0.7	20
CuF_2	3.55	528/250	1874	4.23	7927	0.8	20

In order to achieve higher energy densities and maintain the benefit of high specific capacity, bismuth fluoride[121,125] and bismuth oxyfluoride[126] turned out as interesting candidates. In 2005 it was shown that a BiF_3/C composite could deliver a gravimetric capacity

of around 230 mAh/g at an average redox potential of 3 V vs. Li^+/Li^0, however fast capacity fading (Figure 29).[121]

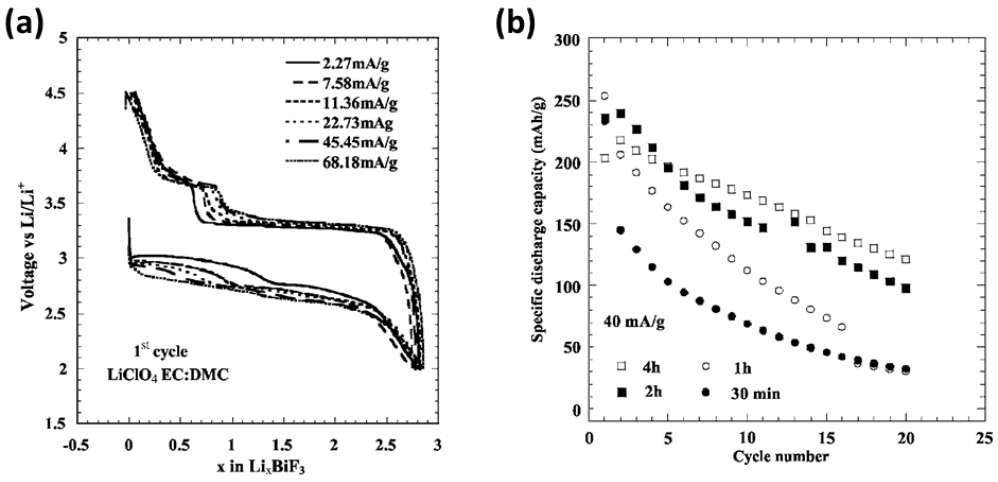

Figure 29: (a) *Galvanostatic curve of BiF_3 versus lithium for different current rates and* ***(b)*** *the capacity retention for ab BiF_3/C ball milled for different times composite with 20wt% carbon.*[121,125]

1.4 Borate based cathode materials for lithium- and sodium-ion batteries

Boron, the fifth element of the periodic table, doesn't occur in its elemental form in nature, only as its oxide form. More than 200 borate minerals are found in earth's crust, so called borates, but only a few of them are of commercial interest: *borax*, *kernite*, *ulexite* and *colemanite* (Table 4).[127]

Table 4: *The four main borate based minerals found in earth's crust with their chemical formula and the main deposit location.*[127]

Mineral	Formula	Location
Borax	$Na_2B_4O_7{\cdot}10H_2O$	USA, Turkey, Argentinia
Kernite	$Na_2B_4O_7{\cdot}4H_2O$	USA
Ulexite	$NaCaB_5O_9{\cdot}8H_2O$	Turkey, South America
colemanite	$Ca_2B_6O_{11}{\cdot}5H_2O$	Turkey

Starting in the 19th century, borates based glasses have been studied for their optical properties and later on for alkali ion conduction.[128,129] Nevertheless crystalline borate based

materials were mainly investigated because of its non-linear optical properties and as host structures for light emitting phosphors. Since the discovery of β-BaB_2O_4 and LiB_3O_5 in the mid 1980's (which are up to now still the most frequently used borate based non-linear optical properties (NLO) materials) an increased interest in the scientific community has led to the discovery of a large variety of borate based compounds.'[132] It is believed that these optical properties derive from the unique crystal- and electronic resulting from the small boron atoms inside an oxide matrix.[133]

1.4.1 Why borate based materials?

As mentioned above, borate based minerals can form a variety of different structures, therefore an uncountable number of borate based materials has been reported in literature. In terms of application of borates as electrode materials for Li-ion batteries, they present two main advantages. First of all, in the context of the polyanionic concept for cathode materials, the borate anion represent the lightest anionic group among all others (Table 5), hence having the possibility to increase the gravimetric capacity significant in contrast to phosphates or silicates.

Table 5: *Comparison of the most common polyanions in terems of the molecular weight.*

Polyanion	Molecular weight [g/mol]
$\mathbf{BO_3^{3-}}$	59
$\mathbf{CO_3^{2-}}$	60
$\mathbf{SiO_4^{4-}}$	92
$\mathbf{PO_4^{3-}}$	95
$\mathbf{SO_4^{2-}}$	96

A second reason, to explore borate based cathode materials is the very rich chemistry since boron can adopt trigonal planar- or tetrahedral oxygen coordination (Figure 30), leading to unique condensed polyanions.[132,134]

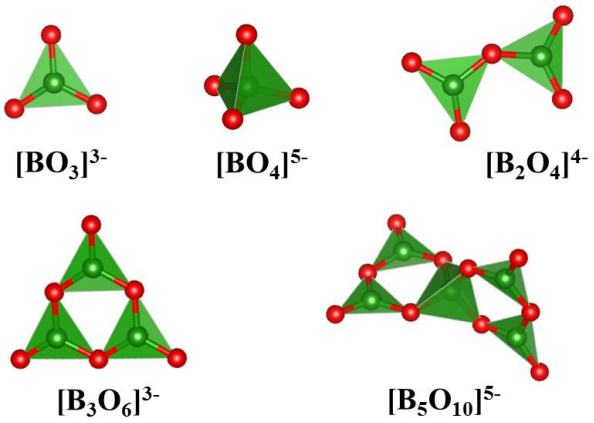

Figure 30: *Different oxygen coordination and borate polyanions. Oxygen- and boron atoms are drawn in red and green respectively.*

Driven by these two points, the investigation of borates as cathode materials took its course starting around 2000, however involving exclusively compounds based on the trigonal planar BO_3 group, the so called *ortho* borate group.

1.4.2 Lithium transition metal borates

The first transition metal borate compounds $LiMBO_3$ were investigated since the late 1990's for their optical and structural properties (M = Mg, Co, Cd, Zn),[135–137] it was first in 2001 when *Legagneur et al.* introduced the family of lithium 3d-metal borates $LiMBO_3$ (M = Fe, Mn, Co) as potential cathode materials for Li-ion batteries, with theoretical capacities exceeding 200 mAh/g. The three compounds were prepared by classical ceramic synthesis at high temperatures.[138] The crystal structures for M = Mn, Fe, Co crystallizing in a monoclinic space group are shown in Figure 31, and are built up of edge sharing $[MO_5]$ trigonal-bipyramids running along the c-axis. These columns are connected through planar BO_3-groups and split lithium sites in tetrahedral coordination. In general the three compounds differ only in the size of the trigonal-bipyramid depending on the transition metal ion. Only for M = Mn a hexagonal polymorph is reported (Figure 31d) which can be obtained from the monoclinic form if heated above 550°C.

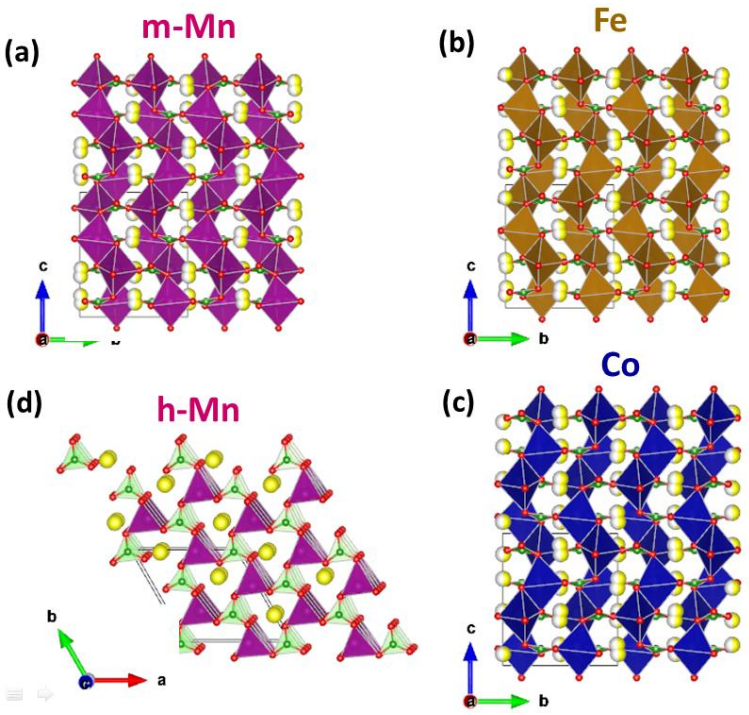

Figure 31: *Crystal structures of $LiMBO_3$ for* ***(a)*** *M = Mn (monoclinic),* ***(b)*** *Fe,* ***(c)*** *Co and* ***(d)*** *Mn (hexagonal). Oxygen, lithium and boron atoms are shown in red, yellow and green respectively.*

Initially *Legagneur et al.* reported an electrochemical negligible activity versus lithium even if very slow current rates were applied (Figure 32).

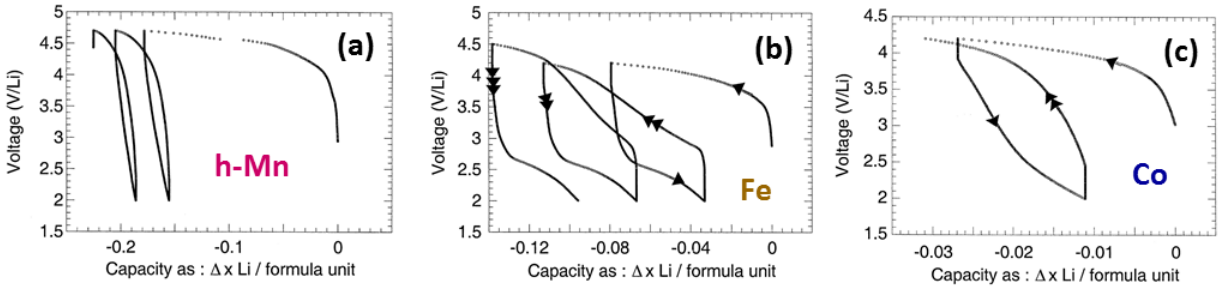

Figure 32: *Voltage composition curve of $LiMBO_3$ cycled with different C-rates for* ***(a)*** *hexagonal-Mn, C/60,* ***(b)*** *Fe, C/250 and* ***(c)*** *Co, C/100.*[138]

It took around one decade to optimize synthesis conditions,[139–142] so that by preparing nano-sized particles[143–146] or controlling antisite-disorder[147,148] the experimental capacities could be significantly improved. However only for $LiFeBO_3$ the theoretical capacity of 220

mAh/g could be achieved. In contrast the theoretical capacities could not be reached for $LiMBO_3$ (M = Mn, Co) (Figure 33).

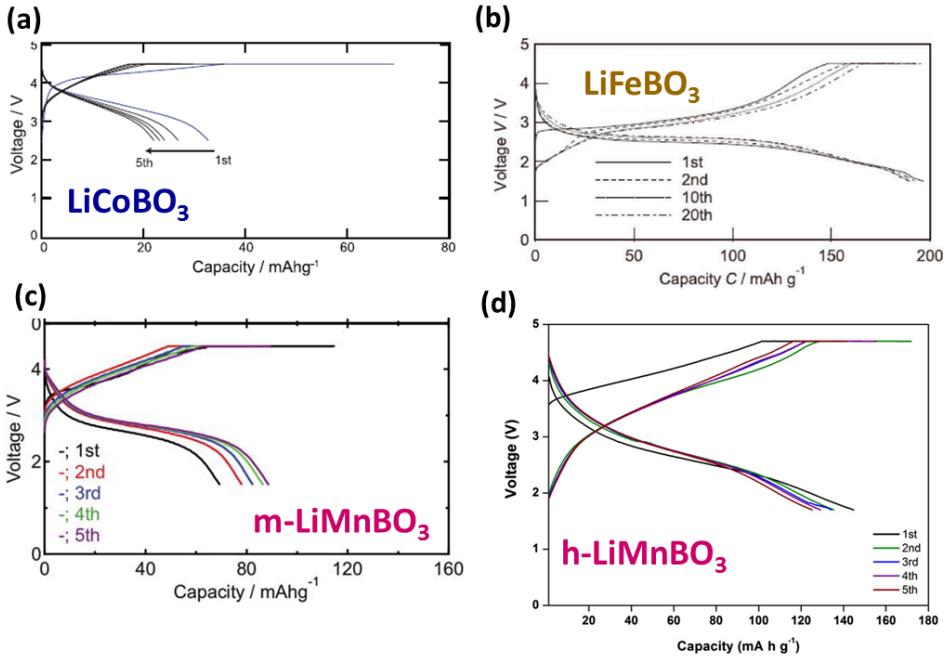

Figure 33: *Galvanostatic charge-discharge curves for* ***(a)*** *LiCoBO3,*[140] ***(b)*** *LiFeBO3,*[139] ***(c)*** *m-LiMnBO3*[141] *and* ***(d)*** *h-LiMnBO3*[144] *cycled at a C/20 rate versus lithium.*

After the initial report of *Yamada at al.* where he almost achieved the theoretical capacity for $LiFeBO_3$, this material turned into a serious earth abundant cathode material for lithium ion batteries, confirmed by following publications.[149,150] As mentioned in the initial paper, $LiFeBO_3$ displays a redox potential versus lithium of around 2.8 V vs. Li^+/Li^0, rendering this compound moisture sensitive.[139] Therefore this material has to be handled carefully in inert atmosphere during the whole synthesis and cell preparation process. If not, it undergoes a fast degradation process as studied deeply in literature leading to a considerably reduced capacity.[151,152]

Besides the above describe class of lithium transition metal borates $LiMBO_3$ (M = Mn, Fe, Co) only one more compound has been reported in literature as a candidate for cathode materials in Li-ion batteries, a lithium manganese borate $Li_7Mn(BO_3)_3$. This material crystalizes in a triclinic space group having Mn^{2+} in a tetrahedral environment surrounded by planar BO_3 groups and lithium in tetrahedral sites. The authors claim to be able to reach a

reversible capacity of around 120 mAh/g with an average redox potential centered around 3 V vs. Li^+/Li^0 (Figure 34), but again this material has to be handled thorough under inert atmosphere since it is decomposed by moisture.[153] However no following publication reporting on the synthesis and electrochemical activity on this material was able to confirm their results so far.

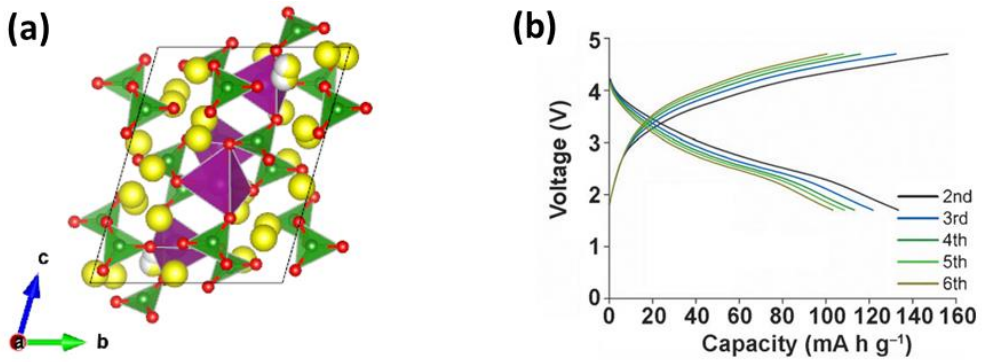

Figure 34: (a) *Structure of $Li_7Mn(BO_3)_3$ viewed along the a-axis. Oxygen, lithium boron and manganese are represented in red, yellow, green and purple respectively.* ***(b)*** *Galvanostatic charge-discharge curve for $Li_7Mn(BO_3)_3$ between 4.7 and 1.7 V vs. Li^+/Li^0 with 10 mA/g.*[153]

1.4.3 Borophosphates

The low potential ~2.8 V vs. Li^+/Li^0 of $LiFeBO_3$ prevents it from being a commercial challenger to state-of-the-art cathode materials. Following the polyanionic concept, borophosphates, a combination of borate- and phosphate groups could offer elevated redox potentials compared to pure borate based compounds. Generally speaking borophosphates are compounds out of the system M_xO_y-B_2O_3-P_2O_5-(H_2O) with complex anionic structures built up of BO_3, BO_4 and PO_4 anions and their partially protonated species, thus offering an incredible huge amount of possible structures and compounds.[154] Known already for one century, only about one decade ago a systematic investigation of this class of inorganic compounds has been started and pushed forward mainly by *Kniep* and coworkers.[155,156]

Borophosphates are usually prepared using hydrothermal synthesis methods leading often to open framework and microporous structures, investigated in the past for their optical and catalytic properties.[157–161] These open structures providing possible Li- and Na-ion migration pathways made borophosphate materials attractive candidates as possible cathode

materials for Li- and Na-ion batteries. Recently two examples reported in literature show indeed possible extraction/ insertion of Li- or Na-ions at redox potentials slightly higher than $LiFeBO_3$, nevertheless the capacity (even theoretical) is relatively low due to the high molecular weight of this class of materials (Figure 35).[162,163]

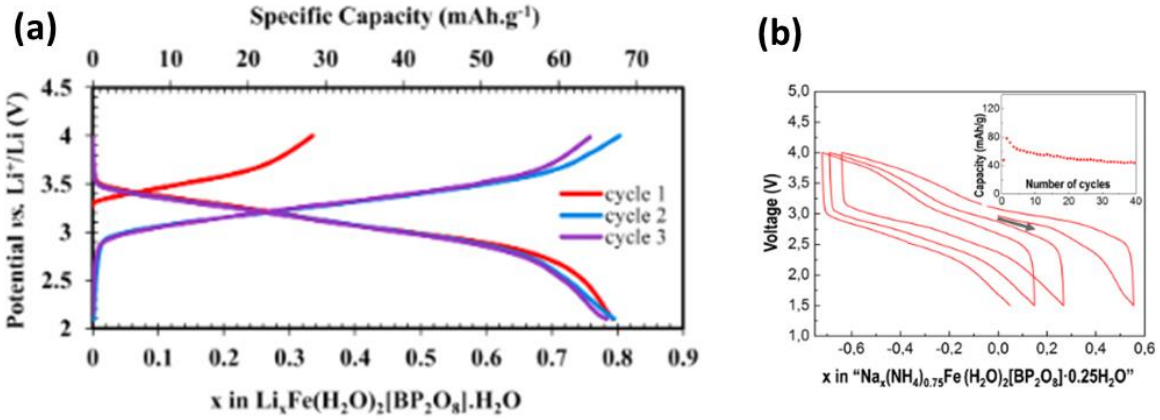

Figure 35: (a) *Galvanostatic charge/ discharge curve of $Li_{0.8}Fe(H_2O)_2[BP_2O_8]\cdot H_2O$ versus lithium and* ***(b)*** *voltage composition curve of $(NH_4)_{0.75}Fe(H_2O)2[BP_2O_8]\cdot 0.25H_2O$ versus sodium.*[162,163]

1.5 Motivation and aim of the thesis

As mentioned, lithium transition metal borates $LiMBO_3$ can be attractive candidates as polyanionic cathode materials for Li-ion batteries. It has been shown in the case of $LiFeBO_3$ that high gravimetric capacities (~200 mAh/g) are accessible if BO_3 is used instead of PO_4 or SO_4 as the polyanionic group.[139] Despite the weight gain coming along with borates, in any case the redox potential will be lower compared to phosphate PO_4 or sulfate SO_4 based materials, which it not surprising if one takes a look at the *Pauling* electronegativity of the following atoms: [164]

$$\mathbf{B}(2.09) < \mathbf{C}(2.55) < \mathbf{P}(2.19) < \mathbf{S}(2.58) < \mathbf{O}(3.44) < \mathbf{F}(3.98).$$

Recently it was shown in the case of $LiFePO_4$, that the redox potential of 3.45 V vs. Li^+/Li^0 could be shifted up around 500 mV by using a pyrophosphate $[P_2O_7]^{4-}$ based material $Li_2FeP_2O_7$.[86] Although the voltage increase is not outstanding and its origin is not fully understood yet,[165] it was a first hint to apply this concept to the exploration of borate based cathode materials beyond BO^{3-}based materials.

Even though *pyroborate (or diborate)*- $[B_2O_5]^{4-}$ and other various *polyborate* ($[B_5O_{10}]^{5-}$, $[B_3O_6]^{3-}$, etc.) based compounds are well known in literature, there is certainly a lack of compounds suitable as potential cathode materials.[166–169] Only two alkali-3d-metal *pyroborate* materials, $NaScB_2O_5$ and $Li_6CuB_4O_{10}$ and no other alkali-3d-metal *polyborate* based material was reported so far.[170–173] This was an inspiration to get involved in the search for new pyroborates as described in the following sections.

Thus, the work presented in this thesis was aimed to design new borate based cathode materials for lithium and sodium ion batteries. To achieve this goal a synthetic exploration combined with fundamental examination of structure-properties relationship has been conducted. The following manuscript presents the main results obtained during this study, and is divided into five chapters.

First an introduction into electrochemical energy storage in batteries (emphasis on Lithium- and Sodium ion batteries) with a brief overview about the development and state-of-the-art cathode materials is given. Furthermore the motivation to explore explicit borate based materials will be pointed out and the approaches applied during this work will be described in detail.

Secondly the experimental techniques and approaches employed within this thesis will be described in details, to inspire further studies or experimental work in this field.

The third chapter shows as a proof of concept the investigation of the structural electrochemical properties of a lithium copper borate $Li_6CuB_4O_{10}$, displaying a high redox potential of 4.25 V vs. Li/Li^+ and a surprisingly high ionic conductivity around 1.4 mS/cm at 500°C.

The fourth chapter focuses on new compounds synthesized, namely sodium transition metal pentaborates $Na_3MB_5O_{10}$ (M = Fe, Co). Their crystal structures are solved and electrochemical properties versus sodium are revealed, showing that it is possible to reversible desodiate $Na_3FeB_5O_{10}$ at elevated temperatures (55°C) at a redox potential of 2.5 V vs Na^+/Na^0 (~30 mAh/g) whereas $Na_3CoB_5O_{10}$ is electrochemically inactive, due to kinetic limitations within these materials, revealed by AC and DC conductivity measurements

To overcome the limitations of insertion/ deinsertion reactions for borate based compounds, a bismuth oxyborate $Bi_4B_2O_9$ is tested as a conversion type cathode material versus lithium. The reaction mechanism is revealed and it is shown that this material undergoes a conversion reaction around 2.3 V vs. Li^+/Li^0 with surprisingly little carbon additive and no need for nano-sized particles as usual for conversion type cathode materials.

Finally all the results presented within this thesis work are summarized and compared to materials studied up to now for the same purpose. At the end a broader context and outlook regarding borate based materials for energy storage applications is given.

2 Search for new pyroborate B_2O_5 based compounds

It is nowadays established that by modifying the polyanion of a cathode material, elevated redox potentials versus Li/ Na can be achieved. Following this direction, we tried in this thesis to increase the potential of borate based materials, since for instance $LiFeBO_3$ shows a voltage of 2.8 V which is rather low compared to other polyanionic cathode materials. To increase the redox potential condensed polyanions can be introduced, as previous recalled in switching from $LiFePO_4$ to $Li_2FeP_2O_7$.

Thus, for Fe-based materials, the expected potential should be well above 2.8 V vs. Li^+/Li^0 if going from BO_3 to B_2O_5 or even B_2O_5F.

We have followed this strategy and our results are reported in this chapter which first gives a general overview about the reactivity of borates and possible synthetic routes for crystalline borate materials and then focuses on the experimental description of our first synthetic approaches, theoretically leading to pyroborate cathode materials.

2.1 A few synthesis considerations

Given by the nature of boric acid H_3BO_3 (mainly used precursor for borates) which contains one boron atom connected to three hydroxyl groups, borate based compounds can be synthesized through different synthetic methods. It is known that H_3BO_3 can easily undergo dehydration/ polymerization reactions leading to unpredictable crystal structures. As schematically shown in Figure 36, a complete- or a partial dehydration of H_3BO_3 can be realized, leading to new polyanions that can be viewed as a polymerization of the *ortho* borate group BO_3. These different synthetic routes can involve more or less all techniques used in solid state/ inorganic chemistry including high temperature ceramic-, or low temperature mechanochemical or solvothermal methods. Some of these approaches will exemplary be described in the next sections, whether successful or not, however with the aim to possibly provide ideas for future synthetic work.

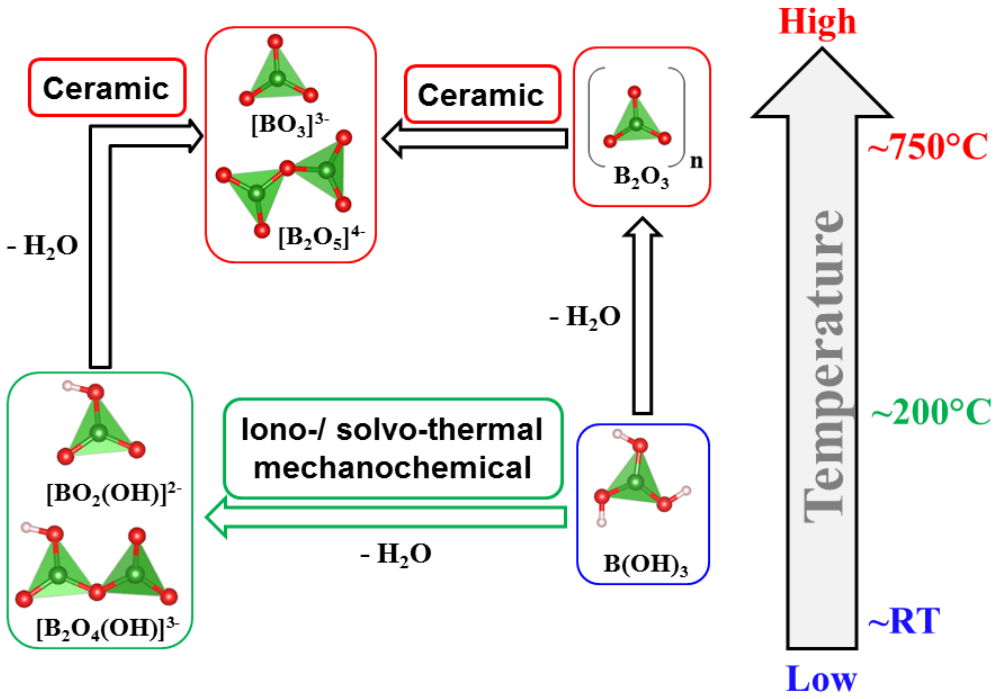

Figure 36: *Schematic illustration of the synthetic concept applied within this thesis. Starting from boric acid different ways can be chosen, involving different synthetic approaches and temperatures. For reasons of clarity only ortho- and pyroborate based groups are shown. However one has to keep in mind that borate based species can not only polymerize in two-, but also in three-dimensions involving trigonal BO_3 and tetrahedral BO_4 coordinated species.*

Dealing with cathode materials, compounds like $A_2MB_2O_5$ (A = Li, Na; M = Mn, Fe, Co) are of interest. However as known from preliminary work,[174] a lot of difficulties were encountered on the way to stabilize these phases. Even if different type of metathesis reactions starting from pyroborate based precursors ($M_2B_2O_5$ or $Li_4B_2O_5$)[168,175,176] were tried, no progress was made. Since these preliminary results were not promising, other model compounds were needed, and along that line $Li_{0.8}Mg_{2.1}B_2O_5F$, a lithium containing fluoro pyroborate was recently published.[177] If Mg^{2+} could be replaced by a redox active divalent *3d* metal, it should be theoretically possible to achieve a capacity of 121 mAh/g by reversible extracting 0.8 Li^+. Needless to say that the capacity value is not outstanding, however it could act as a proof of concept that pyroborate based materials offer elevated redox potentials versus Li compared to $LiMBO_3$. In the following sections different synthetic approaches are described as attempts to synthesize $Li_{0.8}M_{2.1}B_2O_5F$ (M = Mn, Fe, Co).

2.2 Ceramic synthesis

A straight forward solid state synthesis was originally reported by Wang *et al.* consisting of mixing stoichiometric amount of lithium carbonate Li_2CO_3, magnesium fluoride MgF_2, magnesium nitrate $Mg(NO_3)_2{\cdot}6H_2O$ and boric acid H_3BO_3 with a subsequent annealing at 750°C for 60 h in a platinum crucible with intermediate regrinding. So our first attempts consisted in replacing MgF_2 by a 3d metal fluoride MF_2 (M = Co, Mn, Fe) and $Mg(NO_3)_2{\cdot}6H_2O$ through the corresponding oxalate.[3] However this first approach failed entirely, instead more thermodynamically stable $M_2B_2O_5$ and lithium fluoride LiF were formed in all cases, guiding us to directly start from the pyroborate precursor $M_2B_2O_5$ and react it with LiF (equation 3). Therefore the approach was again unsuccessful for M = Mn; Fe, Co as more stable $LiMBO_3$ and $Li_2B_4O_7$ with other unidentified impurity phases were formed. Note that in the case of M = Mg the desired phase was formed.

$$LiF + M_2B_2O_5 \rightarrow LiM_2B_2O_5F \quad \textbf{(3)}$$

This unfruitful experiments let us to explore unconventional synthetic approaches, involving more reactive precursors and low temperature solution based approaches, with the aim to stabilize metastable phases which are not accessible through high temperature ceramic methods.

2.3 Low temperature synthesis

Given the difficulties to obtain alkali-3d metal pyroborates we decided to start from more reactive borate based precursors to form *in situ* a pyroborate. One way is to use a precursor containing a borate hydroxide group which can undergo a *in situ* dehydration reaction upon thermal treatment as shown in Figure 36.

Magnesium borate hydroxide $MgBO_2OH$ is well known as the mineral *szaibelyite* and the preparation of MBO_2OH (M = Mg, Mn, Fe, Co) was reported.[178] These compounds which contain a $[B_2O_4OH]$ structural unit closely related to a pyroborate B_2O_5 group, are synthesized

[3] 3d metal nitrates were not considered since the nitrous gases evolved during heating easily oxidize the divalent metal.

hydrothermally at temperatures ranging from 180 to 200°C with reaction times between 5 and 10 days.

Using a stoichiometric mixture of $MgBO_2OH$ and LiF (5-10 mol% excess), $Li_{0.8}Mg_{2.1}B_2O_5F$ could be synthesized at temperatures around 600°C contrary to the reported synthesis (equation 4). Switching to MBO_2OH (M = Mn, Fe, Co) didn't bring the desired success, driving us to consider different reaction media. As it is known ionic liquids can promote reaction between two insoluble solids. We used a solvothermal approach in 1-Ethyl-3-methyl imidazolium bis (trifluoro methyl sulfonyl) imide (EMI-TFSI) where MBO_2OH was dispersed together with AF (A = Li, Na, K) and exposed to temperatures around 250°C for 24 h. Unfortunately for all these reactions MF_2 and AMF_3 were formed.

$$LiF + 2\ MBO_2OH \rightarrow LiM_2B_2O_5F + H_2O \quad \textbf{(4)}$$

Facing this failure, we next considered Tris (pentafluorophenyl) borane TPFPB as a "catalyst" to drive the reaction at temperatures below 100°C. TPFPB well known in organometallic catalysis as strong Lewis acid and is able to "disolve" LiF in organic solvents by forming a $[TPFPB{-}F]^-$ anion releasing Li^+ as a counter ion (Figure 37).

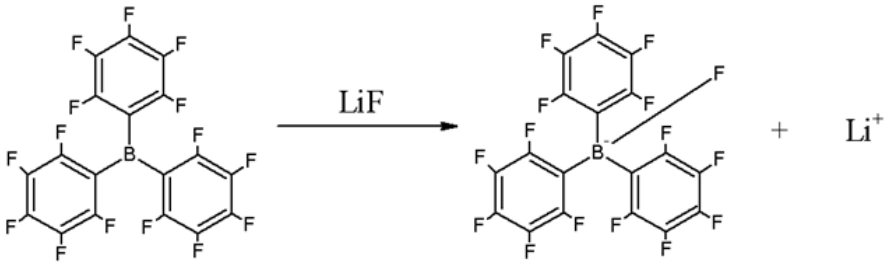

Figure 37: *Abstraction of a fluorine ion from LiF by TPFPB.*

Our idea was to dissolve stoichiometric amounts of LiF and TPFPB in organic solvents like propylene carbonate PC, to achieve a reaction with MBO_2OH (equation 5), however no reactivity at all was observed in this system.

$$Li^+ + TPFPB \cdot F + 2\ MBO_2OH \rightarrow LiM_2B_2O_5F + TPFPB \cdot H_2O \quad \textbf{(5)}$$

At this stage bearing in mind the difficulties encountered in preparing fluoroborates we decided to switch our efforts towards pure pyroborates.

There are only two alkali-3d-metal pyroborate compounds reported so far: a) sodium scandium pyroborate $NaScB_2O_5$ and b) lithium copper pyroborate $Li_6CuB_4O_{10}$ for which two polymorphs α and β were reported. As Sc is not redox active, particular attention has been given to $Li_6CuB_4O_{10}$ which contains two pyroborate units and Cu^{2+} as the redox active transition metal. Combining both features, theoretical high redox potentials are expected for the reversible extraction/ insertion of Li, hence this material was subjected to a thoroughly investigation of its electrochemical and structural properties, although its theoretical capacity associated to the Cu^{3+}/Cu^{2+} redox couple is only 87 mAh/g.

3 Structural and electrochemical properties of a lithium copper pyroborate $Li_6CuB_4O_{10}$

The synthesis of $Li_6CuB_4O_{10}$ was first reported in 2006 by Pan *et al.*,[171] but already mentioned in Sparta's PhD thesis in 2003. The synthesis of this phase was done by the authors through mixing stoichiometric amounts of Li_2CO_3, CuO and H_3BO_3 and annealing the mixture at 590°C for 2-3 days, denoted as α-$Li_6CuB_4O_{10}$ afterwards.[173] To obtain a better crystallized product our synthesis consisted in mixing stoichiometric amounts of the same precursors with mortar and pestle, followed by a decomposition of H_3BO_3 at 450°C for 4 h and annealing the mixture for 48 h at 650°C. A royal blue powder of pure α-$Li_6CuB_4O_{10}$ was obtained, showing a particle size from 20 to 50 µm with no signs of impurities (Figure 38a).

Later in 2013, Kuratieva *et al.* isolated a crystal of another $Li_6CuB_4O_{10}$ polymorph denoted as β-$Li_6CuB_4O_{10}$, in exploring the Li_2O-CuO-B_2O_3 ternary system.[172] Through the course of this thesis we found that bulk samples of β-$Li_6CuB_4O_{10}$ can be obtained from α-$Li_6CuB_4O_{10}$ if the latter is annealed for at least 9 days at 500°C in air with a particle size distribution from 10 to 50 µm,.

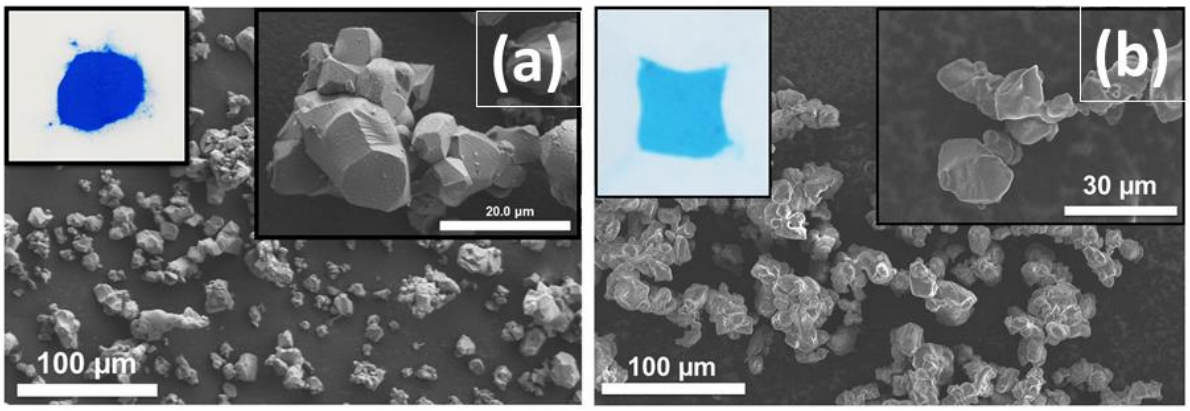

Figure 38: *Representative SEM images of* ***(a)*** *α- $Li_6CuB_4O_{10}$ and* ***(b)*** *β- $Li_6CuB_4O_{10}$. Insets show a magnified view on the crystallites and a colored picture of the as-prepared powder.*

The different color of both polymorphs (α-$Li_6CuB_4O_{10}$: royal blue, β-$Li_6CuB_4O_{10}$: pale blue) let us consider a slightly different oxidation state of Cu as well a slightly different stoichiometry. To check both of these issues electron paramagnetic resonance (EPR)

spectroscopy was conducted (experimental details see annexes chapter 7.3.2). The room temperature EPR spectrum for both polymorphs are identical and show a signal for Cu^{2+} ($3d^9$) of the same amplitude (Figure 39). Moreover the two α- and β-polymorph have the same stoichiometry as determined from inductive coupled plasma optical emission spectroscopy (ICP-OES) (Table 6).

Table 6: *Theoretical and experimental values obtained from the ICP-OES elemental analysis of Li, Cu and B for α- and β- $Li_6CuB_4O_{10}$.*

Atom	theoretical stoichimetry	Wt% theoretical	Wt% exp. α-LCB	Stoichiometry exp. α-LCB	Wt% exp. β-LCB	Stoichiometry exp. β-LCB
Li	6	13.5	12.1	5.4	12.1	5.4
Cu	1	20.6	20.4	1	20.6	1
B	4	14.02	13.5	3.9	13.7	3.9
O	10	51.87	-	-	-	-

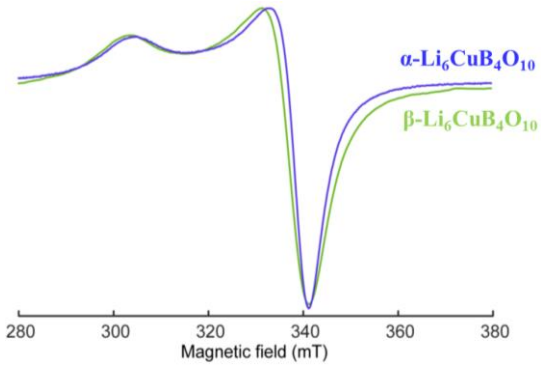

Figure 39: *EPR spectra recorded at room temperature for both polymorphs of $Li_6CuB_4O_{10}$.*

The differences in terms of the crystal structure, relationship and electrochemical properties of the both polymorphs will be described consecutively.

3.1 Structure and polymorphism

Two structural models were reported for $Li_6CuB_4O_{10}$, the first one by Pan *et al.* (α-polymorph) and the second one by Kuratieva *et al.* (β-polymorph) both crystallizing in a triclinic unit cell. Their structural models were originally derived from single crystal diffraction and reported without any structural or synthetic relationship between them. For α-$Li_6CuB_4O_{10}$ the XRD pattern can be indexed using Pan's triclinic cell, with the exception of weak peaks which could not be indexed suggesting a superstructure. This superstructural peaks (Figure 40, inset) were already mentioned in Sparta's PhD thesis and explained in a structural model including a tripled unit cell. This structural model fits perfectly the recorded XRD pattern (Figure 40a) with lattice parameters listed in Table 7. Regarding β-$Li_6CuB_4O_{10}$ the XRD pattern could be proper fitted using the triclinic model described by Kuratieva *et al.* (Figure 40b) with lattice parameters shown in Table 8.

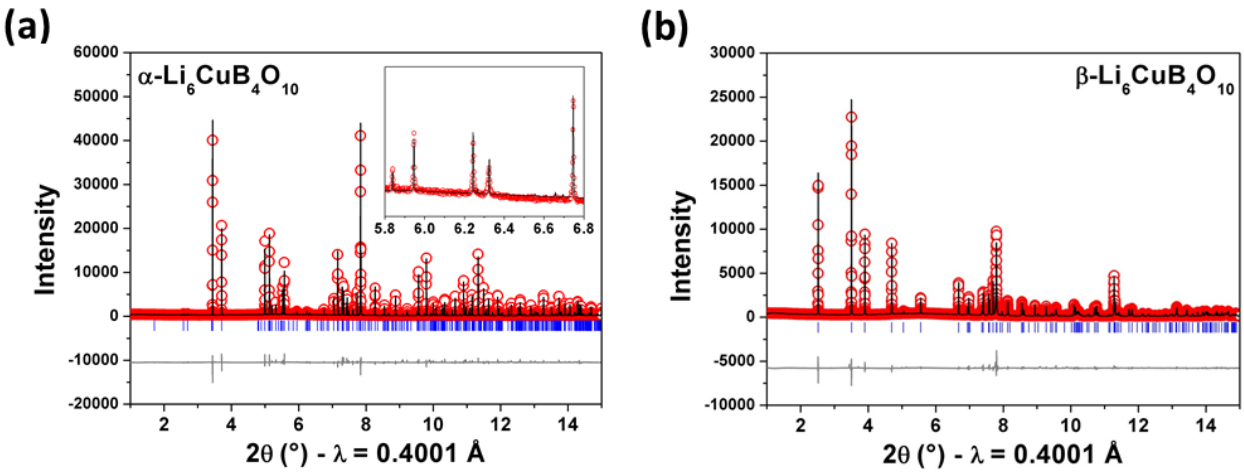

Figure 40: *Rietveld refinement of the synchrotron XRD pattern of* ***(a)*** *α- and* ***(b)*** *β- $Li_6CuB_4O_{10}$. The red circles, black line and the bottom grey line represent the observed, calculated and difference pattern respectively. Bragg positions are marked with blue vertical thick bars.*

Table 7: *Structural parameters and atomic positions of α-$Li_6CuB_4O_{10}$.*

α-$Li_6CuB_4O_{10}$					
Space Group *P* -1 *a*=4.821340(3) Å, *b*=9.234549(7) Å, *c*=13.964087(11) Å α=104.31439(5) °, β=96.21839(5)°, γ=94.57957(5)° *V*=595.195(1) Å^3, ϱ= 2.582 g/cm^3, Z=3, R_{Bragg} = 11.9 %, χ^2 = 8.44					
Atom	**Wyckoff site**	***x***	***y***	***z***	**B(Å^2)**
B1	2*i*	0.0852(19)	0.4463(9)	0.3336(7)	0.39(14)
B2	2*i*	0.1779(20)	0.6796(10)	0.4822(7)	0.65(16)
B3	2*i*	0.190(2)	0.6607(10)	0.1849(7)	1.31(19)
B4	2*i*	0.276(2)	0.8972(10)	0.3284(7)	1.15(19)
B5	2*i*	0.4190(20)	0.7715(9)	0.9908(7)	0.66(17)
B6	2*i*	0.4720(19)	0.0004(9)	0.1452(6)	0.20(15)
Cu1	1*a*	0	0	0	0.55(3)
Cu2	2*i*	0.3000(2)	0.31614(10)	0.67137(8)	0.43(2)
Li1	2*i*	0.038(2)	0.8018(12)	0.8149(9)	-0.08(20)
Li2	2*i*	0.068(4)	0.3786(17)	0.0345(12)	3.2(4)
Li3	2*i*	0.078(3)	0.0713(14)	0.8176(10)	2.5(3)
Li4	2*i*	0.221(3)	0.9290(15)	0.6293(10)	1.7(3)
Li5	2*i*	0.333(3)	0.1367(12)	0.4883(9)	0.3(2)
Li6	2*i*	0.368(3)	0.4314(12)	0.9148(9)	1.0(2)
Li7	2*i*	0.370(2)	0.1719(12)	0.3115(9)	0.9(2)
Li8	2*i*	0.414(3)	0.5709(13)	0.6101(9)	1.8(3)
Li9	2*i*	0.475(3)	0.3997(14)	0.1973(9)	1.9(3)
O1	2*i*	0.0246(10)	0.5885(5)	0.0998(4)	0.55(10)
O2	2*i*	0.0668(10)	0.2575(5)	0.5419(3)	0.60(10)
O3	2*i*	0.1071(10)	0.7874(5)	0.2506(3)	0.26(9)
O4	2*i*	0.1604(11)	0.8056(5)	0.9530(4)	0.74(10)
O5	2*i*	0.1579(10)	0.0242(5)	0.3609(3)	0.26(9)
O6	2*i*	0.1917(10)	0.5242(5)	0.6976(4)	0.47(9)
O7	2*i*	0.1846(9)	0.0295(5)	0.1315(3)	0.13(8)
O8	2*i*	0.2232(10)	0.3413(5)	0.2815(3)	0.40(9)
O9	2*i*	0.2392(11)	0.5498(5)	0.4203(4)	0.55(10)
O10	2*i*	0.3505(10)	0.7487(5)	0.5606(4)	0.17(9)
O11	2*i*	0.3435(11)	0.9223(5)	0.7707(4)	0.22(10)
O12	2*i*	0.4361(10)	0.1228(5)	0.9209(3)	0.03(9)
O13	2*i*	0.4692(11)	0.1276(5)	0.6251(4)	0.48(9)
O14	2*i*	0.4751(11)	0.3536(5)	0.0435(4)	0.97(12)
O15	2*i*	0.4624(10)	0.6166(5)	0.2042(3)	0.24(8)

Table 8: *Structural parameters and atomic positions of β-$Li_6CuB_4O_{10}$.*

β-$Li_6CuB_4O_{10}$					
Space Group *P* -1					
***a*=3.31175(7) Å, *b*=6.6799(9) Å, *c*=9.27284(12) Å**					
α=104.31439 °, β=89.7329(3)°, γ=86.57145(2)°					
***V*=200.89(1) Å^3, ϱ= 2.551 g/cm^3, Z=1, R_{Bragg} = 7.007 %, χ^2 = 5.63**					
Atom	**Wyckoff site**	***x***	***y***	***z***	**B(Å^2)**
Cu1	1*a*	0	0	0	0.94(3)
O1	2*i*	0.6452(9)	0.2087(4)	0.0682(3)	0.29(4)
O2	2*i*	0.9758(9)	0.7959(4)	0.1849(3)	0.29(4)
O3	2*i*	0.6794(9)	0.0418(4)	0.3240(3)	0.29(4)
O4	2*i*	0.5287(10)	0.3937(4)	0.2653(3)	0.29(4)
O5	2*i*	0.9405(9)	0.7180(4)	0.4458(3)	0.29(4)
B1	2*i*	0.6149(18)	0.2213(8)	0.2137(6)	0.47(9)
B2	2*i*	0.8652(18)	0.8476(9)	0.3145(6)	0.47(9)
Li1	2*i*	0.567(3)	0.2047(12)	0.4669(8)	0.63(11)
Li2	2*i*	0.028(3)	0.4827(12)	0.3551(8)	0.63(11)
Li3	2*i*	0.470(3)	0.6482(12)	0.1214(8)	0.63(11)

The basic building unit of both polymorphs can be described as a $[Cu(B_2O_5)_2]^{6-}$ structural unit, which consists of a Cu^{2+} square planar coordinated by two pyroborate B_2O_5 groups (Figure 41). In the α-polymorph 2 independent Cu sites are present, contrary to the β-polymorph which contains only one crystallographic site for Cu.

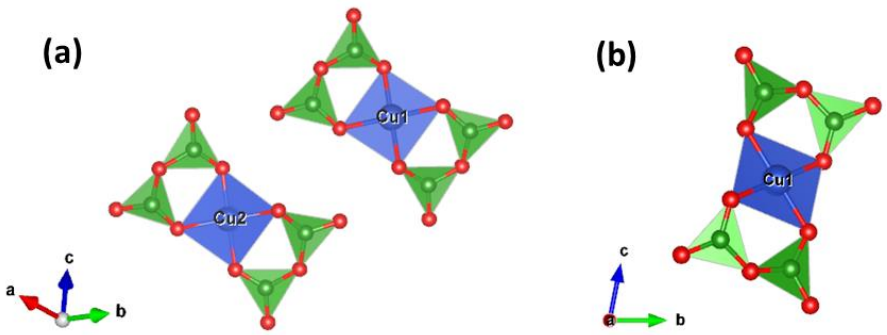

Figure 41: *View of the $[Cu(B_2O_5)_2]^{6-}$ structural unit in* ***(a)*** *α-$Li_6CuB_4O_{10}$ (Cu1 and Cu2) and* ***(b)*** *β-$Li_6CuB_4O_{10}$ (Cu1). Copper, boron and oxygen atoms are shown in blue, green and red respectively.*

These units are stacked independently in a parallel way on top of each other along crystallographic directions, with Li sitting in tetrahedral sites in between these units (Figure 42). The α-polymorph presents 9 different Li-sites whereas in the β-polymorph Li occupies 3 different sites. The main difference between the two polymorphs is located in the way Li connects the $[Cu(B_2O_5)_2]^{6-}$ units, which forms layers along the ac-plane in β-$Li_6CuB_4O_{10}$ compared to α-$Li_6CuB_4O_{10}$ (Figure 42b, d).

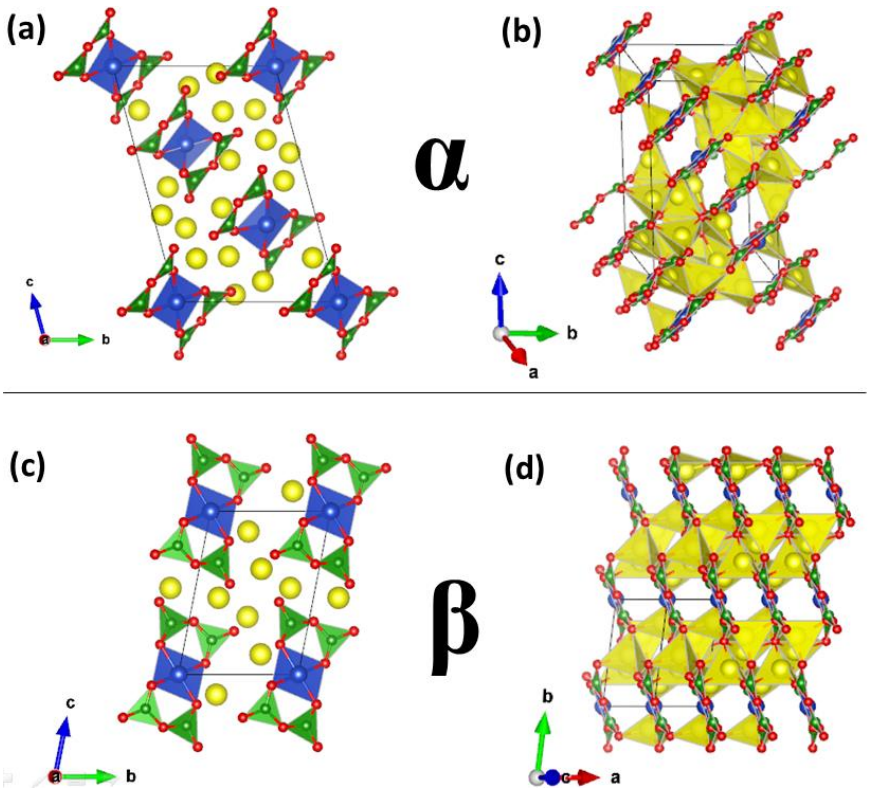

Figure 42: *Structure of* ***(a, b)*** *α- and* ***(c, d)*** *β- $Li_6CuB_4O_{10}$ along different crystallographic directions. Copper, boron and oxygen are drawn in blue, green and red. Li, Cu, B and O atoms are drawn in yellow, blue, green and red respectively.*

Although in the initial publication from Pan *et al.*[171] no phase transition was observed with differential scanning calorimetry (DSC) for α-$Li_6CuB_4O_{10}$, Sparta[173] mentioned a reversible transition around 350°C. To check this point in detail DSC measurements coupled with thermogravimetric analysis (TGA) were measured with a STA 449C Netzsch (experimental details see annexes chapter 7.3.1). A heating rate of 2°C/min was applied under

flowing air using around 15-20 mg of the pristine material between room temperature and 500 or 650°C for the α- and β-polymorph respectively.

For α-$Li_6CuB_4O_{10}$ one large endothermic phase transition is visible during heating followed by a very tiny one at 346 and 372°C respectively. These transitions are perfectly reversible upon cooling since equivalent exothermic peaks are visible, suggesting a structural transition between a low temperature (LT) and a high temperature (HT) form of α-$Li_6CuB_4O_{10}$ (Figure 43a). Note that this reversible structural transition between an LT-α and a HT-α form was further supported by the complementary TGA measurement where only a negligible mass change was observed, most likely due to the removal of absorbed water during heating of the sample (Figure 43c).

Regarding β-$Li_6CuB_4O_{10}$ one broad endothermic phase transition is present with a maximum at 570°C upon heating (Figure 43b), whereas during cooling a smaller but well-defined exothermic peak shows up at 330°C. The huge temperature difference of the peaks in the DSC measurement during heating and cooling indicated two different structural transitions. Based on the observed color change of the sample from pale- to royal blue, we could assume a change from the β- to the α-polymorph on cooling. The structural nature of this transition was further confirmed through the TGA measurement whereas in the case of α-$Li_6CuB_4O_{10}$ again no mass change is observed (Figure 43d).

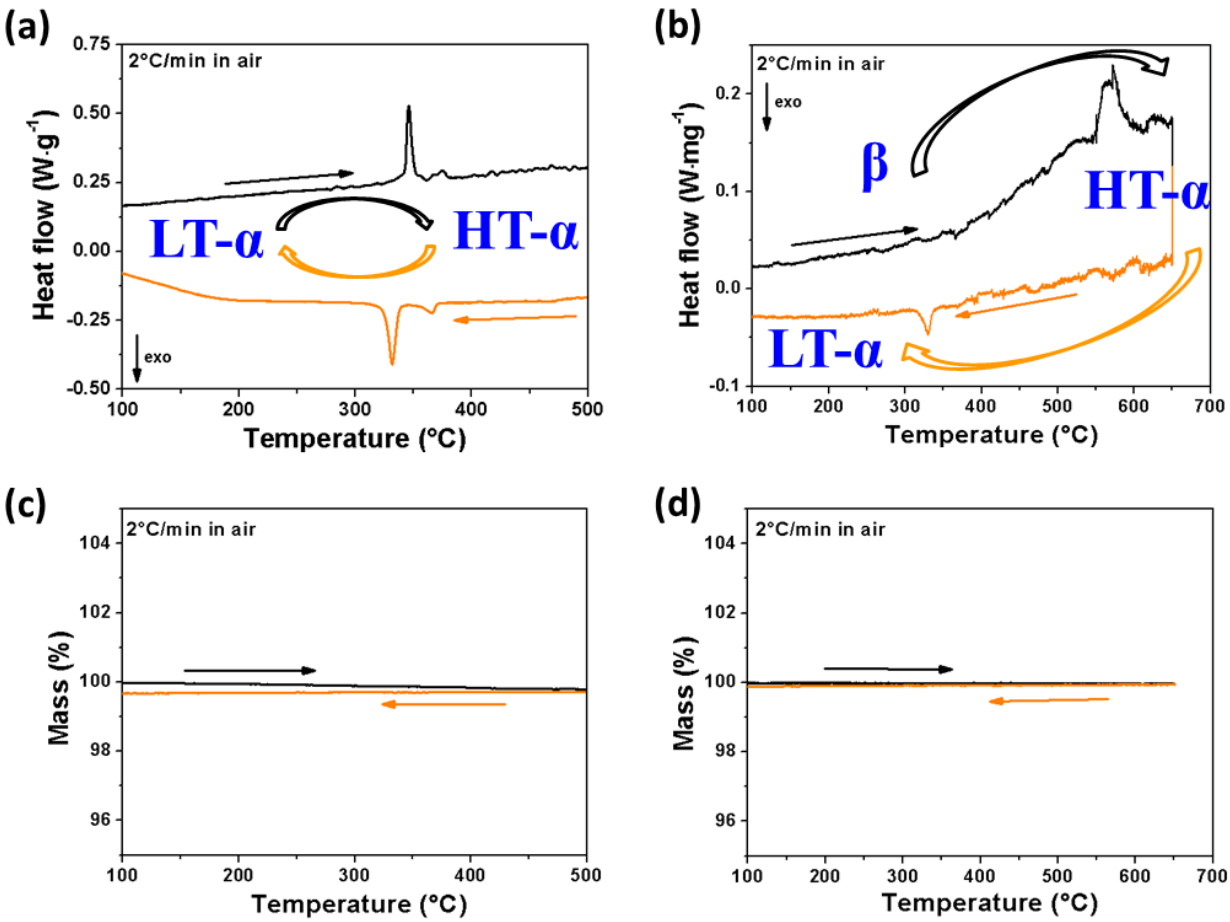

Figure 43*: DSC and TGA curve for* ***(a,c)*** *α- and* ***(b,d)*** *β-$Li_6CuB_4O_{10}$ respectively. The black- and the orange line are recorded during heating and cooling respectively. LT- and HT- refers to the low temperature- and high temperature form of α-$Li_6CuB_4O_{10}$.*

To get more insights into the structural changes taking place during the phase transitions observed in DSC, *in situ* synchrotron XRD pattern were recorded (experimental details see annexes chapter 7.2.2) for α- and β-$Li_6CuB_4O_{10}$, during heating, and after the sample was cooled down to room temperature (Figure 44, 45). As seen in Figure 44, upon heating a gradual shift of the reflections around 3.5 and 5.1° 2θ is visible, till a striking jump at 350°C, where a sudden strong shift is observed. All the patterns can be indexed with the same triclinic unit cell as for the room temperature one, but with different lattice parameters *a*= 4.90122 Å, *b*= 9.18486 Å, *c*= 14.49619 Å, α= 105.5898°, β= 98.0462(11)° and γ= 94.1337° for the pattern recorded at T= 500 °C. Note that after the 350°C phase transition the superstructure reflections between 5.8 and 6.8° disappear. This gives the possibility to index the patterns with the smaller unit cell reported by Pan.[171] This corresponds to an increase of

the *a* and *c* lattice parameters and a decrease of *b* as compared to the room temperature phase (Figure 45). Overall, the volume is enlarged by 4% to reach 618.248 $Å^3$ at 500 °C (Figure 45a). All the changes in the XRD pattern are perfectly reversible if the sample is cooled down to room temperature, in agreement with the DSC measurements (Figure 43a). Note that we were not able to stabilize the HT α-$Li_6CuB_4O_{10}$ at RT by quenching from temperatures above 500°C even if liquid nitrogen was used.

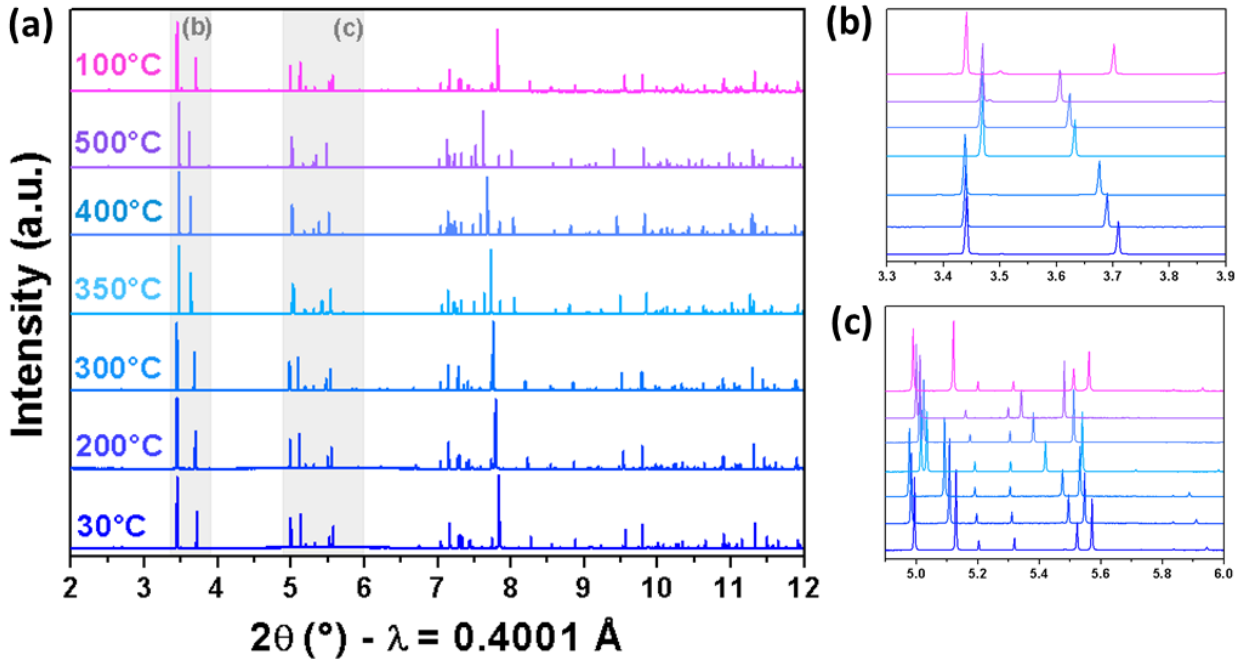

Figure 44: *In situ synchrotron XRD pattern for α-$Li_6CuB_4O_{10}$ during heating up to 500°C and after cooled down to 100°C. A global view is given in* ***(a)*** *while* ***(b)*** *and* ***(c)*** *highlight the grey marked areas.*

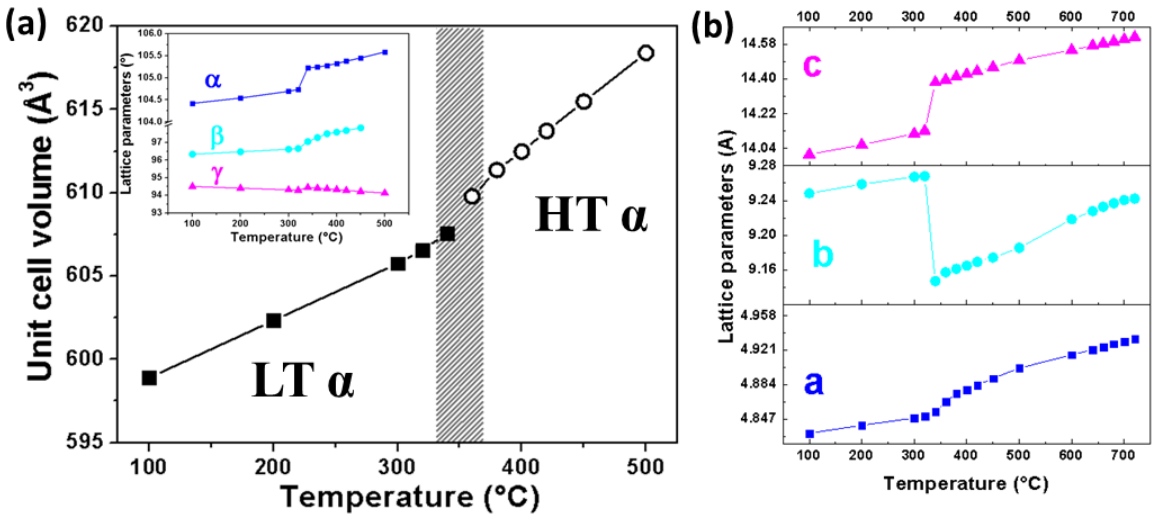

Figure 45: *Change in lattice parameters as a function of temperature for α-$Li_6CuB_4O_{10}$ during heating as derived from in situ high temperature XRD. The grey shaded bar marks the temperature region where the structural transition from the LT- to the HT α-$Li_6CuB_4O_{10}$ occurs.* ***(a)*** *Volume of the unit cell and angles shown in the inset.* ***(b)*** *Variation of unit cell parameters.*

If β-$Li_6CuB_4O_{10}$ is gradually heated up to 600°C (Figure 46), first a slight shift of the reflections is observed up to 550°C coming along with the linear increase of the lattice parameters *a*, *b*, *c* (Figure 47a) and a decrease of all angles (Figure 47c) followed by a transformation from the β- to the α-polymorph starting around 550°C. The XRD pattern at this temperature can be indexed with the same triclinic unit cell used at room temperature for β-$Li_6CuB_4O_{10}$, with increased lattice parameters *a*= 3.37791 Å, *b*= 6.73946 Å, *c*= 9.33539 Å, α= 78.66432°, β= 89.15504° and γ= 85.41164° leading to a unit cell volume of 207.709 $Å^3$ which is ~3% enlarged compared to the one at 30°C. Already visible at 550°C, reflections of the HT α-polymorph start to show up and are constantly growing, becoming the major phase at 600°C. After the sample was cooled down to room temperature an almost pure LT α-$Li_6CuB_4O_{10}$ is obtained, confirming the phase transition from β to HT α around 550°C as seen in the corresponding DSC measurement (Figure 43b).

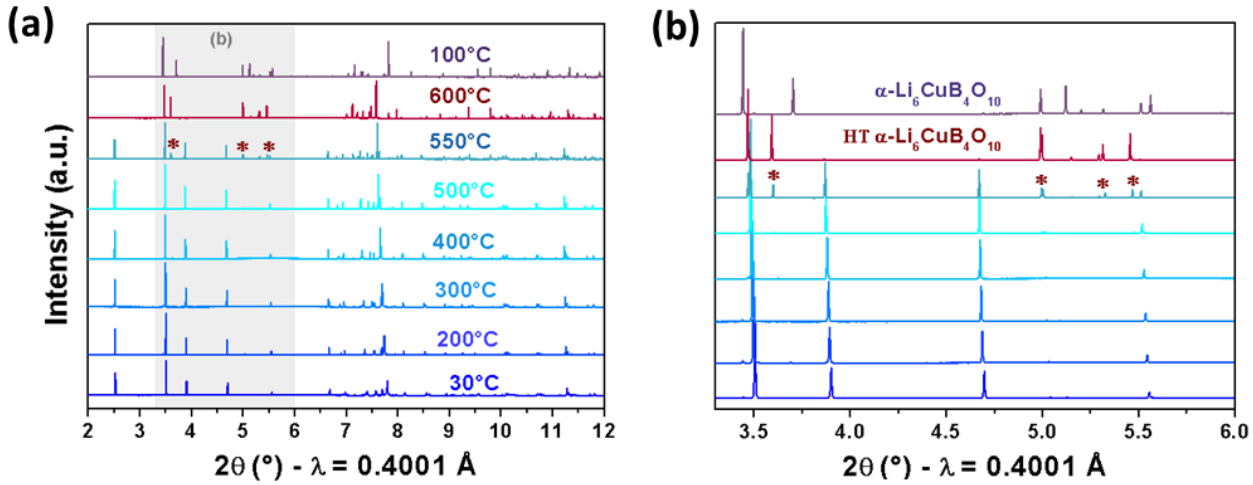

Figure 46: ***(a)*** *In situ synchrotron XRD pattern for β-$Li_6CuB_4O_{10}$ during heating up to 600°C and after cooled down to room temperature with* ***(b)*** *a magnification of the grey shaded region marked in* ***(a)****. The brown asterisks mark the appearance of reflections from the HT α-$Li_6CuB_4O_{10}$ phase.*

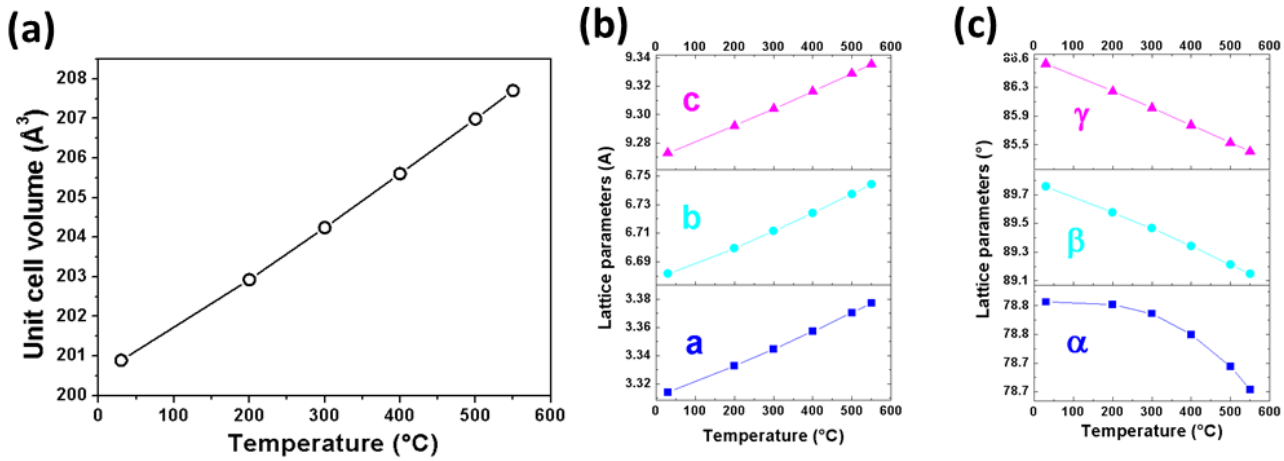

Figure 47: *Change of the lattice parameters of β-$Li_6CuB_4O_{10}$ with temperature.* ***(a)*** *Shows the evolution of the unit cell volume,* ***(b)*** *unit cell edges and* ***(c)*** *the unit cell angles.*

From the complementary XRD and DSC measurements, the relationship between the two known polymorphs of $Li_6CuB_4O_{10}$ could be established and a schematic overview is shown in Figure 48. From our experimental observations it seems like the direct synthesis of β-$Li_6CuB_4O_{10}$ at 500°C starting from the ternary Li_2O-CuO-B_2O_3 system is not possible or requires infinite long annealing times. However as described above, the β-polymorph could be obtained if α-$Li_6CuB_4O_{10}$ is annealed for at least 9 days at temperatures not above 500°C. If β-$Li_6CuB_4O_{10}$ is exposed to temperatures higher than 550°C, a rapid biphasic phase transformation back to α-$Li_6CuB_4O_{10}$ occurs. Regarding the α-polymorph, whenever exposed

to temperatures above 350°C a HT form is observed, which turns back into LT α-$Li_6CuB_4O_{10}$ if the temperature drops below 350°C.

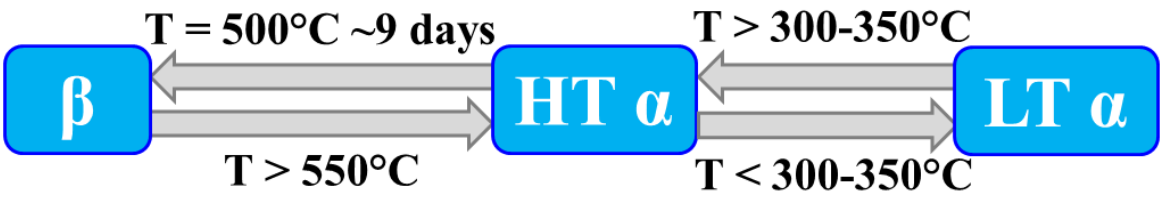

Figure 48: *Schematic representation of the synthetic relationship different polymorphs of $Li_6CuB_4O_{10}$.*

3.2 Electrochemical characterization

3.2.1 Activity versus lithium

Both $Li_6CuB_4O_{10}$ polymorphs were tested versus Li in Swagelok type cells (previously mixed with 20 wt% carbon SP in a SPEX high energy miller in argon). The positive electrode was separated from the negative electrode through two sheets of glass fiber separator soaked with electrolyte (detailed description of the setup see annexes chapter 7.1).

Initially we used a 1M solution of $LiPF_6$ in a mixture of ethylene carbonate (EC), dimethyl carbonate (DMC) and propylene carbonate (PC) in a weight ratio of 1/1/3 respectively (commercial name LP100) as electrolyte. However, as we observed a fast degradation of the electrolyte during galvanostatic cycling, leading to dry cells after only a few cycles, we screened different electrolytes towards their oxidative stability. Two carbonate based electrolytes and one composed of a mixture of a 1M LiTFSI solution in the ionic liquid N-Propyl-N-methyl pyrrolidinium bis(trifluoro methane sulfonyl) imide ($PYR_{13}TFSI$) were tested. This was done by means of cyclic voltammetry of α-$Li_6CuB_4O_{10}$/Li half cells with a scan speed of 0.1 $mV \cdot s^{-1}$ in a potential window from 4.5 to 1.0 V starting on oxidation (Figure 49). One can clearly see a pronounced degradation for the carbonate based electrolytes, as the anodic currents is higher compared to the ionic liquid based one (Figure 49 inset). Such degradation is even more pronounced for the cathodic current. As a result of this electrolyte screening, the ionic liquid based electrolyte described above was selected for all electrochemical experiments further described in this section.

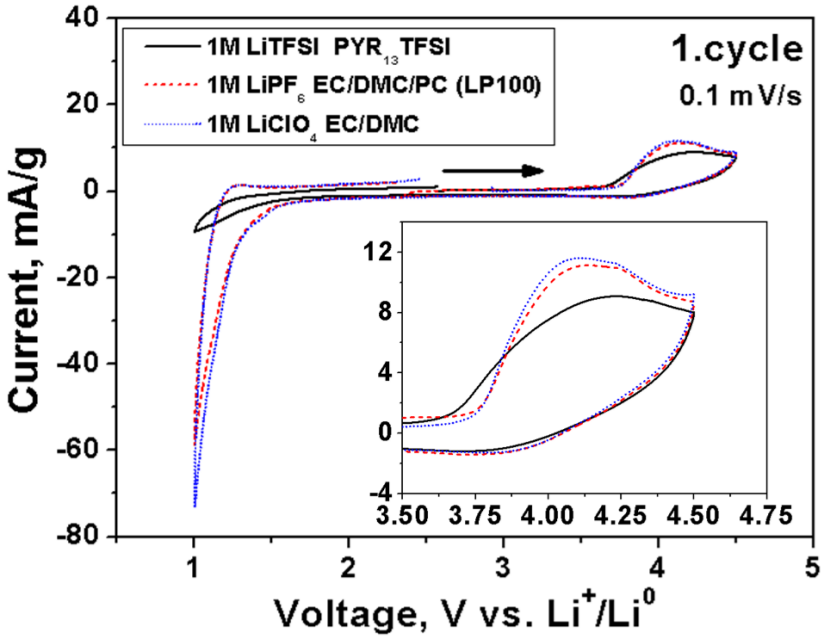

Figure 49: *Cyclic voltammetry of α-$Li_6CuB_4O_{10}$/Li half cells in a potential window from 4.5 to 1.0 V during the first cycle.*

A typical voltage composition curve of a α-$Li_6CuB_4O_{10}$/Li half-cell is shown in Figure 50. The voltage rapidly increases up to 3.8 V and then smoothly slopes up to the cutoff voltage of 4.5 V. The derivative plot of the first charge shows the presence of two oxidation peaks located at ~3.8 and ~4.25 V vs Li^+/Li^0 with the first one shifted by ~0.1 V during the following cycles. As only one single redox center is present in α-$Li_6CuB_4O_{10}$, the two peaks observed in the derivative curve can be most likely correlated to the Cu1 and Cu2 crystallographic site. Around 0.9 Li^+ ions are removed on charge, part of which come from the structure and the rest being associated to electrolyte decomposition, however upon subsequent discharge only 0.3 Li^+ are reinserted. During reduction the derivative curve shows two peaks at ~4.2 V and ~4.0 V vs Li^+/Li^0 which are remarkably more close together compared to the corresponding peaks on oxidation pointing towards an irreversible structural transformation during the first charge, however we don't have a full explanation for this phenomenon yet. Furthermore the large amount of irreversible loss during the first and following cycles can be partially attributed to catalytic electrolyte decomposition as well as irreversible Li loss, since on subsequent cycles between 4.5 and 2.5 V (Figures 50) only 0.3 Li^+ can be reversibly inserted leading to an reversible capacity of 20 mAh/g (Figure 50a inset) fading down about 50% during 10 cycles.

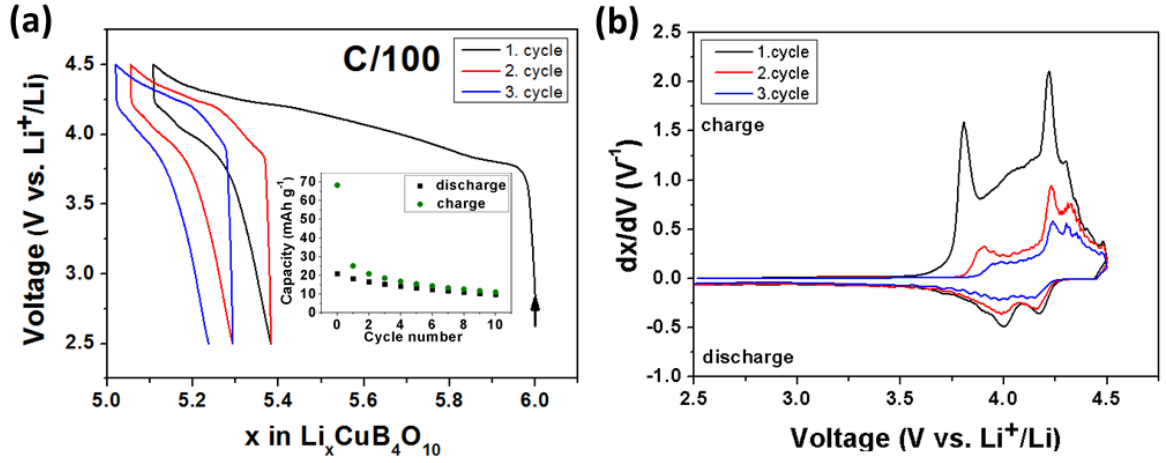

Figure 50: (a) *Voltage-composition curve and* ***(b)*** *the corresponding derivative plot for α-$Li_6CuB_4O_{10}$ vs. Li. Inset in (a) shows the capacity retention.*

To confirm the redox activity versus Li being correlated to the Cu^{3+}/Cu^{2+} redox couple, we decided to use EPR spectroscopy to monitor the Cu^{2+} evolution since Cu^{2+} ($3d^9$) is EPR active, whereas Cu^{3+} ($3d^8$) is EPR silent. Measured spectra of the pristine- and cycled samples are shown in Figure 51 and show similar EPR spectra with axial symmetry ($g_{\parallel}$=2.29, $g_{\perp}$=2.07), signature of Cu^{2+} ($3d^9$), and small sharp peaks (g=2.00) arising from the conductive carbon SP (delocalized electrons) (experimental details see annexes chapter 7.3.2).[179] After oxidation to 4.5 V a decrease of the Cu^{2+} signal is observed (~50%), indicating the formation of Cu^{3+}. On subsequent reduction to 2.5 V, a part of the initial intensity (~80%) is recovered suggesting an incomplete reversibility of the Cu^{3+}/Cu^{2+} redox process as suggested by galvanostatic measurements.

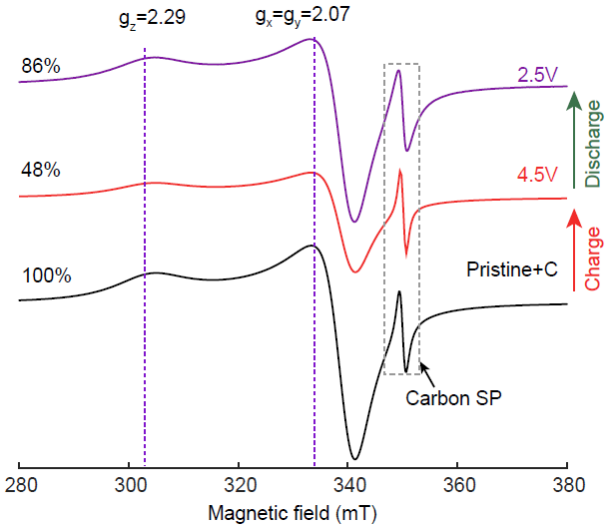

Figure 51: *Room temperature EPR spectra of α-$Li_6CuB_4O_{10}$ ball-milled with carbon at pristine (black), charged (4.5 V, red) and discharged (2.5 V, purple) states.*

To rationalize such a Cu^{3+}/Cu^{2+} redox couple, density functional calculations (DFT+*U*) were performed (detailed description see annexes chapter 7.3.6).[180] First of all, using a *U* parameter at 4 eV for copper (correction factor taken from literature for Cu d-electrons),[180] the structure of α-$Li_6CuB_4O_{10}$ could be well reproduced with less than 2% difference. By considering different delithiation paths from the pristine material, a potential at 3.6 V was obtained, which is about 0.3 to 0.5 V lower than the experimental one, however a pronounced distortion of the CuO_4 square plane is observed for the delithiated phase after the structure was relaxed (Figure 52). This distortion was only accessible from DFT calculations, since we were not able to refine the atomic positions from our *in situ* XRD experiment (Figure 53). To confirm the possibility of having Cu^{3+} at 4.5 V, the projected density of states (DOS) and crystal orbital overlap population (COOP) of α-$Li_6CuB_4O_{10}$ were calculated (Figure 52a). Clearly, the band below the Fermi level, involved in the oxidation process, has an important oxygen contribution and a Cu-O anti-bonding character as seen in the COOP. To probe the redox process the hole Fukui function of α-$Li_6CuB_4O_{10}$ was computed (difference in the charge density induced by the removal of electrons in $Li_6CuB_4O_{10}$, Figure 52b) and the electron Fukui function of the $Li_5CuB_4O_{10}$ phase as found by DFT calculation (difference in the charge density induced by the addition of electrons in $Li_5CuB_4O_{10}$, Figure 52c). The comparison of both Fukui functions together with Highest Occupied Molecular Orbital (HOMO) of square planar CuO_4 (Figure 52d) indicates that the distortion of the Cu square plane upon delithiation allows an orbital mixing between Cu d orbitals and the non-bonding O

p orbitals (which is forbidden in a regular square planar due to symmetry). This distortion re-equilibrates the weight of Cu/O in the redox band in order to involve primarily Cu in the redox process and stabilizes oxygen atoms in the structure.[181]

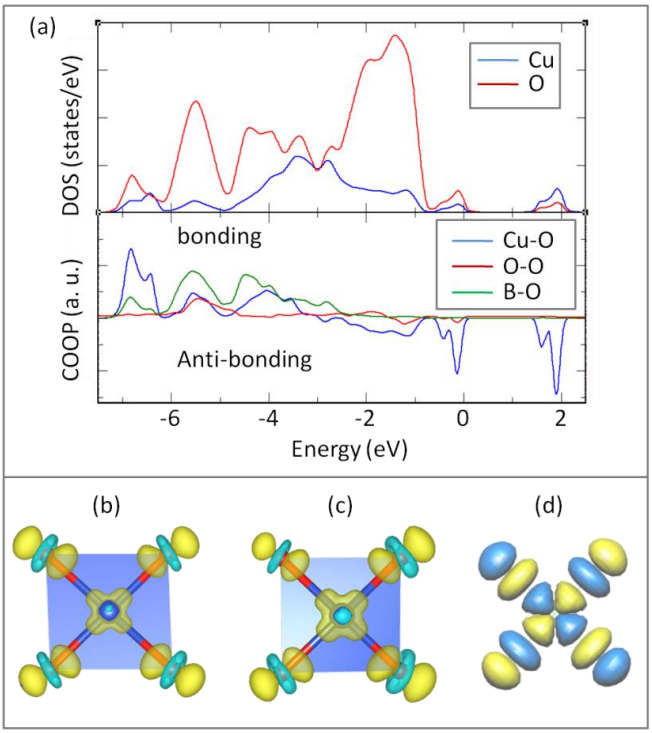

Figure 52: (a) *Cu- and O-projected density of states (DOS) and Crystal orbital overlap population (COOP) for the α-$Li_6CuB_4O_{10}$ phase. The bands lying just below the Fermi level (at 0 eV) show an important O(2p) contribution and a strong Cu-O covalency as highlighted by the computed hole-Fukui function* ***(b)*** *shown in the CuO_4 square plane. Blue and red spheres represent copper and oxygen atoms respectively; the yellow volume corresponds to electron density depletion (holes) while the small cyan regions correspond to electron density accumulation (electrons) due to orbital polarization.* ***(c)*** *Electron-Fukui function computed in the $Li_5CuB_4O_{10}$ phases where the Cu square plane is distorted. The yellow volume corresponds to electron density accumulation (electrons) while the small cyan regions correspond to electron density depletion (hole) due to orbital polarization. It shows a more pronounced implication of the metal thanks to the distortion.* ***(d)*** *Illustration of the local electronic levels involved in the redox band of the $Li_6CuB_4O_{10}$ system, the Highest Occupied Molecular Orbital (HOMO).*

To follow the structural changes during Li uptake/removal in α-$Li_6CuB_4O_{10}$, *in situ* XRD was performed using a homemade electrochemical cell equipped with a beryllium window transparent to X-rays (experimental details see annexes chapter 7.1).[182] XRD patterns were collected for every 0.05 Li removed/ inserted (Figure 53). During charge no major changes with the exception of i) two reflections centered around 19.50° which merge gradually together (Figure 53b), and of ii) a reflection at 27.75° is shifted towards 28.0° (Figure 53b).

On the subsequent discharge down to 2.5 V no reverse changes can be observed (Figure 53a, green XRD pattern). Only if continuing the discharge from 2.5 to 1.0 V, a plateau around 1.5 V appears, leading to the insertion of additional Li-ions and the complete reverse of the *in situ* XRD patterns. More specifically the XRD pattern of the phase charged to 4.5 V can be indexed with the same triclinic cell as pristine $Li_6CuB_4O_{10}$ but with different lattice parameters (Table 9), since there is a contraction of the *a* axis and an extension of the *b* and *c* axis. During Li reinsertion, the unit cell volume is slightly enlarged if compared to the pristine value (599 $Å^3$ versus 595 $Å^3$, see Table 9), which is consistent with the nominal composition of material at the end of discharge to 1 V of "$Li_{6.5}CuB_4O_{10}$" (see Figure 53a). In general the Li-extraction/ insertion in α-$Li_6CuB_4O_{10}$ represents a reversible biphasic processes from a structural point of view.

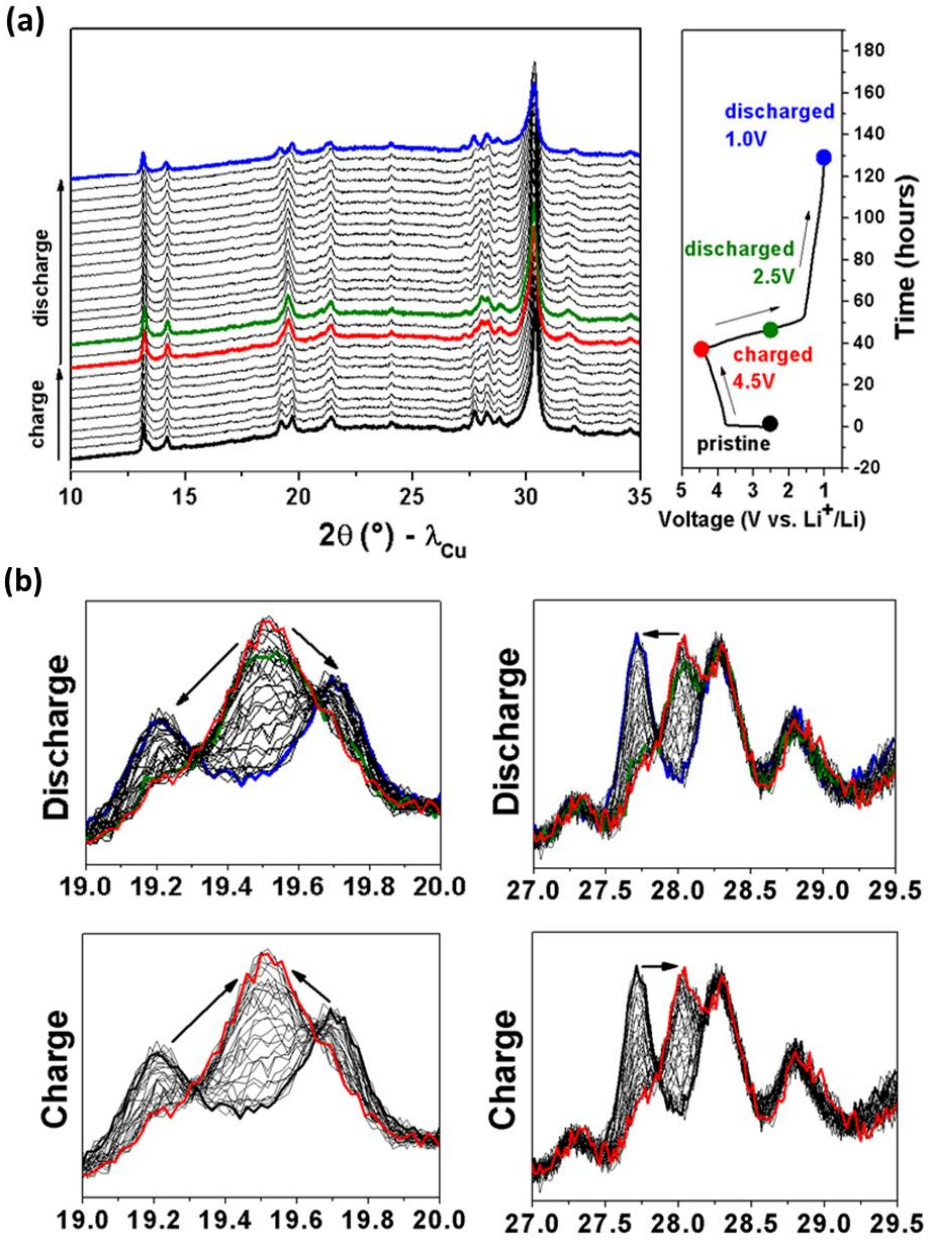

Figure 53: ***(a)*** *In situ XRD patterns during charge and subsequent discharge in relation to the voltage versus time curve.* ***(b)*** *The reversible changes of the reflections indicated centered around 19.5 and 25.0°.*

Table 9: *Lattice parameters and the corresponding voltage of α-$Li_6CuB_4O_{10}$ during galvanostatic charge and following discharge.*

	a (Å)	b (Å)	c (Å)	α (°)	β (°)	γ (°)	V (Å^3)
Charged 4.5V	4.837(5)	9.119(5)	14.088(5)	104.082(5)	96.936(5)	94.115(5)	595.052(5)
Discharged 1.0V	4.829(5)	9.251(5)	14.021(5)	104.36(5)	96.538(5)	94.472(5)	599.244(5)

To further explore the electrochemical behavior, $Li/Li_6CuB_4O_{10}$ cells were either started on oxidation or reduction using a C/50 rate. As shown in Figure 54a,c, similar curves are observed for both independently of what we started on charge or discharge. Equally both cells show similar capacity fading upon subsequent cycling (Figure 54b,d inset). Between 4.5 and 2.5 V. Turning to the lower voltage part of the curve note that there is the appearance of a plateau around 1.5 V which smoothly decreased down to 1 V with the concomitant uptake of additional Li. Nearly around 1 Li is additionally inserted around 1.5 V if the cell is initially started in discharge (Figure 54c), however the corresponding derivative plots represent similar voltages for the oxidation/ reduction process (Figure 54b,d). The inserted Li can be fully removed when the cell is charged back to ~4.0 V with additional 0.7 Li being removed when the cell voltage is further increased to 4.5 V (Figure 54a,c). Although not fully understood yet, we believe that this low voltage process is more related to a Li-driven conversion than insertion/ deinsertion mechanism in agreement with the absence of additional Bragg peaks in the *in situ* XRD when the cell is discharged.

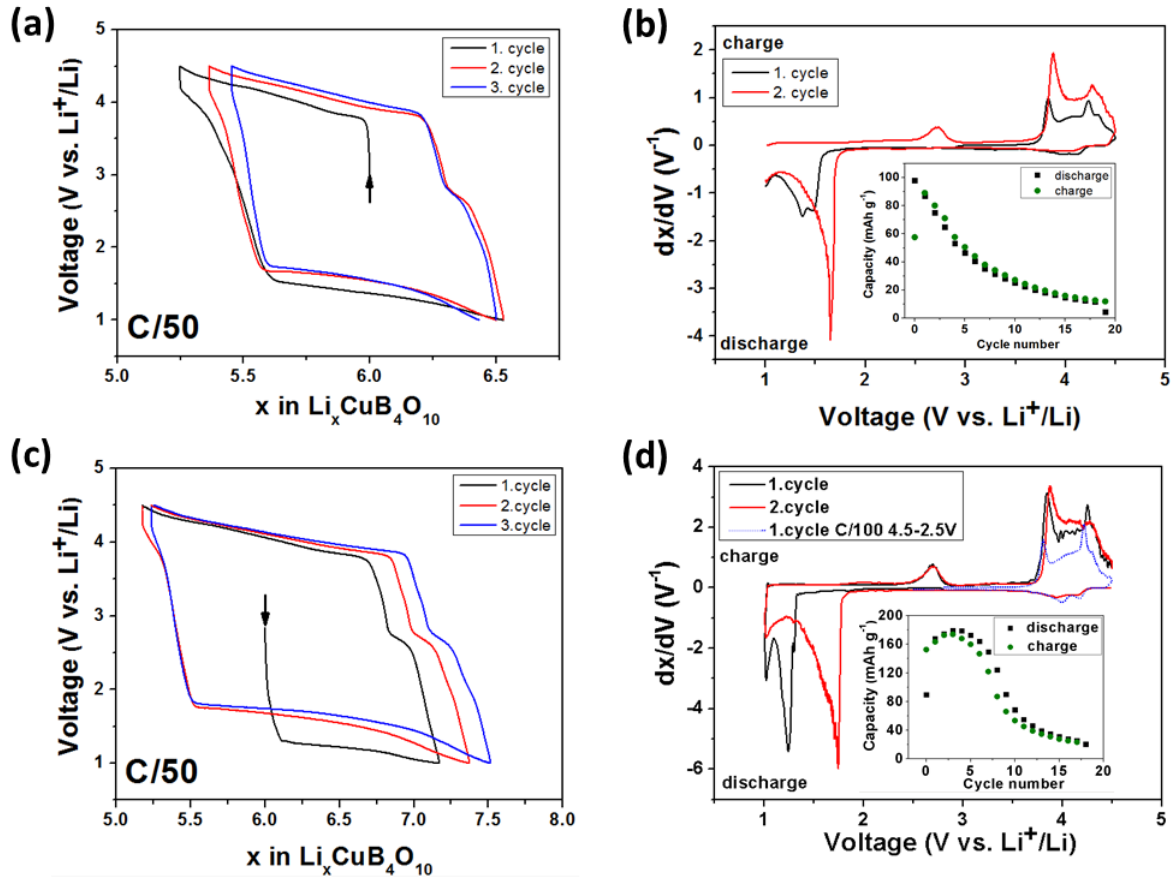

Figure 54: *Voltage composition curve* ***(a)*** *and* ***(c)*** *and the corresponding derivative plot* ***(b)*** *and* ***(d)*** *for galvanostatic cycling of α-$Li_6CuB_4O_{10}$ in a potential window from 4.5 to 1.0 V started either upon oxidation or reduction. The specific charge and discharge capacities versus cycle number are given in the insets of* ***(b)*** *and* ***(d)***.

At this stage it is worth to mention the observation of a reddish color in the inside of the cells disassembled cycled down to 1 V for a few cycles. We hypothesize the formation of elemental copper. To check this issue, cells which have been cycled for 5 times were disassembled within the dry box in their discharge state and the recovered powders were washed with DMC, dried in vacuum and examined by TEM (experimental details see annexes chapter 7.3.5). Figure 55 clearly indicates the appearance of nanograins (size between 1 and 5 nm, too small to be detected by XRD), distributed over the surface of $Li_6CuB_4O_{10}$ carbon composite particles. The chemical nature of these nanograins was identified as pure Cu by both, single area electron diffraction (SAED) andenergy dispersive X-ray spectroscopy (EDS) measurements. This extrusion is most likely responsible for the fast capacity fading (90% fading during 15 cycles, Figure 54 b,d inset) leading to a partial amorphization of the material as deduced by XRD.

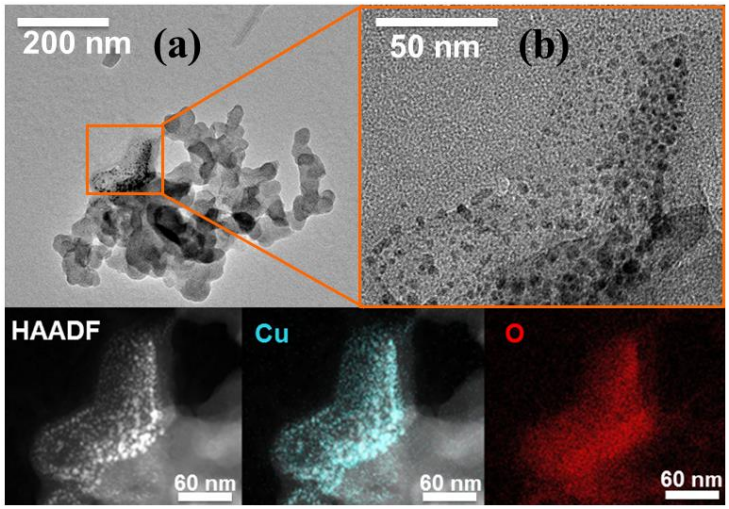

Figure 55: *TEM image of α-$Li_6CuB_4O_{10}$ carbon composite discharged to 1.0 V.* ***(a)*** *shows an overview of agglomerated particles whereas* ***(b)*** *highlights one particle where copper nanograins can be seen on the surface, as confirmed by the corresponding EDS mapping shown below for copper (pale blue) and oxygen (red).*

Turning to β-$Li_6CuB_4O_{10}$, a typical voltage composition curve is shown in Figure 56 After a quick rise to 3.8 V, the curve smoothly slopes up to 4.5 V, showing one well defined oxidation domain centered around 4.2 V as seen in the derivative plot (Figure 56b) most likely associated to the single Cu crystallographic site. Initially ~0.8 Li^+ can be extracted and only 0.2 Li^+ can be reinserted around 3.8 V suggesting irreversible Li extraction owing to copious electrolyte oxidation. During the following cycle only 0.4 Li^+ can be extracted and again 0.2 Li^+ can be reinserted, however the onset of the oxidation potential is shifted up around 0.5 V and the reduction potential is shifted down to 3.6 V, indicating irreversible structural modifications during the first cycle.

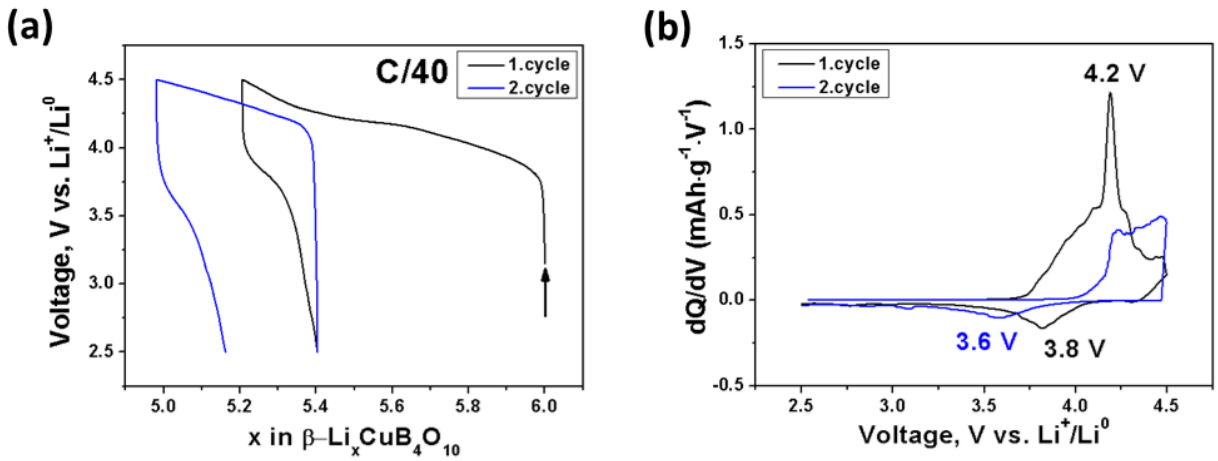

Figure 56: (a) *Typical voltage composition curve and* ***(b)*** *the corresponding derivative plot of β-$Li_6CuB_4O_{10}$ vs. Li at a C/40 rate.*

3.2.2 Ionic conductivity

The poor electrochemical activity of this phase is somewhat surprising because it consists of an open structure and possesses a large amount of Li with additionally absence of thermodynamic limitations as deduced by DFT. This led us to hypothesize that the phase poor electrochemical activity was mainly due to poor ionic conductivity of Li^+ in $Li_6CuB_4O_{10}$. To check the capability of the structure towards Li conduction, bond valence energy landscapes (BVEL) were generated for the α- and β-polymorph, based on the methodology developed by S. Adams (for details see annexes chapter 7.3.7).[183] Figure 57 shows the calculated BVEL maps representing the Li^+ conduction pathways, taking into account the polarizability of the Li^+ species and the influence of the counterions of the structure considering anionic neighbors up to 8 Å at 1.0 eV above the minimum energy (Figure 57). One can first note a huge difference between the LT-α and β-polymorph, whereas the latter one shows only limited 2D pathways in contrast to LT-α where a 3D Li conduction network is visible. Regarding the HT form of α-$Li_6CuB_4O_{10}$, clearly a 3D network is visible slightly enhanced compared to the LT form. The results from BVEL calculations suggest an ionic conductivity which is increased in the order from β << LT-α < HT-α.

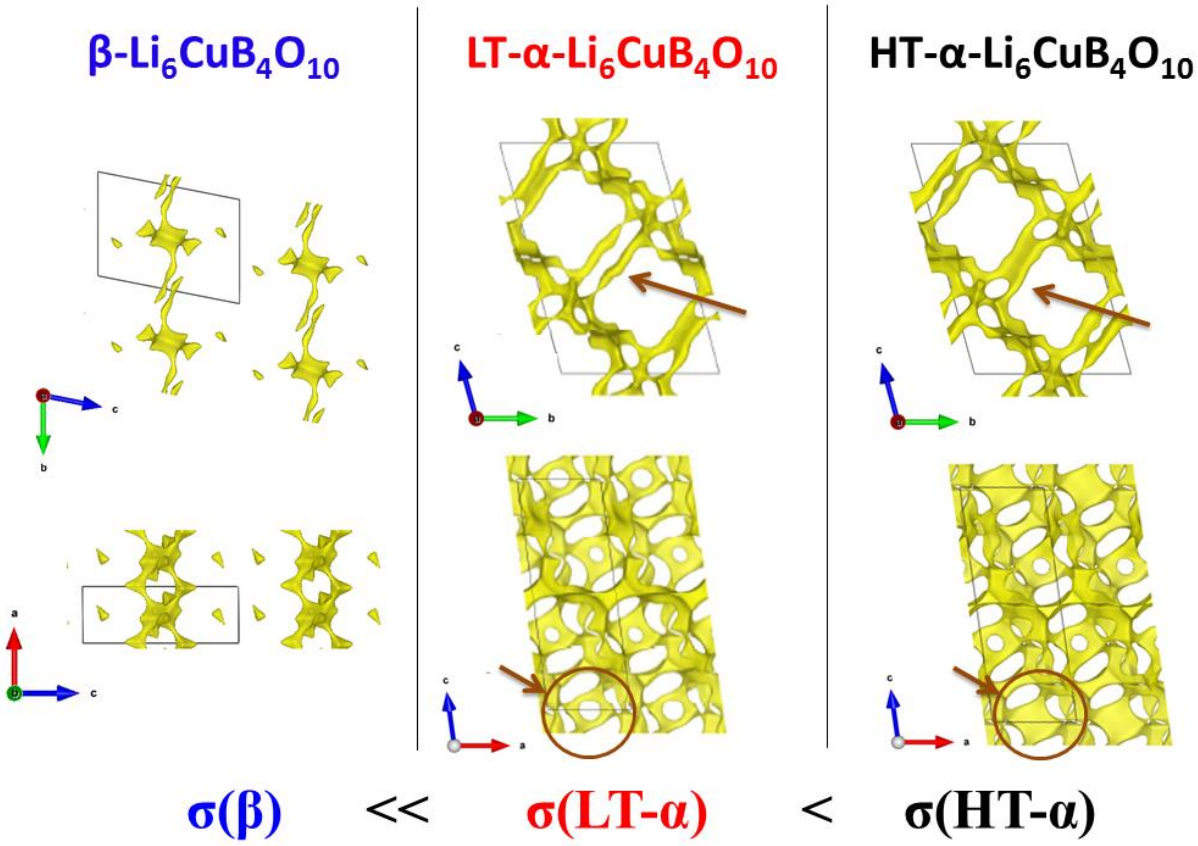

Figure 57: *Bond valence energy landscape (BVEL) for the different polymorphs of $Li_6CuB_4O_{10}$, LT- and HT refers to the Low- and high-temperature form of α-$Li_6CuB_4O_{10}$. The energy values chosen for the plots are 1.0 eV above the minimum energy. Iso-energy yellow domains indicate paths for Li conduction. Slight differences in the Li conduction pathways between the LT and HT form of α-$Li_6CuB_4O_{10}$ are marked with brown arrow and circles.*

To confirm the predictions given by the BVEL calculations, combined AC and DC impedance measurements were conducted on a pellet with ionically blocking platinum electrodes in a temperature range of 150 up to 500°C in air. A pellet suitable for the conductivity measurement was prepared according to the following procedure. Stoichiometric amounts of Li_2CO_3, CuO and H_3BO_3 were ground with mortar and pestle and heated up to 450°C for 6 h in air. After regrinding, the powder was pressed into a pellet with 13 mm diameter and a thickness of ca. 1 mm by applying approximately 3 t pressure. The pellet was then sintered for 48 h at 650°C in air, and placed in the apparatus (detailed description of the setup please see annexes chapter 7.1.3). The obtained density was around 65% of the theoretical density.

First of all, the AC impedance spectra were recorded between 140 and 400°C with a voltage amplitude of 10 mV in a frequency range from 30 MHz to 0.1 Hz. Both $Li_6CuB_4O_{10}$ polymorph spectra present a nearly perfect semi-circle with a linear Warburg diffusion resistance tail at low temperatures (~180°C) (Figure 58a, b). With increased temperature the shape of the spectra is preserved for the β-polymorph as opposed to the α-polymorph where for temperatures higher than 350°C, an almost straight line with a slope ≈45° is visible (Figure 58c), indicating an unexpected high ionic conductivity after the structural transition.

The depressed semi-circles derived from the complex AC impedance spectra were fitted by an R_0- R_1/CPE_1 (Figure 58 a,b inset) equivalent circuit, where R_0 represents an initial shift of impedance arc from zero, R_1 is the sum of the grain boundary and bulk resistance and CPE_1 is a constant phase element.

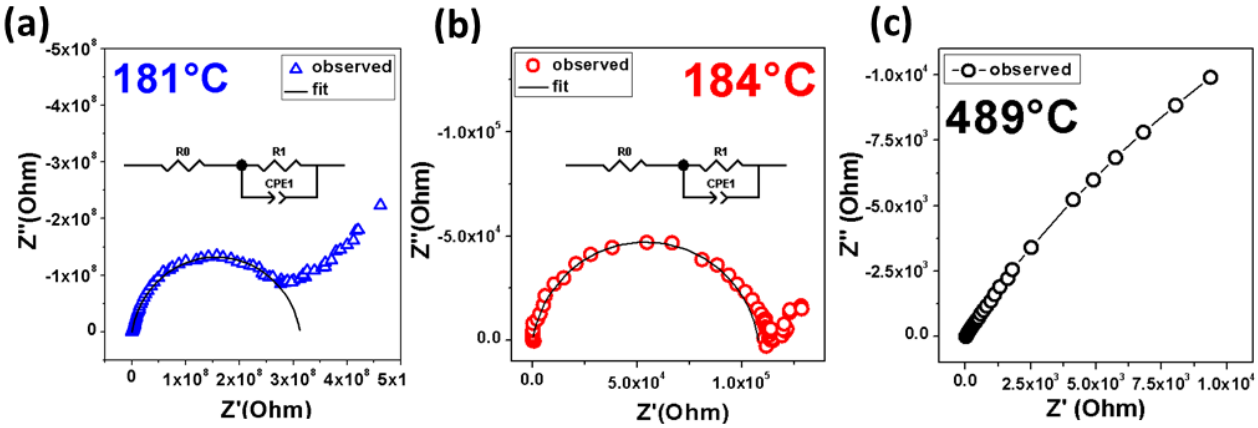

Figure 58: *Complex AC impedance spectra for* ***(a)*** *β-,* ***(b)*** *LT α- and* ***(c)*** *HT α-$Li_6CuB_4O_{10}$. The equivalent circuit shown as inset was used to fit the spectra, whereas in the case of* ***(c)*** *the interception with the x-axis was taken as R1.*

To clearly separate the electronic from the ionic contribution to the total conductivity of this material, DC polarization measurements on $Li_6CuB_4O_{10}$ samples were done (experimental details see chapter 7.1.4). After applying a potential across the pellet and following the current response, a sharp increase followed by a fast decay to a steady state value was observed (Figure 59), representing the pure electronic conduction of the material. The electronic resistance was then calculated according to Ohm's law (equation 6).

$$R = \frac{U}{I} \qquad \textbf{(6)}$$

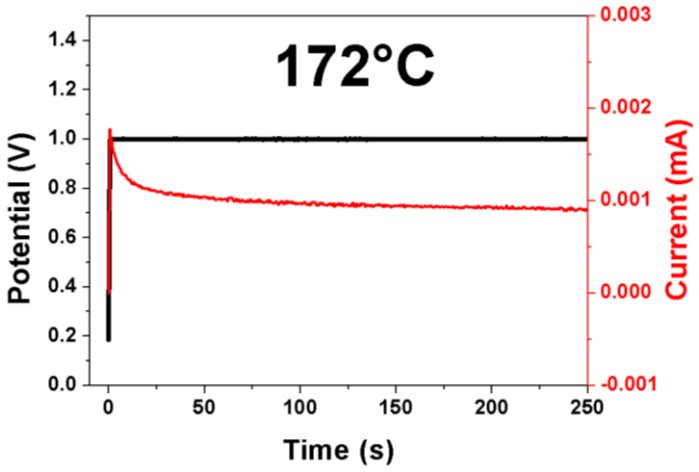

Figure 59: (a) *DC polarization of a pellet of α-$Li_6CuB_4O_{10}$ with 1.0 V at 172°C using Pt-electrodes.*

From the experimental values for the AC and DC resistance, the corresponding conductivity σ was calculated (details see annexes chapter 7.1.3) and summarized in the Arrhenius plot shown in Figure 60. For α-$Li_6CuB_4O_{10}$ the values for conductivity increase from $3 \cdot 10^{-8}$ to $1.4 \cdot 10^{-2}$ $S \cdot cm^{-1}$ as the temperature raises from 140 and 500°C. This increase is not continuous but enlists two different regimes; a low temperature and a high temperature one, corresponding to activation energies of 1.07 and 0.52 eV respectively. Both regimes referring to the LT-α and HT-α polymorph, are separated by a strikingly jump in conductivity between 320 and 370°C, the same temperature range over which a structural transition was previously shown to occur by both, DSC and synchrotron XRD experiments. In contrast, the conductivity for β-$Li_6CuB_4O_{10}$ increases linearly from $5.5 \cdot 10^{-10}$ to $7.9 \cdot 10^{-7}$ $S \cdot cm^{-1}$ for 180 and 390°C respectively and is associated to an activation energy of 0.92 eV. A linear extrapolation of log (σ) = *f*(1000/T) at 25°C gives room temperature ionic conductivities in the range of 10^{-13} $S \cdot cm^{-1}$ for the both polymorphs, explaining their similar poor electrochemical activity versus lithium.

Regarding electronic conductivity, the values for α-$Li_6CuB_4O_{10}$ versus temperature slightly increase linearly from $2.3 \cdot 10^{-7}$ to $1.1 \cdot 10^{-6}$ $S \cdot cm^{-1}$ for 172 and 492°C, respectively, related to an activation energy of 0.17 eV (Figure 60). For β-$Li_6CuB_4O_{10}$ the electronic conductivity rises more significant from $5.3 \cdot 10^{-10}$ to $1.1 \cdot 10^{-8}$ $S \cdot cm^{-1}$ as the temperature raises from 180 to 390°C respectively with an activation energy of 0.57 eV.

The difference between the ionic- and electronic part of the conductivity for both $Li_6CuB_4O_{10}$ polymorphs indicates that the strong increase in conductivity we measured (especially for α- $Li_6CuB_4O_{10}$) reflects the material's ionic conductivity. Overall, the low

room temperature ionic conductivity for both polymorphs imply a low Li-ion mobility which partially explains the encountered difficulties to reversibly remove Li from this material. The ionic conductivity of the HT-α, which is 10^{-2} S·cm^{-1} could be quite attractive for applications if we could achieve such values at RT.

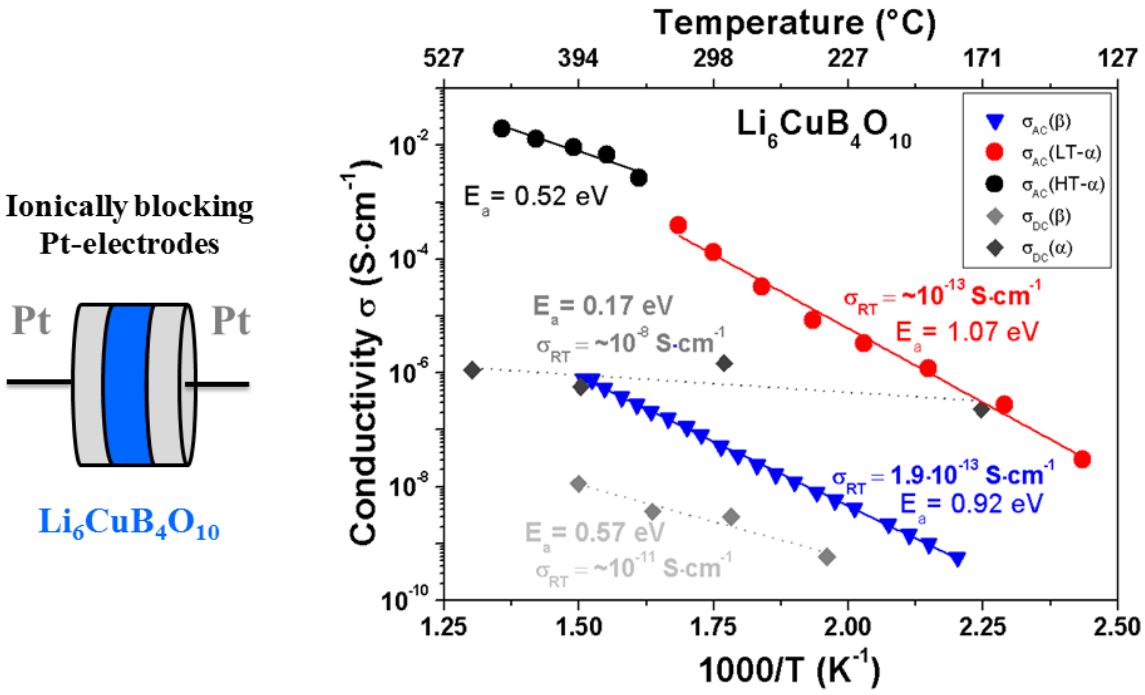

Figure 60: *Arrhenius plot of the AC- and DC conductivity of α- and β-$Li_6CuB_4O_{10}$ and a schematic view of the sample pellet between two ionically blocking Pt-electrodes used for AC- as well as for DC measurements.*

This calls for further effort in lowering the transition temperature. Work on this direction was realized via chemical substitution of Cu (through Al, Mg, etc.), but without consequent success.

3.3 Conclusion

In this section $Li_6CuB_4O_{10}$ was initially chosen as a model compound to show that elevated redox potentials can be achieved within the Li 3d metal borate family. Initially TGA-DSC and *in situ* synchrotron XRD established the relationship between the α- and β-polymorph of $Li_6CuB_4O_{10}$. In terms of synthesis and structure we show that both polymorphs react towards Li around 4.25 and 3.9 V for α- and β-$Li_6CuB_4O_{10}$ respectively. Such redox activity associated to the Cu^{3+}/Cu^{2+} redox couple, lying well above lithium copper oxides (Li_2CuO_2 ≈3.1 V, $LiCuO_2$ ≈3.0 V),[184] but below the one of lithium copper oxysulfate $Li_2Cu_2O(SO_4)_2$ (4.7 V) whose potential is governed by anionic redox processes (Figure 61a).[185,186] The participation of the Cu^{3+}/Cu^{2+} redox couple in the insertion/ deinsertion reaction of Li between 4.5 and 2.5 V was confirmed by EPR spectroscopy and rationalized through DFT calculations. As the voltage window is enlarged down to 1.0 V, a conversion type reaction takes place, leading to the extrusion of copper nanograins as observed with TEM. Moreover the limitation of the electrochemical performance of these materials, were addressed using AC impedance spectroscopy and DC polarization with complementary BVEL calculations, revealing strong kinetic limitations as seen from the low ionic/ electronic conductivity at RT in combination with high activation energies ~1.0 eV. Surprisingly due to a structural transition around 350°C, α-$Li_6CuB_4O_{10}$ shows a high ionic conductivity of 1.4 $mS \cdot cm^{-1}$ at 500°C with a low activation energy of 0.52 eV, comparable to other solid state Li-ion conductors (Garnet-type $Li_7La_3Zr_2O_{12}$, lithium borohydride $LiBH_4$ and lithium yttrium borate $Li_6Y(BO_3)_3$, Figure 61b).[187–190]This unexpected finding may renew the interest in borate based ionic conductors, prompting to shift the phase transition to lower temperatures applying suitable doping strategies etc.

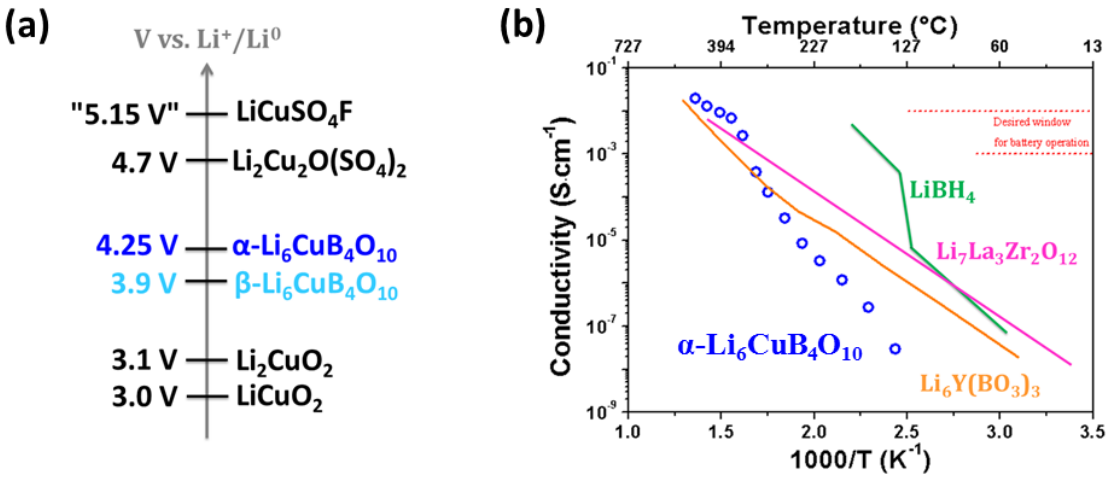

Figure 61: (a) *Schematic illustration of the Cu^{3+}/Cu^{2+} redox potentials versus Li for different compounds including α- and β-$Li_6CuB_4O_{10}$. Note that the potential in quotation marks was derived from DFT calculations but never experimentally observed.* ***(b)*** *Comparison of the ionic conductivity of α-$Li_6CuB_4O_{10}$ with different borate based materials and a Garnet type solid electrolyte.*

4 Synthesis, structural and electrochemical properties of sodium transition metal pentaborates $Na_3MB_5O_{10}$ (M = Fe, Co)

4.1 Synthesis and structure

In the previous chapter we have demonstrated through the synthesis of $Li_6CuB_4O_{10}$ the feasibility to obtain high potentials in borate compounds. Therefore at the same time we show the difficulty in making new pyroborates. This was an impetus to explore other borate anions, hence our interest for the family of sodium metal pentaborates $Na_3MB_5O_{10}$. Solid state synthesis and structures have been reported to prepare these phases with M = Mg, Ca, Zn. Their preparation consists briefly in mixing stoichiometric amounts of Na_2CO_3, M(II)carbonate/nitrate and H_3BO_3 followed by annealing of the mixture at temperatures between 650-700°C in air for several days.[191,192] Our first attempts by replacing the M(II)-carbonate/nitrate through Co/Fe(II)-oxalate and heating the mixture under argon to avoid oxidation of the transition metal were not successful. Using NaOH instead of Na_2CO_3, led to the formation of $Na_3FeB_5O_{10}$, but was again not successful in the case of Co. $Na_3CoB_5O_{10}$ could solely be obtained if $Co(OH)_2$ was used as precursor. If the oxalate was used, we always end up with Co metal due to the easy reduction of Co^{2+} in Co-oxalate if heated under argon. Since the precursors are prone to react with ambient atmosphere, all steps of the synthesis were carried out in an argon filled glove box or under argon flow in a tube furnace. All chemicals were stored in argon, sodium hydroxide NaOH and boric acid H_3BO_3 were dried prior to be used at 200°C for 4 h in vacuum, and at 55°C for 24 h in air respectively.

In general, stoichiometric amounts of NaOH, $Fe(C_2O_4)\cdot 2H_2O$ or $Co(OH)_2$ and H_3BO_3 were mixed together for 15 min in argon using a SPEX milling apparatus. We observed that the mechanochemical process causes most likely a reaction between the precursors which solidified within the milling jar, yielding in an amorphous intermediate product. The resulting solid was then reground with a mortar and pestle, and heated with a rate of 10°C/min up to 700°C for 1 h under argon flow. Once the synthesis is finished, the formed product $Na_3FeB_5O_{10}$ was immediately transferred to the glove box for further use, since we observed degradation in ambient atmosphere. At the opposite, $Na_3CoB_5O_{10}$ is stable in air. Both

compounds possess particle sizes ranging from 1 to 50 µm as show in Figure 62 with grey and blue color for M=Fe and Co respectively.

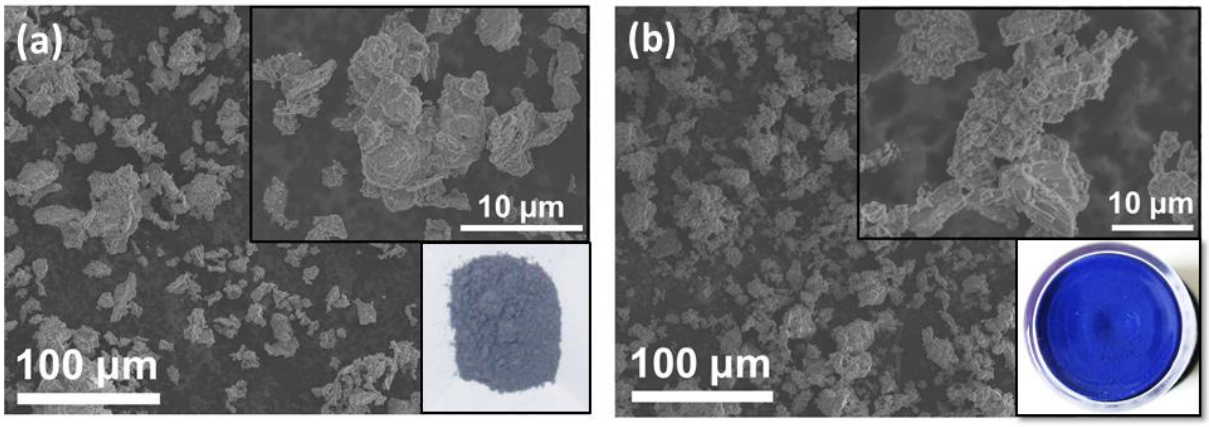

Figure 62: *SEM images of* ***(a)*** *$Na_3FeB_5O_{10}$ and* ***(b)*** *$Na_3CoB_5O_{10}$.*

The structure of $Na_3FeB_5O_{10}$ was examined by means of synchrotron XRD (Figure 63a). Besides a few weak peaks attributed to an Fe_3BO_5 impurity (~4 %), all peaks could be perfectly indexed in an orthorhombic unit cell having a *Pbca* space group with lattice parameters a= 7.95493(1) Å, b= 12.30669(1) Å and c= 18.03978(1) Å and a unit cell volume V=1766.073 $Å^3$ (Table 10), based on a structural model reported for $Na_3MgB_5O_{10}$.[191] All atoms are placed in general positions 8*c* with one crystallographic site for iron, three for sodium, 5 for boron and 10 for oxygen. The final atomic positions are given in Table 10 and their atomic positions within a unit cell are illustrated in Figure 64a,b. Iron atoms are located in the center of slightly distorted tetrahedra (Fe-O distances ranging from 1.970 to 2.116 Å) with an average bond length of 2.0243 Å, in well agreement with reported Fe-O in tetrahedral oxygen coordination.[97,193]

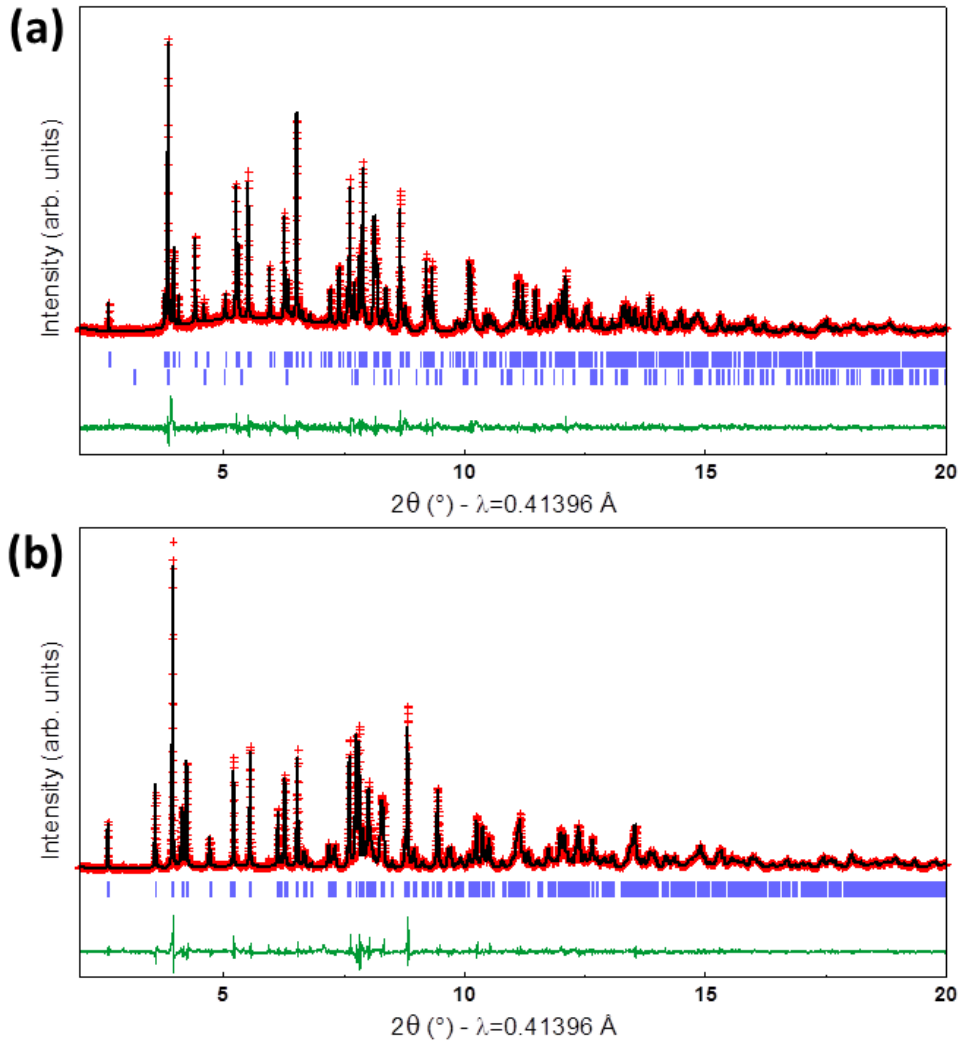

***Figure 63**: Synchrotron XRD pattern and the corresponding Rietveld refinement of **(a)** $Na_3FeB_5O_{10}$ and **(b)** $Na_3CoB_5O_{10}$. The red crosses, black-, and green line represent the observed, calculated and difference patterns, respectively. The positions of the Bragg reflections are shown as vertical blue bars. For $Na_3FeB_5O_{10}$, the lower set of tick marks is Fe_3BO_5 (~4 w%).*

All four oxygen ligands of the FeO_4 tetrahedra belong to terminal oxygen atoms of distinct pentaborate anions $[B_5O_{10}]^{5-}$, which consists of one BO_4 tetrahedra (average bond length 1.4799 Å) surrounded by 4 trigonal planar BO_3 groups forming pyroborate units $[B_2O_5]^{4-}$ (Figure 64). The FeO_4 tetrahedra are connected through the pentaborate anions to form a 2D layer along the *ab*-plane (Figure 64c). These layers are stacked along the *c*-axis with sodium atoms sitting between the layers as well as in channels along the *a*-axis.

Table 10: *Structural parameters and atomic positions of $Na_3FeB_5O_{10}$.*

$Na_3FeB_5O_{10}$					
Space group *P b c a*					
a= 7.95493(5) Å, b= 12.30668(9) Å, c= 18.03983(13) Å					
V=1766.07(2) Å^3 Z=8 ϱ= 2.548 g/cm^3 R_{Bragg} =5.96%, χ^2=1.02					
Atom	**Wyckoff site**	**x**	**y**	**z**	**B (Å^2)**
Na1	8*c*	0.8292(5)	0.4179(4)	0.0800(3)	1.97(7)
Na2	8*c*	0.6936(5)	0.6544(3)	0.2548(3)	1.97(7)
Na3	8*c*	0.7908(5)	0.4278(4)	0.4330(2)	1.97(7)
Fe1	8*c*	0.4135(3)	0.68078(13)	0.09531(9)	1.29(4)
B1	8*c*	0.414(2)	0.1491(10)	0.0758(7)	1.09(14)
B2	8*c*	0.7215(19)	0.1756(12)	0.0763(7)	1.09(14)
B3	8*c*	0.5457(17)	0.2864(10)	0.1604(7)	1.09(14)
B4	8*c*	0.5578(17)	0.3620(11)	0.3004(7)	1.09(14)
B5	8*c*	0.4911(16)	0.4776(10)	0.1874(7)	1.09(14)
O1	8*c*	0.2900(10)	0.1182(6)	0.0430(4)	1.53(6)
O2	8*c*	0.4238(12)	0.2192(5)	0.1266(3)	1.53(6)
O3	8*c*	0.5902(11)	0.1222(5)	0.0472(4)	1.53(6)
O4	8*c*	0.7243(9)	0.2498(6)	0.1277(3)	1.53(6)
O5	8*c*	0.8771(9)	0.1416(5)	0.0435(3)	1.53(6)
O6	8*c*	0.5657(8)	0.2707(5)	0.2427(4)	1.53(6)
O7	8*c*	0.5371(8)	0.3980(5)	0.1466(3)	1.53(6)
O8	8*c*	0.4969(8)	0.4514(5)	0.2724(4)	1.53(6)
O9	8*c*	0.5762(10)	0.3344(5)	0.3713(3)	1.53(6)
O10	8*c*	0.4102(9)	0.5690(5)	0.1844(3)	1.53(6)

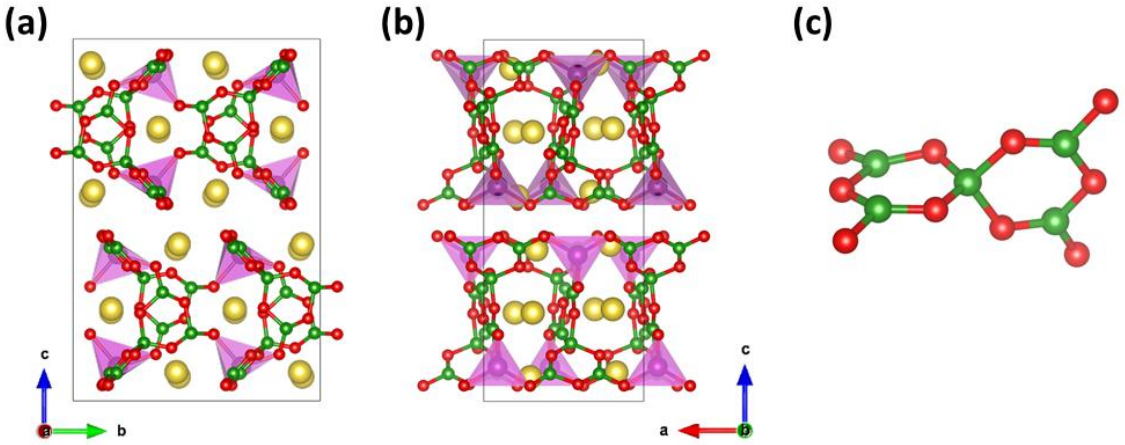

Figure 64: *Structure of $Na_3FeB_5O_{10}$ viewed along the a-axis* ***(a)*** *and the b-axis* ***(b)***. *Oxygen, boron, sodium and iron atoms indicated in red, green, yellow and pink respectively.* ***(c)*** *Pentaborate unit.*

The Fe-Mössbauer spectrum for as synthesized $Na_3FeB_5O_{10}$ is shown in Figure 65 (details see annexes chapter 7.3.3). The majority of the Fe signal in $Na_3FeB_5O_{10}$ can be fitted with a single doublet, confirming the occurrence of one single crystallographic site for Fe in $Na_3FeB_5O_{10}$. The isomer shift IS = 1.02 mm/s and a quadrupole splitting QS = 2.10 mm/s are typical of Fe^{2+} in tetrahedral coordination.[19,20] Note that the Mössbauer spectrum contains about 4% of Fe_3BO_5 impurity, in agreement with the values obtained from the XRD pattern (Figure 63a).

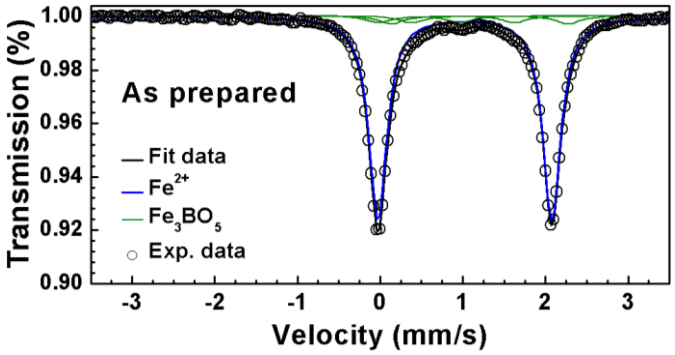

Figure 65: *Room temperature Fe-Mössbauer spectrum of the as prepared $Na_3FeB_5O_{10}$.*

Regarding $Na_3CoB_5O_{10}$, the corresponding synchrotron XRD pattern and the Rietveld refinement are shown in Figure 63b. All peaks could be perfectly indexed using a structural model reported for $KCdB_5O_{10}$ by replacing K and Cd through Na and Co respectively.[194] The

$Na_3CoB_5O_{10}$ compound crystallizes in a monoclinic space group $P2_1/n$ with lattice parameters a = 6.65143(1) Å, b = 18.20986(1) Å, c = 7.80513(1) Å and β = 114.79220(1)° resulting in a unit cell volume V = 858.240 $Å^3$ (Table 11). The atomic positions within the unit cell are shown in Figure 66. All atoms are placed in general position 4*e* with one crystallographic site for cobalt, three for sodium, five for boron and ten for oxygen (refined atomic positions are given in Table 11). Cobalt is in a slightly distorted tetrahedral oxygen environment with average Co-O bond lengths of 1.98 Å in agreement with values reported in the case of other compounds possessing Co^{2+} in tetrahedral environment.[195] All four oxygen ligands belong to terminal oxygen atoms of distinct pentaborate anions $[B_5O_{10}]^{5-}$, connecting the CoO_4 tetrahedra to form a 2D layer along the *ac*-plane. The layers are stacked along the *b*-axis with sodium atoms placed in between the layers as well as in channels.

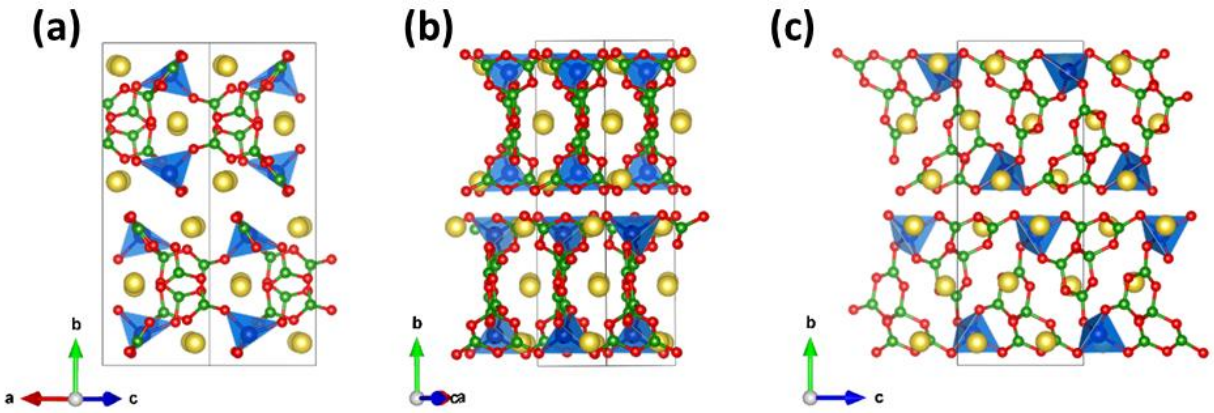

Figure 66: *Structure of $Na_3CoB_5O_{10}$ viewed along different crystallographic directions. Oxygen, boron, sodium and cobalt atoms indicated in red, green, yellow and blue respectively.*

Table 11: *Structural parameters and atomic positions of $Na_3CoB_5O_{10}$.*

$Na_3CoB_5O_{10}$					
Space group *P* $2_1/n$					
a= 6.65143(6) Å, b= 18.20981(15) Å, c= 7.80512(7) Å and					
β= 114.79223(3)°					
V= 858.235 (12) Å^3, Z=4, ϱ = 2.647 g/cm^3, R_{Bragg}=6.56%, χ^2=1.47					
Atom	**Wyckoff site**	**x**	**y**	**Z**	**B (Å^2)**
Co1	4*e*	0.4938(2)	0.09529(6)	0.12100(16)	0.97(3)
Na1	4*e*	1.0215(5)	0.06927(15)	0.1537(4)	1.31(7)
Na2	4*e*	0.5356(5)	0.07253(15)	-0.2967(4)	2.25(9)
Na3	4*e*	0.2007(5)	0.24423(14)	-0.0962(4)	0.85(3)
B1	4*e*	0.7050(15)	0.2127(5)	-0.0092(14)	0.7(2)
B2	4*e*	0.1192(16)	0.0766(4)	-0.2204(12)	0.5(2)
B3	4*e*	0.1200(19)	0.1643(6)	-0.4532(14)	1.9(3)
B4	4*e*	0.2734(16)	0.1881(6)	0.3233(13)	1.7(3)
B5	4*e*	0.8089(15)	0.0738(5)	0.4833(12)	0.52(20)
O1	4*e*	0.3823(8)	0.3659(3)	-0.0583(6)	0.85(3)
O2	4*e*	0.6864(9)	0.1334(2)	0.0034(6)	0.85(3)
O3	4*e*	0.6234(8)	0.0399(2)	0.3567(6)	0.85(3)
O4	4*e*	0.2150(8)	0.1274(3)	-0.2604(7)	0.85(3)
O5	4*e*	0.2347(8)	0.1406(2)	-0.5576(7)	0.85(3)
O6	4*e*	0.2214(8)	0.0375(2)	-0.0479(6)	0.85(3)
O7	4*e*	0.1189(7)	0.2431(3)	-0.4250(6)	0.85(3)
O8	4*e*	1.0892(9)	-0.0428(2)	0.3357(7)	0.85(3)
O9	4*e*	0.3217(8)	0.1712(2)	0.1747(6)	0.85(3)
O10	4*e*	-0.2188(8)	0.2304(2)	-0.1428(7)	0.85(3)

Regarding the structures of $Na_3MB_5O_{10}$ (M = Fe, Co) described above, clearly significant similarities despite their different space groups are obvious. Note that the lattice basis vectors of both structures are related through the following matrix:

$$\begin{pmatrix} \boldsymbol{a}_{Fe} \\ \boldsymbol{b}_{Fe} \\ \boldsymbol{c}_{Fe} \end{pmatrix} = \begin{pmatrix} 1 & 0 & 1 \\ -1 & 0 & 1 \\ 0 & -1 & 0 \end{pmatrix} \begin{pmatrix} \boldsymbol{a}_{Co} \\ \boldsymbol{b}_{Co} \\ \boldsymbol{c}_{Co} \end{pmatrix}$$

The thermal stability of $Na_3FeB_5O_{10}$ and $Na_3CoB_5O_{10}$ was investigated using TGA-DSC analysis (details see annexes chapter 7.3.1). Measurements were recorded during heating a sample of around 20-30 mg under flowing air from RT to 850°C with a rate of 5°C/min (Figure 67a,b). For $Na_3FeB_5O_{10}$ a broad exothermic peak is observed around 640°C in the DSC curve, which is most likely associated with the decomposition of $Na_3FeB_5O_{10}$ into iron oxide Fe_2O_3 and $Na_2B_4O_7$. This is confirmed by the XRD pattern of the $Na_3FeB_5O_{10}$ sample recovered after 12h at 650°C in air (Figure 67c) which shows reflections corresponding to Fe_2O_3 and $Na_2B_4O_7$. The formation of Fe_2O_3 is consistent with the 2% weight gain that is visible in the TGA curve when the temperature increases from 500°C to 650°C. If the temperature is further raised the DSC plot shows a sharp endothermic peak ~710°C which can be correlated to the melting of the $Na_2B_4O_7$ formed during the decomposition of $Na_3FeB_5O_{10}$. In the case of $Na_3CoB_5O_{10}$ only one large endothermic peak is observed in the DSC curve ~770°C, referring to the melting point of the compound. Note that the initial mass loss ~1 % for $Na_3CoB_5O_{10}$ can most likely be correlated to the removal of absorbed moisture.

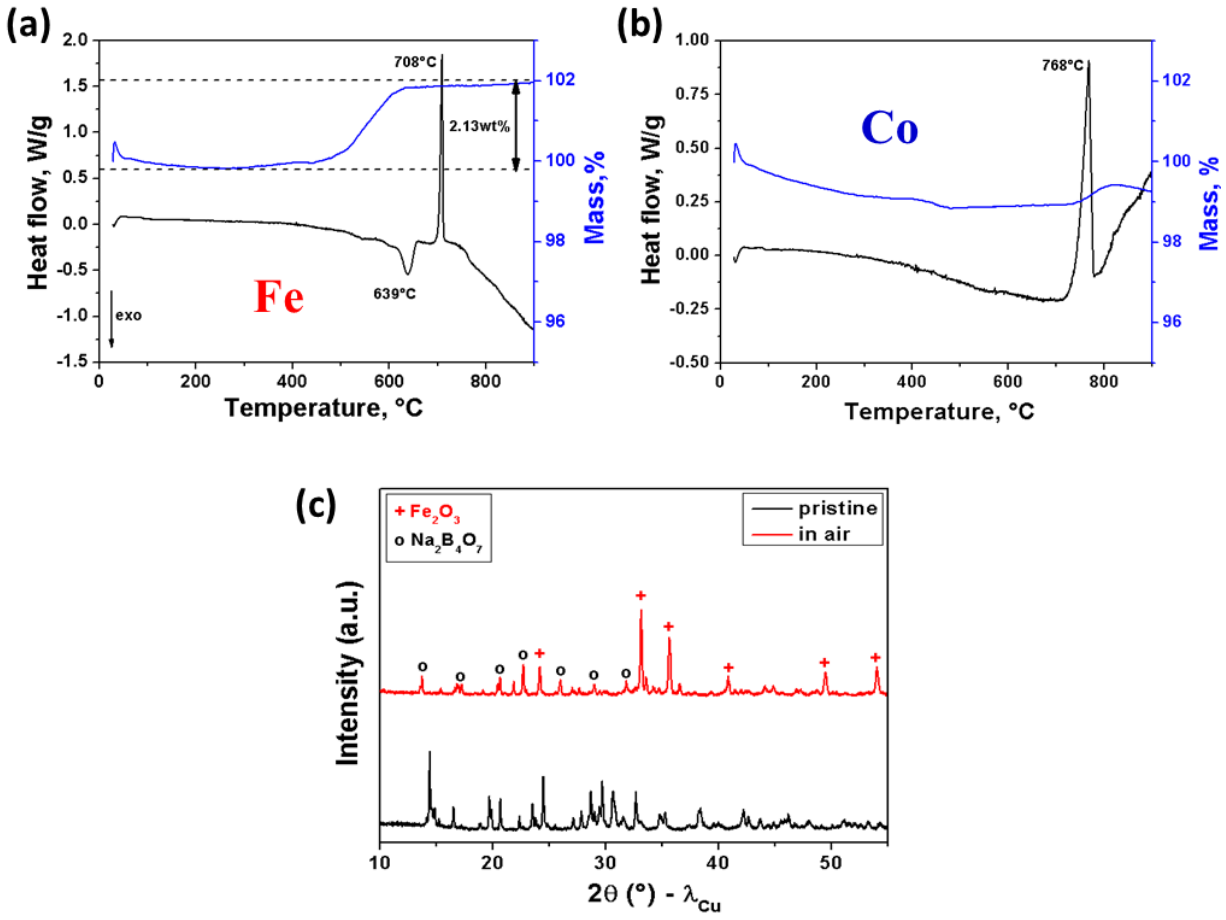

Figure 67: *TGA-DSC curves of* ***(a)*** *$Na_3FeB_5O_{10}$ and* ***(c)*** *$Na_3CoB_5O_{10}$ recorded in air flow with a heating rate of 5°C/min.* ***(c)*** *XRD patterns of $Na_3FeB_5O_{10}$ taken before and after annealing for 12h at 650°C in air.*

4.2 Electrochemical characterization

4.2.1 Activity versus sodium

Given the possibility of feasible Na^+ mobility due to the open structure of $Na_3MB_5O_{10}$, we decided to check the electrochemical activity of this compound towards Na. The experiments were conducted in Swagelok type half cells versus metallic sodium using a 1M solution of $NaClO_4$ in a 1/1 (w/w) mixture of EC and DMC with 1 wt.% fluoro ethylene carbonate (FEC) (details see annexes chapter 7.1). The positive electrode powder was

prepared by mixing the active material with 20 wt.% carbon SP with mortar and pestle under inert atmosphere for 10 min.

A typical voltage composition curve of $Na_3FeB_5O_{10}$ versus Na with a C/40 rate at 55°C is shown in Figure 68a. Initially the potential rapidly increases up to ~4 V, and then continuously increases but at a lower slope till 4.5 V with a corresponding removal of ~0.6 Na^+. During following discharge, a steep potential drop down to ~2 V is observed, and it is followed by a smooth voltage decrease till 1.5 V with in total the uptake of ~0.25 Na^+. Note that the amount of reversible Na^+ inserted in the initial cycle compared to the second one is much lower, indicating an irreversible Na loss during the first oxidation. However during conventional galvanostatic cycling no defined potential for the Fe^{3+}/Fe^{2+} redox couple could be unambiguously determined. Thus we decided to conduct galvanostatic intermittent titration technique (GITT) measurements by applying a positive or negative current pulse for 4 h (corresponding to the extraction/ insertion of 0.1 Na^+) alternating with open circuit voltage (OCV) periods of 12 h between 4.5 and 1.5 V at 55°C. As seen in Figure 68b, after each current pulse, the potential initially drops and increases strongly afterwards revealing an equilibrium potential of 2.5 V vs. Na^+/Na^0 pointing towards a biphasic process for Na extraction/insertion. As in the GITT curve large overpotentials in the range from 0.5 to almost 2 V during charge/ discharge are observed, suggesting a strong kinetic limitation for Na^+ diffusion. At this point we suppose that these limitations are routed either in the poor ionic/ electronic transport properties of one of the phases present during the biphasic process ($Na_3FeB_5O_{10}$ vs. $Na_xFeB_5O_{10}$).

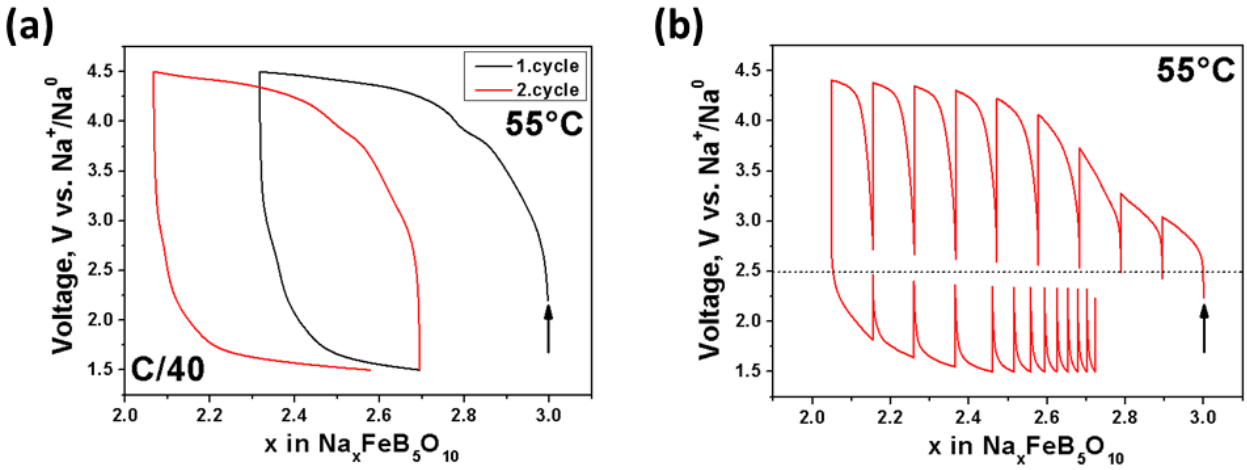

Figure 68: (a) *Voltage-composition curve of $Na_3FeB_5O_{10}$ versus Na cycled at a C/40 rate between 4.5 and 1.5 V vs. Na^+/Na^0 at 55°C.* ***(b)*** *GITT measurement with 4 h current pulse and 12 h open circuit voltage (OCV) period during the first charge and discharge.*

In order to confirm the Fe^{3+}/Fe^{2+} redox process, *ex situ* Mössbauer spectra were recorded for charged and discharged samples of $Na_3FeB_5O_{10}$ (details see annexes chapter 7.3.3). To do so, cells that have been fully charged (4.5 V) or discharged (1.5 V) were disassembled inside the glove box, the electrode powder was recovered, washed twice with DMC and dried under vacuum prior to examination. As shown in Figure 69 at the end of charge, the Fe^{2+} doublet is reduced (49 at%) to the benefit of an additional contribution of Fe^{3+} (51 at%) which is diminished upon subsequent discharge, although not fully reversible as 27 at% of Fe^{3+} are remaining (together with 73 at% Fe^{2+}). The percentage of Fe^{3+} and Fe^{2+} given in Table 12 are in agreement with the amount of extracted/ inserted Na compared to the voltage composition curve (Figure 68a).

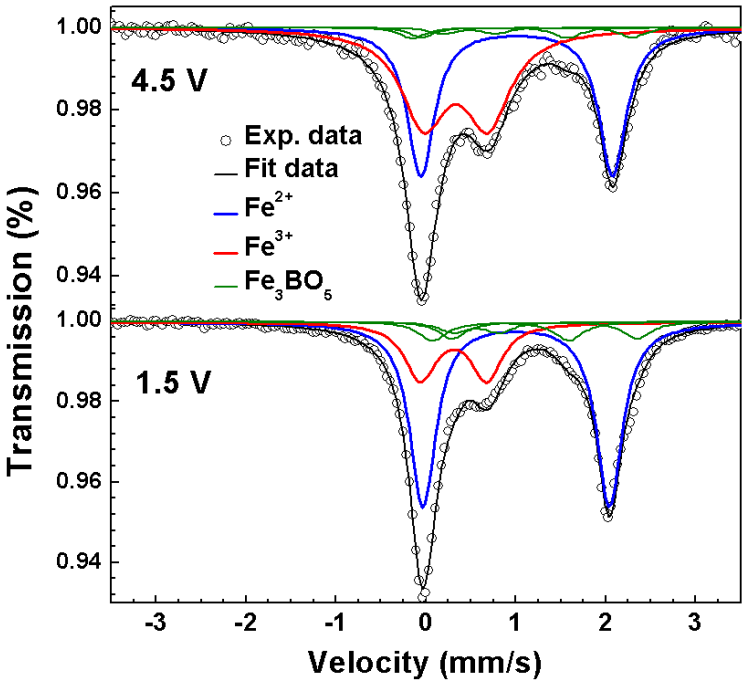

Figure 69: *Room temperature ex situ Mössbauer spectra recorded for $Na_3FeB_5O_{10}$ at 4.5 V (charged) and at 1.5 V (discharged).*

Table 12: *Fitted Mössbauer parameters of the pristine sample shown in Figure 69 and the spectra for the cycled samples given in Figure 73. IS, QS, LW and area are the isomer shift, the quadrupole splitting, the linewidth and the relative areas respectively.*

Sample	IS (mm/s)	SQ (mm/s)	LW (mm/s)	at%	Attribution
pristine	1.02	2.10	0.26	100	Fe^{2+}
4.5 V	1.01	2.13	0.36	49	Fe^{2+}
	0.33	0.71	0.61	51	Fe^{3+}
1.5 V	1.00	2.07	0.35	73	Fe^{2+}
	0.31	0.73	0.42	27	Fe^{3+}

$Na_3CoB_5O_{10}$ was equally tested versus Na using a similar protocol as $Na_3FeB_5O_{10}$, however no electrochemical activity was observed. This does not come as a surprise as it is well known from DFT calculations that the redox potential of a 3d metal redox couple M^{3+}/M^{2+} in a family of polyanionic compounds increases in the order from Fe < Mn < Co < Ni with differences of ~1.5 V if going from Fe^{3+}/Fe^{2+} to Co^{3+}/Co^{2+} in olivine-type materials

$LiMPO_4$ for instance.[196] Thus we believe that even such a compound will present an activity we won't be able to reach it with the present electrolytes.

4.2.2 Ionic conductivity

At this stage an intriguing question regards the poor electrochemical performance of $Na_3MB_5O_{10}$ in light of its open structure. We hypothesize that such poor activity were routed in the poor electronic and ionic transport of the material. To check this hypothesis, BVEL calculations were generated according to the method developed by S. Adams to reveil possible ion diffusion pathways for Na^+ (details see annexes chapter 7.3.7).[183] To determine the possible transport ways, the theoretical oxidation state of the mobile species (Na^+) is calculated as a function of the position inside the structure. Positions with only a small deviation (typically 10%) from the oxidation state are regarded as a part of the Na^+ diffusion pathway and are visualized in Figure 70 for $Na_3MB_5O_{10}$ (M =Fe (a), Co (b)). For $Na_3FeB_5O_{10}$, 1D Na^+ conduction paths, involving Na1 and Na3 sites appear along the a-axis at 1.00 eV above the minimum energy[4] however Na2 is sterically hindered. Note that to involve also Na2 into the Na^+ migration network, an energy of 1.7 eV above the minimum is required, hence Na2 is most likely not contributing to the materials ionic conductivity. For $Na_3CoB_5O_{10}$ a percolation energy of 1.09 eV above the minimum is required to get fully connected pathways for Na migration involving all Na sites. Moreover the Na^+ conduction pathways are lying in between the layers consisting of the MO_4 tetrahedra connected through the pentaborate B_5O_{10} units, implying an anisotropic Na^+ conduction.

[4] Minimum energy refers to the calculated ground energy of the imaginary mobile Na^+ ion in the structure.

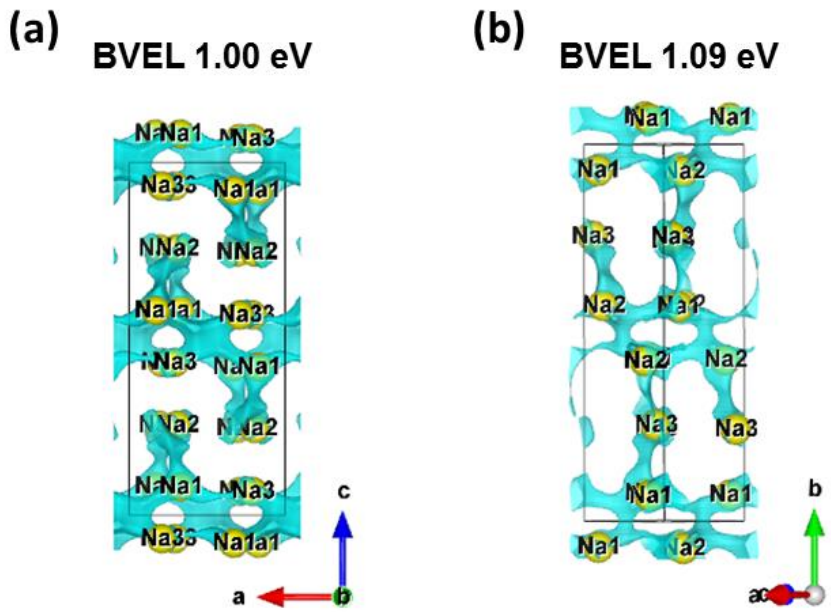

Figure 70: *Bond valence energy landscape (BVEL) of* ***(a)*** *$Na_3FeB_5O_{10}$ and* ***(b)*** *$Na_3CoB_5O_{10}$. The percolation energies are given in the figure. Iso-energy blue domains indicate paths for Na (yellow spheres) conduction.*

To experimentally validate the results derived from the BVEL calculations, complementary AC/DC measurements on sintered pellets of $Na_3MB_5O_{10}$ between ionically blocking Pt electrodes were done. Pellet suitable for the measurement were prepared by pressing around 300 mg of powdered sample in a 10 mm die. The pellet was annealed for 124 hours at 650°C under argon, or for 124 hours at 600°C in a vacuum sealed tube for M = Co and M = Fe, respectively. The obtained density was around 65 to 75 % of the theoretical one deduced frim structural data. After placing the pellet in the apparatus, AC impedance spectra were recorded for temperatures ranging from 250 up to 400°C while applying a voltage amplitude of 200 mV in a frequency range between 30 MHz and 0.01 Hz during heating under argon flow (detailed description of the setup see annexes chapter 7.1.3).

First of all, the AC complex impedance spectra for $Na_3MB_5O_{10}$ (M = Fe, Co) present a depressed semicircle with a Warburg diffusion resistance tail over the whole measured temperature range, suggesting the AC conductivity to be mostly ionic (Figure 71). The spectra can be expressed with an equivalent circuit R_0─R_1/CPE_1─R_2/CPE_2 (Figure 71 inset) where each parallel R/CPE circuit gives raise to one semicircle (schematically plotted as grey lines in Figure 71). For each semicircle the resistance R_1 and R_2 (intercept with the x-axis, indicated in Figure 71) plus the corresponding capacitance C_1 and C_2 can be obtained from the fitting parameters (details see annexes chapter 7.1.3), whereas the latter one usually differs

from 10^{-12} to 10^{-9} F for the bulk and grain boundary contribution respectively.[197,198] This allows us to separate between both contributions, corresponding to R_1 and R_2 for the bulk- and grain boundary resistance.

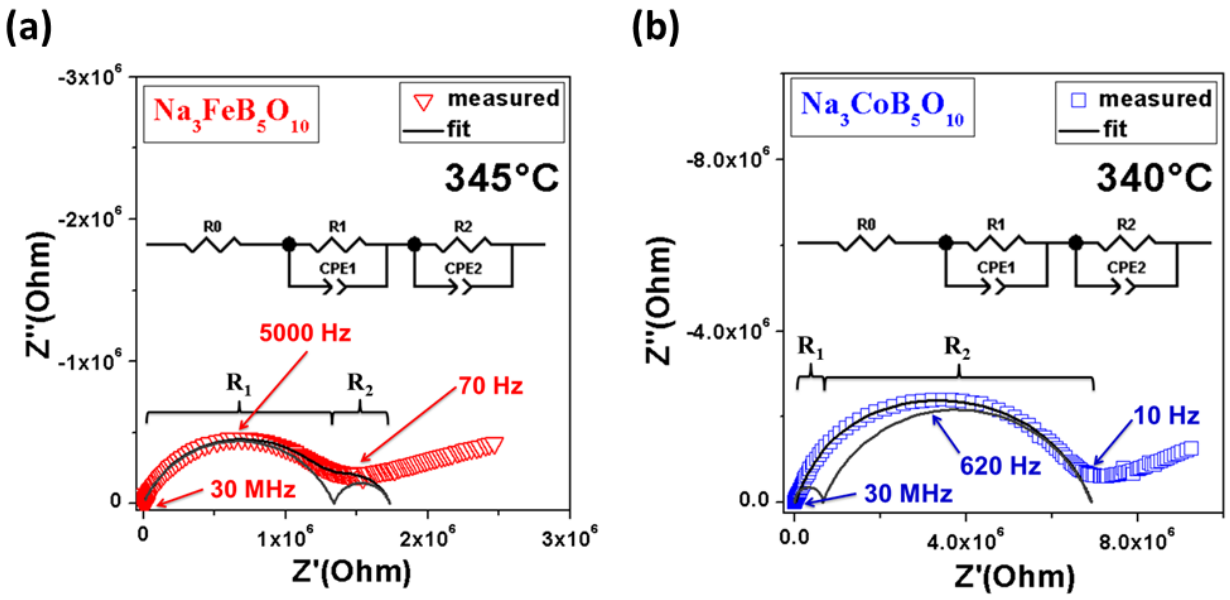

Figure 71: *Representative complex impedance spectra of* ***(a)*** *$Na_3FeB_5O_{10}$ and* ***(b)*** *$Na_3CoB_5O_{10}$ recorded at 345 and 340°C respectively. The equivalent circuits are shown as inset, and the corresponding bulk (R_1) - and grain boundary (R_2) resistance are shown schematically as grey semicircles.*

To clearly separate between ionic and electronic conductivity, DC polarization measurements were conducted (Figure 72) on sintered $Na_3MB_5O_{10}$ (M = Fe, Co) pellets sandwiched between two Pt-electrodes. After applying a constant potential of 0.5 V across the pellet, the current response was recorded. First a sharp increase followed a slow decay to a steady state value was observed. Initially, both ions and electrons account for the measured current, whereas the ionic current decays to zero after waiting a sufficiently long time, as Na^+ gets blocked at the Pt-electrodes. Electrons however are conducted through Pt, thus the steady-state current can be related to the pure electronic conduction of the material. As seen in Figure 72, the time to reach a constant current value took 4 times longer for $Na_3CoB_5O_{10}$ compared to $Na_3FeB_5O_{10}$ implying faster Na^+ migration for the latter one. The pure electronic resistance was calculated according to Ohm's law from the steady state current value and the applied potential.

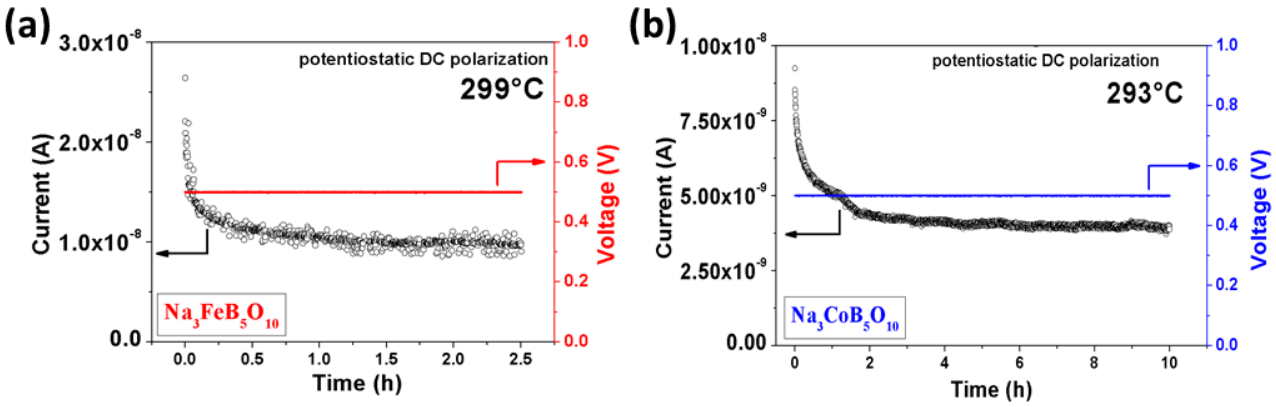

Figure 72: *Representative potentiostatic DC polarization of* ***(a)*** *$Na_3FeB_5O_{10}$ and* ***(b)*** *$Na_3CoB_5O_{10}$ recorded at 299 and 293°C respectively.*

From the experimentally determined values for the AC and DC resistance, the corresponding conductivity was derived and the activation energy was obtained using the Arrhenius equation (details see annexes chapter 7.1.3). All results obtained from AC and DC measurements are summarized in the Arrhenius plot for $Na_3FeB_5O_{10}$ and $Na_3CoB_5O_{10}$ as shown in Figure 73a and b, respectively.

For $Na_3FeB_5O_{10}$ one can first note a linear increase of the bulk ionic conductivity between 250 and 380°C from $1.5 \cdot 10^{-8}$ and $1.9 \cdot 10^{-7}$ $S \cdot cm^{-1}$ with an activation energy of 0.65 eV (Figure 73a). Conductivities associated to the grain boundaries also increase in the same temperature range from $1.7 \cdot 10^{-7}$ and $4.7 \cdot 10^{-7}$ $S \cdot cm^{-1}$ correlated to an activation energy of 0.24 eV. Obviously the grain boundary conductivity is higher than the bulk one. One possibility to account for this observation is most likely rooted in the existence of a minor Fe_3BO_5 impurity (4%) which sits at the grain boundaries within our sample. The interaction between such an ionically insulating impurity and $Na_3FeB_5O_{10}$ could then lead to a redistribution of ions in the narrow interface region introducing structural defects/ disorder which lead as a consequence to a non-uniform charge distribution. This so called space-charge region can strongly improve the ionic conductivity through interfacial transport, hence our experimental values for the grain boundary conductivity may be overestimated.[199–203] The electronic conductivity increases between 250 to 350°C from $6.3 \cdot 10^{-10}$ to $1.0 \cdot 10^{-8}$ $S \cdot cm^{-1}$ with a corresponding activation energy of 0.72 eV. By extrapolating the high temperature part of the curves to RT,

conductivities of $1.1 \cdot 10^{-10}$, $7.6 \cdot 10^{-9}$ and $1.2 \cdot 10^{-14}$ $S \cdot cm^{-1}$ for the bulk-, grain boundary- and electronic conductivity are obtained respectively.

Regarding $Na_3CoB_5O_{10}$, the bulk ionic conductivity increases linearly from $6.9 \cdot 10^{-8}$ to $9.8 \cdot 10^{-7}$ $S \cdot cm^{-1}$ between 280 and 390°C with a corresponding activation energy of 0.73 eV. The grain boundary ionic conductivity follows the same trend in parallel, however the absolute values are about one order of magnitude lower than the values obtained for the bulk conductivity ($5.9 \cdot 10^{-9}$ to $8.6 \cdot 10^{-8}$ S/cm), corresponding to an activation energy of 0.83 eV. As the materials appears to be free of impurities, we hypothesize these lower values for the grain boundary conductivity arise from structural disorder/ defects at the grain interfaces, impeding the ionic conduction, although an insulating amorphous layer at the grain surface cannot be excluded either.[204–206] The electronic conductivity increases between 290 to 390°C from $1.1 \cdot 10^{-9}$ to $2.2 \cdot 10^{-8}$ $S \cdot cm^{-1}$ respectively, correlated to an activation energy of 0.97 eV. Linear extrapolation of the experimental values leads to RT conductivities of $4.0 \cdot 10^{-13}$, $9.1 \cdot 10^{-17}$ and $5.4 \cdot 10^{-17}$ $S \cdot cm^{-1}$ for the bulk-, grain boundary- and electronic conductivity, respectively.

For comparison, it should be recalled that the RT bulk ionic conductivity values for $Na_3FeB_5O_{10}$ are one only order of magnitude lower than the one of $LiFePO_4$ ($\approx 2 \cdot 10^{-9}$ $S \cdot cm^{-1}$)[106] and two order of magnitudes higher than Li_2FeSiO_4 ($\approx 6 \cdot 10^{-14}$ $S \cdot cm^{-1}$),[100] both of which can reversibly insert one Li per unit formula. Having this in mind, the poor electrochemical performance of $Na_3FeB_5O_{10}$ comes still as a surprise since it should not be limited by the ionic transport. Furthermore, it is worth mentioning that the electronic conductivity of $LiFePO_4$ is higher than that of $Na_3FeB_5O_{10}$. This may explain the poor electrochemical activity as we need ionic an electronic conductivity to electrochemically trigger insertion/ deinsertion reactions. Such a limitation can also be structural related with the under-stoichiometric $Na_{3-x}FeB_5O_{10}$ phase being thermodynamically unstable, the reason why for instance the de-insertion of Li from Li_2FeSiO_4 could not be extended below one, as confirmed by DFT calculations. Turning back to the GITT measurement (Figure 68b), one can note that the equilibrium potential reaches a plateau at 2.5 V vs. Na^+/Na^0 which is indicative of a two-phase Na insertion/ deinsertion reaction, hence one can assume the formation of a second phase $Na_xFeB_5O_{10}$ which is most likely the limiting factor for electrochemical activity, similar to what was observed in the case of $LiFeBO_3$.[151,207]

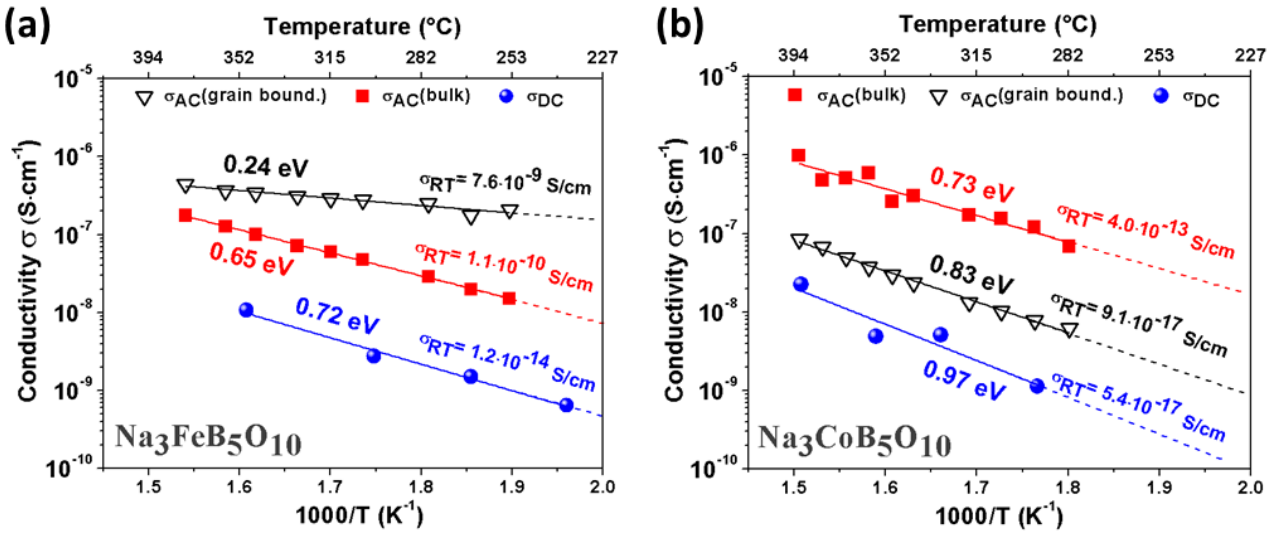

Figure 73: *Arrhenius plot of the AC and DC conductivity of* ***(a)*** *$Na_3FeB_5O_{10}$ and* ***(b)*** *$Na_3CoB_5O_{10}$ derived in the temperature range from around 250 to 400°C during heating in argon flow.*

4.3 Conclusion

In this section were report about the synthesis, structure and electrochemical properties of two new sodium transition metal pentaborates $Na_3MB_5O_{10}$ (M = Fe, Co) where M = Fe presents the first ever reported compound out of the ternary Na_2O-FeO-B_2O_3 system. The structures were solved by means of synchrotron XRD. They consist of layers built up by MO_4 tetrahedra connected through pentaborate units B_5O_{10} with sodium sitting in voids inside these layers as well as in between them. Complementary galvanostatic- and *ex situ* Mössbauer measurements have confirmed a Fe^{3+}/Fe^{2+} redox activity centered around 2.5 V vs. Na^+/Na^0 for $Na_3FeB_5O_{10}$ in contrast to $Na_3CoB_5O_{10}$ which is electrochemical inactive. Combined BVEL calculations and AC/DC conductivity measurements reveal strong kinetic limitations for $Na_3CoB_5O_{10}$, reflected in the low RT ionic- and electronic conductivities of $4.0 \cdot 10^{-13}$ and $5.4 \cdot 10^{-17}$ $S \cdot cm^{-1}$ respectively. $Na_3FeB_5O_{10}$ in contrast shows RT ionic conductivity of $1.1 \cdot 10^{-10}$ $S \cdot cm^{-1}$ comparable to $LiFePO_4$, however one limiting factor is nested in the much lower RT electronic conductivity ($1.2 \cdot 10^{-14}$ $S \cdot cm^{-1}$). An additional limitation for the electrochemical performance could equally be due to the structural /thermodynamic instability of the intermediate phase $Na_xFeB_5O_{10}$ formed during the two-phase (de)sodiation reaction.

Although a reversible electrochemical activity could be demonstrated for $Na_3FeB_5O_{10}$, this material cannot be considered for practical applications. Note that our attempts to circumvent the poor electronic conductivity by employing carbon coated particles failed. Nevertheless these results call for further exploration of borate based materials in terms of their ionic mobility, despite difficulties encountered during the design of new compounds out of this family.

In general we have shown possible insertion/ deinsertion reaction for Li and Na in borate based materials beyond $LiMBO_3$ in the last two chapters, however the limited electrochemical activity led us to consider other reaction mechanism, namely conversion type reactions as explored in the next chapter.

5 Study of the electrochemical driven reaction mechanism of bismuth oxyborate $Bi_4B_2O_9$ versus lithium

5.1 Synthesis and structure

In the previous chapters, we have shown through the synthesis of $Li_6CuB_4O_{10}$ the feasibility to obtain high redox potentials for borate materials, however our further exploration for new pyroborate based compounds has encountered strong synthetic difficulties. Nevertheless, this had led us to the synthesis of two new sodium 3d metal pentaborates $Na_3MB_5O_{10}$ (M = Fe, Co) with poor electrochemical performances. Therefore we considered another reaction mechanism, namely conversion type reactions. They differ from classical insertion/ deinsertion reactions in which Li^+/Na^+ is incorporated into a host structure while the metal M changes its oxidation state to account for charge balance. In a reversible conversion reaction, M is fully reduced upon lithiation and forms nanoparticles embedded in an amorphous matrix composed of Li_nX (X = O^{2-}, S^{2-}, F^-, P^{3-}, etc.) (equation 7). Upon charge this process is reversible to a certain extend.

$$M_aX_b + n\,e^- + n\,Li^+ \leftrightarrow a\,M^0 + b\,Li_nX \qquad \textbf{(7)}$$

An interesting tool to tune the redox potential of electrode materials relies on the inductive effect. In short the ionicity of the M─X bond influences the average redox potential of the conversion reaction with compounds having the highest ionicity showing the highest redox potentials. As fluorine is the most electronegative element, fluorides were widely studied in the past, however one has to note that highly ionic compounds are usually poor electronic conductors.[123,208–212]. Therefore in most cases these materials have to be "activated" through a prolonged high energy milling process with a large amount of carbon to achieve good electronic contact. Worthwhile mentioning that this addition of carbon diminishes drastically the volumetric energy density which is one problem regarding applications. Thus the quest for denser materials, with the most promising among them being bismuth fluoride BiF_3 (5.23 $g{\cdot}cm^{-3}$). But again due to the insulating nature of this compound, a relatively large polarization was observed (~1 V), hence we decided to switch to Bi-borates. Owing to the weaker inductive effect of the borate BO_3 group compared to fluorine, they should show a lower polarization while keeping the benefit of the high volumetric density (around 5 to 8

$g \cdot cm^{-3}$), comparable to BiF_3. Among all reported Bi-borates, $Bi_4B_2O_9$ presents the highest theoretical capacity correlated to the reduction of Bi^{3+} to Bi^0 (~320 mAh/g) therefore, we chose this material to investigate its reaction mechanism versus Li. So far this materials was solely investigated for its structural and photocatalytical properties.

Although the theoretical capacity is rather low for conversion type electrode materials (usually > 600 mAh/g), we strongly emphasize the fact that this material presents a very high volumetric density ~8.2 $g \cdot cm^{-3}$, hence being favorable from the viewpoint of volumetric energy density.

$Bi_4B_2O_9$ was obtained by mixing stoichiometric amounts of bismuth oxide Bi_2O_3 and boric acid H_3BO_3 with a mortar and pestle and annealing the mixture at 600°C for 36 h in air with one intermediate regrinding. After the synthesis a pale white powder was recovered, consisting of particles with sizes ranging from 5 to 30 µm (Figure 74, inset).

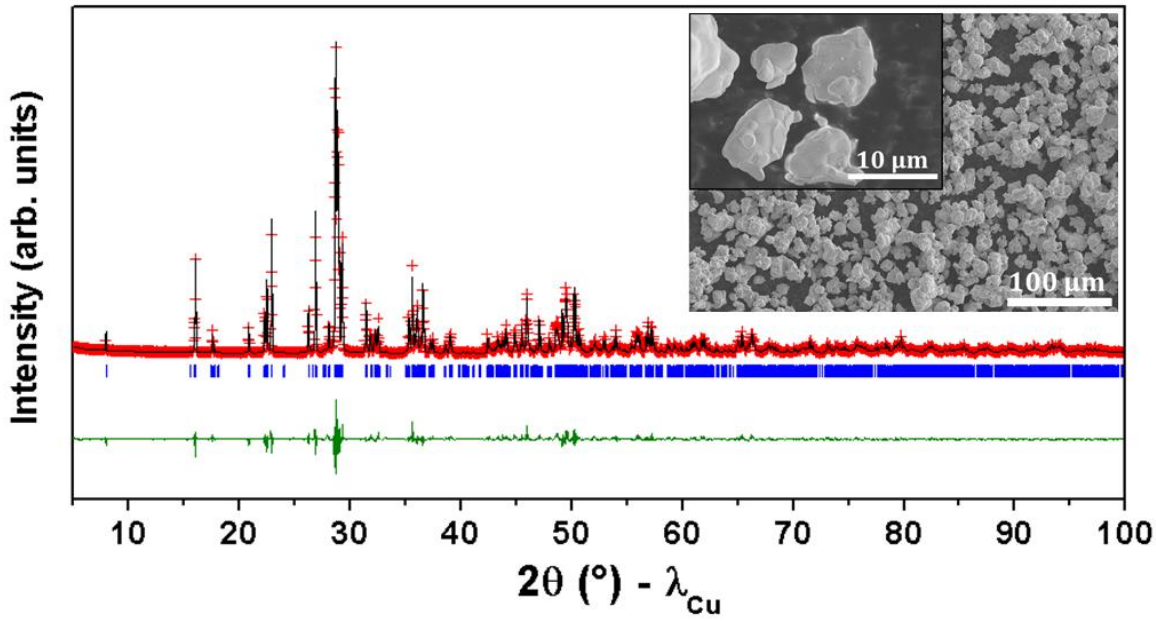

Figure 74: *XRD pattern and Rietveld refinement of $Bi_4B_2O_9$. Observed, calculated pattern and their difference are shown as red crosses, black- and green line respectively. Bragg reflections are indicated as vertical blue bars. The inset show a representative SEM image of the as synthesized compound with two different magnifications.*

The corresponding XRD pattern and the Rietveld refinement are shown in Figure 74 and the refined atomic positions are given in Table 13. All peaks could be indexed in a monoclinic space group $P2_1/c$ with the unit cell parameters a = 11.11652(4) Å, b = 6.63300(3)

Å, c = 11.04575(4) Å, β = 91.04795(16)° and V = 814.331(5) $Å^3$, similar to those reported in literature.[213,214] The atomic arrangement within the unit cell is shown in Figure 75, built up of 4 different crystallographic sites for Bi, 2 for B and 9 for O. Among them Bi4 and Bi2 form BiO_4-, and Bi1 and Bi3 form BiO_5 asymmetric truncated polyhedra respectively, with Bi-O distances ranging from 2.150 to 2.492 Å. Boron is trigonal planar coordinated by oxygen forming regular BO_3^{3-} triangles (average B-O bond distance 1.3396 Å) which are stacked on top of each other perpendicular to *b*-axis (Figure 75a). The structure also contains three O atoms (O1, O2, O4) which are non-coordinated to boron, only bond to Bi atoms with bond length ranging from 2.177 to 2.381 Å, referring $Bi_4B_2O_9$ to oxyborate which can be more precisely expressed in the formula $Bi_4O_3(BO_3)_2$.

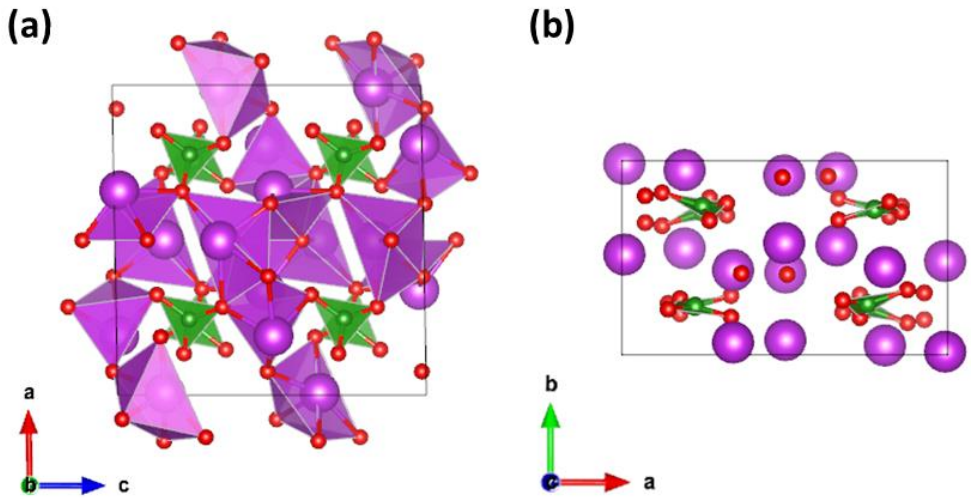

Figure 75: *Crystal structure of $Bi_4B_2O_9$ shown along the* ***(a)*** *b- and* ***(b)*** *c-axis. Bismuth atoms/ polyhedral, boron and oxygen are shown in purple, green and red respectively.*

Table 13: *Structural parameters and atomic positions of $Bi_4B_2O_9$.*

$Bi_4B_2O_9$					
Space group *P 2$_1$/c*					
a= 11.11652(4) Å, b= 6.63300(3) Å, c= 11.04575(4) Å, β= 91.04795(16)°					
V=814.331(5) Å^3 Z=8 ϱ= 8.169 g/cm^3 R_{Bragg} =8.44%, χ^2=9.91					
Atom	**Wyckoff site**	**x**	**y**	**z**	**B (Å^2)**
Bi1	2a	0.9920(1)	0.4822(2)	0.3460(1)	0.19(3)
Bi2	2a	0.8083(1)	0.0480(2)	0.4920(1)	0.36(3)
Bi3	2a	0.5014(1)	0.4236(2)	0.1597(1)	0.18(3)
Bi4	2a	0.3402(1)	0.4366(2)	0.4825(1)	0.31(4)
O1	2a	0.5003	0.1076	0.1050	1.89
O2	2a	0.3833	0.0994	0.4944	1.99
O3	2a	0.8652	0.1597	0.2828	2.24
O4	2a	0.9231	0.1577	0.0134	1.96
O5	2a	0.1879	0.2030	0.1427	2.77
O6	2a	0.6762	0.2268	0.3676	2.81
O7	2a	0.1472	0.2420	0.3527	2.14
O8	2a	0.3433	0.3144	0.2792	1.30
O9	2a	0.7152	0.3195	0.1549	2.00
B1	2a	0.7534	0.2356	0.2633	2.00
B2	2a	0.2244	0.2520	0.2533	2.15

The thermal stability of $Bi_4B_2O_9$ was investigated using TGA-DSC analysis (for details see annexes chapter 7.3.1). Measurements were recorded during heating a sample of around 20-30 mg under flowing air from RT to 500°C with a rate of 5°C/min (Figure 76). In the whole temperature range the mass of the sample stays constant and no peak in the DSC curve indicative of a possible structural transition is visible, as already suggested through XRD measurements at 200 and 450°C by Filatov *et al.*.[213] In general $Bi_4B_2O_9$ is stable up to 500°C in air.

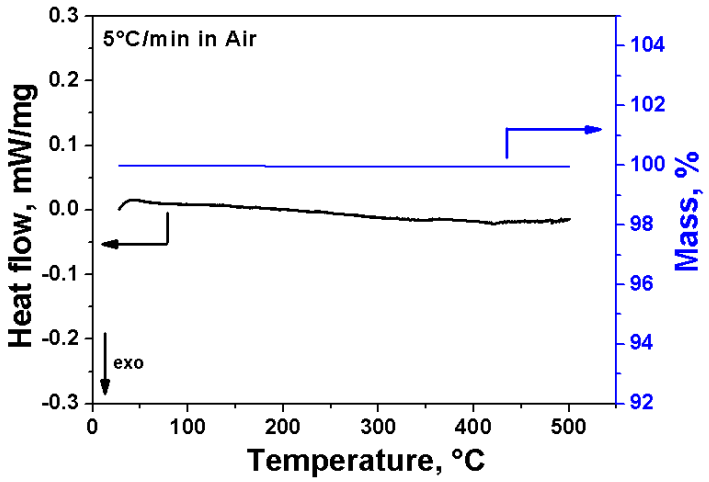

Figure 76: *TGA-DSC curve of $Bi_4B_2O_9$ recorded in air from RT to 500°C during heating under air flow.*

5.2 Electrochemical characterization

Given the possibility of the reduction from Bi^{3+} to metallic Bi^0 and expected higher redox potentials than pure oxides owing to the inductive effect of the borate group, we measured the electrochemical activity of $Bi_4B_2O_9$ versus lithium. Electrochemical testing was done in Swagelok half cells using a 1M solution of $LiPF_6$ in EC/DMC/PC 1/1/3 (w/w/w) as electrolyte soaked into two sheets of glass fiber which separate the positive electrode from metallic lithium. The positive electrode powder was prepared by mixing $Bi_4B_2O_9$ with 5 wt.% carbon for 10 min using a SPEX high energy miller.

First $Bi_4B_2O_9$/Li half cells were cycled between 0.0 and 3.5 V at a C/10 rate in order to ensure a complete reduction of the material. A typical voltage composition curve, together with the corresponding derivative plot and the capacity retention are shown in Figure 77. First of all one can note that the initial discharge corresponds to the reaction of 24 mol of Li^+ with 1 mol of $Bi_4B_2O_9$. Such a Li uptake is associated with three different voltage regimes. At the beginning, a flat plateau at 1.8 V is visible concomitant with the uptake of ~8 Li^+, followed by an S-shaped curve centered at 1.4 V and corresponding to the uptake of 4 Li^+. Finally the potential reaches a low voltage flat plateau around 0.8 V, accompanied with the uptake of ~12 Li^+. On subsequent charge, only ~9 Li^+ can be extracted, solely correlated to the redox activity ~0.8 V (Figure 77b, inset). The irreversible loss in capacity between the first discharge and first charge is quite important as it is about 60%. Moreover the reversible

capacity decays initially very fast upon cycling while becoming almost negligible after 5 cycles, indicative of a large irreversible Li-reactivity.

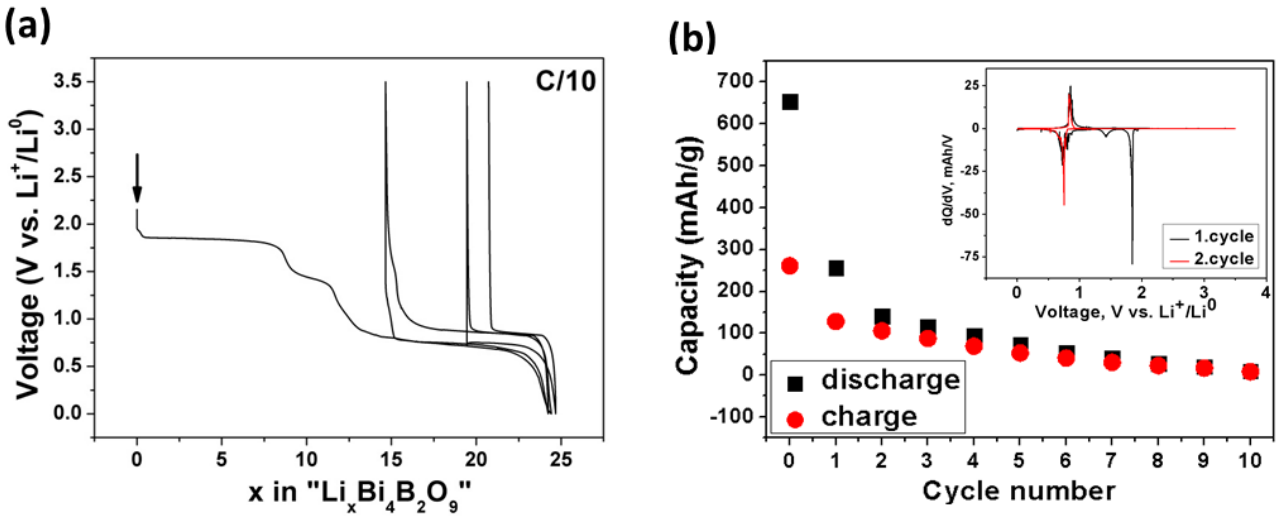

Figure 77: (a) *Voltage-composition curve of $Bi_4B_2O_9$/Li half-cell and* ***(b)*** *the capacity retention and the corresponding derivative plot of voltage-composition curve is show as inset.*

The Li^+ uptake during the first discharge can be explained by first considering a reduction of $Bi_4B_2O_9$ to metallic Bi involving the reaction with 12 Li^+ (equation 8), and second an alloying of the as-formed Bi with lithium to yield Li_3Bi (equation 9). By summing these two reactions, one exactly reaches the value of 24 Li^+ incorporated during the initial reduction (equation 10), consistent with the electrochemical data (Figure 77a).

$$Bi_4B_2O_9 + 12\,Li^+ + 12\,e^- \leftrightarrow 3\,Li_2O + 2\,Li_3BO_3 + 4\,Bi^0 \qquad \textbf{(8)}$$

$$4\,Bi^0 + 12\,Li^+ + 12\,e^- \leftrightarrow 4\,Li_3Bi \qquad \textbf{(9)}$$

$$Bi_4B_2O_9 + 24\,Li^+ + 24\,e^- \leftrightarrow 3\,Li_2O + 2\,Li_3BO_3 + 4\,Li_3Bi \qquad \textbf{(10)}$$

To get insights from a structural point of view, *ex situ* XRD pattern were recorded for $Bi_4B_2O_9$ powder recovered at different stages of discharge and charge. To do so $Bi_4B_2O_9$ /Li half cells discharged to 1.0, 0.0 and charged at 3.5 V were disassembled inside the glove box, the recovered powder was washed twice with DMC and dried under vacuum prior to

examination. As seen in Figure 78 at 1.0 V one can note a strong decrease in intensity and a highly pronounced broadening of the main reflections around a 2θ value of 28.6°, suggesting a strong amorphisation/decomposition of the pristine phase. Based on the electrochemical data this phase should have fully decomposed leading to a featureless XRD. This is not the case and the main reason is most like rooted in the presence of secondary Li consuming reactions leading to the formation of a Li containing solid electrolyte interface (SEI) or a Li containing organic layer around the active material.

However, one might expect that during initial lithiation Li_2O and Li_3BO_3 are formed (equation 8). This decomposition seems to be reasonable as similar reactions were observed in the case of other TM borates.[215] Now the question arises, why these conversion products are not visible in the XRD patterns. Either because their amorphous/ nanocrystalline nature, or the large difference of X-ray scattering between Li_2O/ Li_3BO_3 (light elements) and heavy atoms such as Bi. To check the morphology of the active material discharged to 1.0 V, TEM images were recorded. As shown in Figure 78a one can clearly see nanoparticles with the size ranging from 2 to 10 nm embedded in an amorphous matrix. To analyze the crystal structure of the nanoparticles, selected area electron diffraction (SAED) was performed showing diffraction rings which could be attributed to a trigonal R-3m symmetry indicative of the presence of metallic α-Bi (Figure 78b). To analyze the elemental distribution of the composite we used EDX analysis. Note that the analysis of Li and B is not possible due to the low energy of the emitted X-rays which cannot be detected with the instrument. However the nanoparticles were confirmed to consist of metallic Bi and tend to form agglomerates (Figure 78c). Furthermore in contrast to the locally defined appearance of Bi, the contribution of oxygen seems to be homogenous over the whole area, supporting the existence of an evenly distributed amorphous Li_2O/ Li_3BO_3 matrix (Figure 78c).

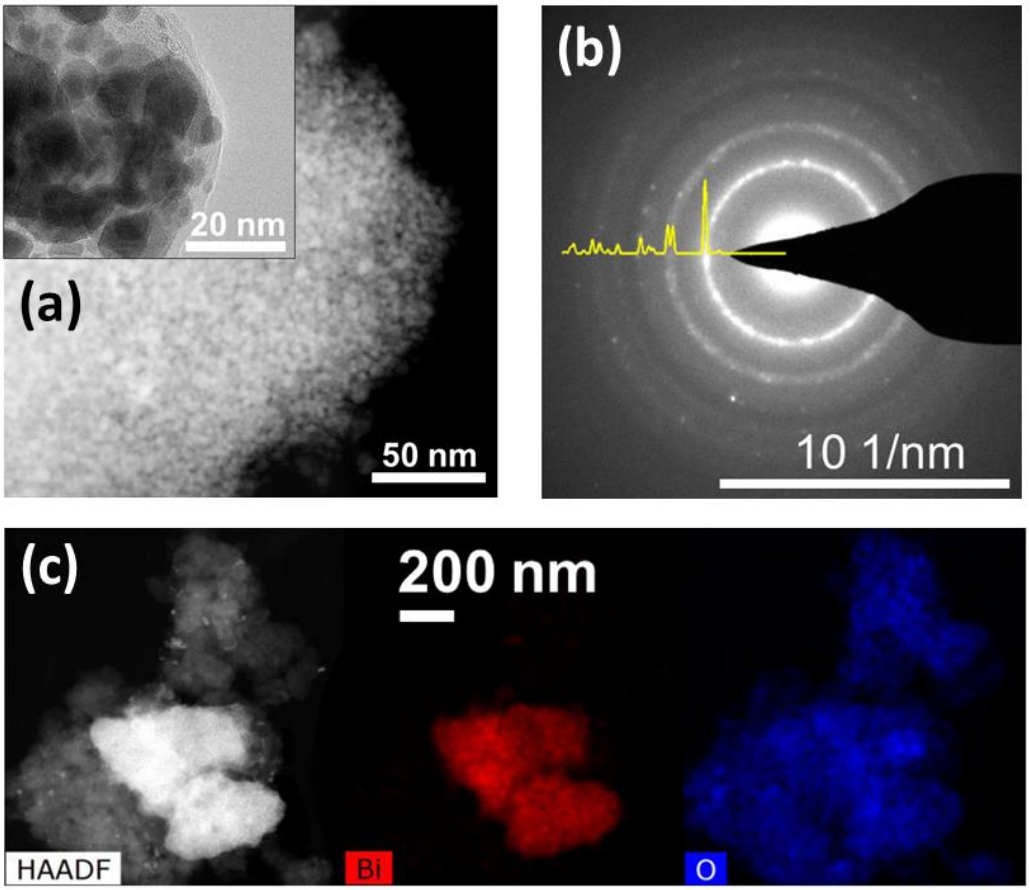

Figure 78: *$Bi_4B_2O_9$/C sample discharged to 1.0 V.* ***(a)*** *Representative TEM image,* ***(b)*** *SAED pattern of the nanoparticles with the simulated diffraction profile of α-Bi shown for comparison and* ***(c)*** *another TEM image and the corresponding EDX map of bismuth (red) and oxygen (blue).*

For samples fully reduced to 0.0 V, sharp reflections of Li_3Bi are observed from XRD. On subsequent charge to 3.5 V peaks of metallic Bi^0 show up in the XRD pattern (Figure 79). This is consistent with our assumptions of a reversible alloying reaction between Li and Bi as stated in equation 9 associated to the redox process around 0.8 V seen in the derivative plot (Figure 79b). The reversible electrochemical driven alloying/ dealloying process of Bi with Li has been reported.[216,217] Nevertheless the reversibility here is much lower compared to literature which originates most likely from the progressive separation/ isolation of the active material (Bi/ Li_3Bi) through the surrounding components formed during the initial conversion process (Li_2O, Li_3BO_3, and organic layers) impeding ionic/ electronic transport.[215]

A still pending question deals with inability to trigger the conversion reaction (equation 8) once Li_3Bi has been formed (equation 9). We believe that once Li_3Bi is formed, the de-alloying reaction leads to large Bi^0 crystallites (evidenced by the sharp reflections from

XRD) separated from the remaining Li_2O and Li_3BO_3 matrix. Thus in light of this lack of ionic/ electronic percolation through the composite, the simultaneous delithiation of the Li-containing matrix (Li_2O/ Li_3BO_3) and oxidation of the Bi crystallites is not possible anylonger.

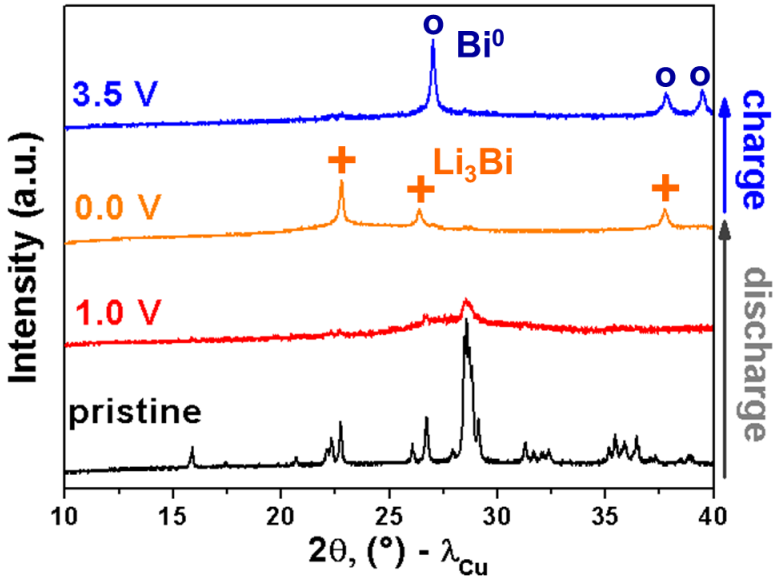

Figure 79: *XRD pattern of $Bi_4B_2O_9$ discharged to 1.0 and 0.0 V and after the subsequent charge to 3.5V.*

As the reversibility of $Bi_4B_2O_9$/Li half-cells cycled between 0.0 and 3.5 V is very poor, we investigated the effect of higher discharge cutoff potentials in order to exclude the alloying/ dealloying part and trigger only the conversion process.

$Bi_4B_2O_9$/Li half-cells were assembled and cycled between 1.0 and 3.5 V. A typical voltage-composition curve together with the corresponding derivative plot and the capacity retention are shown in Figure 80. During the initial reduction 8 Li^+ are incorporated via a flat plateau at 1.8 V with an additional uptake of 4 Li^+ during a S-shaped voltage profile centered around 1.4 V. Upon following charge, around 8 Li^+ can be reversible extracted associated to two different oxidation processes at average redox potential of 1.5 and 2.5 V (Figure 80b). During the first discharge the theoretical capacity for Bi^{3+} to Bi^0 of 320 mAh/g is reached, however upon following charge, ~33% irreversible capacity remains, corresponding to a resulting charge capacity of ~214 mAh/g. Moreover the capacity is fading very fast upon cycling, decreasing down to 50% of the initial value after 3 cycles.

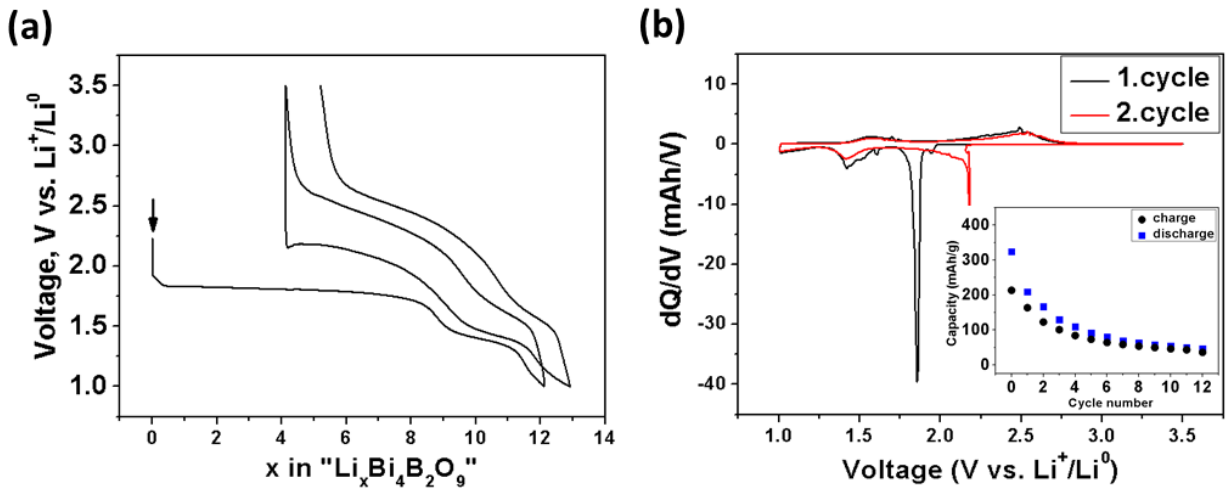

Figure 80: (a) *Voltage-composition curves and* ***(b)*** *the corresponding derivative plots and capacity retention of a $Bi_4B_2O_9$/Li half-cell cycled between 1.0 and 3.5 V.*

In short, if the discharge is limited to 1.0 V, the initial reduction processes around 1.8 and 1.5 V become reversible with the former one shifted up to 2.2 V through the subsequent discharges (Figure 80b). This potential difference between the initial and following discharge is typically observed for conversion type materials since different reaction pathways occur during the initial and subsequent reductions. During the first discharge, the potential drop is larger as an higher activation energy is necessary to trigger the conversion reaction. After this formation step, the second and subsequent discharges will be kinetically less limited owing to the nano character of the formed composite hence the discharge potential is increased.[218]

The two different redox processes occurring at average voltages of 1.5 and 2.5 V suggest the presence of two different reactions. We assume that during the initial reduction at 1.8 V metallic Bi and Bi_2O_3 nanoparticles are formed and are accompanied with the formation of amorphous matrix of Li_3BO_3 according to equation 11. Upon further discharge the remaining Bi_2O_3 is reduced to Bi^0 and amorphous Li_2O around 1.5 V (equation 12). If both reactions are summed up, the total amount of reacted Li is consistent with the value deduced from the electrochemical curve during the initial reduction (Figure 80a).

$$Bi_4B_2O_9 + 6\,Li^+ + 6\,e^- \leftrightarrow 2\,Li_3BO_3 + Bi_2O_3 + 2\,Bi^0 \quad \textbf{(11)}$$

$$Bi_2O_3 + 6\,Li^+ + 6\,e^- \leftrightarrow 2\,Bi^0 + 3\,Li_2O \quad \textbf{(12)}$$

$$Bi_4B_2O_9 + 12\,Li^+ + 12\,e^- \leftrightarrow 3\,Li_2O + 2\,Li_3BO_3 + 4\,Bi^0 \quad \textbf{(13)}$$

Although we do not have evidence for the existence of Bi_2O_3 from electron microscopy at present, our hypothesis of starting the formation of Li_3BO_3 and then Li_2O (equation 11, 12) seems to be reasonable, and similar observations have been made for the bismuth oxyfluoride $BiO_{0.5}F_2$/ BiOF system. Moreover this system was shown to react with Li via a conversion reaction, but the conversion of the fluoride occurs first, followed by the conversion of the as-formed bismuth oxide.[208] Further literature reports assume the conversion reaction of Bi_2O_3 versus Li around 1.2/ 1.4 V and 1.8 V for α-Bi_2O_3 and δ-Bi_2O_3[5] respectively.[208,220,221] So in light of these results we believe that the reduction of Bi_2O_3 (equation 12) starts most likely before all $Bi_4B_2O_9$ is converted (equation 11).

On subsequent galvanostatic cycling we assume the reaction defined in equation 13 to be partially reversible as $Bi_4B_2O_9$ is formed back on oxidation, although the nano sized morphology of the active material composite prevents us to fully support this statement (Figure 81).

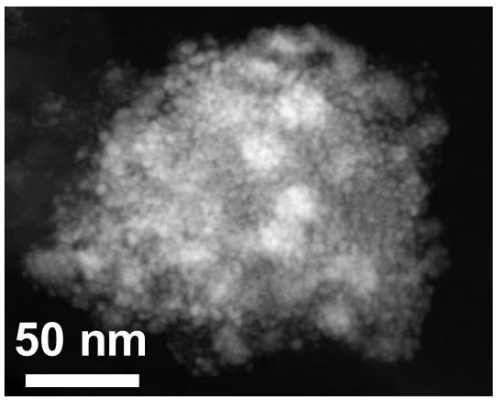

Figure 81: *TEM image of a $Bi_4B_2O_9$/C sample discharged to 1.0 V and recharged to 3.5 V.*

[5] Although it is well known δ-Bi_2O_3 is only stable above 730°C,[219] Bervas *et al* .[208] claim on the basis of *ex situ* XRD that this particular phase exists as an intermediate product during the reduction of $BiO_{0.5}F_2$.

So far we have investigated the electrochemical behavior of $Bi_4B_2O_9$ versus Li in two different potential regimes (0.0-3.5 V and 1.0-3.5 V). It reveals an electrochemically driven reaction with a large amount of Li that cumulates conversion and alloying processes, but both of them being poorly reversible. Hence our desire to further increase the lower cutoff potential to 1.7 V in order to exclude the 1.5 V redox activity Figure 82. After the initial discharge plateau at 1.8 V coming along with the uptake of ~8 Li^+, there is a shift of the electrochemical curve to an S-shape on subsequent charge to 3.5 V. Approximately 5 Li^+ can be reversible extracted, hence an irreversible capacity of 35% still remains. Upon on following discharge, the potential drops vertically reaching a pseudo-plateau at 2.2 V as visualized by a sharp reduction peak in the derivate plot (Figure 82b). Once the first cycle is achieved, the average voltage of the cell is about 2.3 V with a reversible capacity of 150 mAh/g that stays at least stable over 10 charge/ discharge cycles.

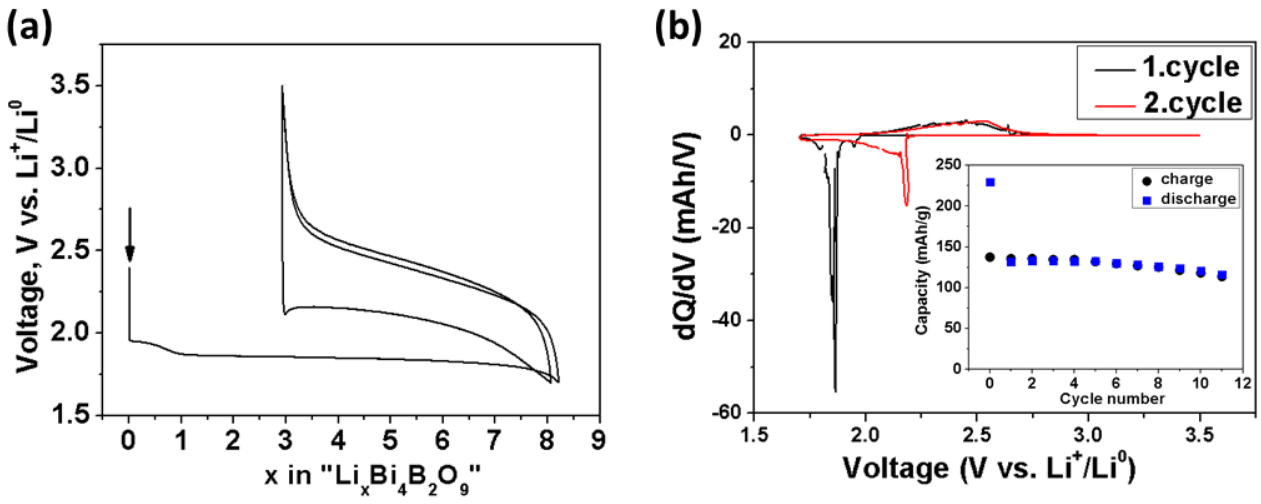

Figure 82: (a) *Voltage-composition curves and* ***(b)*** *the corresponding derivative plots and capacity retention of a $Bi_4B_2O_9$/Li half-cell cycled between 1.7 and 3.5 V.*

The *ex situ* XRD pattern taken on a sample discharged to 1.7 V still showed remaining reflections of pristine $Bi_4B_2O_9$ (Figure 83). To check if these reflections remain upon further cycling, additional *ex situ* XRD patterns were recorded on the active material after the second and fifth discharge for cells cycled between 1.7 and 3.5 V. As shown in Figure 83 a complete amorphization was not achieved until the 5th discharge/ charge cycles. This suggests a gradual consumption of the material during galvanostatic cycling, as already described by cycling $LiCoO_2$ to lower potentials.

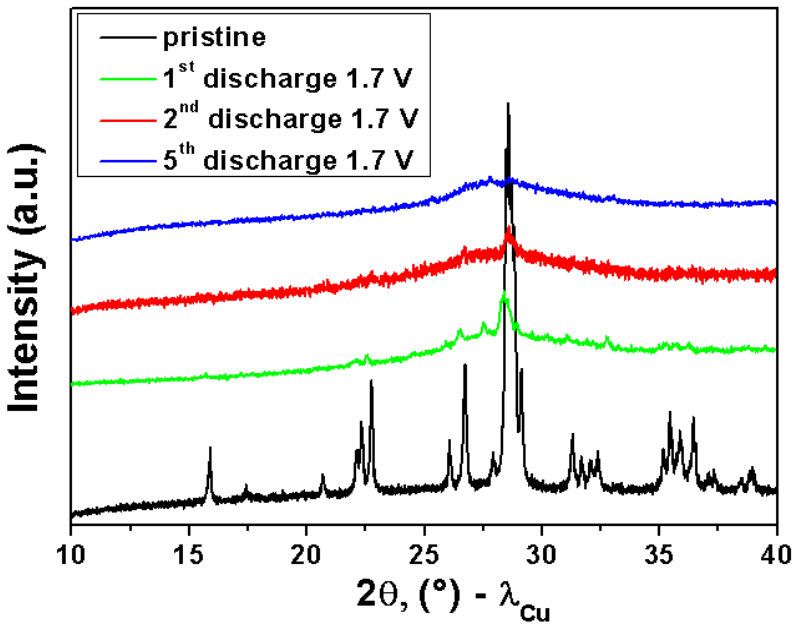

Figure 83: *XRD pattern of $Bi_4B_2O_9$ discharged to 1.7 V after the first, second and fifth cycle.*

To get more insights into the morphology of the active materials composite, samples initially discharged to 1.7 V were examined by means of TEM and EDX spectroscopy. As shown in Figure 84a nanoparticles (2 to 10 nm) embedded in an amorphous matrix are visible in parallel with remaining large crystallites of $Bi_4B_2O_9$ (Figure 84a, indicated with orange arrow). The nanoparticles were analyzed through SAED and are shown to crystallize in an R-3m space group referring most likely to α-Bi. Using EDX mapping, we determined the composition of the nanoparticles and confirmed them to be metallic Bi. However, we could not probe the composition of the amorphous part of the sample, most likely composed of Li_2O/ Li_3BO_3, since EDX analysis cannot spot light elements. Although we have claimed that during the reduction of $Bi_4B_2O_9$ there is the partial formation of Bi_2O_3 (equation 11), we could not reach evidence from electron microscopy yet. Thus we assume Bi_2O_3 to be amorphous,[222,223] but further characterization like pair distribution function (PDF) analysis or X-ray absorption (XAS) measurements are necessary for more information regarding the local structure of Bi.

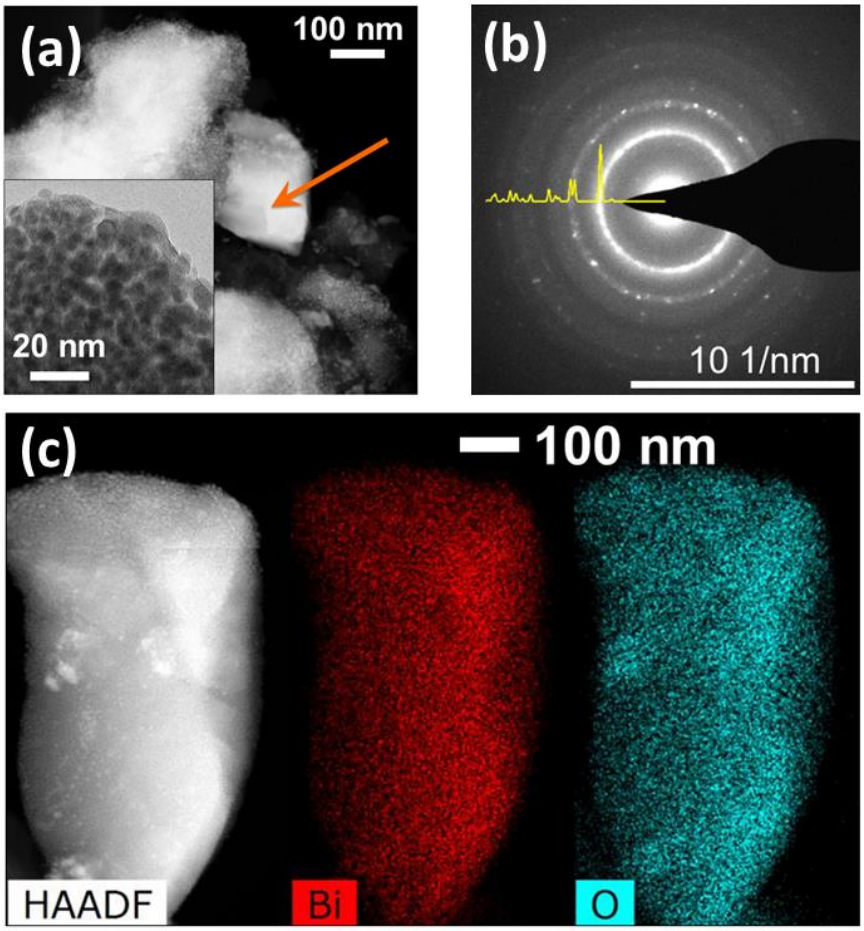

Figure 84: *$Bi_4B_2O_9$/C sample discharged to 1.7 V.* ***(a)*** *Representative TEM image where the orange arrow indicates large particle of not reacted $Bi_4B_2O_9$.* ***(b)*** *SAED pattern of the nanoparticles with the simulated diffraction profile of α-Bi shown for comparison and* ***(c)*** *another TEM image and the corresponding EDX map of bismuth (red) and oxygen (cyan).*

We have presently tested the electrochemical reaction of $Bi_4B_2O_9$ versus Li in three different potential windows between 0.0 and 3.5 V. In the following we mainly address the influence of the lower cutoff potential (0.0, 1.0 and 1.7 V). If the discharge cutoff voltage is raised from 0.0 to 1.7 V the capacity retention seems to be enhanced (Figure 85). Several parameters can account for such difference. First of all if the galvanostatic cycling is conducted in a more narrow potential range, there is less electrolyte decomposition associated to the formation of organic layers (parasitic reactions) with the end result being a minimization of the particle surface. Secondly, the faster capacity decay for lower cutoff potentials can be partially correlated to a stronger phase separation. As shown in Figure 86a and b the bright regions denoted to the amorphous Li_3BO_3/ Li_2O matrix is increased from the sample recovered at 1.7 V compared to 1.0 V. These stronger separation/ textural changes

lower the ionic/ electronic transport, hence a large fraction of the active material is not accessible for the conversion reaction anylonger.

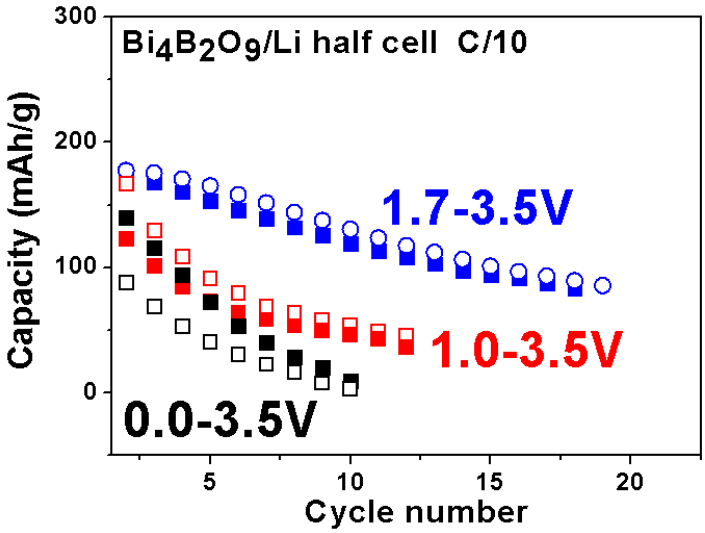

Figure 85: *(Capacity retention of $Bi_4B_2O_9$ mixed for 10 min with 5 wt% carbon and cycled with a C/10 rate in different potential window indicated in the plot. To have a better overview, the first discharge/ charge capacities are excluded.*

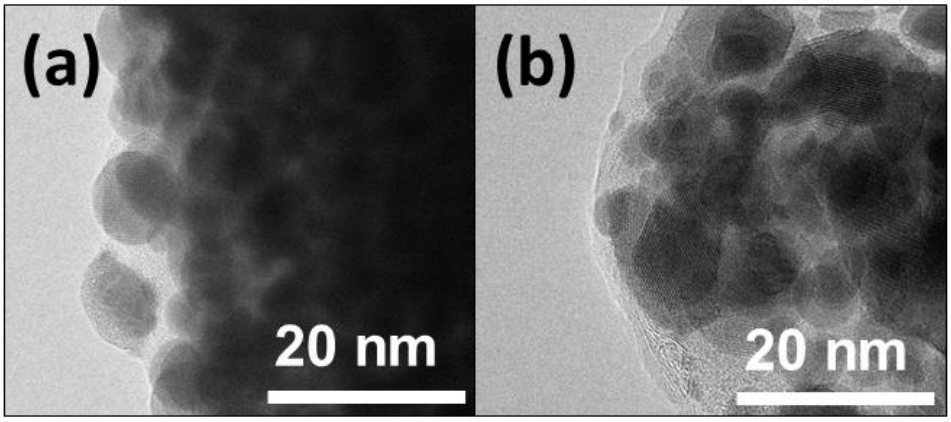

Figure 86: *Typical HRTEM images of the active material discharged at* ***(a)*** *1.7 V and* ***(b)*** *1.0 V.*

Now, at this stage that there are still two important remaining questions regarding the electrochemical performance of $Bi_4B_2O_9$ versus Li remains. They are *i)* the surprisingly small polarization (~300 mV) and *ii)* the tiny amount of carbon additive necessary for cycling. At

this point the alloying/ dealloying process was not anymore of interest due to the poor reversibility at low voltage. So from now on, all electrochemical measurements were conducted above 1.0 V. To address these questions, potentiostatic intermittent titration technique (PITT) measurements were implemented to $Bi_4B_2O_9$/Li half-cells, with 10 mV steps after a current decay corresponding to a C/10 rate in a voltage window from 1.0 to 3.5 V. The shape of the current response can be used to distinguish between two phases and single phase electrochemical processes. For instance a single phase process (solid solution) is usually characterized by a fast current relaxation after each voltage step. This is in contrast to a biphasic process (phase transformation) where a local maximum in the current curve appears in the chronoamperometry plot. For a single phase reaction, the rate limiting step is the chemical diffusion, whereas in the biphasic case, the phase transformation is the limiting factor.[224]

Turning to the PITT data (Figure 87), we initially decrease the potential stepwise from 1.95 to 1.85 V with a fast current relaxation for each voltage step (Figure 87a). In this window ~0.5 Li^+ are incorporated, with the current response pointing towards a single phase process. Afterwards a large plateau located around 1.8 V is observed (Figure 87b) correlated to a multiphasic process supported through the successive bell-shape current responses (Figure 87b). This confirms our assumption regarding the decomposition of $Bi_4B_2O_9$ into amorphous Li_3BO_3, Bi^0 and Bi_2O_3. Between $x \approx 8$ and 11, again a nice S-shape voltage profile is visible centered around 1.4 V (Figure 87c). It is representative of a monophasic process where we hypothesize a reduction of the remaining Bi_2O_3 to Bi^0. If we consider that this reaction is being governed by the Bi^{3+}/Bi^0 redox couple accompanied with a multiphase process, a plateau-like response should be visible, in contrast to what we found. Bearing in mind the formation of Bi/ Bi_2O_3 nanocomposite at 1.7 V (Figure 87a), this discrepancy does not come as a surprise, since it is well known that the particle size can strongly affect the electrochemical signatur.[224,225] and this could be at the origin of the sloping electrochemical trace.

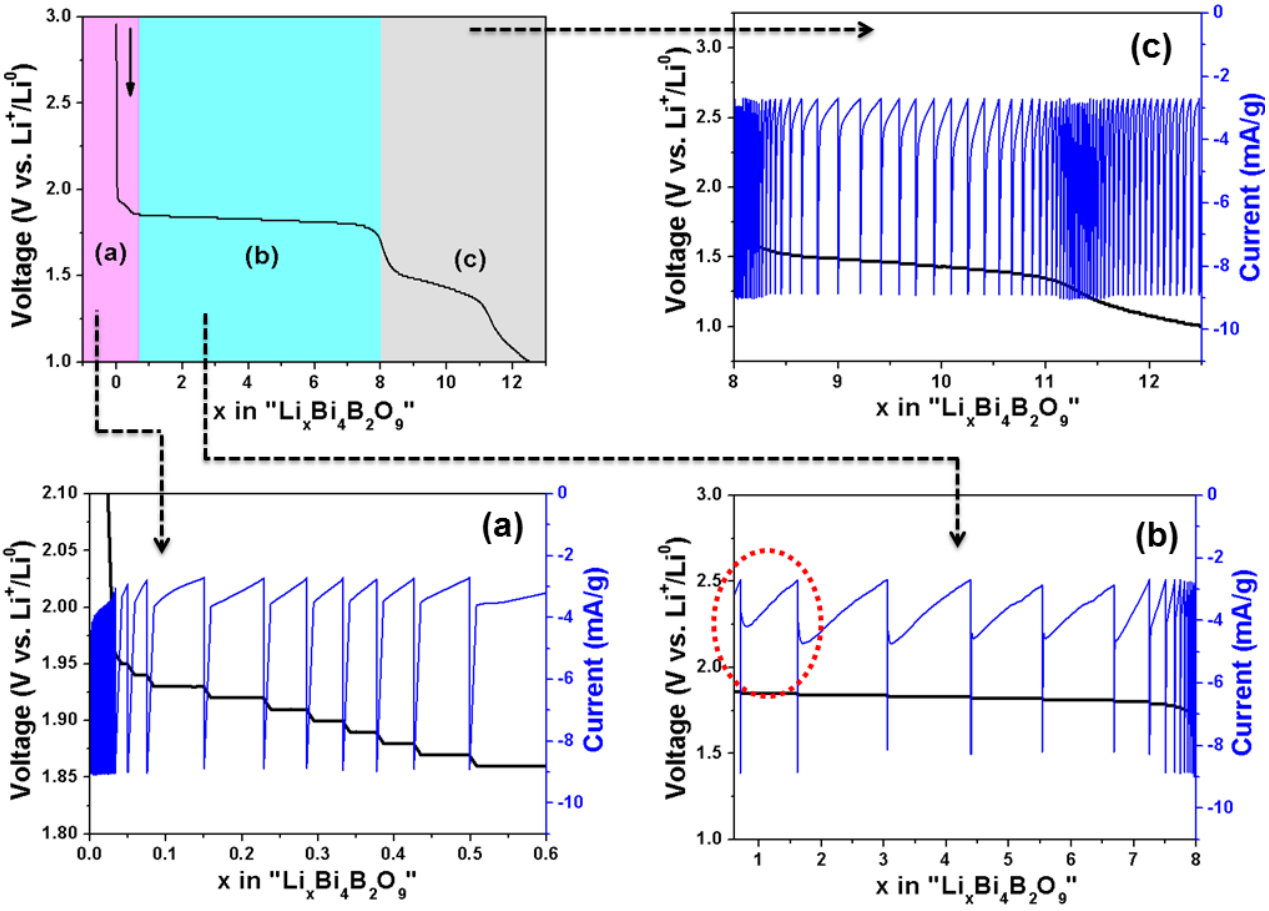

Figure 87: *PITT measurement of $Bi_4B_2O_9$ during the initial discharge down to 1.0 V. The red ellipses point out the chronoamperometry bell-shaped response.*

Lastly, turning back to the sloping anomaly at the beginning of the voltage-composition curve, time has come to check if Li-insertion into $Bi_4B_2O_9$ is taking place here. *In situ* XRD measurements up to a Li uptake of x = 1 was made. For that, a homemade cell equipped with a Be window transparent to X-rays was started with a C/10 rate on discharge and XRD pattern were collected for every change in Li stoichiometry of 0.1. As shown in Figure 88 no shift of the peaks is observed, which could have being indicative of a Li insertion into $Bi_4B_2O_9$. Furthermore neither an amorphization nor a secondary phase is detected. As we could not extract any information at this point, we followed the first discharge by means of *in situ* XRD down to 1.7 V.

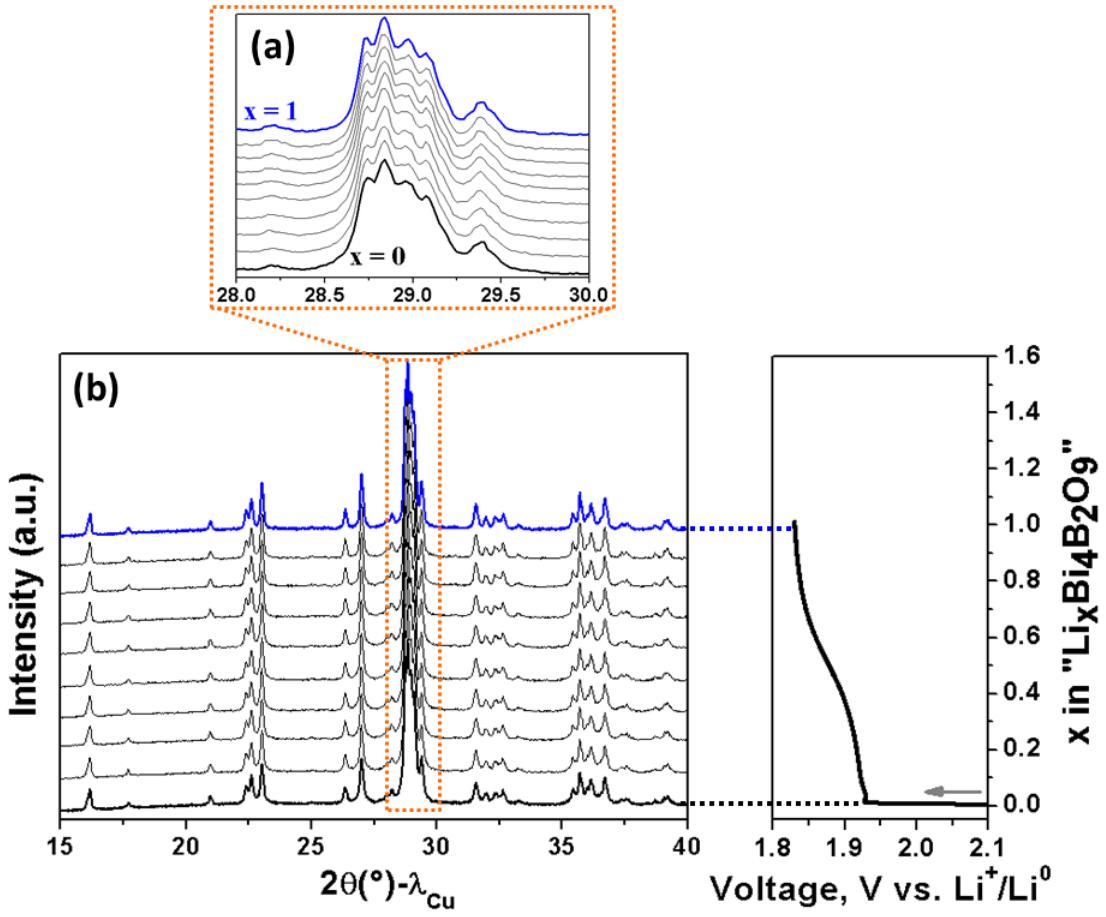

Figure 88: *In situ XRD of the initial discharge of a $Bi_4B_2O_9$/Li half-cell cycled with a C/10 rate till a Li uptake of x = 1.0. XRD pattern were recorded each 0.1 Li^+. A magnification of the main reflections is presented in **(a)** and an overview over the whole XRD pattern and the corresponding voltage-composition curve is shown in **(b)**.*

As shown in Figure 89 the intensity of the Bragg reflections of pristine $Bi_4B_2O_9$ is reduced during discharge and charge indicating a gradual consumption of the pristine material which undergoes a partial conversion during the initial reduction to 1.7 V. The loss in intensity during the first cycle is exemplarily shown on the main reflection (Figure 89a), with its intensity reduced by 60% and then another 10% upon successive charge (Figure 89b). The presence of pristine reflections after the initial lithiation does not come as a surprise as we can expect an incomplete consumption of the pristine $Bi_4B_2O_9$ when the reduction is limited to 1.7 V.

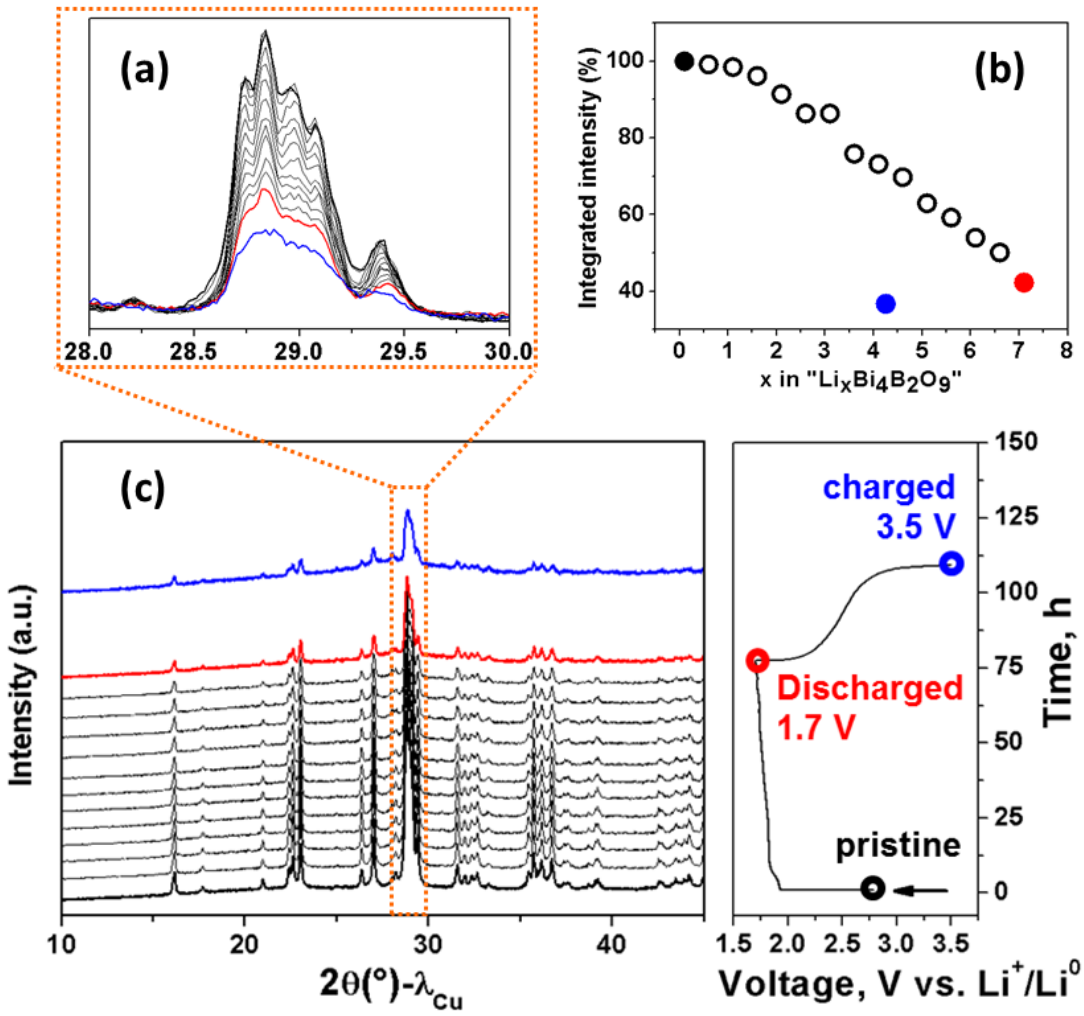

Figure 89: *In situ XRD of the initial discharge/charge cycle of a $Bi_4B_2O_9$/Li half-cell cycled with a C/10 rate in a potential window between 1.7 and 3.5 V. XRD pattern were recorded each 0.1 Li^+, however for reasons of clarity only each 5th pattern is shown in* ***(c)****. A magnification of the main reflections is presented in* ***(a)*** *and their integrated intensity of the main reflection is shown in* ***(b)****.*

To grasp further fundamentals insights into the process occurring at the beginning of the discharge, $Bi_4B_2O_9$/Li cells were discharged with different C-rates, ranging from 1C to C/100 (Figure 90a). When the C-rate decreases we note a more defined pseudo-plateau around 1.95 V which disappears for rates higher than C/5 indicating kinetic limitations of this process. Since *in situ* XRD ruled out a Li^+ insertion process, we assigned the initial pseudo-plateau region to electrochemical oxygen removal leading to the formation of Li_2O on the particle surface.

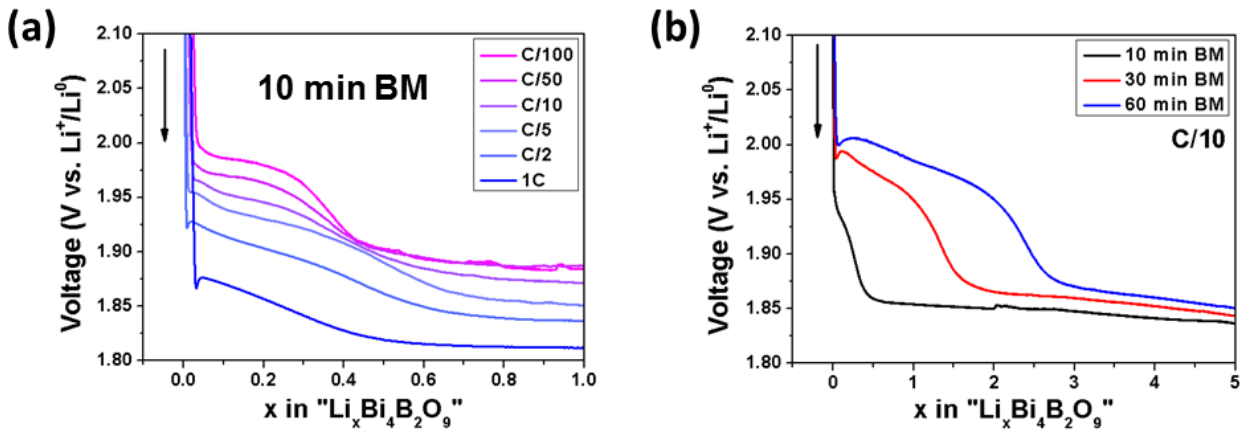

Figure 90: *Initial discharge of $Bi_4B_2O_9$/ carbon composite. In **(a)** the influence of different C-rates is shown for a milling time of 10 min, whereas in **(b)** the impact of the milling time is presented.*

To check this hypothesis we next investigated the effect of the material surface area. Therefore $Bi_4B_2O_9$ was ball milled with 5 wt.% carbon for 10, 30 and 60 min, leading to smaller particles and hence a higher surface area, as witnessed by a progressive broadening of the XRD reflections (Figure 91). We found that the anomaly at initial state of discharge is extended from x ≈ 0.4 up to x ≈ 2.5 as the particles are downsized (Figure 90b). This result strongly points towards an electrochemical driven oxygen removal from $Bi_4B_2O_9$ from near surface regions.

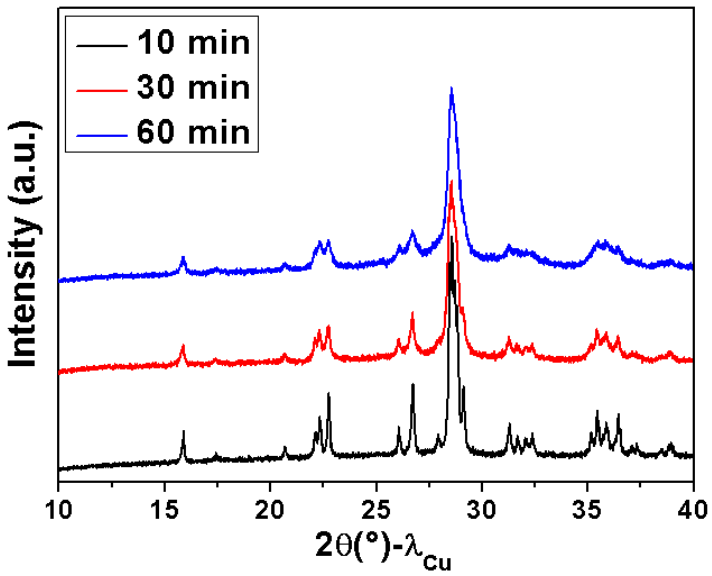

Figure 91: *XRD pattern of $Bi_4B_2O_9$ ball milled for different times with 5 wt% carbon.*

To corroborate our hypothesis of oxygen removal from the particle surface let us recall that the voltage-composition profile of $Bi_4B_2O_9$ versus Li presents a similar shape to that of BIMEVOX phases ($Bi_4V_2O_{11}$, $Bi_{3.6}Pb_{0.4}V_2O_{11-y}$, $Bi_4V_{1.8}Cu_{0.2}O_{11-y}$),[226,227] hence suggesting similar electrochemical reactivity. Early work dealing with the reduction of $Bi_4V_2O_{11}$ has revealed an initial decomposition reaction that was shown to result from the oxygen removal process of the pristine material yielding in $Bi_4V_2O_{10.66}$ and amorphous Li_2O formed around the particles.[226] According to equation 14 we assume similar reaction happens in $Bi_4B_2O_9$ leading to an oxygen deficient material $Bi_4B_2O_{9-x/2}$ in which the less negative charge is compensated by a decrease in the Bi oxidation state from +3 to +1, however spectroscopic techniques are needed to determine it exactly.

$$Bi_4B_2O_9 + x\,Li^+ + x\,e^- \rightarrow [Bi^{3+}_{4-\frac{x}{2}}\,Bi^{1+}_{\frac{x}{2}}]B_2O_{9-\frac{x}{2}} + \left(\frac{x}{2}\right)Li_2O \qquad \textbf{(14)}$$

Based on our assumption of oxygen removal from $Bi_4B_2O_9$, we are now finally able to rationalize the two remaining questions, dealing with the surprisingly small polarization of ~300 mV, which is among the smallest reported for conversion type materials,[228] and the low amount of carbon additive necessary for cycling. Compounds with less electronegative anions were experimentally shown to have lower polarization; the reason why hydrides display lower polarization (0.2 V)[228,229] than phosphides (0.4 V),[230,231] oxides (0.9 V)[232,233] and fluorides (1.1 V).[15,212] Along this line of thinking, $Bi_4B_2O_9$ should show a polarization comparable to oxides. However it is well known that oxygen vacancies can promote high ionic- and/ or electronic conductivity in metal oxides and namely Bi-oxides.[219,234,235] Thus we hypothesize that the creation of oxygen vacancies in $Bi_4B_2O_9$ during cycling is responsible for a great enhanced ionic diffusion and electronic conduction. This hypothesis is able to account for both experimental observations, the small polarization as well as the ability to reversible cycle $Bi_4B_2O_9$ with only 5 wt% conductive carbon additive.

To check the importance of ionic and electronic conductivity in $Bi_4B_2O_9$, we carried out AC/DC impedance measurements. For that a sintered pellet of $Bi_4B_2O_9$ was prepared by pressing ~300 mg of powder in a 10 mm die at a pressure of around 2.5 tons followed by an annealing for 24h at 600°C in air (around 65 to 75 % of theoretical density was obtained). After placing the pellet in the apparatus between two Pt-electrodes, AC impedance spectra were recorded for temperatures ranging from 340 up to 430°C while applying voltage amplitude of 500 mV in a frequency range between 30 MHz and 0.01 Hz during heating in air (detailed description of the setup see annexes chapter 7.1.3).

First of all, the AC complex impedance spectra for $Bi_4B_2O_9$ presents a slightly depressed semicircle over the whole measured temperature range with the absence of a Warburg diffusion resistance tail implying poor ionic conductivity. The spectra can be expressed with an equivalent circuit R_0─R_1/CPE_1─R_2/CPE_2 (Figure 92 inset) where each parallel R/CPE circuit gives raise to one semicircle (schematically plotted as grey lines in Figure 92). For each semicircle the resistance R_1 and R_2 (intercept with the x-axis, indicated in Figure 92) plus the corresponding capacitance C_1 and C_2 can be obtained from the fitting parameters (details see annexes chapter 7.1.3). Typically capacitive values around 10^{-12} and 10^{-9} F refer to the bulk- and grain boundary contribution respectively, allowing us to differ between them.[197,198]

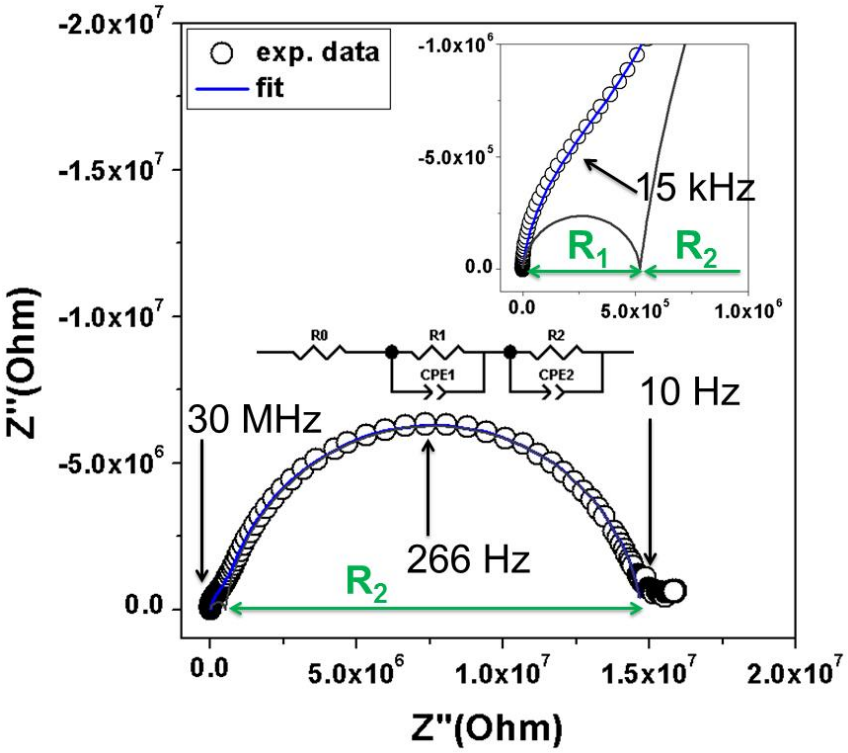

Figure 92: *Representative AC complex impedance spectra of $Bi_4B_2O_9$ measured at 384°C in air. The semi circles corresponding to the bulk- and grain boundary resistance are schematically drawn as grey lines, and the real resistance values are indicated with green arrows.*

To clearly separate the ionic and electronic contributions to the overall conductivity, galvanostatic DC polarization measurements were conducted (Figure 93) on sintered $Bi_4B_2O_9$ pellets sandwiched between two ionically blocking Pt-electrodes. After applying a constant current, both ions and electrons are moving, however the blocking of ions gives rise to a gradient of the chemical potential. At sufficiently long waiting time, a stationary state is reached, and the chemical potential gradient is compensated by an electrical potential gradient denoted to the polarization voltage. This polarization voltage yields to the resistance of the non-blocked charge carriers which are in our case are electrons, hence refering to the pure electronic conduction of the material.[236] Next we applied a constant current of 5 nA across the pellet, and monitored the potential response. The DC polarization plot shown in Figure 93 indicates that a true steady state potential value is instantaneously reached implying that the charge transport in $Bi_4B_2O_9$ is carried out by electrons/ holes.

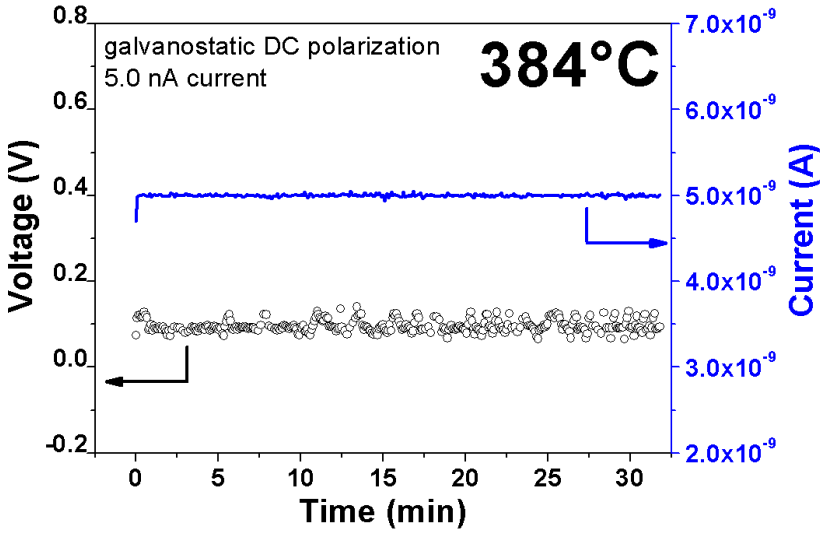

Figure 93: *Representative galvanostatic DC polarization of $Bi_4B_2O_9$.*

From the experimentally determined values for the AC and DC resistance, the corresponding conductivity was derived and the activation energy was obtained using the Arrhenius equation (details see annexes chapter 7.1.3). All results obtained from AC and DC measurements are summarized in the Arrhenius plot as shown in Figure 94.

The bulk ionic conductivity increases linearly from $3.77 \cdot 10^{-8}$ up to $5.31 \cdot 10^{-7}$ $S \cdot cm^{-1}$ for 344 and 426°C (Table 14), respectively and it is associated to an activation energy of 1.28 eV. The grain boundary conductivity increases also linearly in the same temperature range

from $5.5 \cdot 10^{-10}$ to $2.43 \cdot 10^{-8}$ $S \cdot cm^{-1}$ (Table 14) correlated to an activation energy of 1.75 eV, however around one magnitude of order lower than the bulk conductivity. We hypothesize that the lower values for grain boundary- compared to the bulk contribution can be correlated to the formation of disorder/ defects at the grain interfaces, impeding ionic conduction.[206,237,238] Regarding the electronic conductivity, it also increases linearly from $2.74 \cdot 10^{-9}$ to $1.46 \cdot 10^{-8}$ $S \cdot cm^{-1}$ (Table 14) in the temperature range from 364 to 406°C with an activation energy of 1.46 eV. Extrapolation of the experimental values leads to RT conductivities of $9.1 \cdot 10^{-19}$, $6.1 \cdot 10^{-22}$ and $1.1 \cdot 10^{-24}$ $S \cdot cm^{-1}$ for the bulk-, grain boundary- and electronic conductivity respectively. The poor extrapolated RT electronic conductivity is in agreement with the large optical bandgap of 3.02 eV calculated for $Bi_4B_2O_9$, implying strong insulating properties.[214]

Table 14: *Values for bulk-, grain boundary and electronic conductivity of $Bi_4B_2O_9$, extracted from the AC and DC impedance measurements, recorded at certain temperatures.*

Temperature (°C)	σ_{AC}(bulk) ($S \cdot cm^{-1}$)	σ_{AC}(grain boundaries) ($S \cdot cm^{-1}$)	σ_{DC}(electronic) ($S \cdot cm^{-1}$)
344	$3.77 \cdot 10^{-8}$	$5.5 \cdot 10^{-10}$	-
364	$8.87 \cdot 10^{-8}$	$2.01 \cdot 10^{-9}$	$2.74 \cdot 10^{-9}$
384	$1.70 \cdot 10^{-7}$	$6.25 \cdot 10^{-9}$	$5.15 \cdot 10^{-9}$
406	$3.95 \cdot 10^{-7}$	$1.28 \cdot 10^{-8}$	$1.46 \cdot 10^{-8}$
426	$5.31 \cdot 10^{-7}$	$2.43 \cdot 10^{-8}$	-

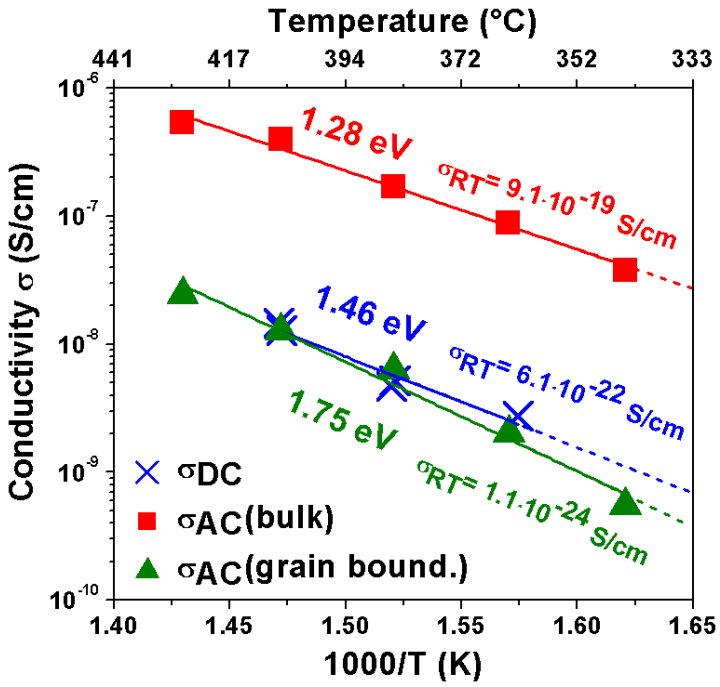

Figure 94: *Arrhenius plot of the AC and DC conductivity of $Bi_4B_2O_9$ derived in the temperature range from around 340 to 430°C during heating in air.*

5.3 Conclusion

Within this chapter, bismuth oxyborate $Bi_4B_2O_9$ was studied towards its reaction mechanism versus lithium between 0.0 and 3.5 V. This material was initially chosen due to its very high density (~8.2 $g \cdot cm^{-3}$) in order to maximize the volumetric energy density, which is presently very low for other conversion type cathode materials as they are usually mixed with ~20 wt% carbon. In the course of this study we find that it is possible to reversible cycle $Bi_4B_2O_9$ versus Li, via combined conversion/ alloying processes between 0.0 and 3.5 V (Figure 95a). We show that depending on the lower cutoff voltage, the alloying/ dealloying of Bi with Li can be circumvented and only a conversion reaction of $Bi_4B_2O_9$ can be triggered. For this reaction the reversibility between 1.0 and 3.5 V can be enhanced if the discharge is limited to 1.7 V (Figure 95b), where the material can be cycled at an average potential of 2.3 V, with therefore a fast capacity decay. Most surprisingly a small amount of carbon additive as little as 5 wt% was necessary to achieve electrochemical activity. Interestingly our

combined AC/DC impedance measurement reveal RT conductivities of $1.1 \cdot 10^{-24}$, $9.1 \cdot 10^{-19}$ and $6.1 \cdot 10^{-22}$ $S \cdot cm^{-1}$ for the grain boundary-, bulk- and electronic conductivity respectively, extrapolated from high temperature measurements. On the basis of this measurement we suppose $Bi_4B_2O_9$ to be a very poor conductor for ionic and electronic transport.

However, these insulating properties are in sharp contrast to our experimental observation as $Bi_4B_2O_9$ needs only 5 wt% carbon additive for achieving attractive electrode performance polarization-wise. We believe this effect to be rooted in the Li-driven formation of $Bi_4B_2O_{9-x/2}$ at the surface of the particles showing better electronic/ ionic conductivity than the pristine material. It should be recalled that minor addition of Li to $Li_4Ti_5O_{12}$ (LTO) trigger drastically the transport properties as this compound nearly evolves from a semiconductor to a metal.[239] We believe a similar phenomenon to be present in $Bi_4B_2O_9$ but related to oxygen content contrary to LTO.

Furthermore we observed a surprisingly small voltage polarization of ~300 mV where we hypothesize that the small value and reversibility of the conversion reaction versus Li, is most likely correlated to the appearance of Bi_2O_3 and oxygen deficient phases (in Bi_2O_3 and $Bi_4B_2O_9$) during the conversion, lowering the kinetic barriers for ionic/ electronic transport.

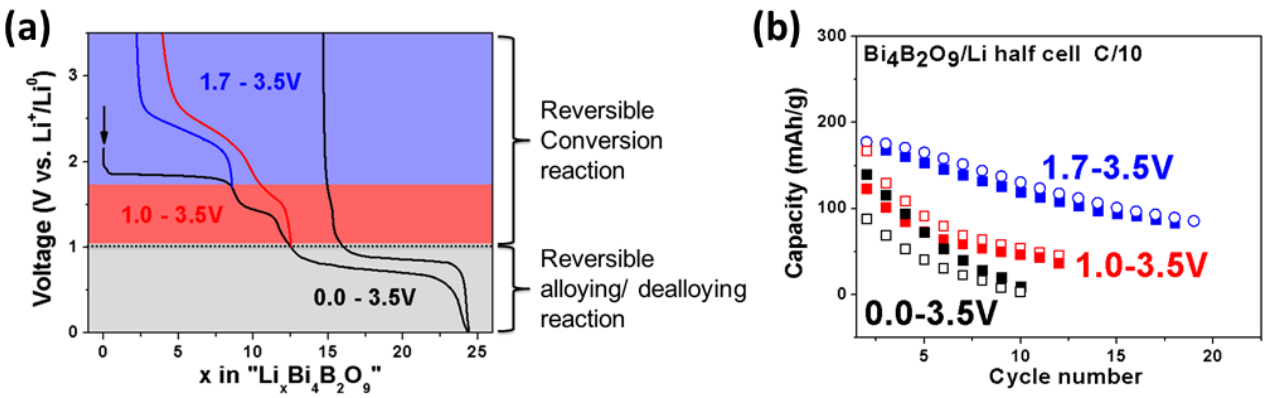

Figure 95: (a) *Schematic illustration of the different voltage-composition curve of $Bi_4B_2O_9$ versus Li depending on the lower cutoff potential referring to the conversion- and alloying part of the electrochemical reaction versus Li.* ***(b)*** *Capacity retention depending on the voltage window applied for galvanostatic cycling.*

The presence of carbon within our electrodes prevents the determination of the transport properties for the oxygen deficient phase $Bi_4B_2O_{9-x/2}$. To circumvent this difficulty we have tried to prepare this non-stoichiometry by heating $Bi_4B_2O_9$ in an Ar/H_2 atmosphere at

moderate temperatures ~350°C. When doing so we observed the formation of metallic Bi^0 as deduced from XRD. Milder reducing agents are needed. One possibility hence most probably more soft synthesis approaches are necessary. One possibility might be the reaction of $Bi_4B_2O_9$ with CaH_2 in sealed quartz tubes which allows to further decrease the reaction temperature.

6 General conclusion

This thesis was aimed to explore new borate based positive electrode materials for Li- and Na-ion batteries. Previous studies have shown very attractive electrochemical properties for $LiFeBO_3$ but also revealed its major limitations related to i) a low redox potential versus Li (~2.8 V), ii) fast degradation in ambient atmosphere and iii) poor kinetics.[139,151,152] Moreover, it was also reported, that the redox potential of the same 3d metal can be shifted up by moving for instance from PO_4 to P_2O_7.[86] This was an impetus for us to deviate from BO_3 based materials, and embark into an exploration of the polyborates (e.g. pyroborate B_2O_5), with the aim to design new high voltage cathode materials.

We initially focused in the synthetic exploration of pyroborate B_2O_5 and pyroborate fluoride B_2O_5F compounds, however during this survey, we encountered several synthetic difficulties in stabilizing the desired phases, even though a large variety of high- and low temperature synthetic approaches were tested. After this unsuccessful exploration, we selected $Li_6CuB_4O_{10}$ as a model compound to show the feasibility to achieve elevated redox potential towards Li in a pyroborate-based compound; such a high potential being routed in the presence of both Cu as a 3d-metal and of B_2O_5 groups as polyanions. Through this study, we first established the structural and synthetic relationship between the two reported structural polymorphs (α- and β- $Li_6CuB_4O_{10}$) by means of thermogravimetric analysis coupled with differential scanning calorimetry (TGA-DSC) and high temperature (HT) synchrotron X-ray diffraction (XRD) measurements. Moreover we have shown that both polymorphs react with Li in a reversible way through a classical insertion/ deinsertion reaction with average redox potentials of 4.25 and 3.9 V vs. Li^+/Li^0 for α- and β- $Li_6CuB_4O_{10}$ respectively. This activity was correlated to the Cu^{3+}/Cu^{2+} redox couple through combined electron paramagnetic resonance (EPR) spectroscopy and density functional (DFT) calculations. Aside from this high voltage activity we reveal a conversion type reaction if the voltage is lowered down to 1.0 V, leading to the extrusion of elemental Cu nanograins as deduced by transmission electron microscopy (TEM) imaging. Finally to get an explanation for the poor electrochemical performance, bond valence energy landscape (BVEL) calculations in combination with complementary AC/DC conductivity measurements were conducted. Both polymorphs show very poor ionic/ electronic conductivities at room temperature (RT) and high activation energies for Li^+ migration (1.07 and 0.92 eV for the α- and β-phase respectively). In particular the RT ionic conductivity is in the order of 10^{-13} $S \cdot cm^-$

[1] for the α- and β-polymorph, and electronic conductivities are around 10^{-8} and 10^{-13} $S \cdot cm^{-1}$ respectively. Despite these very low values, we surprisingly reveal the existence of a structural transition of α-$Li_6CuB_4O_{10}$ at 350°C into a HT polymorph, with this transition be accompanied with a drastic increase in the ionic conductivity, reaching values of 1.4 $mS \cdot cm^{-1}$ at 500°C associated to an activation energy for Li^+ mobility of 0.52 eV.

As we have shown the feasibility to obtain high redox potentials versus Li with borates, but also encountered strong difficulties in obtaining new phases, we exploited other borate anions, hence our interest for the family of sodium metal pentaborates $Na_3MB_5O_{10}$. We were able to stabilize two new compounds out of this family for M = Fe and Co and solve their crystal structure with the help of synchrotron XRD. These materials are basically built up of layers consisting of MO_4 tetrahedra connected through B_5O_{10} units with sodium sitting in voids inside these layers as well as in between them. In light of such structural features favorable to Na^+ mobility, we examined their electrochemical activity versus Na and show a redox potential of 2.5 V vs. Na^+/Na^0 correlated to the Fe^{3+}/Fe^{2+} redox couple as confirmed by *ex situ* Mössbauer spectroscopy. In light of a bulk ionic conductivity of $7.6 \cdot 10^{-10}$ $S \cdot cm^{-1}$ similar to what was measured for $LiFePO_4$, we deduce that the poor electrochemical performance of $Na_3FeB_5O_{10}$ is most likely nested in its much lower RT electronic conductivity ($1.2 \cdot 10^{-14}$ $S \cdot cm^{-1}$). In contrast $Na_3CoB_5O_{10}$ is electrochemical inactive as expected from its very low RT ionic- and electronic conductivity of $4.0 \cdot 10^{-13}$ $S \cdot cm^{-1}$ and $5.4 \cdot 10^{-17}$ $S \cdot cm^{-1}$ respectively. Although $Na_3FeB_5O_{10}$ cannot be considered for practical applications, it stands as the first compound out of the Na_2O-FeO-B_2O_3 ternary system which shows a reversible reactivity towards sodium.

Owing to difficulties in designing new insertion type borate based cathode materials, we then considered other type of reaction mechanisms, namely conversion reactions. In this context we studied the conversion reaction of a bismuth oxyborate $Bi_4B_2O_9$ versus Li. This particular material was chosen as it combines elevated redox potentials versus Li due to the inductive effect of the borate group. Moreover, its high density (~8.2 $g \cdot cm^{-1}$) offers an alternative to combat the practical low volumetric energy density of conversion type electrode materials. The material was studied by means of electrochemical methods combined with TEM and XRD measurements. Throughout the study we found that it shows an electrochemical activity centered at 2.3 V, vs. Li^+/Li^0, that is associated to the reversible reduction of Bi^{3+} to Bi^0 and the formation of amorphous Li_3BO_3 and Li_2O. Surprisingly, such an activity comes out with a polarization of solely ~300 mV that is among the smallest reported for conversion materials, while we have only used 5wt% carbon and without

nanosizing. We rationalize this finding with first an electrochemical driven oxygen removal from the particle surface of $Bi_4B_2O_9$ enabling strong enhanced charge/ mass transport properties through the grain boundaries so the actual conversion reaction can proceed. After the initial formation step, a nanocomposite is achieved, in which we hypothesize the appearance of oxygen vacancies in $Bi_4B_2O_9$/ Bi_2O_3 plays a crucial role to promote ionic conductivity, hence responsible for the low polarization. If the potential window is enlarged to 0.0 - 3.5 V an additional alloying/ dealloying reactions between Li and Bi are observed at around 0.8 V. Therefore, there are poorly reversible due to very strong textural changes.

Overall within this thesis we have shown the feasibility of achieving high redox potentials versus Li in the borate family as exemplified with $Li_6CuB_4O_{10}$. As we have discussed in chapter one, the potential of a given $M^{(n+1)+}/M^{n+}$ redox couple is highly related to the ionicity of the M─O bond, described by the inductive effect. It was argued in literature that using condensed anionic species (BO_3 vs. B_2O_5 or PO_4 vs. P_2O_7, etc.) should further strengthen the inductive effect hence resulting in higher potentials.[165] This explanation is consistent with our experimental finding for $Li_6CuB_4O_{10}$, however several other parameters influencing the redox potential have to be taken into account as well, namely the TM polyhedral connectivity and coordination number, and the nature of the TM itself. The situation becomes even more complicated in the particular case of borates, as it is well known that boron can adopt trigonal planar BO_3 as well as tetrahedral oxygen BO_4 coordination which can additionally be connected in an unpredictable way forming complex polyanions. Although we are far away from designing tailor-made borates for cathode application, the multifaceted borate chemistry is prone to form open crystal structures with possible pathways for alkali-in migration. In the course of our exploration we succeeded in synthesizing two new pentaborates $Na_3MB_5O_{10}$ (M = Fe, Co) possessing an open structure with the possibility of 1D- and 2D Na^+ migration. However their poor electrochemical performance/ inactivity reminds us that searching for new electrode materials does not systematically led to outstanding compounds. Nevertheless during the rationalization of our findings in terms of electrochemical activity, other interesting properties popped up such as an unexpected high Li^+ ionic conductivity in HT-α-$Li_6CuB_4O_{10}$ described above. However, it out of the scope of this thesis due to times constraints to fully correlate this finding to the crystal structure, for which exact solution HT neutron measurements are required.

Finally through the exploration and study of the structure-property relationships in borates, we have encountered synthetic difficulties somewhat compensated by other interesting physical properties which could render these materials attractive for a broader

audience, beside the battery community. Moreover we hope to encourage researcher to still hunt for new borate based compounds, as their crystal structure can be hardly predicted so unexpected properties remain to be discovered.

7 Annexes

7.1 Electrochemical characterization

To characterize the electrochemical properties of possible electrode materials, all tests were done in 2 electrode *Swagelok*® half cells. A schematic view of the setup is given in Figure 96 where the positive electrode material is separated by two sheets of glass fiber discs (*Whattman GF/D borosilicate*) soaked with electrolyte from the anode (lithium or sodium metal). The entire assembly of the cells was conducted in an air- and water free atmosphere inside a glove box (*MBraun, Germany, O_2 and H_2O < 0.1 ppm*), the positive electrode material was prepared prior to use by mixing an appropriate amount of carbon (carbon SP) with the as synthesized compound by means of ball milling or hand grinding.

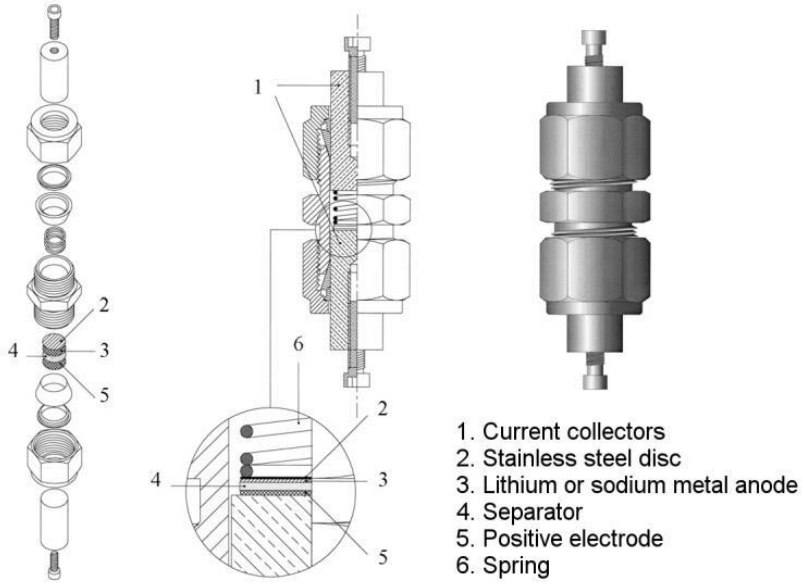

***Figure 96**: Schematic view of a Swagelok type 2 electrode cell.*

For *in situ* XRD experiments a special homemade cell was used, adapted to the sample holder of the diffractometer (Figure 97).[240] The assembly of parts is basically the same as for normal Swagelok type cells shown above with the main difference that the current collector for the positive electrode materials is made of Beryllium, almost transparent to X-rays. If voltages above ~3.5 V vs. Li^+/Li^0 are applied, the Be window is protected through a 3 µm thick aluminium foil (*Goodfellow*) to prevent Be from oxidation. As this type of cell setup is capable of a higher loading of the active material compared to the normal Swagelok setup,

this kind of cells were also used to prepare large quantities of *ex situ* samples of positive electrode materials for further characterization. In that case the Be window was replaced by stainless steel covered with aluminium foil.

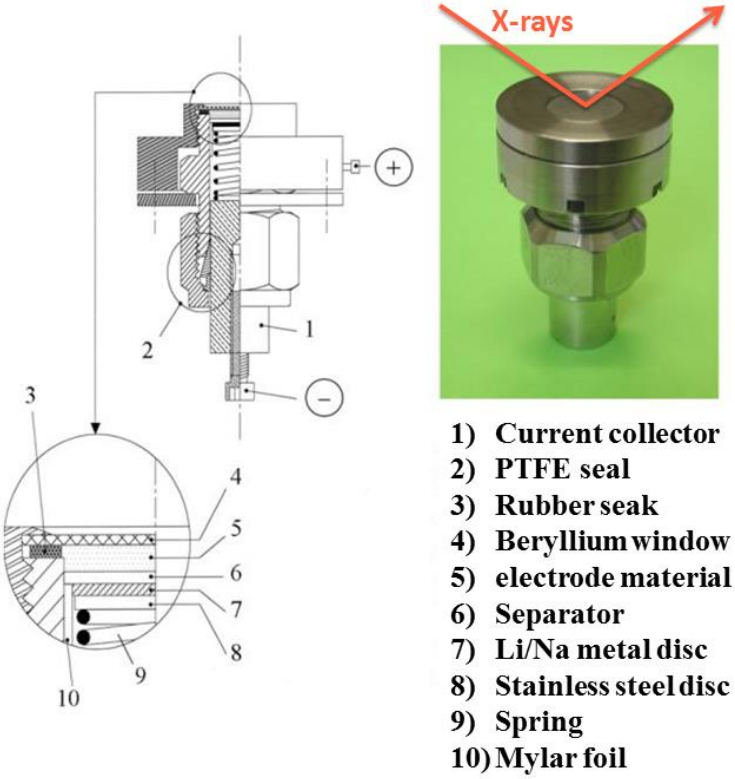

***Figure 97**: Schematic view of a modified Swagelok type 2 electrode cell used for I situ XRD experiments.*

If not other stated, all electrochemical tests were carried out with a *VMP3* potentiostat/ galvanostat (*BioLogic S.A.,Claix, France*) at room temperature.

7.1.1 Galvanostatic techniques

Typically all materials were first tested in galvanostatic mode, enabling to trace the voltage-composition curve $V = f(x)$ of a certain compound. First information can be extracted from the shape of the curve (S-shape for a solid-solution process vs. plateau for a single-phase process). Furthermore, by calculated the derivative of the voltage-composition curve $-\delta x/\delta V = f(V)$, the redox potentials and its change upon subsequent cycling of an electrode material can be determined more precisely.

However if a cell is cycled in classical galvanostatic mode, the system in general not in equilibrium and the redox potentials are shifted compared to the theoretical one. Thus, to determine the thermodynamic equilibrium potential more precisely, galvanostatic cycling with relaxation was done. The principle of this measurement consists of alternating times of normal galvanostatic charge/ discharge steps followed by an open circuit voltage (OCV) period, where the system is allowed to reach the equilibrium potential.

7.1.2 Potentiostatic techniques

A potentiostatic intermittent titration technique (PITT) experiment consists in increasing the potential applied to the cell by small steps of a few mV (~10 mV) and following the evolution of the current response until it reaches a limit value (corresponding to a certain C-rate). Such an experiment provides information about the charge/discharge mechanism (solid solution vs. biphasic process) depending on the shape of the current decay.[224]

7.1.3 Electrochemical impedance spectroscopy

AC impedance measurements were carried out using a *BioLogic MTZ-35* setup with ionically blocking platinum electrodes equipped with a *HTF-1100* furnace. Impedance measurements were recorded from 30 MHz to 0.01 Hz in a certain temperature range in argon or air applying a voltage amplitude from 10 to 200 mV.

Electrochemical impedance spectroscopy (EIS) is a widely used method, able to determine a variety of different phenomena ranging from electrochemical reactions, ionic diffusion etc. However, within the context of this thesis this technique is exclusively used for the determination of transport properties of solids (ionic/ electronic). In general a sinusoidal voltage is applied over a wide frequency range, and the current response is followed. The measured impedance usually contains resistive (R) and capacitive (C)/ inductive components and the data is drawn in the form of imaginary Z" (capacitive) versus real Z' (resistive) impedance, the so called Nyquist plot. Each parallel R/C element results in a perfect semicircle from which both values (R and C) can be extracted (Figure 98), where R values are obtained from the intercept of the semicircle with the Z'-axis.[197]

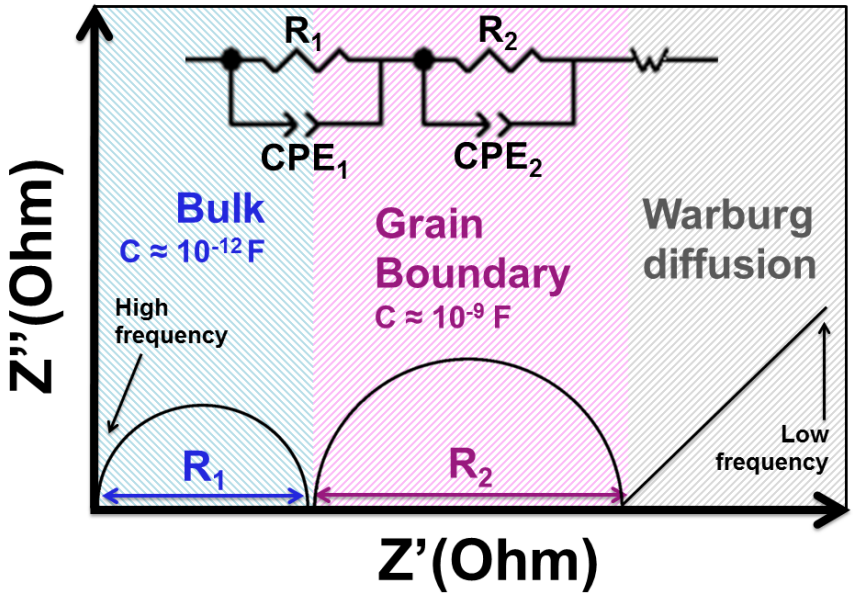

Figure 98: *Representative Nyquist plot with the equivalent circuit to referring to bulk- and grain boundaries respectively.(Adapted from Ref.*[197]*).*

In practice, deviations from ideal semicircles are often observed in the Nyquist plot of real materials, which can be explained by the overlap of different phenomena in the sample. This effect can be taken into account in the model of the equivalent circuit by using a constant phase element (CPE). From the fitting parameters Q, R and n of the CPE, the capacitance of the relaxation process can be estimated according to the following equation:

$$C = (R^{1-n} \cdot Q)^{\frac{1}{n}} \qquad \textbf{(15)}$$

In this study conductivity measurements were carried out using a *BioLogic MTZ-35* impedance analyzer with ionically blocking electrodes, equipped with an *HTF-1100 furnace* upon heating and cooling under a flow of argon. For AC measurements, a voltage amplitude ranging usually from 10 to 200 mV over a frequency range from 35 MHz to 0.1 Hz was applied and the current response was followed.

The depressed semi-circles derived from the complex AC impedance spectra were fitted with a corresponding equivalent circuit, where R_0 represents an initial shift of impedance arc from zero, R_1 is the bulk- and R_2 grain boundary resistance (in case it is

possible to distinguish between them), CPE stands for a constant phase element. The conductivity σ was calculated from the resistance R, the pellet's thickness l, and area A according to the following equation:

$$\sigma = \frac{l}{A \cdot R} \quad \textbf{(16)}$$

The activation energy E_a (eV) for Li^+ migration and electron conduction was calculated from fitting the experimentally derived values using the Arrhenius equation,

$$\sigma T = \sigma_0 \cdot e^{-\left(\frac{E_a}{k_B T}\right)} \quad \textbf{(17)}$$

where σT ($S \cdot cm^{-1} \cdot K$) is the temperature dependent conductivity, σ_0 ($S \cdot cm^{-1}$) is a pre-exponential factor, and k_B is the Boltzmann constant. Note that the conductivity values are not corrected by the pellet porosities, thus the values are underestimated.

7.1.4 Direct current polarization measurements

The current/ voltage of a mixed conductor if a DC potential (*U*) or current (*I*) is applied corresponds to the dc resistance (R_{DC}), where R_{el} and R_{ion} represent the partial electronic and ionic resistances respectively:

$$\frac{I}{U} = \frac{1}{R_{DC}} = \frac{1}{R_{el}} + \frac{1}{R_{ion}} \quad \textbf{(18)}$$

The partial resistances can be extracted when selective reversible or blocking electrodes are used (Pt as reversible electrode for electrons and blocking electrode for ions). The blocking of one charge carrier leads to a polarization and a gradient of potential of the blocked component. At sufficiently long waiting times, a steady state is reached which accounts only for the electronic part of the charge transport, if ionically blocking electrode are used.[236]

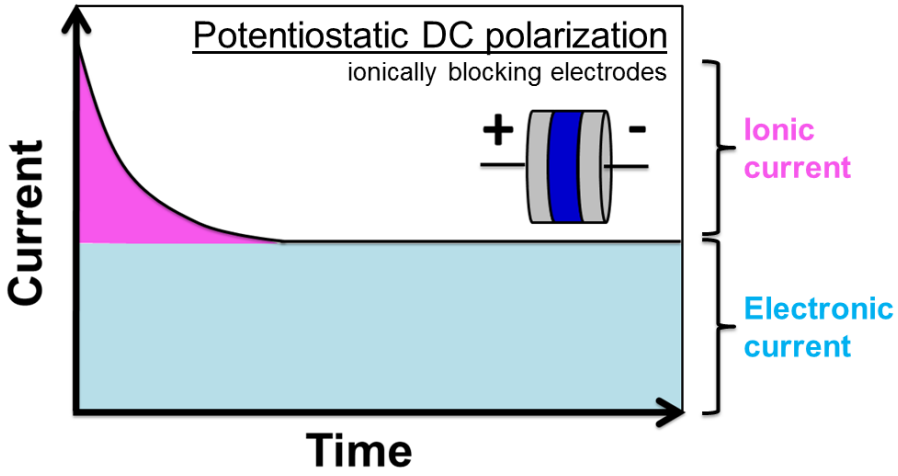

Figure 99: *Representative current response curve of a potentiostatic DC polarization if an mixed conductor is measured between two ionically blocking electrodes. The ionic- and electronic current contributions over time are indicated.*

Out of the steady state current value the corresponding resistance can be calculated according to Ohm's law:

$$R = \frac{U}{I} \qquad \textbf{(19)}$$

The corresponding conductivity σ was calculated according to the formula given in equation 19. DC polarization measurements were done on similar pellets used for AC impedance spectroscopy with platinum blocking electrodes, by applying a constant voltage or current till the current- or potential response reached a constant value, respectively. The same setup like for the AC impedance measurements was used, with the difference that the applied potential/ current was controlled/ recorded with a *VMP3 potentiostat (BioLogic S.A.,Claix, France).*

7.2 Structural characterization

X-ray diffraction (XRD) was used within this thesis as a regular characterization method to verify the purity of the samples or to perform Rietveld refinement of structural models proposed in literature. All powder patterns were refined using the Rietveld method[241] as implemented in the FullProf program.[242]

The crystal structures show in this thesis were drawn with the *VESTA* visualization program.[243] Data that were not obtained from our refinements was received as CIF files from the *ICSD* database.[244]

7.2.1 Laboratory XRD

Laboratory XRD patterns were recorded in Bragg-Brentano geometry with a *Bruker D8 Advance* diffractometer equipped with a copper source ($\lambda_{Cu\text{-}K\alpha1}$ = 1.54056 Å, $\lambda_{Cu\text{-}K\alpha2}$ = 1.54439 Å) and a LynxEye detector. If samples were air/ moisture sensitive, a homemade sample holder was used which, covered with a Kapton window, which could be sealed air tight inside the glove box.

Temperature-controlled XRD experiments were carried out at the same diffractometer described above, equipped with an *Anton Paar HTK1200* furnace chamber.

7.2.2 Synchrotron XRD

In order to get more precise structural information of the samples, selected samples were measured either at the 11-BM beamline at the Argonne National Laboratory through the mail-in service of the 11-BM beamline of the Advanced Photon Source (APS) at Argonne National Laboratory (ANL, Argonne, USA) with a wavelength of λ = 0.4139 Å.

HT synchrotron XRD was conducted at the ID 22 – High resolution powder diffraction beamline at the European Synchrotron Radiation Facility (ESRF) using a wavelength of λ = 0.4001 Å.

7.3 Other physical characterization

7.3.1 Thermal analysis

Thermal stability and phase transition were investigated using thermogravimetric analysis coupled with differential scanning calorimetry (TGA-DSC). The data was recorded with a *STA 449C Netzsch* apparatus. Around 20-30 mg of sample was utilized which was heated/ cooled in flowing air or argon with heating rates from 1 to 10°C/min.

7.3.2 EPR spectroscopy

EPR spectroscopy is a technique to study materials with unpaired electrons. As unpaired electrons possess a magnetic moment, they adopt discrete energy levels, if an external magnetic field is applied (also called Zeeman effect). To induce a transition between these two energy levels, the probe is subjected to microwave radiation. The absorption signal presents the energy required for the transition, and is described as its first derivative (Figure 100).[245]

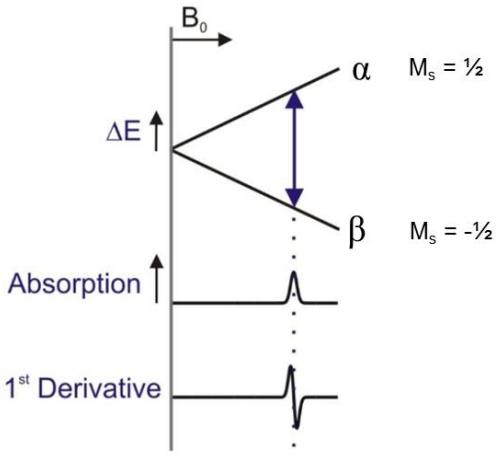

Figure 100: *Energy levels for an electron with spin (S= ±1/2) in an applied magnetic field B, where it can adopt two different states (α and β), and the corresponding absorption spectrum and its first derivative.*

One important parameter which can be extracted from EPR measurements, is the so called *g*-factor. It can give information about the electronic structure of the paramagnetic center

The spectra were recorded at room temperature on a *Bruker ELEXSYS E580* spectrometer using X-band continuous wave (CW) mode. Microwave power and modulation amplitude were respectively set to 2 mW and 1 G. Converse time and time constant were set to be 40.96 ms and 20.48 ms, respectively. The weight of samples and measuring Q values were normalized for the spectra to analyze the intensity of all paramagnetic species.

7.3.3 Mössbauer spectroscopy

Mössbauer spectroscopy is a versatile spectroscopic technique which can provide information about the chemical, structural magnetic properties of a material, mainly used to probe ^{57}Fe. It is based on the "Mössbauer effect", a recoilless gamma ray emission and absorption, which implies a transition between the ground- and a first excited state of a nucleus. Typically three types of nuclear interactions are observed, which are also called hyperfine interactions: *i)* isomeric shift, *ii)* quadrupole splitting and *iii)* magnetic splitting (Figure 101. If source and absorber nucleus are identical, a simple spectrum is observed, with a single absorption peak at 0 mm/s velocity. Depending on the electronic configuration or the ligand environment, the absorption peak or the center of the spectrum is shifted from zero respectively, referring to the isomeric shift and quadrupole splitting. Typically the Mössbauer spectrum of Fe^{2+} presents an isomer shift around 1.0 mm/s and a quadrupole splitting ranging from 0.2 to 3.5 mm/s, while the doublet of Fe^{3+} has an isomer shift close to 0.3-0.4 mm/s and a quadrupole splitting smaller than 2 mm/s.[246,247]

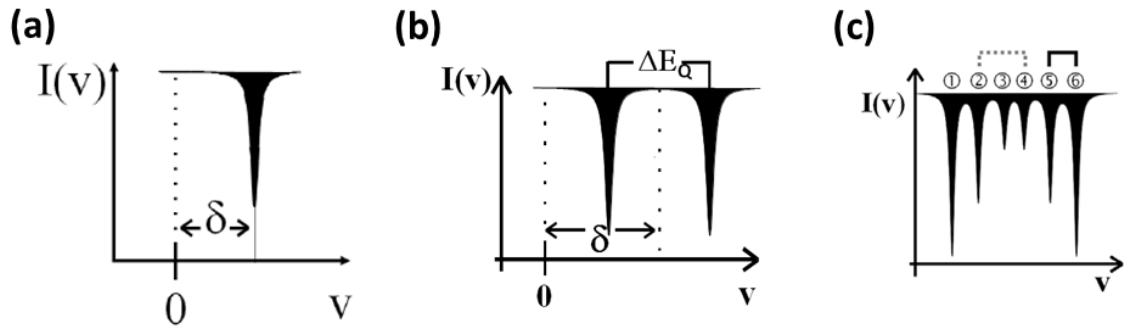

Figure 101: *The energy changes are different in the source (S) and absorber (A) as a result of different electron densities at the source and absorber nuclei, the result is manifested as isomer shift in the Mössbauer spectrum.*[247]

^{57}Fe Mössbauer spectra were collected using 20-30 mg/cm² powder. The spectrometer is operated in the constant acceleration mode and in transmission geometry. A ^{57}Co(Rh) source with a nominal activity of 370 MBq was used. The source and the absorber were always kept at 295 K. All the isomer shifts are given relative to α-Fe standard at 295 K.

7.3.4 Scanning- and transmission electron microscopy

High Resolution transmission electron microscopy (TEM) and scanning transmission electron microscopy (STEM) was done in collaboration with two different persons. In both cases samples for TEM was prepared by grinding the material in an agate mortar and dipping a Cu holey carbon TEM grid into the powder. The microscope was equipped with a high brightness source X-FEG Schottky and a Cs probe corrector (DCOR). The chemical mapping EDS is acquired with Super-X detector system based on 4 windowless Silicon Drift Detector (SDD), which enhanced acquisition efficiency and spatial resolution. All observations were performed at 200 kV on nickel TEM grids with carbon films (300 mesh).

Further TEM data (SAED patterns, STEM-EDX elemental maps and the HRTEM images) were acquired on an *FEI Osiris* microscope operated at 200 kV and equipped with a Super-X EDX detector. In this case a special *Gatan* vacuum transfer holder was used for the analysis.

7.3.5 Density functional theory calculations

Spin-polarized DFT+U calculations were performed using the VASP code (Vienna Ab initio Simulation Package)[248,249] and using the rotationally invariant Dudarev method[250] and the generalized gradient approximation with PBE functional to describe electron exchange and correlation.[251] The effective Hubbard corrections were taken from the literature for the copper d-electrons (U_{eff}=4.0 eV).[252] A plane-wave cut-off of 600 eV was used to define the basis set, with well-converged k-point sampling for each compound. The COOPs were computed using the Lobster program developed by Dronskowski and coworkers.[253–255]

7.3.6 Bond valence energy landscape calculations

The Bond Valence Energy Landscape (BVEL) method allows the calculation and visualization of ion diffusion pathways of a mobile species in a 3D framework and is often applied for identifying potentially interesting ionic conductors. The BVEL method is based on the Bond Valence Sum (BVS) approach, which calculates the oxidation state of an atom as a function of the distances to its neighboring atoms and their oxidation state, and is an extension of the Bond Valence Sum Maps (BVSM). To determine the possible ion transport pathways in a structure, the theoretical oxidation state of the mobile ion is calculated as a function of a position in the structure, where positions with a low valence mismatch (low deviation from the ideal oxidation state ~10%) are regarded as part of the diffusion pathway. In contrast to the BVS approach, the BVEL calculations transform the valence units (v.u.) given for the BVS into energy units (eV). Furthermore, soft bond valence (softBV) parameters are applied, which allow to take into account the polarizability of the mobile species as well as the influence of the counterions on the ion mobility. Further included in the BVEL calculations is the cut-off length to the surrounding coordination spheres, which in our case is set to 8 Å.[183,256]

BVEL calculations are performed by the BondStr software as implemented in the Fullprof suite.[242] The program calculates the isosurfaces in the structure, which are accessible for the mobile ion and which must be infinitely connected in at least one direction to permit diffusion through the structure. From the difference of the calculated minimum energy isosurface and the minimum energy value inside this isosurface, we obtain the “activation energy” necessary for the ion diffusion in this structure. The isosurface can be visualized with the VESTA program.

8 References

(1) Annual Energy Outlook 2015 - 0383(**2015**).pdf.

(2) CO_2 Emissions From Fuel Combustion Highlights 2015 - CO_2 Emissions From Fuel CombustionHighlights2015.pdf https://www.iea.org/publications/freepublications/publication/CO_2EmissionsFromFuelCombustionHighlights2015.pdf (accessed Apr 25, **2016**).

(3) Energy and Climate Change - World Energy Outlook Special Report - WEO2015SpecialReportonEnergyandClimateChange.pdf.

(4) Thesis_JGL_final.doc - MSThesis_JGLevine_final.pdf http://www.colorado.edu/engineering/energystorage/files/MSThesis_JGLevine_final.pdf (accessed Apr 25, 2016).

(5) Dunn, B.; Kamath, H.; Tarascon, J.-M. Electrical Energy Storage for the Grid: A Battery of Choices. *Science* **2011**, *334* (6058), 928–935.

(6) Tran, M.; Banister, D.; Bishop, J. D. K.; McCulloch, M. D. Realizing the Electric-Vehicle Revolution. *Nat. Clim. Change* **2012**, *2* (5), 328–333.

(7) Toyota Unveils 2015 Fuel Cell Sedan, Will Retail in Japan For Around ¥7 Million | Transport Evolved http://transportevolved.com/2014/06/25/toyota-unveils-2015-fuel-cell-sedan-will-retail-japan-around-%C2%A57-million/ (accessed Apr 25, 2016).

(8) Gröger, O.; Gasteiger, H. A.; Suchsland, J.-P. Review—Electromobility: Batteries or Fuel Cells? *J. Electrochem. Soc.* **2015**, *162* (14), A2605–A2622.

(9) gigafactory.pdf https://www.teslamotors.com/sites/default/files/blog_attachments/gigafactory.pdf (accessed Apr 25, **2016**).

(10) electro-mobility-report,property=pdf,bereich=bmwi2012,sprache=en,rwb=true.pdf http://www.bmwi.de/English/Redaktion/Pdf/electro-mobility-report,property=pdf,bereich=bmwi2012,sprache=en,rwb=true.pdf (accessed Apr 25, 2016).

(11) Larcher, D.; Tarascon, J.-M. Towards Greener and More Sustainable Batteries for Electrical Energy Storage. *Nat. Chem.* **2014**, *7* (1), 19–29.

(12) Tarascon, J.-M. Key Challenges in Future Li-Battery Research. *Philos. Trans. R. Soc. Math. Phys. Eng. Sci.* **2010**, *368* (1923), 3227–3241.

(13) Volta, A. On the Electricity Excited by the Mere Contact of Conducting Substances of Different Kinds. In a Letter from Mr. Alexander Volta, F. R. S. Professor of Natural Philosophy in the University of Pavia, to the Rt. Hon. Sir Joseph Banks, Bart. K. B. P. R. S. *Philos. Trans. R. Soc. Lond.* **1800**, *90*, 403–431.

(14) Goodenough, J. B.; Park, K.-S. The Li-Ion Rechargeable Battery: A Perspective. *J. Am. Chem. Soc.* **2013**, *135* (4), 1167–1176.

(15) Palacín, M. R. Recent Advances in Rechargeable Battery Materials: A Chemist's Perspective. *Chem. Soc. Rev.* **2009**, *38* (9), 2565.

(16) Tarascon, J.-M.; Armand, M. Issues and Challenges Facing Rechargeable Lithium Batteries. *Nature* **2001**, *414* (6861), 359–367.

(17) Murphy, D. W.; Trumbore, F. A. Metal Chalcogenides as Reversible Electrodes in Nonaqueous Lithium Batteries. *J. Cryst. Growth* **1977**, *39* (1), 185–199.

(18) The lithium intercalates of the transition metal dichalcogenides http://www.sciencedirect.com/science/article/pii/0025540875900069 (accessed Jan 12, 2016).

(19) Murphy, D. W.; Christian, P. A. Solid State Electrodes for High Energy Batteries. *Science* **1979**, *205* (4407), 651–656.

(20) Whittingham, M. S. Electrical Energy Storage and Intercalation Chemistry. *Science* **1976**, *192* (4244), 1126–1127.

(21) Mizushima, K.; Jones, P. C.; Wiseman, P. J.; Goodenough, J. B. Li_xCoO_2. *Mater. Res. Bull.* **1980**, *15* (6), 783–789.

(22) Thackeray, M. M.; David, W. I. F.; Bruce, P. G.; Goodenough, J. B. Lithium Insertion into Manganese Spinels. *Mater. Res. Bull.* **1983**, *18* (4), 461–472.

(23) Rao, B. M. L.; Francis, R. W.; Christopher, H. A. Lithium-Aluminum Electrode. *J. Electrochem. Soc.* **1977**, *124* (10), 1490–1492.

(24) Murphy, D. W.; Di Salvo, F. J.; Carides, J. N.; Waszczak, J. V. Topochemical Reactions of Rutile Related Structures with Lithium. *Mater. Res. Bull.* **1978**, *13* (12), 1395–1402.

(25) Lazzari, M.; Scrosati, B. A Cyclable Lithium Organic Electrolyte Cell Based on Two Intercalation Electrodes. *J. Electrochem. Soc.* **1980**, *127* (3), 773–774.

(26) Mohri, M.; Yanagisawa, N.; Tajima, Y.; Tanaka, H.; Mitate, T.; Nakajima, S.; Yoshida, M.; Yoshimoto, Y.; Suzuki, T.; Wada, H. Rechargeable Lithium Battery Based on Pyrolytic Carbon as a Negative Electrode. *J. Power Sources* **1989**, *26* (3–4), 545–551.

(27) Ambient Temperature Rechargeable Battery.

(28) T. Nagaura, K. T. Lithium-Ion Rechargeable Battery. *Prog. Batter. Amp Sol. Cells* **1990**.

(29) Whittingham, M. S. Chemistry of Intercalation Compounds: Metal Guests in Chalcogenide Hosts. *Prog. Solid State Chem.* **1978**, *12* (1), 41–99.

(30) Hong, S. Y.; Kim, Y.; Park, Y.; Choi, A.; Choi, N.-S.; Lee, K. T. Charge Carriers in Rechargeable Batteries: Na Ions vs. Li Ions. *Energy Environ. Sci.* **2013**, *6* (7), 2067.

(31) Kubota, K.; Komaba, S. Review—Practical Issues and Future Perspective for Na-Ion Batteries. *J. Electrochem. Soc.* **2015**, *162* (14), A2538–A2550.

(32) Kundu, D.; Talaie, E.; Duffort, V.; Nazar, L. F. The Emerging Chemistry of Sodium Ion Batteries for Electrochemical Energy Storage. *Angew. Chem. Int. Ed.* **2015**, *54* (11), 3431–3448.

(33) Palomares, V.; Casas-Cabanas, M.; Castillo-Martínez, E.; Han, M. H.; Rojo, T. Update on Na-Based Battery Materials. A Growing Research Path. *Energy Environ. Sci.* **2013**, *6* (8), 2312.

(34) Pan, H.; Hu, Y.-S.; Chen, L. Room-Temperature Stationary Sodium-Ion Batteries for Large-Scale Electric Energy Storage. *Energy Environ. Sci.* **2013**, *6* (8), 2338.

(35) Amatucci, G. G.; Tarascon, J. M.; Klein, L. C. CoO_2, The End Member of the Li_xCoO_2 Solid Solution. *J. Electrochem. Soc.* **1996**, *143* (3), 1114–1123.

(36) Lee, K. T.; Jeong, S.; Cho, J. Roles of Surface Chemistry on Safety and Electrochemistry in Lithium Ion Batteries. *Acc. Chem. Res.* **2013**, *46* (5), 1161–1170.

(37) MRS Bulletin - Layered $Li(Ni,M)O_2$ Systems as the Cathode Material in Lithium-Ion Batteries - Cambridge Journals Online http://journals.cambridge.org.accesdistant.upmc.fr/action/displayAbstract?fromPage=online&aid=7965397&fulltextType=RA&fileId=S0883769400021722 (accessed Jan 25, **2016**).

(38) Delmas, C.; Fouassier, C.; Hagenmuller, P. Structural Classification and Properties of the Layered Oxides. *Phys. BC* **1980**, *99* (1–4), 81–85.

(39) Fouassier, C.; Delmas, C.; Hagenmuller, P. Evolution Structurale et Proprietes Physiques Des Phases A_xMO_2 (A = Na, K; M = Cr, Mn, Co) ($X \leqslant 1$). *Mater. Res. Bull.* **1975**, *10* (6), 443–449.

(40) Yabuuchi, N.; Hara, R.; Kajiyama, M.; Kubota, K.; Ishigaki, T.; Hoshikawa, A.; Komaba, S. New O2/P2-Type Li-Excess Layered Manganese Oxides as Promising

Multi-Functional Electrode Materials for Rechargeable Li/Na Batteries. *Adv. Energy Mater.* **2014**, *4* (13), n/a-n/a.

(41) Han, M. H.; Gonzalo, E.; Singh, G.; Rojo, T. A Comprehensive Review of Sodium Layered Oxides: Powerful Cathodes for Na-Ion Batteries. *Energy Env. Sci* **2015**, *8* (1), 81–102.

(42) Berthelot, R.; Carlier, D.; Delmas, C. Electrochemical Investigation of the P2–NaxCoO2 Phase Diagram. *Nat. Mater.* **2011**, *10* (1), 74–80.

(43) Lei, Y.; Li, X.; Liu, L.; Ceder, G. Synthesis and Stoichiometry of Different Layered Sodium Cobalt Oxides. *Chem. Mater.* **2014**, *26* (18), 5288–5296.

(44) Clément, R. J.; Bruce, P. G.; Grey, C. P. Review—Manganese-Based P2-Type Transition Metal Oxides as Sodium-Ion Battery Cathode Materials. *J. Electrochem. Soc.* **2015**, *162* (14), A2589–A2604.

(45) Yabuuchi, N.; Kajiyama, M.; Iwatate, J.; Nishikawa, H.; Hitomi, S.; Okuyama, R.; Usui, R.; Yamada, Y.; Komaba, S. P2-Type $Na_x[Fe_{1/2}Mn_{1/2}]O_2$ Made from Earth-Abundant Elements for Rechargeable Na Batteries. *Nat. Mater.* **2012**, *11* (6), 512–517.

(46) Capitaine, F.; Gravereau, P.; Delmas, C. A New Variety of $LiMnO_2$ with a Layered Structure. *Solid State Ion.* **1996**, *89* (3–4), 197–202.

(47) Armstrong, A. R.; Bruce, P. G. Synthesis of Layered $LiMnO_2$ as an Electrode for Rechargeable Lithium Batteries. *Nature* **1996**, *381* (6582), 499–500.

(48) Tarascon, J. M.; Wang, E.; Shokoohi, F. K.; McKinnon, W. R.; Colson, S. The Spinel Phase of $LiMn_2O_4$ as a Cathode in Secondary Lithium Cells. *J. Electrochem. Soc.* **1991**, *138* (10), 2859–2864.

(49) Tarascon, J. M.; McKinnon, W. R.; Coowar, F.; Bowmer, T. N.; Amatucci, G.; Guyomard, D. Synthesis Conditions and Oxygen Stoichiometry Effects on Li Insertion into the Spinel $LiMn_2O_4$. *J. Electrochem. Soc.* **1994**, *141* (6), 1421–1431.

(50) Thackeray, M. M. Manganese Oxides for Lithium Batteries. *Prog. Solid State Chem.* **1997**, *25* (1–2), 1–71.

(51) Amatucci, G.; Tarascon, J.-M. Optimization of Insertion Compounds Such as LiMn2 O 4 for Li-Ion Batteries. *J. Electrochem. Soc.* **2002**, *149* (12), K31–K46.

(52) Tarascon, J. M.; Guyomard, D. Li Metal-Free Rechargeable Batteries Based on $Li_{1+x}Mn_2O_4$ Cathodes ($0 \leq X \leq 1$) and Carbon Anodes. *J. Electrochem. Soc.* **1991**, *138* (10), 2864–2868.

(53) Amatucci, G. G.; Pereira, N.; Zheng, T.; Plitz, I.; Tarascon, J. M. Enhancement of the Electrochemical Properties of Li1Mn2O4 through Chemical Substitution. *J. Power Sources* **1999**, *81–82*, 39–43.

(54) Numata, T.; Amemiya, C.; Kumeuchi, T.; Shirakata, M.; Yonezawa, M. Advantages of Blending $LiNi_{0.8}Co_{0.2}O_2$ into $Li_{1+x}Mn_{2-x}O_4$ Cathodes. *J. Power Sources* **2001**, *97–98*, 358–360.

(55) Boulineau, A.; Croguennec, L.; Delmas, C.; Weill, F. Reinvestigation of Li_2MnO_3 Structure: Electron Diffraction and High Resolution TEM. *Chem. Mater.* **2009**, *21* (18), 4216–4222.

(56) Strobel, P.; Lambert-Andron, B. Crystallographic and Magnetic Structure of Li_2MnO_3. *J. Solid State Chem.* **1988**, *75* (1), 90–98.

(57) Rossouw, M.; Thackeray, M. Lithium Manganese Oxides from Li_2MnO_3 for Rechargeable Lithium Battery Applications. *Mater. Res. Bull.* **1991**, *26* (6), 463–473.

(58) Kalyani, P.; Chitra, S.; Mohan, T.; Gopukumar, S. Lithium Metal Rechargeable Cells Using Li_2MnO_3 as the Positive Electrode. *J. Power Sources* **1999**, *80* (1–2), 103–106.

(59) Sathiya, M.; Rousse, G.; Ramesha, K.; Laisa, C. P.; Vezin, H.; Sougrati, M. T.; Doublet, M.-L.; Foix, D.; Gonbeau, D.; Walker, W.; Prakash, A. S.; Ben Hassine, M.; Dupont, L.; Tarascon, J.-M. Reversible Anionic Redox Chemistry in High-Capacity Layered-Oxide Electrodes. *Nat. Mater.* **2013**, *12* (9), 827–835.

(60) Rozier, P.; Sathiya, M.; Paulraj, A.-R.; Foix, D.; Desaunay, T.; Taberna, P.-L.; Simon, P.; Tarascon, J.-M. Anionic Redox Chemistry in Na-Rich $Na_2Ru_{1-y}Sn_yO_3$ Positive Electrode Material for Na-Ion Batteries. *Electrochem. Commun.* **2015**, *53*, 29–32.

(61) McCalla, E.; Abakumov, A. M.; Saubanère, M.; Foix, D.; Berg, E. J.; Rousse, G.; Doublet, M.-L.; Gonbeau, D.; Novák, P.; Tendeloo, G. V.; Dominko, R.; Tarascon, J.-M. Visualization of O-O Peroxo-like Dimers in High-Capacity Layered Oxides for Li-Ion Batteries. *Science* **2015**, *350* (6267), 1516–1521.

(62) Thackeray, M. M.; Johnson, C. S.; Vaughey, J. T.; Li, N.; Hackney, S. A. Advances in Manganese-Oxide "composite" Electrodes for Lithium-Ion Batteries. *J. Mater. Chem.* **2005**, *15* (23), 2257–2267.

(63) Padhi, A. K.; Nanjundaswamy, K. S.; Goodenough, J. B. Phospho-olivines as Positive-Electrode Materials for Rechargeable Lithium Batteries. *J. Electrochem. Soc.* **1997**, *144* (4), 1188–1194.

(64) Padhi, A. K.; Manivannan, V.; Goodenough, J. B. Tuning the Position of the Redox Couples in Materials with NASICON Structure by Anionic Substitution. *J. Electrochem. Soc.* **1998**, *145* (5), 1518–1520.

(65) Padhi, A. K.; Nanjundaswamy, K. S.; Masquelier, C.; Okada, S.; Goodenough, J. B. Effect of Structure on the Fe^{3+}/Fe^{2+} Redox Couple in Iron Phosphates. *J. Electrochem. Soc.* **1997**, *144* (5), 1609–1613.

(66) Reiff, W. M.; Zhang, J. H.; Torardi, C. C. Topochemical Lithium Insertion into Fe2(MoO4)3: Structure and Magnetism of $Li_2Fe_2(MoO_4)_3$. *J. Solid State Chem.* **1986**, *62* (2), 231–240.

(67) Nadiri, A.; Delmas, C.; Salmon, R.; Hagenmuller, P. Chemical and Electrochemical Alkali Metal Intercalation in the 3D-Framework of $Fe_2(MoO_4)_3$. *Rev. Chim. Minérale* **1984**, *21* (4), 537–544.

(68) Weppner, W.; Schulz, H.; Delmas, C.; Nadiri, A.; Soubeyroux, J. L. Proceedings of the 6th International Conference on Solid State IonicsThe Nasicon-Type Titanium Phosphates $ATi_2(PO_4)_3$ (A=Li, Na) as Electrode Materials. *Solid State Ion.* **1988**, *28*, 419–423.

(69) Manthiram, A.; Goodenough, J. B. Lithium Insertion into $Fe_2(MO_4)_3$ Frameworks: Comparison of M = W with M = Mo. *J. Solid State Chem.* **1987**, *71* (2), 349–360.

(70) Manthiram, A.; Goodenough, J. B. Lithium Insertion into $Fe_2(SO_4)_3$ Frameworks. *J. Power Sources* **1989**, *26* (3–4), 403–408.

(71) Goodenough, J. B.; Kim, Y. Challenges for Rechargeable Li Batteries †. *Chem. Mater.* **2010**, *22* (3), 587–603.

(72) Masquelier, C.; Padhi, A. K.; Nanjundaswamy, K. S.; Goodenough, J. B. New Cathode Materials for Rechargeable Lithium Batteries: The 3-D Framework Structures $Li_3Fe_2(XO_4)_3$ (X=P, As). *J. Solid State Chem.* **1998**, *135* (2), 228–234.

(73) Ravet, N.; Chouinard, Y.; Magnan, J. F.; Besner, S.; Gauthier, M.; Armand, M. Electroactivity of Natural and Synthetic Triphylite. *J. Power Sources* **2001**, *97–98*, 503–507.

(74) Wang, Y.; Wang, Y.; Hosono, E.; Wang, K.; Zhou, H. The Design of a LiFePO4/Carbon Nanocomposite With a Core–Shell Structure and Its Synthesis by an In Situ Polymerization Restriction Method. *Angew. Chem. Int. Ed.* **2008**, *47* (39), 7461–7465.

(75) Huang, H.; Yin, S.-C.; Nazar, L. F. Approaching Theoretical Capacity of LiFePO4 at Room Temperature at High Rates. *Electrochem. Solid-State Lett.* **2001**, *4* (10), A170–A172.

(76) Lithium Ion Cells | Cylindrical Cells | 26650 Lithium Cells http://www.a123systems.com/lithium-ion-cells-26650-cylindrical-cell.htm (accessed Jan 26, **2016**).

(77) Brutti, S.; Panero, S. Recent Advances in the Development of $LiCoPO_4$ as High Voltage Cathode Material for Li-Ion Batteries. In *Nanotechnology for Sustainable Energy*; Hu, Y. H., Burghaus, U., Qiao, S., Eds.; American Chemical Society, Series Ed.; American Chemical Society: Washington, DC, 2013; Vol. 1140, pp 67–99.

(78) Ellis, B. L.; Makahnouk, W. R. M.; Makimura, Y.; Toghill, K.; Nazar, L. F. A Multifunctional 3.5 V Iron-Based Phosphate Cathode for Rechargeable Batteries. *Nat. Mater.* **2007**, *6* (10), 749–753.

(79) Zhu, Y.; Xu, Y.; Liu, Y.; Luo, C.; Wang, C. Comparison of Electrochemical Performances of Olivine $NaFePO_4$ in Sodium-Ion Batteries and Olivine $LiFePO_4$ in Lithium-Ion Batteries. *Nanoscale* **2013**, *5* (2), 780–787.

(80) Oh, S.-M.; Myung, S.-T.; Hassoun, J.; Scrosati, B.; Sun, Y.-K. Reversible $NaFePO_4$ Electrode for Sodium Secondary Batteries. *Electrochem. Commun.* **2012**, *22*, 149–152.

(81) Moreau, P.; Guyomard, D.; Gaubicher, J.; Boucher, F. Structure and Stability of Sodium Intercalated Phases in Olivine $FePO_4$. *Chem. Mater.* **2010**, *22* (14), 4126–4128.

(82) Wurm, C.; Morcrette, M.; Rousse, G.; Dupont, L.; Masquelier, C. Lithium Insertion/Extraction Into/From $LiMX_2O_7$ Compositions (M = Fe, V; X = P, As) Prepared via a Solution Method. *Chem. Mater.* **2002**, *14* (6), 2701–2710.

(83) Cathode properties of pyrophosphates for rechargeable lithium batteries http://www.sciencedirect.com.accesdistant.upmc.fr/science/article/pii/S0167273802000693 (accessed Jan 27, **2016**).

(84) Ramana, C. V.; Ait-Salah, A.; Utsunomiya, S.; Mauger, A.; Gendron, F.; Julien, C. M. Novel Lithium Iron Pyrophosphate ($LiFe_{1.5}P_2O_7$) as a Positive Electrode for Li-Ion Batteries. *Chem. Mater.* **2007**, *19* (22), 5319–5324.

(85) Adam, L.; Guesdon, A.; Raveau, B. A New Lithium Manganese Phosphate with an Original Tunnel Structure in the $A_2MP_2O_7$ Family. *J. Solid State Chem.* **2008**, *181* (11), 3110–3115.

(86) Nishimura, S.; Nakamura, M.; Natsui, R.; Yamada, A. New Lithium Iron Pyrophosphate as 3.5 V Class Cathode Material for Lithium Ion Battery. *J. Am. Chem. Soc.* **2010**, *132* (39), 13596–13597.

(87) Nishimura, S.; Natsui, R.; Yamada, A. A New Polymorph of Lithium manganese(II) Pyrophosphate β-$Li_2MnP_2O_7$. *Dalton Trans.* **2013**, *43* (4), 1502–1504.

(88) Barpanda, P.; Lu, J.; Ye, T.; Kajiyama, M.; Chung, S.-C.; Yabuuchi, N.; Komaba, S.; Yamada, A. A Layer-Structured $Na_2CoP_2O_7$ Pyrophosphate Cathode for Sodium-Ion Batteries. *RSC Adv.* **2013**, *3* (12), 3857.

(89) Kim, H.; Shakoor, R. A.; Park, C.; Lim, S. Y.; Kim, J.-S.; Jo, Y. N.; Cho, W.; Miyasaka, K.; Kahraman, R.; Jung, Y.; Choi, J. W. $Na_2FeP_2O_7$ as a Promising Iron-Based Pyrophosphate Cathode for Sodium Rechargeable Batteries: A Combined Experimental and Theoretical Study. *Adv. Funct. Mater.* **2013**, *23* (9), 1147–1155.

(90) Barpanda, P.; Liu, G.; Ling, C. D.; Tamaru, M.; Avdeev, M.; Chung, S.-C.; Yamada, Y.; Yamada, A. $Na_2FeP_2O_7$: A Safe Cathode for Rechargeable Sodium-Ion Batteries. *Chem. Mater.* **2013**, *25* (17), 3480–3487.

(91) Chen, C.-Y.; Matsumoto, K.; Nohira, T.; Hagiwara, R.; Orikasa, Y.; Uchimoto, Y. Pyrophosphate $Na_2FeP_2O_7$ as a Low-Cost and High-Performance Positive Electrode Material for Sodium Secondary Batteries Utilizing an Inorganic Ionic Liquid. *J. Power Sources* **2014**, *246*, 783–787.

(92) Barpanda, P.; Ye, T.; Nishimura, S.; Chung, S.-C.; Yamada, Y.; Okubo, M.; Zhou, H.; Yamada, A. Sodium Iron Pyrophosphate: A Novel 3.0V Iron-Based Cathode for Sodium-Ion Batteries. *Electrochem. Commun.* **2012**, *24*, 116–119.

(93) Barpanda, P.; Ye, T.; Avdeev, M.; Chung, S.-C.; Yamada, A. A New Polymorph of $Na_2MnP_2O_7$ as a 3.6 V Cathode Material for Sodium-Ion Batteries. *J. Mater. Chem. A* **2013**, *1* (13), 4194.

(94) Tamaru, M.; Barpanda, P.; Yamada, Y.; Nishimura, S.; Yamada, A. Observation of the Highest Mn3+/Mn2+ Redox Potential of 4.45 V in a $Li_2MnP_2O_7$ Pyrophosphate Cathode. *J. Mater. Chem.* **2012**, *22* (47), 24526.

(95) EP 1134826 B1 20080806 - New lithium insertion electrode materials based on orthosilicate derivatives https://data.epo.org/gpi/EP1134826B1-New-lithium-insertion-electrode-materials-based-on-orthosilicate-derivatives (accessed Jan 26, **2016**).

(96) Islam, M. S.; Dominko, R.; Masquelier, C.; Sirisopanaporn, C.; Armstrong, A. R.; Bruce, P. G. Silicate Cathodes for Lithium Batteries: Alternatives to Phosphates? *J. Mater. Chem.* **2011**, *21* (27), 9811–9818.

(97) Sirisopanaporn, C.; Masquelier, C.; Bruce, P. G.; Armstrong, A. R.; Dominko, R. Dependence of Li_2FeSiO_4 Electrochemistry on Structure. *J. Am. Chem. Soc.* **2011**, *133* (5), 1263–1265.

(98) Nishimura, S.; Hayase, S.; Kanno, R.; Yashima, M.; Nakayama, N.; Yamada, A. Structure of Li_2FeSiO_4. *J. Am. Chem. Soc.* **2008**, *130* (40), 13212–13213.

(99) Saracibar, A.; Van der Ven, A.; Arroyo-de Dompablo, M. E. Crystal Structure, Energetics, And Electrochemistry of Li_2FeSiO_4 Polymorphs from First Principles Calculations. *Chem. Mater.* **2012**, *24* (3), 495–503.

(100) Dominko, R. Li_2MSiO_4 (M = Fe And/Or Mn) Cathode Materials. *J. Power Sources* **2008**, *184* (2), 462–468.

(101) Dominko, R.; Conte, D. E.; Hanzel, D.; Gaberscek, M.; Jamnik, J. Impact of Synthesis Conditions on the Structure and Performance of Li2FeSiO4. *J. Power Sources* **2008**, *178* (2), 842–847.

(102) Gong, Z. L.; Li, Y. X.; He, G. N.; Li, J.; Yang, Y. Nanostructured Li_2FeSiO_4 Electrode Material Synthesized through Hydrothermal-Assisted Sol-Gel Process. *Electrochem. Solid-State Lett.* **2008**, *11* (5), A60–A63.

(103) Muraliganth, T.; Stroukoff, K. R.; Manthiram, A. Microwave-Solvothermal Synthesis of Nanostructured Li_2MSiO_4/C (M = Mn and Fe) Cathodes for Lithium-Ion Batteries. *Chem. Mater.* **2010**, *22* (20), 5754–5761.

(104) Dominko, R.; Sirisopanaporn, C.; Masquelier, C.; Hanzel, D.; Arcon, I.; Gaberscek, M. On the Origin of the Electrochemical Capacity of $Li_2Fe_{0.8}Mn_{0.2}SiO_4$. *J. Electrochem. Soc.* **2010**, *157* (12), A1309–A1316.

(105) Sebastian, L.; Gopalakrishnan, J.; Piffard, Y. Synthesis, Crystal Structure and Lithium Ion Conductivity of $LiMgFSO_4$. *J. Mater. Chem.* **2002**, *12* (2), 374–377.

(106) Recham, N.; Chotard, J.-N.; Dupont, L.; Delacourt, C.; Walker, W.; Armand, M.; Tarascon, J.-M. A 3.6 V Lithium-Based Fluorosulphate Insertion Positive Electrode for Lithium-Ion Batteries. *Nat. Mater.* **2010**, *9* (1), 68–74.

(107) Rousse, G.; Tarascon, J. M. Sulfate-Based Polyanionic Compounds for Li-Ion Batteries: Synthesis, Crystal Chemistry, and Electrochemistry Aspects. *Chem. Mater.* **2014**, *26* (1), 394–406.

(108) Zhang, L.; Tarascon, J.-M.; Sougrati, M. T.; Rousse, G.; Chen, G. Influence of Relative Humidity on the Structure and Electrochemical Performance of Sustainable $LiFeSO_4F$ Electrodes for Li-Ion Batteries. *J. Mater. Chem. A* **2015**, *3* (33), 16988–16997.

(109) Barpanda, P.; Ati, M.; Recham, N.; Chotard, J.-N.; Walker, W.; Armand, M.; Tarascon, J.-M. Crystal Structure and Electrochemical Study of $A(Fe_{1-x}M_x)SO_4F$ (A = Li/Na; M = Co/Ni/Mn) Fluorosulfates Prepared by Low Temperature Ionothermal Synthesis. *ECS Trans.* **2010**, *28* (31), 1–9.

(110) Barpanda, P.; Chotard, J.-N.; Recham, N.; Delacourt, C.; Ati, M.; Dupont, L.; Armand, M.; Tarascon, J.-M. Structural, Transport, and Electrochemical Investigation of Novel $AMSO_4F$ (A = Na, Li; M = Fe, Co, Ni, Mn) Metal Fluorosulphates Prepared Using Low Temperature Synthesis Routes. *Inorg. Chem.* **2010**, *49* (16), 7401–7413.

(111) Barpanda, P.; Ati, M.; Melot, B. C.; Rousse, G.; Chotard, J.-N.; Doublet, M.-L.; Sougrati, M. T.; Corr, S. A.; Jumas, J.-C.; Tarascon, J.-M. A 3.90 V Iron-Based Fluorosulphate Material for Lithium-Ion Batteries Crystallizing in the Triplite Structure. *Nat. Mater.* **2011**, *10* (10), 772–779.

(112) Ati, M.; Melot, B. C.; Chotard, J.-N.; Rousse, G.; Reynaud, M.; Tarascon, J.-M. Synthesis and Electrochemical Properties of Pure $LiFeSO_4F$ in the Triplite Structure. *Electrochem. Commun.* **2011**, *13* (11), 1280–1283.

(113) Ati, M.; Sougrati, M.-T.; Rousse, G.; Recham, N.; Doublet, M.-L.; Jumas, J.-C.; Tarascon, J.-M. Single-Step Synthesis of $FeSO_4F_{1-Y}OH_Y$ ($0 \leq Y \leq 1$) Positive Electrodes for Li-Based Batteries. *Chem. Mater.* **2012**, *24* (8), 1472–1485.

(114) Subban, C. V.; Ati, M.; Rousse, G.; Abakumov, A. M.; Van Tendeloo, G.; Janot, R.; Tarascon, J.-M. Preparation, Structure, and Electrochemistry of Layered Polyanionic Hydroxysulfates: $LiMSO_4OH$ (M = Fe, Co, Mn) Electrodes for Li-Ion Batteries. *J. Am. Chem. Soc.* **2013**, *135* (9), 3653–3661.

(115) Brodd, R. J.; Bullock, K. R.; Leising, R. A.; Middaugh, R. L.; Miller, J. R.; Takeuchi, E. Batteries, 1977 to 2002. *J. Electrochem. Soc.* **2004**, *151* (3), K1.

(116) Zeitschrift für Naturforschung / B / 33 (1978) - ZNB-1978-33b-0279.pdf http://zfn.mpdl.mpg.de/data/Reihe_B/33/ZNB-1978-33b-0279.pdf (accessed Nov 2, **2015**).

(117) Poizot, P.; Laruelle, S.; Grugeon, S.; Dupont, L.; Tarascon, J.-M. Nano-Sized Transition-Metal Oxides as Negative-Electrode Materials for Lithium-Ion Batteries. *Nature* **2000**, *407* (6803), 496–499.

(118) Débart, A.; Dupont, L.; Patrice, R.; Tarascon, J.-M. Reactivity of Transition Metal (Co, Ni, Cu) Sulphides versus Lithium: The Intriguing Case of the Copper Sulphide. *Solid State Sci.* **2006**, *8* (6), 640–651.

(119) Pereira, N.; Dupont, L.; Tarascon, J. M.; Klein, L. C.; Amatucci, G. G. Electrochemistry of Cu[sub 3]N with Lithium. *J. Electrochem. Soc.* **2003**, *150* (9), A1273.

(120) Badway, F.; Pereira, N.; Cosandey, F.; Amatucci, G. G. Carbon-Metal Fluoride Nanocomposites. *J. Electrochem. Soc.* **2003**, *150* (9), A1209.

(121) Bervas, M.; Badway, F.; Klein, L. C.; Amatucci, G. G. Bismuth Fluoride Nanocomposite as a Positive Electrode Material for Rechargeable Lithium Batteries. *Electrochem. Solid-State Lett.* **2005**, *8* (4), A179.

(122) Badway, F.; Cosandey, F.; Pereira, N.; Amatucci, G. G. Carbon Metal Fluoride Nanocomposites. *J. Electrochem. Soc.* **2003**, *150* (10), A1318.

(123) Li, L.; Jacobs, R.; Gao, P.; Gan, L.; Wang, F.; Morgan, D.; Jin, S. Origins of Large Voltage Hysteresis in High-Energy-Density Metal Fluoride Lithium-Ion Battery Conversion Electrodes. *J. Am. Chem. Soc.* **2016**, *138* (8), 2838–2848.

(124) Nitta, N.; Wu, F.; Lee, J. T.; Yushin, G. Li-Ion Battery Materials: Present and Future. *Mater. Today* **2015**, *18* (5), 252–264.

(125) Bervas, M.; Mansour, A. N.; Yoon, W.-S.; Al-Sharab, J. F.; Badway, F.; Cosandey, F.; Klein, L. C.; Amatucci, G. G. Investigation of the Lithiation and Delithiation Conversion Mechanisms of Bismuth Fluoride Nanocomposites. *J. Electrochem. Soc.* **2006**, *153* (4), A799.

(126) Bervas, M.; Klein, L. C.; Amatucci, G. G. Reversible Conversion Reactions with Lithium in Bismuth Oxyfluoride Nanocomposites. *J. Electrochem. Soc.* **2006**, *153* (1), A159.

(127) Briggs, M. Boron Oxides, Boric Acid, and Borates. *Kirk-Othmer Encycl. Chem. Technol.* **2001**.

(128) Pye, L. D.; Fréchette, V. D.; Kreidl, N. J. *Borate Glasses: Structure, Properties, Applications*; Springer Science & Business Media, 2012.

(129) D, E. Structure, Properties and Applications of Borate Glasses. *Eur. J. Glass Sci. Technol. Part Glass Technol.* **2000**, *41* (6), 182–185.

(130) Chen, C.; Wu, B.; Jiang, A.; You, G. A New-Type Ultraviolet SHG Crystal - Beta-BaB2O4. *Sci China Ser B* **1985**, *28*, 235–243.

(131) Chen, C.; Wu, Y.; Jiang, A.; Wu, B.; You, G.; Li, R.; Lin, S. New Nonlinear-Optical Crystal: LiB_3O_5. *J. Opt. Soc. Am. B* **1989**, *6* (4), 616.

(132) Becker, P. Borate Materials in Nonlinear Optics. *Adv. Mater.* **1998**, *10* (13), 979–992.

(133) Keszler, D. A. Synthesis, Crystal Chemistry, and Optical Properties of Metal Borates. *Curr. Opin. Solid State Mater. Sci.* **1999**, *4* (2), 155–162.

(134) Christ, C. L.; Clark, J. R. A Crystal-Chemical Classification of Borate Structures with Emphasis on Hydrated Borates. *Phys. Chem. Miner.* **1977**, *2* (1–2), 5987.

(135) Piffard, Y.; Rangan, K. K.; An, Y.; Guyomard, D.; Tournoux, M. Cobalt Lithium Orthoborate, $LiCoBO_3$. *Acta Crystallogr. Sect. C* **1998**, *54* (11), 1561–1563.

(136) Belkebir, A.; Tarte, P.; Rulmont, A.; Gilbert, B. ChemInform Abstract: Synthesis, Structural and Vibrational Analysis of $LiMBO_3$ Orthoborates (M: Mg, Co, Zn). *ChemInform* **2010**, *27* (28), no-no.

(137) Crystal Structure of $LiCd(BO_3)$ http://crystallography-online.com/structure/1511019 (accessed Apr 22, **2016**).

(138) Legagneur, V.; An, Y.; Mosbah, A.; Portal, R.; La Salle, A. L. G.; Verbaere, A.; Guyomard, D.; Piffard, Y. LiMBO**3** (M= Mn, Fe, Co):: Synthesis, Crystal Structure and Lithium Deinsertion/Insertion Properties. *Solid State Ion.* **2001**, *139* (1), 37–46.

(139) Yamada, A.; Iwane, N.; Harada, Y.; Nishimura, S.; Koyama, Y.; Tanaka, I. Lithium Iron Borates as High-Capacity Battery Electrodes. *Adv. Mater.* **2010**, *22* (32), 3583–3587.

(140) Yamashita, Y.; Barpanda, P.; Yamada, Y.; Yamada, A. Demonstration of Co^{3+}/Co^{2+} Electrochemical Activity in $LiCoBO_3$ Cathode at 4.0 V. *ECS Electrochem. Lett.* **2013**, *2* (8), A75–A77.

(141) Yamada, A.; Iwane, N.; Nishimura, S.; Koyama, Y.; Tanaka, I. Synthesis and Electrochemistry of Monoclinic $Li(Mn_xFe_{1-x})BO_3$: A Combined Experimental and Computational Study. *J. Mater. Chem.* **2011**, *21* (29), 10690.

(142) Kim, J. C.; Moore, C. J.; Kang, B.; Hautier, G.; Jain, A.; Ceder, G. Synthesis and Electrochemical Properties of Monoclinic $LiMnBO_3$ as a Li Intercalation Material. *J. Electrochem. Soc.* **2011**, *158* (3), A309.

(143) Afyon, S.; Kundu, D.; Krumeich, F.; Nesper, R. Nano $LiMnBO_3$, a High-Capacity Cathode Material for Li-Ion Batteries. *J. Power Sources* **2013**, *224*, 145–151.

(144) Afyon, S.; Kundu, D.; Darbandi, A. J.; Hahn, H.; Krumeich, F.; Nesper, R. A Low Dimensional Composite of Hexagonal Lithium Manganese Borate ($LiMnBO_3$), a Cathode Material for Li-Ion Batteries. *J Mater Chem A* **2014**, *2* (44), 18946–18951.

(145) Afyon, S.; Mensing, C.; Krumeich, F.; Nesper, R. The Electrochemical Activity for Nano-$LiCoBO_3$ as a Cathode Material for Li-Ion Batteries. *Solid State Ion.* **2014**, *256*, 103–108.

(146) Lee, Y.-S.; Lee, H. Improved Lithium Storage Capacities of $LiMnBO_3$/C via Simple High-Energy Milling. *Mater. Lett.* **2014**, *132*, 401–404.

(147) Kim, J. C.; Seo, D.-H.; Chen, H.; Ceder, G. The Effect of Antisite Disorder and Particle Size on Li Intercalation Kinetics in Monoclinic $LiMnBO_3$. *Adv. Energy Mater.* **2015**, *5* (8), n/a-n/a.

(148) Kim, J. C.; Seo, D.-H.; Ceder, G. Theoretical Capacity Achieved in a $LiMn_{0.5}Fe_{0.4}Mg_{0.1}BO_3$ Cathode by Using Topological Disorder. *Energy Env. Sci* **2015**, *8* (6), 1790–1798.

(149) Dong, Y. Z.; Zhao, Y. M.; Shi, Z. D.; An, X. N.; Fu, P.; Chen, L. The Structure and Electrochemical Performance of $LiFeBO_3$ as a Novel Li-Battery Cathode Material. *Electrochimica Acta* **2008**, *53* (5), 2339–2345.

(150) Tao, L.; Rousse, G.; Chotard, J. N.; Dupont, L.; Bruyère, S.; Hanžel, D.; Mali, G.; Dominko, R.; Levasseur, S.; Masquelier, C. Preparation, Structure and Electrochemistry of $LiFeBO_3$: A Cathode Material for Li-Ion Batteries. *J Mater Chem A* **2014**, *2* (7), 2060–2070.

(151) Bo, S.-H.; Nam, K.-W.; Borkiewicz, O. J.; Hu, Y.-Y.; Yang, X.-Q.; Chupas, P. J.; Chapman, K. W.; Wu, L.; Zhang, L.; Wang, F.; Grey, C. P.; Khalifah, P. G. Structures of Delithiated and Degraded $LiFeBO_3$, and Their Distinct Changes upon Electrochemical Cycling. *Inorg. Chem.* **2014**, *53* (13), 6585–6595.

(152) Bo, S.-H.; Wang, F.; Janssen, Y.; Zeng, D.; Nam, K.-W.; Xu, W.; Du, L.-S.; Graetz, J.; Yang, X.-Q.; Zhu, Y.; Parise, J. B.; Grey, C. P.; Khalifah, P. G. Degradation and (De)lithiation Processes in the High Capacity Battery Material $LiFeBO_3$. *J. Mater. Chem.* **2012**, *22* (18), 8799.

(153) Afyon, S.; Wörle, M.; Nesper, R. A Lithium-Rich Compound $Li_7Mn(BO_3)_3$ Containing Mn^{2+} in Tetrahedral Coordination: A Cathode Candidate for Lithium-Ion Batteries. *Angew. Chem. Int. Ed.* **2013**, *52* (48), 12541–12544.

(154) Kniep, R.; Engelhardt, H.; Hauf, C. A First Approach to Borophosphate Structural Chemistry. *Chem. Mater.* **1998**, *10* (10), 2930–2934.

(155) van Klooster, H. S. Über Das Verhalten Der Metabor- Und Der Metaphosphorsäure in Den Schmelzen Ihrer Alkalisalze. *Z. Für Anorg. Chem.* **1911**, *69* (1), 122–134.

(156) Kniep, R.; Gözel, G.; Eisenmann, B.; Röhr, C.; Asbrand, M.; Kizilyalli, M. Borophosphates—A Neglected Class of Compounds: Crystal Structures of $M^{II}[BPO_5]$ (M^{II} = Ca, Sr) and $Ba_3[BP_3O_{12}]$. *Angew. Chem. Int. Ed. Engl.* **1994**, *33* (7), 749–751.

(157) Kniep, R.; Will, H. G.; Boy, I.; Röhr, C. 61-Helices Aus Tetraederbändern $\infty 1[BP_2O_8]$: Isotype Borophosphate $M^IM^{II}(H_2O)_2[BP_2O_8]\cdot H_2O$ Und Ihre Dehydratisierung Zu Mikroporösen Phasen $M^IM^{II}(H_2O)[BP_2O_8]$. *Angew. Chem.* **1997**, *109* (9), 1052–1054.

(158) Ternane, R.; Cohen-Adad, M. T.; Panczer, G.; Goutaudier, C.; Dujardin, C.; Boulon, G.; Kbir-Ariguib, N.; Trabelsi-Ayedi, M. Structural and Luminescent Properties of New Ce^{3+} Doped Calcium Borophosphate with Apatite Structure. *Solid State Sci.* **2002**, *4* (1), 53–59.

(159) Wang, G.; Mudring, A.-V. A New Open-Framework Iron Borophosphate from Ionic Liquids: $KFe[BP_2O_8(OH)]$. *Crystals* **2011**, *1* (4), 22–27.

(160) Yang, W.; Li, J.; Pan, Q.; Jin, Z.; Yu, J.; Xu, R. $Na_2[VB_3P_2O_{12}(OH)]\cdot 2.92H_2O$: A New Open-Framework Vanadium Borophosphate Containing Extra-Large 16-Ring Pore Openings and $12^8\,16^6$ Super Cavities Synthesized by Using the Boric Acid Flux Method. *Chem. Mater.* **2008**, *20* (15), 4900–4905.

(161) Yang, M.; Li, X.; Yu, J.; Zhu, J.; Liu, X.; Chen, G.; Yan, Y. $LiCu_2[BP_2O_8(OH)_2]$: A Chiral Open-Framework Copper Borophosphate via Spontaneous Asymmetrical Crystallization. *Dalton Trans.* **2013**, *42* (18), 6298.

(162) Tao, L.; Rousse, G.; Sougrati, M. T.; Chotard, J.-N.; Masquelier, C. $(NH_4)0.75Fe(H_2O)_2[BP_2O_8]\cdot 0.25H_2O$, a Fe^{3+}/Fe^{2+} Mixed Valence Cathode Material for Na Battery Exhibiting a Helical Structure. *J. Phys. Chem. C* **2015**, *119* (9), 4540–4549.

(163) Yaghoobnejad Asl, H.; Stanley, P.; Ghosh, K.; Choudhury, A. Iron Borophosphate as a Potential Cathode for Lithium- and Sodium-Ion Batteries. *Chem. Mater.* **2015**, *27* (20), 7058–7069.

(164) Pauling, L. *The Nature of the Chemical Bond: An Introduction to Modern Structural Chemistry*; The George Fisher Baker Non-Resident Lectureship in Chemistry at Cornell University; Cornell University Press: Ithaca, NY, 1960.

(165) Gutierrez, A.; Benedek, N. A.; Manthiram, A. Crystal-Chemical Guide for Understanding Redox Energy Variations of $M^{2+/3+}$ Couples in Polyanion Cathodes for Lithium-Ion Batteries. *Chem. Mater.* **2013**, *25* (20), 4010–4016.

(166) He, M.; Chen, X. L.; Lan, Y. C.; Li, H.; Xu, Y. P. Ab Initio Structure Determination of New Compound $LiAlB_2O_5$. *J. Solid State Chem.* **2001**, *156* (1), 181–184.

(167) Guo, G.-C.; Cheng, W.-D.; Chen, J.-T.; Zhuang, H.-H.; Huang, J.-S.; Zhang, Q.-E. Monoclinic $Mg_2B_2O_5$. *Acta Crystallogr. C* **1995**, *51* (12), 2469–2471.

(168) Kawano, T.; Morito, H.; Yamada, T.; Onuma, T.; Chichibu, S. F.; Yamane, H. Synthesis, Crystal Structure and Characterization of Iron Pyroborate ($Fe_2B_2O_5$) Single Crystals. *J. Solid State Chem.* **2009**, *182* (8), 2004–2009.

(169) Heller, G. A Survey of Structural Types of Borates and Polyborates. In *Structural Chemistry of Boron and Silicon*; Springer, 1986; pp 39–98.

(170) Becker, P.; Held, P. Crystal Structure of Sodium Scandium Borate, $NaScB_2O_5$. *Z. Für Krist.-New Cryst. Struct.* **2001**, *216* (1–4), 35–35.

(171) Pan, S.; Smit, J. P.; Watkins, B.; Marvel, M. R.; Stern, C. L.; Poeppelmeier, K. R. Synthesis, Crystal Structure, and Nonlinear Optical Properties of $Li_6CuB_4O_{10}$: A Congruently Melting Compound with Isolated $[CuB_4O_{10}]^{6-}$ Units. *J. Am. Chem. Soc.* **2006**, *128* (35), 11631–11634.

(172) Kuratieva, N. V.; Bànki, M.; Tsirlin, A. A.; Eckert, J.; Ehrenberg, H.; Mikhailova, D. New Lithium Copper Borates with BO_3 Triangles: $Li_6CuB_4O_{10}$, $Li_3CuB_3O_7$, $Li_8Cu_7B_{14}O_{32}$, and $Li_2Cu_9B_{12}O_{28}$. *Inorg. Chem.* **2013**, *52* (24), 13974–13983.

(173) Sparta, K. Structural Investigation of Quaternary Copper Oxides with Low Dimensional Magnetic Properties, Ph. D. thesis, Institut für Kristallographie of the RWTH-Aachen, Aachen, Germany, 2003.

(174) JOSH KURZMAN PYROBORATE SUMMARY.pdf.

(175) Kawano, T.; Morito, H.; Yamane, H. Synthesis and Characterization of Manganese and Cobalt Pyroborates: $M_2B_2O_5$ (M = Mn, Co). *Solid State Sci.* **2010**, *12* (8), 1419–1421.

(176) He, M.; Okudera, H.; Simon, A.; Köhler, J.; Jin, S.; Chen, X. Structure of $Li_4B_2O_5$: High-Temperature Monoclinic and Low-Temperature Orthorhombic Forms. *J. Solid State Chem.* **2013**, *197*, 466–470.

(177) Wang, Z.; Zhang, M.; Pan, S.; Wang, Y.; Zhang, H.; Chen, Z. $Li_{0.8}Mg_{2.1}B_2O_5F$: The First Borate Fluoride with Magnesium–oxygen–fluorine Octahedral Chains. *Dalton Trans* **2014**, *43* (7), 2828–2834.

(178) VIENNEY LEGAGNEUR, V. NOUVELLES APPROCHES POUR LA PREPARATION D'ELECTRODE POSITIVE DE BATTERIES AU LITHIUM: CAS

DE QUELQUES OXYDES MIXTES DE VANADIUM LAMELLAIRES ET DE BORATES D'ELEMENT DE TRANSITION. Thèse de doctorat, France, 1999.

(179) Maurelli, S.; Ruszak, M.; Witkowski, S.; Pietrzyk, P.; Chiesa, M.; Sojka, Z. Spectroscopic CW-EPR and HYSCORE Investigations of Cu^{2+} and O^{2-} Species in Copper Doped Nanoporous Calcium Aluminate ($12CaO{\cdot}7Al_2O_3$). *Phys. Chem. Chem. Phys.* **2010**, *12* (36), 10933.

(180) Deringer, V. L.; Tchougréeff, A. L.; Dronskowski, R. Crystal Orbital Hamilton Population (COHP) Analysis As Projected from Plane-Wave Basis Sets. *J. Phys. Chem. A* **2011**, *115* (21), 5461–5466.

(181) Strauss, F.; Rousse, G.; Alves Dalla Corte, D.; Ben Hassine, M.; Saubanère, M.; Tang, M.; Vezin, H.; Courty, M.; Dominko, R.; Tarascon, J.-M. Electrochemical Activity and High Ionic Conductivity of Lithium Copper Pyroborate $Li_6CuB_4O_{10}$. *Phys Chem Chem Phys* **2016**.

(182) Morcrette, M.; Leriche, J.-B.; Patoux, S.; Wurm, C.; Masquelier, C. In Situ X-Ray Diffraction during Lithium Extraction from Rhombohedral and Monoclinic $Li_3V_2(PO_4)_3$. *Electrochem. Solid-State Lett.* **2003**, *6* (5), A80–A84.

(183) Adams, S. From Bond Valence Maps to Energy Landscapes for Mobile Ions in Ion-Conducting Solids. *Solid State Ion.* **2006**, *177* (19–25), 1625–1630.

(184) Prakash, A. S.; Larcher, D.; Morcrette, M.; Hegde, M. S.; Leriche, J.-B.; Masquelier, C. Synthesis, Phase Stability, and Electrochemically Driven Transformations in the $LiCuO_2$ $-Li_2CuO_2$ System. *Chem. Mater.* **2005**, *17* (17), 4406–4415.

(185) Sun, M.; Rousse, G.; Corte, D. D.; Saubanère, M.; Doublet, M.-L.; Tarascon, J.-M. A Fully Ordered Triplite, $LiCuSO_4F$. *Chem. Mater.* **2016**, *28* (6), 1607–1610.

(186) Sun, M.; Rousse, G.; Abakumov, A. M.; Saubanère, M.; Doublet, M.-L.; Rodríguez-Carvajal, J.; Van Tendeloo, G.; Tarascon, J.-M. $Li_2Cu_2O(SO_4)_2$: A Possible Electrode for Sustainable Li-Based Batteries Showing a 4.7 V Redox Activity vs Li^+/Li^0. *Chem. Mater.* **2015**, *27* (8), 3077–3087.

(187) Murugan, R.; Thangadurai, V.; Weppner, W. Fast Lithium Ion Conduction in Garnet-Type $Li_7La_3Zr_2O_{12}$. *Angew. Chem. Int. Ed.* **2007**, *46* (41), 7778–7781.

(188) Thangadurai, V.; Narayanan, S.; Pinzaru, D. Garnet-Type Solid-State Fast Li Ion Conductors for Li Batteries: Critical Review. *Chem. Soc. Rev.* **2014**, *43* (13), 4714.

(189) Lopez-Bermudez, B.; Zeier, W. G.; Zhou, S.; Lehner, A. J.; Hu, J.; Scanlon, D. O.; Morgan, B. J.; Melot, B. C. Lithium-Ion Conductivity in $Li_6Y(BO_3)_3$: A Thermally

and Electrochemically Robust Solid Electrolyte. *J. Mater. Chem. A* **2016**, *4* (18), 6972–6979.

(190) Matsuo, M.; Nakamori, Y.; Orimo, S.; Maekawa, H.; Takamura, H. Lithium Superionic Conduction in Lithium Borohydride Accompanied by Structural Transition. *Appl. Phys. Lett.* **2007**, *91* (22), 224103.

(191) Chen, X.; Li, M.; Zuo, J.; Chang, X.; Zang, H.; Xiao, W. Syntheses and Crystal Structures of Two Pentaborates, $Na_3CaB_5O_{10}$ and $Na_3MgB_5O_{10}$. *Solid State Sci.* **2007**, *9* (8), 678–685.

(192) Chen, X.; Li, M.; Chang, X.; Zang, H.; Xiao, W. Synthesis and Crystal Structure of a Novel Pentaborate, $Na_3ZnB_5O_{10}$. *J. Solid State Chem.* **2007**, *180* (5), 1658–1663.

(193) Shannon, R. t; Prewitt, C. T. Effective Ionic Radii in Oxides and Fluorides. *Acta Crystallogr. B* **1969**, *25* (5), 925–946.

(194) Yu, H.; Pan, S.; Wu, H.; Han, J.; Dong, X.; Zhou, Z. Synthesis, Structure Characterization and Optical Properties of a New Tripotassium Cadmium Pentaborate, $K_3CdB_5O_{10}$. *J. Solid State Chem.* **2011**, *184* (7), 1644–1648.

(195) Yamaguchi, H.; Akatsuka, K.; Setoguchi, M.; Takaki, Y. Structure of Cobalt Dilithium Silicate βII-Li_2CoSiO_4. *Acta Crystallogr. Sect. B* **1979**, *35* (11), 2680–2682.

(196) Arroyo-de Dompablo, M. E.; Armand, M.; Tarascon, J. M.; Amador, U. On-Demand Design of Polyoxianionic Cathode Materials Based on Electronegativity Correlations: An Exploration of the Li_2MSiO_4 System (M = Fe, Mn, Co, Ni). *Electrochem. Commun.* **2006**, *8* (8), 1292–1298.

(197) Irvine, J. T. S.; Sinclair, D. C.; West, A. R. Electroceramics: Characterization by Impedance Spectroscopy. *Adv. Mater.* **1990**, *2* (3), 132–138.

(198) Sinclair, D. C. Characterization of Electro-Materials Using Ac Impedance Spectroscopy. *Bol. Soc. Esp. Cerámica Vidr.* **1995**, *34* (2), 55–65.

(199) Hui, S. (Rob); Roller, J.; Yick, S.; Zhang, X.; Decès-Petit, C.; Xie, Y.; Maric, R.; Ghosh, D. A Brief Review of the Ionic Conductivity Enhancement for Selected Oxide Electrolytes. *J. Power Sources* **2007**, *172* (2), 493–502.

(200) Huangfoenchung, R. Ionic Conduction in LiI-Alumina: Molecular Dynamics Study. *Solid State Ion.* **2004**, *175* (1–4), 851–855.

(201) Maier, J. Nanoionics: Ion Transport and Electrochemical Storage in Confined Systems. *Nat. Mater.* **2005**, *4* (11), 805–815.

(202) Liang, C. C. Conduction Characteristics of the Lithium Iodide-Aluminum Oxide Solid Electrolytes. *J. Electrochem. Soc.* **1973**, *120* (10), 1289.

(203) Sata, N.; Eberman, K.; Eberl, K.; Maier, J. Mesoscopic Fast Ion Conduction in Nanometre-Scale Planar Heterostructures. *Nature* **2000**, *408* (6815), 946–949.

(204) Guo, X.; Sigle, W.; Maier, J. Blocking Grain Boundaries in Yttria-Doped and Undoped Ceria Ceramics of High Purity. *J. Am. Ceram. Soc.* **2003**, *86* (1), 77–87.

(205) Lin, Y.; Fang, S.; Su, D.; Brinkman, K. S.; Chen, F. Enhancing Grain Boundary Ionic Conductivity in Mixed Ionic–electronic Conductors. *Nat. Commun.* **2015**, *6*, 6824.

(206) Ma, C.; Chen, K.; Liang, C.; Nan, C.-W.; Ishikawa, R.; More, K.; Chi, M. Atomic-Scale Origin of the Large Grain-Boundary Resistance in Perovskite Li-Ion-Conducting Solid Electrolytes. *Energy Environ. Sci.* **2014**, *7* (5), 1638.

(207) Loftager, S.; García-Lastra, J. M.; Vegge, T. A Density Functional Theory Study of the Ionic and Electronic Transport Mechanisms in $LiFeBO_3$ Battery Electrodes. *J. Phys. Chem. C* **2016**.

(208) Bervas, M.; Klein, L. C.; Amatucci, G. G. Reversible Conversion Reactions with Lithium in Bismuth Oxyfluoride Nanocomposites. *J. Electrochem. Soc.* **2006**, *153* (1), A159.

(209) Bervas, M.; Badway, F.; Klein, L. C.; Amatucci, G. G. Bismuth Fluoride Nanocomposite as a Positive Electrode Material for Rechargeable Lithium Batteries. *Electrochem. Solid-State Lett.* **2005**, *8* (4), A179.

(210) Badway, F.; Pereira, N.; Cosandey, F.; Amatucci, G. G. Carbon-Metal Fluoride Nanocomposites. *J. Electrochem. Soc.* **2003**, *150* (9), A1209.

(211) Wang, F.; Kim, S.-W.; Seo, D.-H.; Kang, K.; Wang, L.; Su, D.; Vajo, J. J.; Wang, J.; Graetz, J. Ternary Metal Fluorides as High-Energy Cathodes with Low Cycling Hysteresis. *Nat. Commun.* **2015**, *6*, 6668.

(212) Amatucci, G. G.; Pereira, N. Fluoride Based Electrode Materials for Advanced Energy Storage Devices. *J. Fluor. Chem.* **2007**, *128* (4), 243–262.

(213) Filatov, S. K.; Shepelev, Y. F.; Aleksandrova, Y. V.; Bubnova, R. S. Structure of Bismuth Oxoborate $Bi_4B_2O_9$ at 20, 200, and 450°C. *Russ. J. Inorg. Chem.* **2007**, *52* (1), 21–28.

(214) Huang, H.; He, Y.; Lin, Z.; Kang, L.; Zhang, Y. Two Novel Bi-Based Borate Photocatalysts: Crystal Structure, Electronic Structure, Photoelectrochemical Properties, and Photocatalytic Activity under Simulated Solar Light Irradiation. *J. Phys. Chem. C* **2013**, *117* (44), 22986–22994.

(215) Débart, A.; Revel, B.; Dupont, L.; Montagne, L.; Leriche, J.-B.; Touboul, M.; Tarascon, J.-M. Study of the Reactivity Mechanism of $M_3B_2O_6$ (with M= Co, Ni, and Cu) toward Lithium. *Chem. Mater.* **2003**, *15* (19), 3683–3691.

(216) Park, C.-M.; Yoon, S.; Lee, S.-I.; Sohn, H.-J. Enhanced Electrochemical Properties of Nanostructured Bismuth-Based Composites for Rechargeable Lithium Batteries. *J. Power Sources* **2009**, *186* (1), 206–210.

(217) Xianming, W.; Nishina, T.; Uchida, I. Lithium Alloy Formation at Bismuth Thin Layer Electrode and Its Kinetics in Propylene Carbonate Electrolyte. *J. Power Sources* **2002**, *104* (1), 90–96.

(218) Gillot, F.; Boyanov, S.; Dupont, L.; Doublet, M.-L.; Morcrette, M.; Monconduit, L.; Tarascon, J.-M. Electrochemical Reactivity and Design of NiP_2 Negative Electrodes for Secondary Li-Ion Batteries. *Chem. Mater.* **2005**, *17* (25), 6327–6337.

(219) Sammes, N. M.; Tompsett, G. A.; Näfe, H.; Aldinger, F. Bismuth Based Oxide Electrolytes— Structure and Ionic Conductivity. *J. Eur. Ceram. Soc.* **1999**, *19* (10), 1801–1826.

(220) Li, Y.; Trujillo, M. A.; Fu, E.; Patterson, B.; Fei, L.; Xu, Y.; Deng, S.; Smirnov, S.; Luo, H. Bismuth Oxide: A New Lithium-Ion Battery Anode. *J. Mater. Chem. A* **2013**, *1* (39), 12123.

(221) Fiordiponti, P.; Pistoia, G.; Temperoni, C. Behavior of Bi_2O_3 as a Cathode for Lithium Cells. *J. Electrochem. Soc.* **1978**, *125* (1), 14–17.

(222) Eom, J.-H.; Jung, H.-J.; Han, J.-H.; Lee, J.-Y.; Yoon, S.-G. Formation of Bismuth Nanocrystals in Bi_2O_3 Thin Films Grown at 300 K by Pulsed Laser Deposition for Thermoelectric Applications. *ECS J. Solid State Sci. Technol.* **2014**, *3* (10), P315–P319.

(223) Leontie, L.; Caraman, M.; Alexe, M.; Harnagea, C. Structural and Optical Characteristics of Bismuth Oxide Thin Films. *Surf. Sci.* **2002**, *507*, 480–485.

(224) Meethong, N.; Kao, Y.-H.; Carter, W. C.; Chiang, Y.-M. Comparative Study of Lithium Transport Kinetics in Olivine Cathodes for Li-Ion Batteries. *Chem. Mater.* **2010**, *22* (3), 1088–1097.

(225) Larcher, D.; Sudant, G.; Leriche, J.-B.; Chabre, Y.; Tarascon, J.-M. The Electrochemical Reduction of Co_3O_4 in a Lithium Cell. *J. Electrochem. Soc.* **2002**, *149* (3), A234–A241.

(226) Patoux, S.; Vannier, R.-N.; Mairesse, G.; Nowogrocki, G.; Tarascon, J.-M. Lithium- and Proton-Driven Redox Reactions in BIMEVOX-Type Phases. *Chem. Mater.* **2001**, *13* (2), 500–507.

(227) Arroyo y de Dompablo, M. E.; García-Alvarado, F.; Morán, E. $Bi_4V_2O_{11}$ and Related Compounds as Positive Electrode Materials for Lithium Rechargeable Batteries. *Solid State Ion.* **1996**, *91* (3), 273–278.

(228) Oumellal, Y.; Rougier, A.; Nazri, G. A.; Tarascon, J.-M.; Aymard, L. Metal Hydrides for Lithium-Ion Batteries. *Nat. Mater.* **2008**, *7* (11), 916–921.

(229) Meggiolaro, D.; Gigli, G.; Paolone, A.; Reale, P.; Doublet, M. L.; Brutti, S. Origin of the Voltage Hysteresis of MgH_2 Electrodes in Lithium Batteries. *J. Phys. Chem. C* **2015**, *119* (30), 17044–17052.

(230) Gillot, F.; Monconduit, L.; Morcrette, M.; Doublet, M.-L.; Dupont, L.; Tarascon, J.-M. On the Reactivity of $Li_{8-Y}Mn_YP_4$ toward Lithium. *Chem. Mater.* **2005**, *17* (14), 3627–3635.

(231) Boyanov, S.; Bernardi, J.; Gillot, F.; Dupont, L.; Womes, M.; Tarascon, J.-M.; Monconduit, L.; Doublet, M.-L. FeP: Another Attractive Anode for the Li-Ion Battery Enlisting a Reversible Two-Step Insertion/Conversion Process. *Chem. Mater.* **2006**, *18* (15), 3531–3538.

(232) Poizot, P.; Laruelle, S.; Grugeon, S.; Tarascon, J.-M. Rationalization of the Low-Potential Reactivity of 3d-Metal-Based Inorganic Compounds toward Li. *J. Electrochem. Soc.* **2002**, *149* (9), A1212.

(233) Poizot, P.; Laruelle, S.; Grugeon, S.; Dupont, L.; Tarascon, J.-M. Nano-Sized Transition-Metal Oxides as Negative-Electrode Materials for Lithium-Ion Batteries. *Nature* **2000**, *407* (6803), 496–499.

(234) Skinner, S. J.; Kilner, J. A. Oxygen Ion Conductors. *Mater. Today* **2003**, *6* (3), 30–37.

(235) Kitada, A.; Hasegawa, G.; Kobayashi, Y.; Kanamori, K.; Nakanishi, K.; Kageyama, H. Selective Preparation of Macroporous Monoliths of Conductive Titanium Oxides Ti_nO_{2n-1} (N = 2, 3, 4, 6). *J. Am. Chem. Soc.* **2012**, *134* (26), 10894–10898.

(236) Yokota, I. On the Theory of Mixed Conduction with Special Reference to Conduction in Silver Sulfide Group Semiconductors. *J. Phys. Soc. Jpn.* **1961**, *16* (11), 2213–2223.

(237) Guo, X.; Fleig, J.; Maier, J. Separation of Electronic and Ionic Contributions to the Grain Boundary Conductivity in Acceptor-Doped $SrTiO_3$. *J. Electrochem. Soc.* **2001**, *148* (9), J50–J53.

(238) Balaya, P. Size Effects and Nanostructured Materials for Energy Applications. *Energy Environ. Sci.* **2008**, *1* (6), 645.

(239) Young, D.; Ransil, A.; Amin, R.; Li, Z.; Chiang, Y.-M. Electronic Conductivity in the $Li_{4/3}Ti_{5/3}O_4$-$Li_{7/3}Ti_{5/3}O_4$ System and Variation with State-of-Charge as a Li Battery Anode. *Adv. Energy Mater.* **2013**, *3* (9), 1125–1129.

(240) Leriche, J. B.; Hamelet, S.; Shu, J.; Morcrette, M.; Masquelier, C.; Ouvrard, G.; Zerrouki, M.; Soudan, P.; Belin, S.; Elkaïm, E.; Baudelet, F. An Electrochemical Cell for Operando Study of Lithium Batteries Using Synchrotron Radiation. *J. Electrochem. Soc.* **2010**, *157* (5), A606–A610.

(241) Rietveld, H. M. A Profile Refinement Method for Nuclear and Magnetic Structures. *J. Appl. Crystallogr.* **1969**, *2* (2), 65–71.

(242) Rodríguez-Carvajal, J. Recent Advances in Magnetic Structure Determination by Neutron Powder Diffraction. *Phys. B Condens. Matter* **1993**, *192* (1), 55–69.

(243) Momma, K.; Izumi, F. VESTA 3 for Three-Dimensional Visualization of Crystal, Volumetric and Morphology Data. *J. Appl. Crystallogr.* **2011**, *44* (6), 1272–1276.

(244) ICSD - FIZ Karlsruhe https://www.fiz-karlsruhe.de/de/leistungen/kristallographie/icsd.html (accessed Jul 4, 2016).

(245) Murphy, D. M. EPR (Electron Paramagnetic Resonance) Spectroscopy of Polycrystalline Oxide Systems. In *Metal Oxide Catalysis*; Jackson, S. D., Hargreaves, J. S. J., Eds.; Wiley-VCH Verlag GmbH & Co. KGaA, 2008; pp 1–50.

(246) Gerardin, R.; Evrard, O. Mise En Évidence D'un Échange Électronique Entre Fe2+ ET Fe^{3+} Dans Les Oxydes Rhomboédriques AFe_2O_4 Par Spectroscopie Mossbauer DU57Fe. *J. Phys. Chem. Solids* **1983**, *44* (5), 423–429.

(247) Gütlich, J.M.; The Principle of the Mössbauer Effect and Basic Concepts of Mössbauer Spectrometry.

(248) Kresse, G.; Hafner, J. \textit{Ab Initio} Molecular Dynamics for Liquid Metals. *Phys. Rev. B* **1993**, *47* (1), 558–561.

(249) Kresse, G.; Furthmüller, J. Efficiency of Ab-Initio Total Energy Calculations for Metals and Semiconductors Using a Plane-Wave Basis Set. *Comput. Mater. Sci.* **1996**, *6* (1), 15–50.

(250) Dudarev, S. L.; Botton, G. A.; Savrasov, S. Y.; Humphreys, C. J.; Sutton, A. P. Electron-Energy-Loss Spectra and the Structural Stability of Nickel Oxide: An LSDA+U Study. *Phys. Rev. B* **1998**, *57* (3), 1505–1509.

(251) Perdew, J. P.; Burke, K.; Ernzerhof, M. Generalized Gradient Approximation Made Simple. *Phys. Rev. Lett.* **1996**, *77* (18), 3865–3868.

(252) Mueller, T.; Hautier, G.; Jain, A.; Ceder, G. Evaluation of Tavorite-Structured Cathode Materials for Lithium-Ion Batteries Using High-Throughput Computing. *Chem. Mater.* **2011**, *23* (17), 3854–3862.

(253) Dronskowski, R.; Bloechl, P. E. Crystal Orbital Hamilton Populations (COHP): Energy-Resolved Visualization of Chemical Bonding in Solids Based on Density-Functional Calculations. *J. Phys. Chem.* **1993**, *97* (33), 8617–8624.

(254) Deringer, V. L.; Tchougréeff, A. L.; Dronskowski, R. Crystal Orbital Hamilton Population (COHP) Analysis As Projected from Plane-Wave Basis Sets. *J. Phys. Chem. A* **2011**, *115* (21), 5461–5466.

(255) Maintz, S.; Deringer, V. L.; Tchougréeff, A. L.; Dronskowski, R. Analytic Projection from Plane-Wave and PAW Wavefunctions and Application to Chemical-Bonding Analysis in Solids. *J. Comput. Chem.* **2013**, *34* (29), 2557–2567.

(256) Brown, I. D. Recent Developments in the Methods and Applications of the Bond Valence Model. *Chem. Rev.* **2009**, *109* (12), 6858–6919.

(257) Dreyer, W.; Jamnik, J.; Guhlke, C.; Huth, R.; Moškon, J.; Gaberšček, M. The Thermodynamic Origin of Hysteresis in Insertion Batteries. *Nat. Mater.* **2010**, *9* (5), 448–453.